The Influence of Calcium Handling Variability on Cardiac Electrophysiology in Ventricular and Atrial Myocytes

Maxx Holmes

Submitted in accordance with the requirements for the degree of
Doctor of Philosophy

The University of Leeds
Faculty of Biological Sciences
School of Biomedical Sciences

November 2021

Declaration of Authorship

The candidate confirms that the work submitted is his own, except where work which has formed part of jointly-authored publications has been included. The contribution of the candidate and the other authors to this work has been explicitly indicated below. The candidate confirms that appropriate credit has been given within the thesis where reference has been made to the work of others.

Acknowledgements

I would like to begin this thesis by thanking the people I have worked closely with over the past four years and those who have supported me throughout.

My supervisor, Michael Colman, your passionate supervision, support, and relentless questioning throughout has made my PhD an excellent experience. My co-supervisor, Al Benson, for your expertise and support. I would also like to thank the rest of the Leeds Computational Physiology Lab for their “high-brow” humour and genius.

I want to thank the whole cellular cardiology lab, past and present, for their kindness and for making Garstang Level 7 a second home. Specifically, I would like to thank:

Harley and Tom, for your friendship and shared passion for the finer things in life – now the trio of Tenacious 3 theses are complete! Additionally, I would like to thank Tom for his contributions of imaging data.

Ashlea, for your friendship and enforcement of no-work lunches.

Izzy Jayasinghe, for supplying me with microscopy data and your expertise in all things imaging.

Miriam Hurley, for your contributions of imaging data and your endless jabs about our relative definitions of “what time I call this”.

John Coyler and Sarah Calaghan – for your wisdom and assistance throughout and for your help in preparing me for postdoc interviews.

I want to thank my friends for putting up with me throughout and reminding me constantly how awesome being a scientist really is.

Mum, Dad, Georgia, and our two spaniels, Einstein, and Rosie, for their love and endlessly pushing me forward despite having virtually no idea what I am doing.

Finally, my girlfriend, Claire, for your love and support, motivating me and helping me prepare for the next chapter in my life.

Author Publications

Some parts of the work comprising this thesis have been published or have been submitted for publication in joint-author publications, which are listed below. The contributions of co-authors to the work presented within this thesis have been listed in the various method sections and are clearly stated.

The novel method of quantifying heterogeneity in experimental imaging data, and the image-based computational modelling method described in Chapter 3, and then used in Chapter 4 were included in part of our Lab's Methods publication Colman et al. (2020) [1]. The author of this thesis was responsible for the conceptualisation and development of the novel method, toolkit, and modelling method (Section 4.2 in the publication), while the co-authors were responsible for the rest of that publication; including development of the "MSCSF" framework, and imaging data used in Section 4.2.

The SERCA2a heterogeneity study which comprises the entirety of Chapter 4 has been published in the Philosophical Transactions of the Royal Society B, the manuscript was provisionally accepted before the initial submission of the thesis, and published shortly after, prior to the viva examination (Holmes et al. (2021) [2]). The author of this thesis designed the study, developed the toolkit (see Chapter 3), performed all simulations, analysed data, constructed illustrations, and drafted and edited the manuscript. The co-authors provided supervision, developed computational models, performed all experiments, assisted in data analysis, constructing illustrations, and in drafting and editing the manuscript.

The work contained within Holmes et al. (2018) [3] was not directly used in this thesis, however this work is referenced throughout.

Holmes M., Benson AP, Aslanidi OV & Colman MA (2018). A Novel Model of the Rabbit Atrial Myocyte for the Study of Ca^{2+} Mediated Arrhythmia. *Computing in Cardiology (CinC)* ***45***.

Colman MA, **Holmes M**, Whittaker DG, Jayasinghe I, & Benson AP (2021). Multiscale approaches for the simulation of cardiac electrophysiology: I - Sub-cellular and stochastic calcium dynamics from cell to organ. *Methods*, ***185***, 49–59.

Holmes M, Hurley ME, Sheard TMD, Benson AP, Jayasinghe I, & Colman MA (2021) Increased SERCA2a sub-cellular heterogeneity in right-ventricular heart failure inhibits excitation-contraction coupling and modulates arrhythmogenic dynamics. *Philosophical Transactions B.* ISSN 0962-8436 (In Press).

Published Abstracts

Holmes M, Hurley ME, Sheard TM, Stevenson-Cocks HJ, Benson AP, Jayasinghe I, & Colman MA (2020). Sub-cellular Heterogeneity in SERCA Determines Spatial Calcium Dynamics in Cardiomyocytes. *Biophysical Journal*, *118*(3), 172a-173a.

Author Communications

Oral

Holmes, M., Hurley, M.E, Sheard, T.M.D., Stevenson-Cocks, H.J., Benson, A.P., Jayasinghe, I., & Colman, M.A. "Sub-cellular Heterogeneity in SERCA Determines Spatial Calcium Dynamics in Cardiomyocytes." **Biophysical Society 2020 Travel Award**. *Biophysical Society Annual Meeting 2020, San Diego, California, USA.*

Holmes, M. "Dissecting the Multiscale Models of Cardiac Arrhythmias through the use of Computational Modelling" *Post-graduate Symposium, 2021. University of Leeds, UK.*

Holmes, M., Benson, A.P., Aslanidi, O.V. & Colman, M.A. "A Novel Model of the Rabbit Atrial Myocyte for the Study of Ca^{2+} Mediated Arrhythmia" *Computing in Cardiology (CinC), 2018. Maastricht, Netherlands.*

Poster

Holmes M, Hurley ME, Sheard TMD, Benson AP, Jayasinghe I & Colman MA. Sub-cellular heterogeneity and inter-cellular variability has a significant role in calcium dynamics. *Post-graduate Symposium, 2019. University of Leeds, UK.*

Holmes M, Hurley ME, Sheard TMD, Stevenson-Cocks HJ, Benson AP, Jayasinghe I & Colman MA. "Sub-cellular Heterogeneity in SERCA Determines Spatial Calcium Dynamics in Cardiomyocytes." *The Physiology Society Annual Meeting 2019, Aberdeen, UK.*

Holmes M, Benson AP, Aslanidi OV & Colman MA. "A Novel Model of Rabbit Atrial Cardiomyocytes for the Study of Spontaneous Ca^{2+} Release Mediated Arrhythmic Mechanisms." *Biophysical Society, Heart by Numbers 2018. Berlin, Germany.*

Holmes M, Benson AP, Aslanidi OV & Colman MA. "Investigating Ca^{2+} Mediated Arrhythmias in a Computational Model of a Rabbit Atrial Myocyte" *Europhysiology 2020. London, UK.*

Abstract

Excitation-contraction coupling (ECC) in cardiomyocytes is responsible for the heartbeat through the cycling of intracellular Ca^{2+}. The regulation of Ca^{2+} fluxes into and out of the bulk cytoplasm and sarcoplasmic reticulum (SR) through Ca^{2+} transporters (ryanodine receptors, RyR; SR Ca^{2+}-ATPase pump, SERCA2a; Na^{+}-Ca^{2+} exchanger, NCX; and L-type Ca^{2+} channels, LTCCs) is critical to ensuring a stable cardiac output to meet the body's dynamic physiological demands.

Variability in this Ca^{2+} cycling plays an important role in determining whole-cell electrophysiological behaviour and is observed to increase in heart failure (HF) and other pathologies. Advances in microscopy have evidenced sub-cellular heterogeneity in the expression of ECC channels which may explain these variabilities; however, correlating this underlying structure to function presents a major research challenge. Furthermore, the spatial heterogeneity in channel expression has not yet been systematically quantified.

Image-based models present the only systematic method to directly relate spatial Ca^{2+} to underlying channel expression with total control. This thesis describes the development of one such novel approach to quantify the spatial profile of heterogeneity, and furthermore, correlate sub-cellular heterogeneity in channel expression and its functional implications. This novel approach was applied to quantify adaptions to SERCA2a expression in right-ventricular (RV) HF to inform a comprehensive image-based modelling study aiming to predict the functional implications of heterogeneous SERCA2a expression and its remodelling in RV-HF. This provides novel insight into the role of heterogeneous SERCA2a in ECC and arrhythmogenesis.

Single-source, congruent models offer an excellent alternative approach to studying Ca^{2+} variability. Rabbit models are often used for studying abnormal Ca^{2+}-related behaviours due to their electrophysiological similarities to human, and reasonable cost; however, no such model has been developed in rabbit. This thesis presents a novel, lab-specific, congruent model of rabbit atrial electrophysiology developed with the purpose of elucidating the impact of Ca^{2+} variability on whole-cell electrophysiology.

Table of Contents

List of Tables

List of Figures

List of Abbreviations

0D	Zero-dimensional
1D	One-dimensional
2D	Two-dimensional
3D	Three-dimensional
4-AP	4-Aminopyridine
AF	Atrial fibrillation
AP	Action potential
APA	Action potential amplitude
APD_x	Action potential duration / at x% repolarisation
APDR	Action potential duration restitution
ATP	Adenosine Triphosphate
AVN	Atrial-Ventricular Node
BCL	Base cycle length
Ca^{2+}	Calcium Ion
CaT	Calcium transient
CICR	Calcium-induced calcium release
CL	Cycle length
Cl^-	Chloride ions
C_m	Membrane capacitance
CRU	Calcium release unit
CVD	Cardiovascular disease
DAD	Delayed after-depolarisation
DI	Diastolic interval
DNA-PAINT	DNA points accumulation for imaging in nanoscale topography
ds	Dyadic (cleft) subspace
dSTORM	Direct stochastic optical reconstruction microscopy
EAD	Early after-depolarisation
ECC	Excitation Contraction-Coupling
ECG	Electrocardiogram
E_{Rev}	Reversal potential

ERP	Effective refractory period
E_x	Reversal potential for ion x
F	Faraday's constant
FWHM	Full width at half-maximum
G	Gibb's free energy
GRF	Gaussian random field
GUI	Graphical user interface
g_x	Maximal conductance of current x
HF	Heart Failure
H-H	Hodgkin-Huxley
I_{CaL}	L-type calcium current
I_{CaP}	Sarcolemmal calcium pump current
I_{CaT}	T-type calcium current
I_f	Hyperpolarisation-activated (funny) current
I_{KACh}	Acetylcholine-activated potassium current
I_{Kr}	Rapid delayed rectifier potassium current
I_{Ks}	Slow delayed rectifier potassium current
I_{Kur}	Ultra-rapid delayed rectifier potassium current
I_{Na}	Fast sodium current
I_{NCX}	Sodium-calcium exchanger current
I_{NaK}	Sodium-potassium pump current
I_{NaL}	Late sodium current
IP3R	Inositol triphosphate receptor
ISO	Isoprenaline
I_{sus}	Sustained outward current
I_{to}	Transient outward potassium current
I-V	Current-voltage
J_{leak}	Sarcoplasmic reticulum calcium leak flux
J_{rel}	Sarcoplasmic reticulum calcium release flux
jSR	Junctional sarcoplasmic reticulum
J_{up}	Sarcoplasmic reticulum calcium uptake flux
K^+	Potassium ion
K_{SE}	Squared Exponential (Gaussian) kernel

LTCC	L-type calcium channel
LV	Left ventricular/ventricle
MCT	Monocrotaline
MDP	Maximum diastolic potential
MI	Myocardial infarction
mRNA	Messenger RNA
MSCSF	Multi-scale cardiac simulation framework
MUV (dV/dT_{max})	Maximum upstroke velocity
NA	Numerical aperture
Na^+	Sodium ion
NCX	Sodium calcium exchanger
Nif	Nifedipine
nSR	Network sarcoplasmic reticulum
ODE	Ordinary differential equation
ORd	O'Hara Rudy dynamic *model*
OS	Overshoot
PAH	Pulmonary arterial hypertension
PLB	Phospholamban
PSF	Point spread function
R	Ideal gas constnat
RGB	Red-green-blue
RK4	Fourth order Runge-Kutta method
RMP	Resting membrane potential
RV	Right ventricular/ventricle
RV-HF	Right ventricular heart failure
RyR	Ryanodine receptor
SAN	Sinoatrial Node
SCRE	Spontaneous calcium release event
SD	Standard deviation
SE	Standard error
SEM	Standard error of mean
SERCA2a	sarco/endoplasmic reticulum Ca^{2+} ATP-ase pump
sl	Sarcolemmal subspace
SOCE	Store-Operated Ca^{2+} entry

SR	Sarcoplasmic reticulum
SRF	Spatial random field
ss	Subspace
T	Absolute temperature
TA	Triggered activation
T-tubule	Transverse tubule
VF	Ventricular fibrillation
VTK	Visualization Toolkit

1
Introduction

1.1 The Heart of the Problem

The mammalian heart acts as an electro-mechanical double pump, maintaining blood circulation to and from the lungs and the body to deliver oxygen, nutrition, and hormones and expel metabolic waste from trillions of cells [4, 5]. Human hearts rhythmically and reliably beat approximately 100,000 times every single day throughout an entire lifetime. This pumping action is achieved through the synchronous cardiac muscle contraction, driven by an electrical stimulus provided by pacemaker cells [6]. Cardiovascular diseases (CVDs) such as ischaemic heart diseases, cardiac arrhythmias, and heart failure pathologically disrupt the heart's normal function, which may reduce cardiac output, causing the onset or development of disease, or even death in the absence of treatment [7, 8]. The economic and healthcare burdens which CVDs place upon the UK are significant and ever-growing. The British Heart Foundation (BHF) estimates approximately 7.6 million individuals within the UK living with cardiac and circulatory diseases, directly causing more than 160,000 deaths annually, which is approximately a quarter of all yearly mortality in a given typical year [9]. This problem amounts to an estimated economic cost of £19 billion each year, of which £9 billion is directly attributed to the cost of healthcare alone [9].

Scientific advancements in cardiology have been driven forward by the vast prevalence and severity of CVDs in the UK and around the world. Major advancements in experimental methods [5], imaging technologies [10], and computing [11] have allowed for a reductionist approach to be taken, dissecting the multiscale workings of the heart's function in health and disease structurally and mechanistically. Research has, for example, revealed the subcellular distributions of individual Ca^{2+}-handling proteins within the cell membranes of cardiomyocytes [12, 13], discovered the process of excitation-contraction coupling (ECC) [14], and the importance of intracellular calcium (Ca^{2+}) homeostasis in maintaining stable and sufficient cardiac function [15–17].

Despite the enormous research effort to understand ECC and Ca^{2+} cycling, much is left to be determined. Significant variability in Ca^{2+} handling exists across species, cell types, and cells from the same region [18], and despite the fundamental importance of Ca^{2+} cycling, it is unclear how these heterogeneities play a role in determining electrophysiological behaviours. Recent studies highlight the importance of the subcellular expression of Ca^{2+}-handling proteins (ryanodine receptors, RyR; sarcoplasmic reticulum (SR) Ca^{2+}-ATPase pump, SERCA2a; Na^{+}/Ca^{2+} exchanger, NCX; L-type Ca^{2+} channels, LTCC) in determining ECC [19–21]. Recent experimental and computational studies focus primarily on the RyR and transverse-tubule systems, whereas heterogeneity in SERCA2a expression and activity has been largely unexplored. Moreover, quantification of heterogeneous ion channel expression and the extent of the impact of heterogeneity on the electrophysiological properties of cardiomyocytes is unknown and correlating this underlying structure to function in cardiomyocytes presents a major research challenge. Further elucidation of the underlying mechanisms of ECC and how variability influences these dynamics in both health and disease will contribute towards further development of novel pharmacological and surgical treatment of CVDs, ultimately improving the quality of care and the quality of life for those living with CVDs.

Animal models are effective tools for studying cardiovascular diseases or evaluating novel therapies due to the ethical, practical, and financial difficulties associated with using human tissue [22, 23]. While species evolve differently to meet the relative demands to survive, several domesticated species, including mouse, rat, guinea pig, rabbit, pig, and canine, provide useful models for cardiac studies due to functional similarities to human hearts [22, 24, 25]. Rabbit models are particularly attractive for heart failure research as they mimic human electrophysiology and Ca^{2+} handling more similarly than rodent models [26–28] while being cheaper than larger species [26–28]. With all animal models, physiological differences must be considered when extrapolating results for application in human studies. However, with the vast number of animal models available [23], it is possible to devise appropriate strategies, and animal models remain a suitable tool for advancing global understanding of CVDs in humans.

1.2 Computational Cardiology

Due to the heart's electrical conductance and mechanical contraction, understanding the complexities of cardiac behaviour is inherently an interdisciplinary problem. Integrating mathematics, physics, and computing approaches allows researchers to develop specific cardiac systems models *in silico* [29], providing powerful tools to supplement experimental studies in dissecting the mechanisms underlying cardiac function and pathologies [30, 31]. Since the development of the first computational model of a cardiac action potential by Denis Noble nearly 60 years ago [32], the usage of computational models in combination with experimental techniques has increased substantially. Computational models provide a method to investigate the effects of minor changes in individual components at the smallest scales, for example, altering the activation kinetics of individual ion channel currents, which is experimentally difficult to separate from other channels carrying that ionic species in vivo or situ [33]. Linking whole-cell and tissue level behaviour to sub-cellular processes is a major research challenge due to complexities in biological systems, which may involve additional compensatory responses or intricately coupled processes [11]. This challenge is being met with increasingly complex and more biophysically detailed computational models – experiments inform the development and validation of in silico models, which then, in turn, inform future experiments.

The range of existing computational models now includes atrial and ventricular cell models for a range of species such as rat [34, 35], rabbit [30, 36–39], canine [40–42], and human [43–46]. Additional complexities are integrated into modern computational models, including spatiotemporal descriptions of intracellular Ca^{2+} handling [47–53] , detailed descriptions of ionic transporters [46, 54, 55], dynamic ion concentrations [46, 56] and contraction mechanics [57]. Biophysically detailed cardiomyocyte models can be integrated into larger multiscale frameworks incorporating anatomically detailed heart geometries and tissue orientation to investigate how sub-cellular and cellular phenomena influence tissue and whole-organ level behaviour [58]. These advancements have led to cardiac modelling playing an important role in dissecting the underlying mechanisms of cardiovascular diseases [52] and developing pharmacological and clinical interventions to enhance patient outcomes [59, 60].

Despite the financial, ethical, and practical advantages of simulation studies, there are significant limitations that must be considered when using computational models. Models are, by definition, a simplification of the overwhelming complexity that exists; thus, each model has with it a set of assumptions that must be validated against experimental data. Developing a practical electrophysiology model requires a large amount of empirical data, which may come with its own assumptions and complexities. While specific species models do exist, many models are built from experimental data collected from a range of animal models and cell types, and this itself must be considered when interpreting simulation study results even in the context of the same species. Thus, there is considerable merit in developing new electrophysiological models incorporating new experimental observations and data obtained from a single, congruent source.

1.3 Thesis Overview

The work contained within this thesis is motivated by a desire to understand further the role and importance of variability in intracellular Ca^{2+} handling on determining electrophysiological behaviours. The following three objectives can generally summarise the objectives of this thesis:

1. To develop a novel method to quantify the spatial profile of sub-cellular heterogeneity in channel protein expression within a cardiomyocyte.
2. To assess the importance and role of sub-cellular heterogeneity in the sarco/endoplasmic reticulum Ca^{2+}-ATPase (SERCA2a) pump in determining whole-cell electrophysiological behaviour in control and heart failure.
3. To develop a novel, congruent electrophysiological model of the rabbit atrial myocyte suitable to study the relationship between intracellular Ca^{2+} variability and ionic channel variability.

Following this introduction, the scientific background required to understand the work in this thesis is presented in Chapter 2. The general physiology of the heart is discussed, followed by the concepts of cardiac electrophysiology and a description of experimental techniques utilised to determine the electrophysiological properties of hearts and cardiomyocytes. Cardiac arrhythmias and the mechanisms underlying them are then discussed, along with the remodelling associated with CVDs. Finally, a summary of the mathematic methods used to model cardiac electrophysiology and

the numerical methods used to model cardiomyocytes in silico is given, followed by a description of the previous computational models of cardiac electrophysiology and Ca^{2+} handling used in this thesis.

Three results chapters address these three aims in turn. Chapter 3 addresses the first objective of this thesis and describes the development of a novel methodology for quantifying the spatial profile of heterogeneous channel expression in cardiomyocytes. Following this, a novel image-based computational modelling technique is demonstrated. A mathematical background to this technique is given, followed by its adaption for use in analysing immunofluorescent structural microscopy data and the development of an open-source toolkit that implements these techniques. A short application of this new method gives insight into the heterogeneous distribution of multiple key Ca^{2+} handling proteins. The impact of introducing heterogeneous expression in one or more Ca^{2+} handling channels on Ca^{2+} variability is investigated using a computational spatiotemporal Ca^{2+} handling model.

The toolkit developed in Chapter 3 is then used in Chapter 4 to quantify the correlation length scales of heterogeneous SERCA2a expression in rat ventricular cells in control and right-ventricular (RV) heart failure (HF) models. Following this, the O'Hara-Rudy dynamic human ventricular electrophysiology model and the Colman compartmentalised spatiotemporal Ca^{2+} handling model are used in conjunction with the novel image-based modelling technique to study SERCA2a heterogeneity in simulation. Isotropic correlation length scales associated with control and RV-HF remodelling are introduced into the model, and the functional effects on normal and rapid pacing dynamics are investigated and compared with homogeneous models. Mechanisms underlying resulting spatial heterogeneities in cytosolic and SR Ca^{2+} are presented. Finally, an analysis of the role and importance of SERCA2a heterogeneity and correlation length scale in determining the promotion or inhibition of cellular arrhythmogenic phenomenon is presented, related, and compared to previously published studies.

Chapter 5 describes the development of a novel single-cell rabbit atrial electrophysiology model using a congruent dataset for major ionic currents from the Workman laboratory at the University of Glasgow. Parameterisation of novel Hodgkin-Huxley ionic current models based on this experimental data is discussed,

followed by a description of other minor currents incorporated into the model from other sources and the integration of the Grandi-Bers Ca^{2+} handling model. This model is validated against a wide range of experimentally obtained biomarkers, followed by validation through reproducing experimental protocols. Dynamic clamp intervention studies of the outward transient potassium (K^+) current, I_{to}, and L-type Ca^{2+} channel, I_{CaL}, are reproduced alongside pharmacological intervention studies using the I_{to} blocker, 4-aminopyridine (4-AP) and the I_{CaL} blocker, nifedipine (Nif). Discrepancies between simulated and experimental behaviours are discussed, providing insight into gaps in our understanding of rabbit atrial electrophysiology. Lastly, this novel model is used for a preliminary investigation into variability in ionic current and Ca^{2+} handling.

Chapter 6 discusses the novel contributions to science and the major results of the work presented within this thesis. The significance of this work is discussed in a broader context, alongside potential future directions for research using the tools and models developed within this thesis.

2
Background

2.1 The Heart

The first half of the chapter begins with a description of the basic anatomy and physiology of the human heart and circulatory system. The cardiac conduction system is introduced, which provides and propagates the regular electrical stimulation for the heartbeat through inducing synchronous contraction in cardiomyocytes. This electrical conduction, the action potential, is then described along with the intracellular calcium handling system, which determines ECC followed by the characterisation of action potentials and how they differ between atrial and ventricular myocytes. Experimental protocols used to study the heart's electrical activity and the underlying physical structure within cardiomyocytes in health and cardiovascular disease are discussed, explaining different forms of cardiac arrhythmias and the mechanisms underlying them. The second half of this chapter focuses on the underlying concepts involved in mathematically and computationally modelling cardiac electrophysiology. The biophysics of cardiomyocytes are discussed, leading to the introduction of the electric circuit model of the heart. The individual ion channels are modelled using Hodgkin-Huxley formulations, and Markov formulations are explained, leading into the numerical methods utilised to computationally model cardiomyocytes in time. This chapter finishes by describing previously existing models and frameworks utilised and developed upon in this thesis.

2.1.1 Anatomy of the Heart and Circulatory System

The human circulatory system consists of two connected circuits: the pulmonary circuit connects the heart and lungs, facilitating gas exchange to oxygenate the blood and remove waste products (i.e., carbon dioxide), and the systemic circuit functions to provide the body with this oxygenated, nutrient-rich blood to cells around the body, including major organs [5, 61]. Blood circulation is driven by the heart (Figure 2.1 [62]), a muscular, hollow, four-chambered organ located posterior to the sternum in the anterior wall of the chest. These four chambers form a pair of electro-

mechanical pumps which work synchronously. The left and right sides of the heart form these pumps, with their respective atria sitting at the base of the heart, and the ventricles, which extend downwards towards the hearts' apex [4, 6, 61].

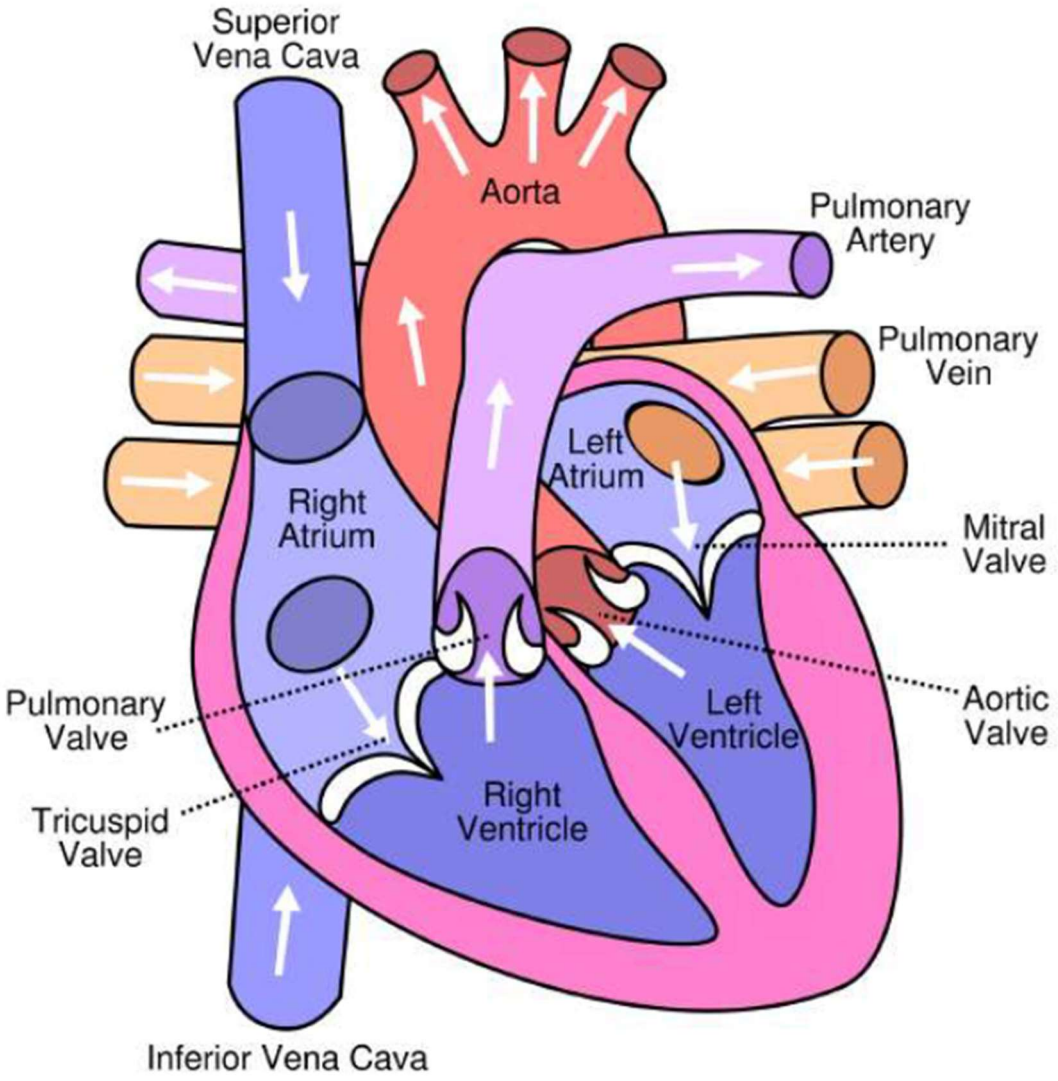

Figure 2.1 Diagram of the human heart.

A labelled diagram of the human heart with arrows indicating the direction of blood flow entering, leaving, or travelling between the heart's four chambers. Image taken from Colman, 2014 [62]

The four chambers connect with the circulatory system via veins and arteries, transporting blood into the atria and away from the ventricles. The left pump drives systemic circulation, pumping blood out of the left ventricle to reach throughout the body, which then returns deoxygenated to the heart's right atrium. This deoxygenated blood is pushed through the mitral valve into the right ventricle,

which pumps the blood to the lungs for gas exchange and ventilation before it returns to the left atrium and ventricle through the tricuspid valve, completing the cycle. The relative thickness of each chamber is determined by its specific function [63]. The left and right atria have thinner walls as they only need to generate smaller pressures to (mostly passively) push the blood through the atrioventricular valves into the ventricles, whereas the ventricles have significantly thicker walls, as the blood is ejected by muscular contraction. Unlike the atria, the ventricles differ in structure, with the left ventricle being significantly thicker than the right ventricle to produce the additional pressure required to pump blood through the larger systemic circulatory system [64]. Each of the valves in the heart is unidirectional, maintaining blood flow by opening and closing depending on pressure differences, preventing backflow [63].

2.1.2 The Cardiac Conduction System and Heartbeat

Cardiomyocytes are electrically excitable and electrically connected through the cardiac conduction system (Figure 2.2); a specialised network of cardiac cells propagating electrical activity throughout the myocardium in such a manner as to ensure coordinated myocardial contraction [65]. Electrical stimuli primarily originate in the sinoatrial node (SAN), located in the right atrium lateral to the superior vena cava junction [6, 66, 67] at rates between 60 and 100 bpm at rest. These stimuli are conducted at speeds of approximately 1 m/s through the atrium towards the atrioventricular node (AVN) located at the interatrial septum (Figure 2.2), the only electrical connection between the atria and ventricles [5]. The AVN is a heterogeneous structure [67] with fast and slow pathways and the penetrating bundle, which has a much lower conduction velocity (~ 0.05 m/s), allowing the atria to contract and fill the ventricles with blood before the ventricular contraction begins [63, 68].

After passing through the AVN, the electrical wavefront reaches the His-Purkinje network – a rapidly conducting network of ventricular myocytes. Electrical impulses are conducted through the bundle of His, and the left and right bundle branches towards the apex of the heart, to the Purkinje fibres, which extend superiorly through the ventricular endocardial surface. This rapid act of spreading conduction from the heart's apex enables almost simultaneous and efficient contraction, forcing the blood upwards into the superior arteries. In the event of SAN failure, other nodal

cells can take over the role of generating electrical stimuli; cardiomyocytes within the AVN can spontaneously generate electrical excitations of rates between 40 – 60 bpm, and Purkinje cells may generate excitations at 20-40 bpm [4].

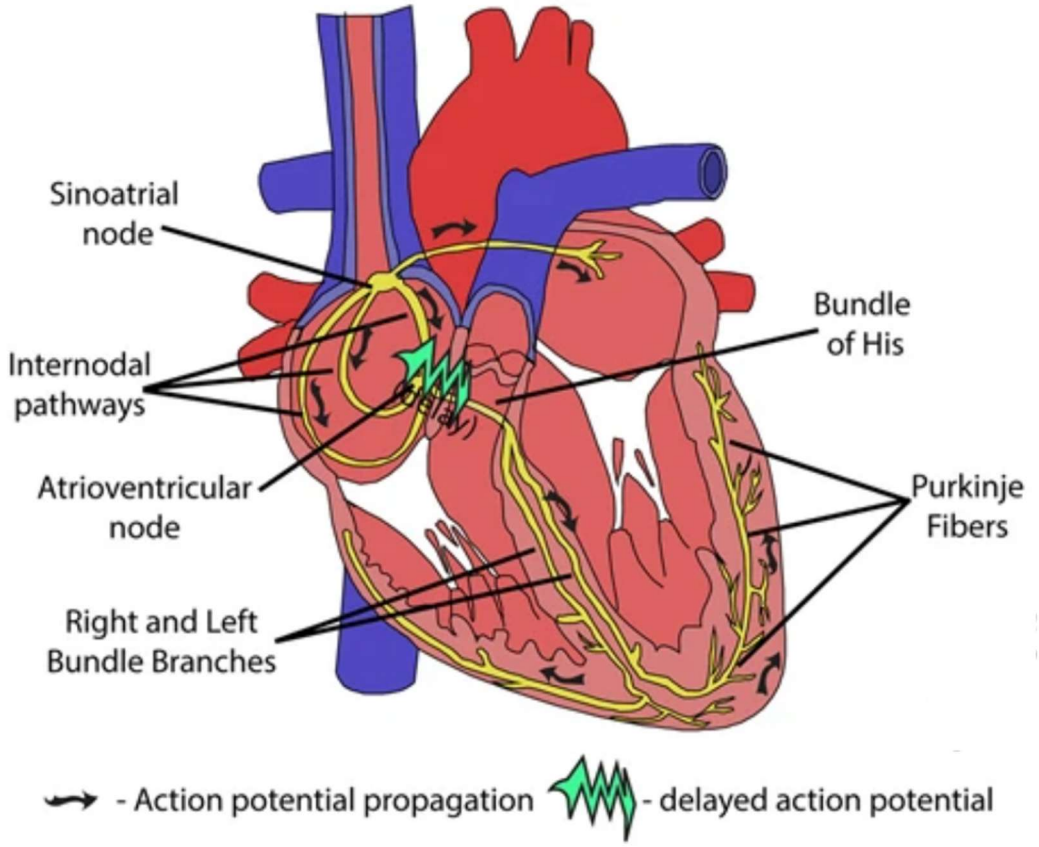

Figure 2.2 Diagram of the cardiac conduction system.

An illustrative representation of the cardiac conduction system. The conduction pathways of the cardiac action potential (AP) propagation are shown by arrows (black, normal; green, delayed). Adapted from Monteiro et al., 2017 [62]

2.1.3 The Cardiomyocyte

Adult mammalian cardiomyocytes (Figure 2.3) are typically between 50-100 μm in length and 10-20 μm in radius [5] and are generally rectangular [68], containing a highly organised network of two types of myofibrils: thick actin filaments and thin myosin filaments. These myofilaments form repeating units called sarcomeres, repeating striations along the length of the cardiomyocyte [69]; during contraction, these myofilaments slide relative to one another, which can be measured in the

distance between two adjacent Z-discs (also known as the sarcomeric length) [70]. This mechanism is known as the sliding filament theory [71]. The intracellular space is filled with a semi-fluid hydrophilic substance known as the cytosol, or cytoplasm [72], in which the organelles such as the mitochondria and nucleus (singular in cardiomyocytes) are embedded, and the free movement of ions and proteins through the intracellular space is facilitated.

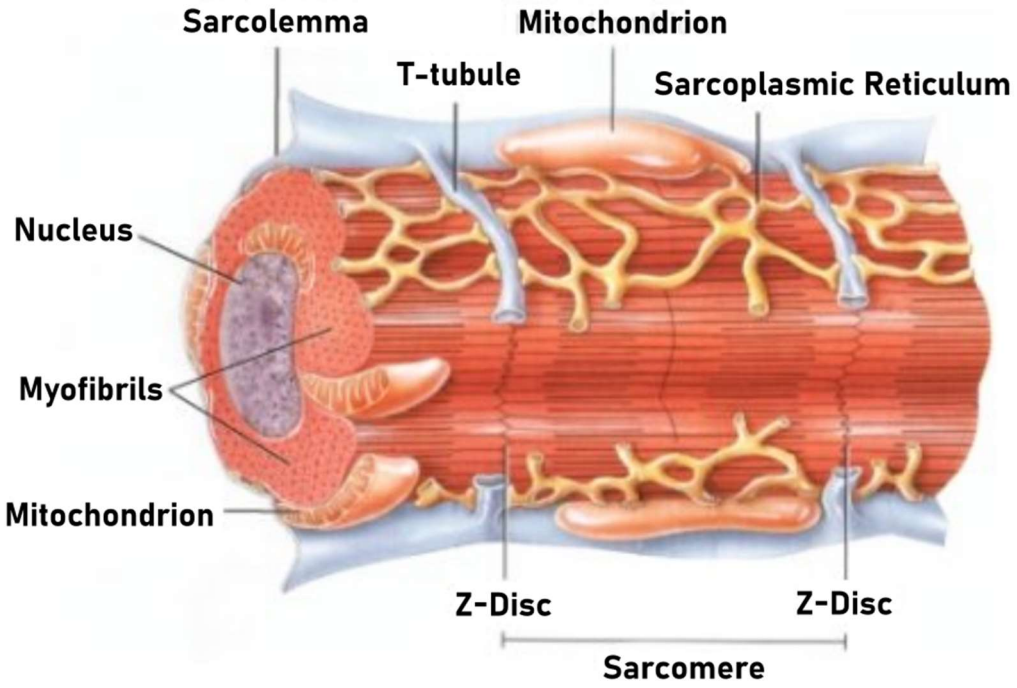

Figure 2.3 Ultrastructure of a cardiomyocyte.

A schematic of a cardiomyocyte. Bundles of contractile myofilaments are surrounded by the sarcoplasmic reticulum (SR) and sarcolemma invaginations known as transverse tubules (t-tubules) and neighboured by mitochondria. T-tubules extend the sarcolemma deep to the centre of cardiomyocytes to ensure the action potential excites every part of the cell. Adapted from Theakston et al. (2010) [69].

The cell membrane, or sarcolemma, envelops the cell and contains many interconnecting invaginations called t-tubules (Figure 2.3) which provide an extensive network for the propagation of the action potentials through the entire thickness of the cell [61]. The t-system accounts for an estimated 27-50% of the total sarcolemma in ventricular myocytes [73, 74], but are more sparse and vary significantly in atrial cells: they have been observed in the atrial cells of large

mammals [75], but vary significantly between species and are heterogeneous even within the same heart [76].

The specific contractility of individual cardiomyocytes is determined by intracellular Ca^{2+} transporters, which control Ca^{2+} entry into and out of the myocyte and the SR [68], an organelle that acts as a Ca^{2+} store and plays a crucial role in intracellular Ca^{2+} cycling. Accordingly, the dimensions and content of cardiomyocytes may vary depending on the heart region: for example, specialised conduction system cells such as those found in the SAN tend to have fewer contractile proteins and are physically smaller [5].

2.2 Cardiac Electrophysiology

The field of cardiac electrophysiology describes the electrophysiological properties of the heart, cardiac tissue, and cardiomyocytes. This includes the transmembrane action potentials and action potential propagation, the flow of ions through specialised ionic channels and the experimental and clinical methods utilised to determine these properties.

2.2.1 The Cell Membrane and Ion Channel Currents

Cellular contraction depends on the intra-cellular cycling of ions (Ca^{2+}, in particular) between the extracellular space, the cytoplasm, and the SR. The cell membrane, or sarcolemma, is a thin, phospholipid bilayer separating the intracellular and extracellular spaces (Figure 2.4) [4, 5, 61]. Pairs of phospholipids making up this barrier consist of a hydrophilic head facing externally and a hydrophobic tail facing internally. Embedded within this membrane are specialised protein transporters selectively permeable to one or two specific ionic species (Figure 2.4). Ions may only flow through these transporters, and thus these proteins are primarily responsible for the excitability of cardiomyocytes.

The three primary types of ionic transporter are the ion channels, ion exchangers and ionic pumps, of which ion channels are the most common in cardiomyocytes. Ionic channels function allosterically – undergoing conformational changes sensitive to different external stimuli (e.g., voltage, stress, neurotransmitters). These conformational changes allow ionic transporters to exist in open, closed, or

inactivated configurations, enabling or inhibiting ions' passive transfer through the sarcolemma [11].

The sarcolemma separates charged ions in the intra- and extracellular spaces, creating an insulating layer, and thus can be considered a capacitor. The embedded ion transporters are analogous to variable resistors, creating an electrical circuit (Figure 2.4) powered by the electrochemical gradient between the intra- and extracellular spaces [77]. The electrical modelling of the sarcolemma as a capacitor will be explained in further detail in Section 2.6.

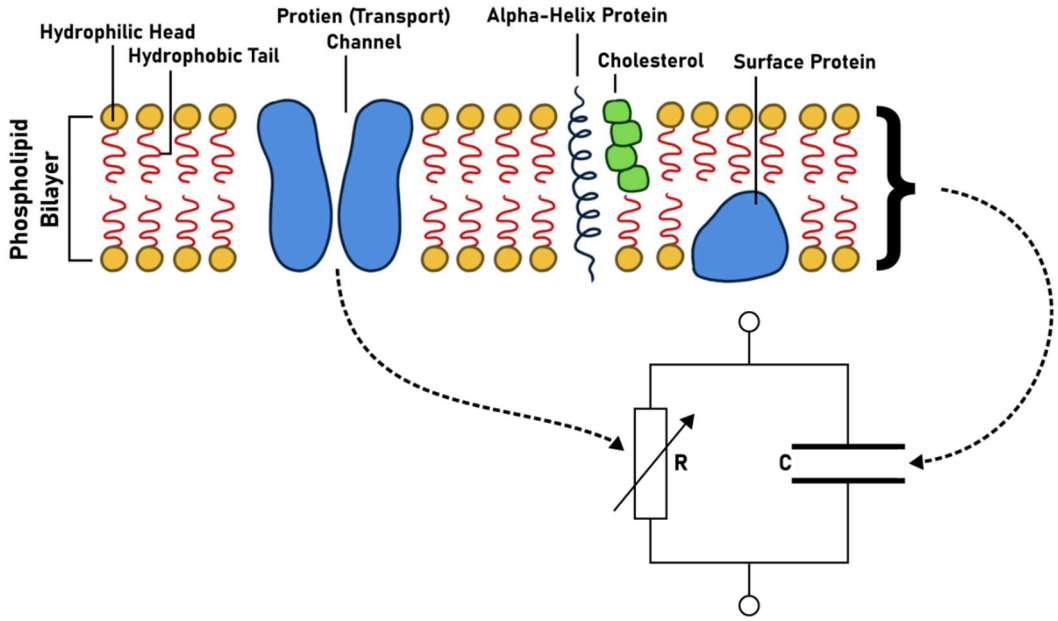

Figure 2.4 Diagram of a plasma membrane.

A simplified schematic of a cell's lipid membrane. Illustrated is the structure of the phospholipid bilayer, protein transport channels, and other proteins embedded within the membrane. A simple circuit diagram illustrates the electrical function of the membrane and transport channels. R, resistance; C, capacitance.

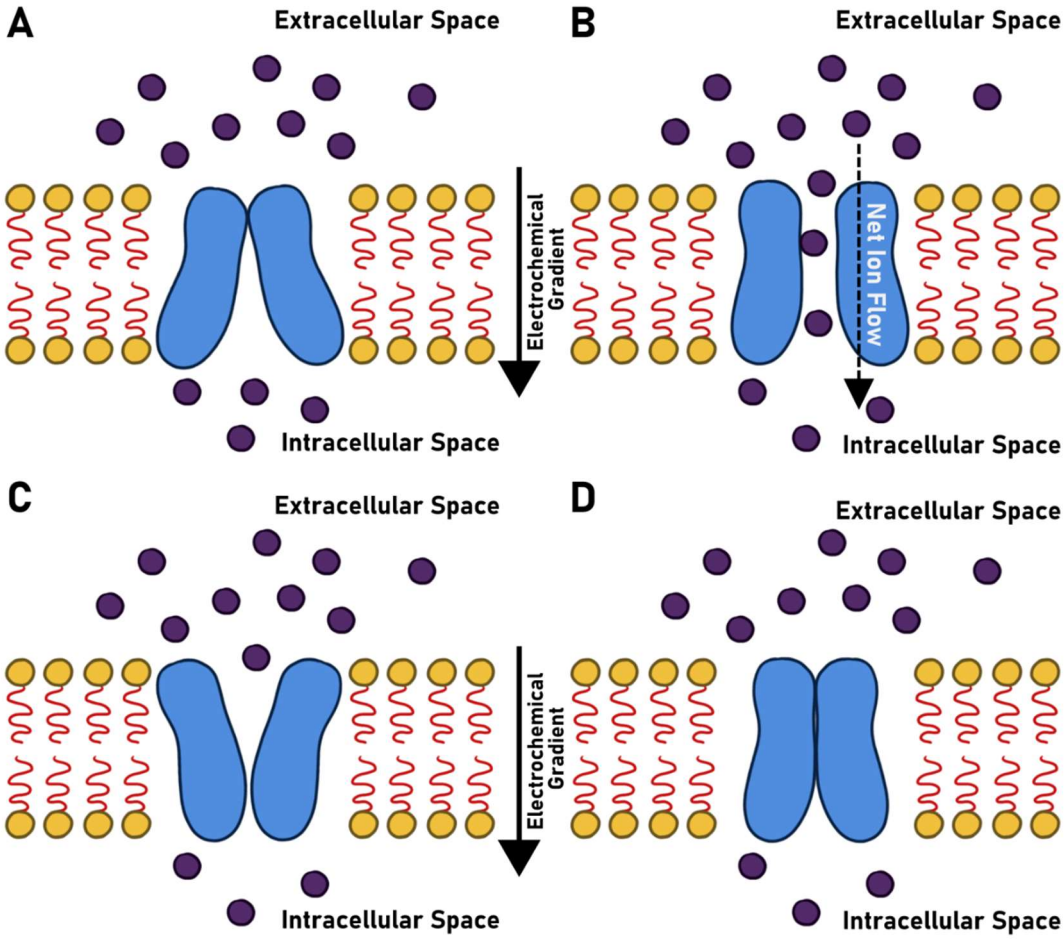

Figure 2.5 Diagram of ionic channel function.

A simplified illustration of an ion channel with both activation and inactivation gates in the four possible configurations. The ions this channel is specifically permeable to are shown as purple circles, with solid arrows indicating the direction of the electrochemical gradient and dashed arrows indicating the net flow of ions through the channel. A – The channel is neither activated nor inactivated. B – The channel is activated and not inactivated. C - The channel is both activated and inactivated. D – The channel is not activated and is inactivated.

Figure 2.5 illustrates an example of a voltage-gated ionic channel with both activation and inactivation processes (represented by the relative opening and closing of each side) referred to as activation and inactivation gates, respectively. An electrochemical gradient is present across the sarcolemma towards the intracellular chamber, so the net flow of ions moves into the cell. Starting from the rest state (where neither gate is activated, Figure 2.5A), the protein responds to the

electrochemical gradient and ion channel morphology changes due to conformational changes in the protein folding, activating the activation gate (Figure 2.5B). While the inactivation gate remains inactive, ions may passively flow through the channel in the direction of the electrochemical gradient. As conditions change, the inactivated gate activates (Figure 2.5C), ions can no longer flow through the channel, followed by the inactivation of the activation gate, stopping ions from entering the channel (Figure 2.5D). Ions may not flow through the channel if either the activation gate is inactive or if the inactivation gate is active, thus resulting in behaviours such as an inactivation recovery time in which no current flows regardless of external factors.

Ionic pumps and exchangers function differently: ionic pumps facilitate the active transport of ions (including against the electrochemical gradient) through the consumption of adenosine triphosphate (ATP). In contrast, ionic exchangers are neither active nor passive and instead co-transport ions using the energy of an ion flowing along its electrochemical gradient to move another species against it. All three types of ionic transporter and their respective activation and inactivation kinetics play critical roles in shaping the morphology of the action potential [11].

Ionic transporter currents in the heart are carried primarily by sodium (Na^+), calcium (Ca^{2+}), and potassium (K^+) ions; however, some ionic transporters also transport chloride (Cl-) ions [6]. By convention, inward and outward currents are defined by the net flow of charge: inward currents act to depolarise the cell membrane by increasing intracellular charge (influx), generally carried by Na^+ and Ca^{2+}, while outward currents repolarise it through the movement of positively charged ions out of the cell (efflux), generally carried by K^+. Multiple ionic channels are permeable for the same ion species, differing through their activation and inactivation kinetics or the type of transport. Therefore, the total current for each ionic species is calculated as the net flow of ions through all channels permeable to that ionic species.

Table 2.1 provides a summary of the primary ionic transporters involved in cardiomyocytes. Ionic transporters are complex proteins that contain a folded unique sequence of amino acids; messenger RNA (mRNA) is involved with the genetic coding of these sequences, and thus mRNA levels can indicate channel expression levels and how these are modulated in disease [78].

Symbol	Name	Type	Permeability
I_{Na}	Fast-acting inward sodium current	Ion Channel	Na^+
$I_{Na,L}$	Late acting inward sodium current	Ion Channel	Na^+
$I_{Ca,L}$	L-type calcium current	Ion Channel	Ca^{2+}
$I_{Ca,T}$	T-type calcium current	Ion Channel	Ca^{2+}
I_{to}	Transient outward current	Ion Channel	K^+
I_{Kur}	Ultra-rapid potassium Current	Ion Channel	K^+
I_{Kr}	Rapid delayed rectifying potassium current	Ion Channel	K^+
I_{Ks}	Slow delayed rectifying potassium current	Ion Channel	K^+
I_{K1}	Inwardly rectifying potassium current	Ion Channel	K^+
I_{KACh}	Acetylcholine activated potassium current	Ion Channel	K^+
I_f	Hyperpolarisation activated funny current	Ion Channel	Na^+, K^+
$I_{NaCA/INCX}$	Sodium calcium exchanger current	Ion Exchanger	Na^+, Ca^{2+}
I_{NaK}	Sodium potassium pump current	Ion Pump	Na^+, K^+
I_{CaP}	Sarcolemmal calcium pump current	Ion Pump	Ca^{2+}

Table 2.1 Primary sarcolemmal ion channel currents in cardiomyocytes

2.2.2 The Cardiac Action Potential

The cumulative action of transmembrane ion fluxes across the sarcolemma is the cyclical electrical excitation of the sarcolemma – the cardiac action potential (AP) (Figure 2.6). This transient change in transmembrane potential stimulates the processes required to induce cellular contraction. The morphology of action potentials is heterogeneous among cell types [79] and different species; general mechanisms are consistent in mammalian hearts; however, the relative contributions

(and indeed, whether specific channels are present) vary [80]. This inter-species heterogeneity has implications for the uses of animal models in cardiac research: observations and studies done on animal models may not necessarily be extrapolated to humans or other species [81]. The distinct phases of the action potential remain consistent among species, though, and are illustrated in Figure 2.6 and described below.

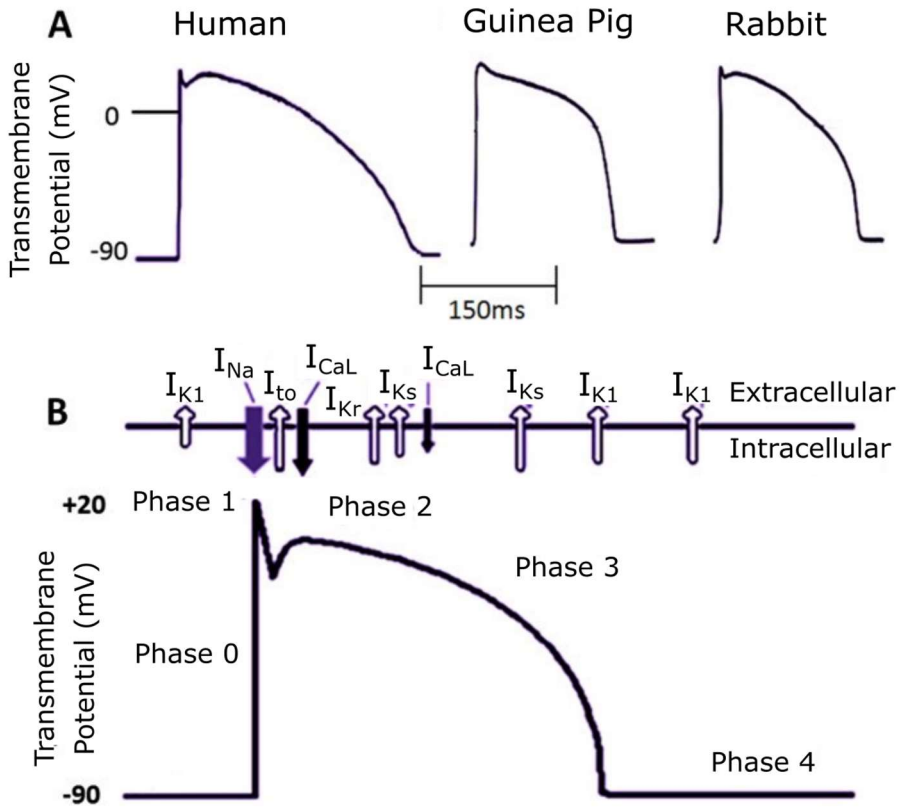

Figure 2.6 Cardiac action potentials.

A – Ventricular action potentials in human, guinea pig and rabbit. B – The primary ionic currents at each stage of the action potential (AP) in a human ventricular myocyte (upper) and a labelled AP trace (lower). Phases of the cardiac AP are labelled. Arrows indicate the direction of net ionic flux associated with the specific ionic channels. Adapted from Joukar, 2021. [80]

The resting membrane potential (RMP) of the AP is the membrane potential without perturbation from inward Na^+ and Ca^{2+} channels; this occurs at phase 4 and is typically in the region of -70 to -85 mV, described as a state where the sarcolemma is hyperpolarised. The RMP is maintained primarily through the action of the inwardly rectifying K^+ current, I_{K1}, the exchanger, I_{NCX}, and background currents

[45, 82]. A suprathreshold electrical stimulus activates the voltage-gated Na^+ channels and initiates rapid depolarisation in transmembrane potential through the fast sodium current, I_{Na}, known as phase 0. In Phase 1, I_{Na} quickly inactivates, and the transient outward K^+ current, I_{to}, becomes active and produces the initial rapid repolarisation through the efflux of K^+ ions. The balance between the inward L-type Ca^{2+} current, I_{CaL}, and the efflux of time-dependent K^+ currents, the slow and rapid delayed rectifier, and ultra-rapid K+ currents (I_{Ks}, I_{Kr}, and I_{Kur}, respectively), produces the phase 2 plateau period. The final stage of repolarisation, phase 3, occurs once I_{CaL} inactivates and the K^+ currents act to fully repolarise the AP back to the RMP, primarily through the action of I_{K1}. The AP is an all-or-nothing phenomenon; the threshold potential to activate the voltage-gated Na^+ channels must be met, or an AP will not be triggered [66]. Electrophysiological heterogeneity in ionic transporters' relative expression or activity manifests in action potential morphologies: for example, a prolonged plateau period indicates larger I_{CaL}, whereas a higher RMP would indicate a drop in I_{K1}.

2.2.3 Excitation-Contraction Coupling and Intracellular Ca^{2+} Cycling

The periodic cycling of Ca^{2+} in cardiac cells couples electrical excitation and mechanical contraction; this process is called ECC [16]. The heart beats 60-100 times per minute at rest, so cellular contraction must be fast and efficient. The delicate equilibrium of Ca^{2+} fluxes maintains the homeostasis of this system through specialised ionic transports, fluxes that must be tightly regulated to ensure a stable, sufficient cardiac output to meet the body's dynamic physiological demands [14, 17].

Unlike other ionic species, Ca^{2+} has an intracellular storage organelle, the SR. The SR is a tubular network that envelops the contractile filaments (Figure 2.3) and forms specialised junctional regions with the transverse and axial tubule system called Ca^{2+}-release units (CRUs) or dyads (Figure 2.7) [83]. Ion channels and pumps found throughout the SR are similar in structure to those in the sarcolemma; RyR, Ca^{2+}-sensitive channels, clustered in arrays embedded in the SR membrane, are analogous to ligand-gated ion channels, while the SR-Ca^{2+} ATPase 2a (SERCA2a) is analogous to an ionic Ca^{2+} pump.

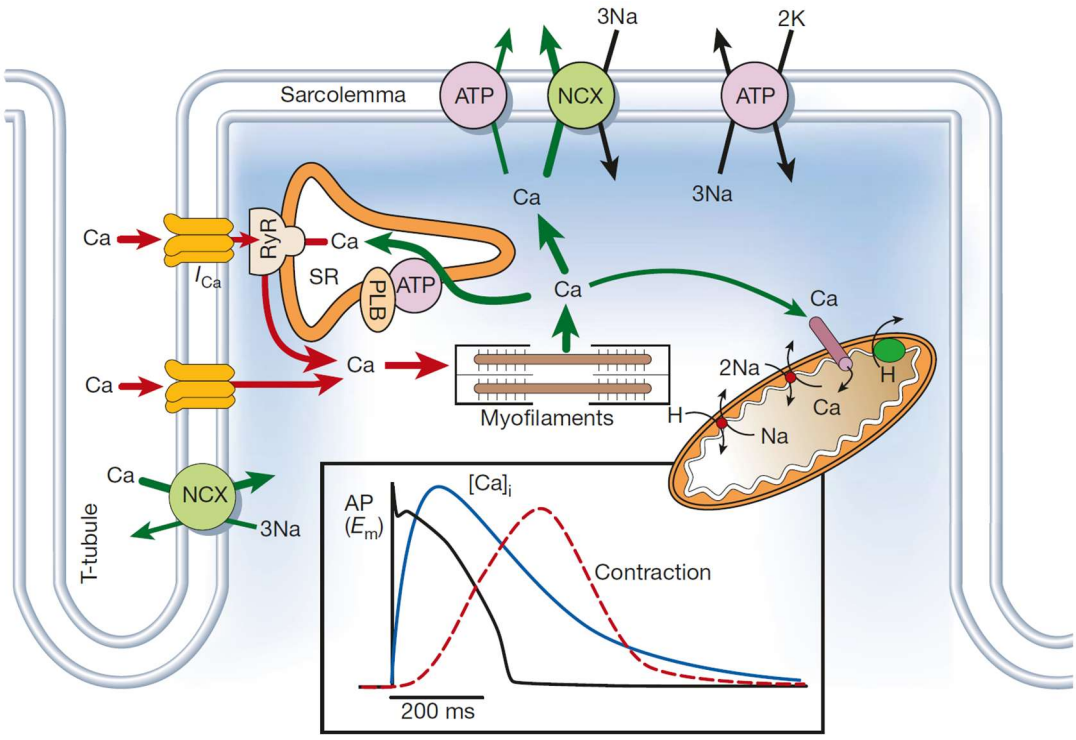

Figure 2.7 Schematic of excitation-contraction coupling.

A schematic of intracellular Ca^{2+} cycling and the mechanisms of excitation-contraction coupling (ECC) in cardiomyocytes. An influx of Ca^{2+} ions through L-type Ca^{2+} channels (LTCC) promotes further Ca^{2+} release from the sarcoplasmic reticulum (SR) by binding with ryanodine receptors (RyR). Increased intracellular Ca^{2+} facilities contraction and then returns to the SR through the action of the SR-Ca^{2+} ATPase pump (SERCA2a) or extruded from the cell by the Na^{+}-Ca^{2+} exchanger (NCX). The inset panel shows the time course of the action potential, intracellular Ca^{2+} transient (CaT), and contractile force. Taken from Bers, 2002. [14]

The SR and its transport proteins play a critical role in the regulation of Ca^{2+} ions within cardiomyocytes. The RyR are clustered at dyads, forming a coupled system with local L-type Ca^{2+} channels (LTCC) approximately 15 nm apart [84], juxtaposing an inlet for the AP near the SR-Ca^{2+} store. During phase 2 of the cardiac action potential, an influx of Ca^{2+} ions occurs through the LTCCs, increasing the local concentration of Ca^{2+} ions in the proximity of the RyRs. RyRs bind with local intracellular Ca^{2+}, activating them and releasing a quantity of Ca^{2+} from the SR into the intracellular space, called a Ca^{2+} spark. This process is known as Calcium-Induced-Calcium-Release (CICR) [14] (Figure 2.7). This increase in local cytosolic

Ca^{2+} propagates centripetally throughout the cell via a diffusion-reaction process, recruiting other CRUs through the process of CICR in a centripetal wave (known as a Ca^{2+} wave). These individual Ca^{2+} release events are summated to produce the Ca^{2+} transient (CaT) [73]; this mechanism is known as the local control model of ECC. Ca^{2+} release is spatially heterogeneous, with complex subcellular Ca^{2+} gradients [85]. This heterogeneity plays an important role in the susceptibility of cardiomyocytes to produce cellular arrhythmogenic phenomena, such as spontaneous Ca^{2+} release events or CaT alternans – beat to beat alternations in the CaT, which may impact AP morphology.

The increased concentration of cytosolic Ca^{2+} ions facilitates the binding of Ca^{2+} with troponin-C, which trigger the contraction of the myofibrils. Ca^{2+} unbinds from contractile proteins (troponin) before being taken back into the SR by SERCA2a (~75% of CaT magnitude) or extruded from the cell by the Na^{+}-Ca^{2+} exchanger (I_{NCX}, ~ 18-19% of CaT magnitude) and the sarcolemmal Ca^{2+}-ATPase channel (I_{CaP}, ~ 1-2%). Sequestration of Ca^{2+} into the SR and extracellular space enables cellular relaxation and restores SR Ca^{2+} content for the following contraction cycle. A representative time-course of the CaT is shown with the associated AP and contraction in Figure 2.7.

The above description is a simplification of the Ca^{2+} cycle sufficient to understand the work in this thesis. Additional protein complexes, intracellular buffers, and interactions are involved in the process of myofibril contraction, and the internal structure of the SR is not described as it is sufficient to consider it as a Ca^{2+} reservoir. For further information on ECC, the reader is directed to Bers' review [14], and for information on the sliding filament model of muscle contraction, the reader is directed to Cooke's review [71].

2.2.4 Action Potential Propagation

Cardiomyocytes are connected end-to-end by specialised junctions known as intercalated discs, which facilitate the propagation of the electric stimulus through one cardiomyocyte to its neighbours via gap junctions. These specialised cell-to-cell contracts mediate conduction through tightly clustered intracellular channels that directly couple the cytosol of neighbouring myocytes [5, 86]. These junctions allow the myocardium to function as a single organ (sometimes described as a functional syncytium – a cytoplasmic mass formed by cell fusion [4, 6, 87]). Gap junctions

permit the flow of ions from the intracellular space of one cell to its neighbour – this flow of charge can produce sufficient depolarisation in the neighbouring cardiomyocyte to reach the threshold for I_{Na} to activate and initiate an action potential; this mechanism allows the propagation of action potentials through the cardiac conduction system and across the myocardium. The orientation of cardiomyocytes in fibres results in anisotropic AP propagation through cardiac tissue; gap junctions are far more abundant at the longitudinal ends of cardiomyocytes. Thus, conduction is faster along the parallel axis of the fibre perpendicularly; thus, the cardiac conduction system contains a high degree of fibre organisation [87] to facilitate rapid conduction, particularly in the ventricles where conduction needs to be faster. Atrial cardiomyocytes are more disorganised in comparison, and these structural differences may play a role in slower observed conduction.

Differences in fibres' morphological and functional properties also influence conduction velocities, such as the diameter and number of cells, relative ion channel expression, and ionic currents [82]; SAN myocytes, which are physically smaller than atrial or ventricular myocytes, have a lower conduction velocity. Connexin proteins that form the gap junctions [88] are observed to be significantly lower in expression within the SAN and AVN, thus reducing the level of inter-myocyte coupling, which may play a role in the slowing of conduction to allow the ventricles to fill before contraction. Disruption to inter-myocyte coupling due to disease remodelling in cardiovascular conditions such as ischaemia or heart failure may play a role in arrhythmogenesis [86].

2.2.5 Action Potential Characterisation

AP morphology is heterogeneous between species, cell type, and even cells of the same type. As such, it is important to characterise APs within a consistent framework such that the AP of two cells or the impact of pharmacological or therapeutic intervention on the AP can be quantifiably measured. Figure 2.8 illustrates some of the most common biomarkers used in non-pacemaking cardiomyocytes; each of these is described below, along with typical values found in human cardiomyocytes.

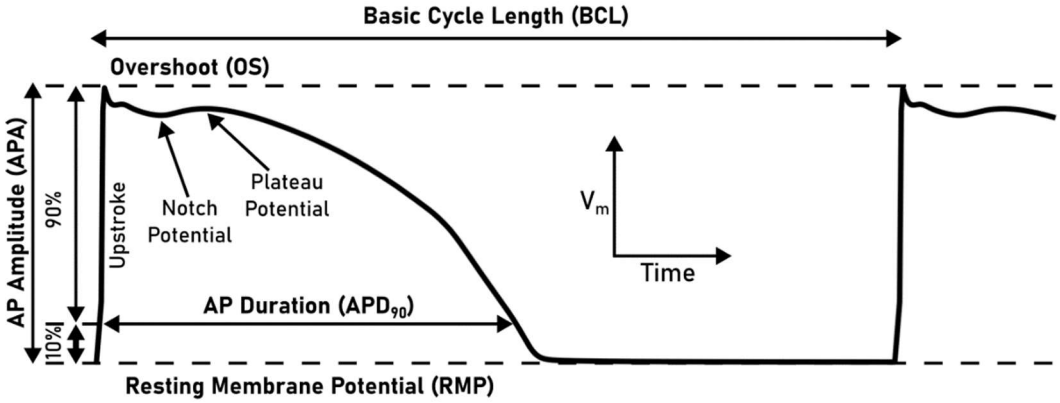

Figure 2.8 Action potential characterisation.

An illustration of common biomarkers utilised to characterise and compare cardiac action potentials in non-pacemaking cardiomyocytes. These measurements provide a tool to quantify differences between species, cell types, and pharmacological or pathophysiological effects.

Resting Membrane Potential (RMP) is the stable resting transmembrane potential of an excitable cell, i.e., a cell that has not been stimulated and is the most negative potential of a non-pacemaking myocyte. RMP is related to the excitability of a cardiomyocyte (the higher the RMP, the close the membrane is to the threshold to trigger an AP), and thus it is an important measurement. In human cardiomyocytes, this typically ranges between -90 and -60 mV.

Overshoot (OS) describes the maximum membrane potential reached during phase 0 of the action potential – the rapid upstroke due to the activation of I_{Na}. In human cardiomyocytes, the OS is typically between 10 and 50 mV.

Maximum Upstroke Velocity (MUV) is the maximum rate of change of transmembrane potential during the AP, occurring during the rapid upstroke phase (hence "maximum upstroke velocity"), and is commonly referred to by the symbol dV/dT_{max}. In humans, this value is typically between 100 and 300 V/s. The MUV relates to the excitability of the cardiomyocyte and has implications for the conductance velocity of the AP across tissue fibres.

Action Potential Amplitude (APA) describes the total size of the transmembrane potential, calculated from the difference in potential between the RMP and the OS. Typically between 90 to 120 mV.

Action Potential Duration (APD) measures transmembrane repolarisation in time. APD is defined as the time interval between the MUV and some level of repolarisation. Common biomarkers are defined using percentage repolarisation, such as APD_{90}, the duration between the MUV and 90% repolarisation, or specific transmembrane potentials. APD_{90} is a common choice relating to the full time-course of an AP, and in humans is typically between 200-400 ms, though other values are often used, such as APD_{30} and $APD_{50,}$ to assess the width of the phase 2 plateau in potential.

Basic Cycle Length (BCL) is the time interval between two consecutive, successful APs. BCL is the inverse of heart rate; as such, it may vary considerably from person to person (a resting heart rate of 60 – 100 bpm would give a BCL of 1000 ms – 600 ms), and from species to species (rodents, for example, generally have much higher resting heart rates).

In addition to the above, additional biomarkers are used to characterise pacemaking cells. There are a few important distinctions to make, such as the lack of a stable resting potential (RMP) in pacemaking cells and a significantly shallower upstroke velocity (MUV). Instead of using RMP, the **Maximum Diastolic Potential (MDP)** refers to a pacemaking cell's most negative transmembrane potential; thus, APA is calculated as the difference between the RMP and MDP. A shallower upstroke velocity makes the exact point of initiation harder to quantify, and as such, the APD is defined to start at the MUV in pacemaker cells.

2.2.6 Refractoriness and Restitution

There exists a period following the elicitation of an AP in a cardiomyocyte, in which a second AP cannot be initiated, regardless of the strength of the electrical stimulus due to the inactivation kinetics of I_{Na}, known as the absolute refractory period [6]. The inactivation gate of I_{Na} activates at high transmembrane potentials and has a relatively long time constant, so there exists a significant delay in its return to the resting position in which no flux through I_{Na} channels exists, and the rapid upstroke does not occur. During phase 3 of the AP, the cell enters the relative refractory period, where some I_{Na} channels have returned to their resting configuration. Smaller APs are possible to initiate in this period but require a much greater stimulus than a normal AP.

The effective refractory period encompasses both the absolute and relative refractory periods and describes a time in which a full action potential cannot occur, thus cannot propagate through cardiac tissue. This refractoriness is an important property of cardiomyocytes. It protects against premature stimuli from resulting in the dyssynchronous contraction of cardiac tissue [89] or from sustained tetanic contraction of cardiac muscle (such as occurs in skeletal muscle), allowing for a diastolic phase and effective normal pumping action in the functioning myocardium.

The pacing rate of a cardiomyocyte influences its' AP characteristics and the morphology of the plateau phase known as AP restitution. It is a critical property of cardiac cells, which describes the hearts' ability to adapt to changes in heart rate to preserve diastole and maintain sufficient cardiac output in exercise and the 'fight or flight' response [90].

At higher pacing rates (i.e., higher heartbeat frequency or a shorter BCL), the APD of a cardiomyocyte shortens. The APD restitution curve describes the time-dependent recovery of the APD as a function of BCL [91], and the shape and gradient of this curve can indicate a predisposition to arrhythmogenesis. Steep APD restitution curves have been shown to give rise to pro-arrhythmic AP and CaT alternans: beat-to-beat oscillations in APD or CaT amplitude, alternating between two or more values.

A commonly used method to characterise the dynamic properties of the specific electrophysiology of a cardiomyocyte is the S1-S2 protocol [92] (Figure 2.9). A regular pacing stimulus (S1) is applied to a cell or tissue preparation and paced at a fixed BCL until a steady state is achieved before the preparation is perturbed by a shortly coupled secondary stimulus (S2) with varied diastolic intervals (DI), defined as the BCL minus APD_{90} of the AP initiated by S1. Plotting AP biomarkers against the length of this diastolic interval gives the restitution curve for that property. Another common method is to produce a steady-state restitution curve by pacing the preparation at different pacing rates to steady-state and then plotting those biomarkers as a function of BCL.

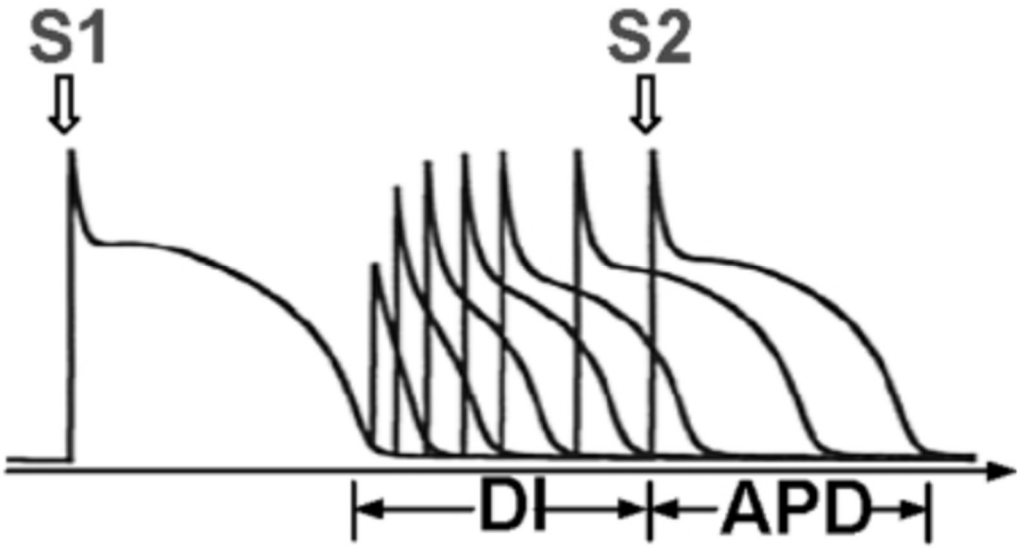

Figure 2.9 S1-S2 protocol for electrical restitution

S1-S2 protocol for determining APD restitution. A cardiomyocyte is paced to a steady-state with a repeated, steady stimulus (S1) before being perturbed by a secondary stimulus (S2) at a given diastolic interval (DI). Adapted from Qu et al. (2010) [92].

2.2.7 Re-entry

Re-entry describes a self-sustaining excitation waveform in cardiac tissue propagating in a rapid circuitous movement, where the effective refractory period of a region has ended before the excitation wavefront reaches that region in its circulation [93]. This self-perpetuating waveform requires a unidirectional conduction block, which is typically caused by heterogeneous refractoriness in cardiac tissue, resulting from dyssynchronous excitation in tissue or the presence of a non-conducting obstacle such as ischemic scar tissue or the junction of a vein or an artery. The wavelength of an excitation wavefront is important in determining whether re-entry may occur, calculated using the conduction velocity of the wavefront and the effective refractory period (ERP), which gives a distance parameter behind the wave in which the propagation of the AP cannot occur [29, 94].

The two conceptual re-entry models are the leading circle model (Figure 2.10A) and the spiral wave model (Figure 2.10B). The leading circle model describes re-entry occurring around some non-conducting obstacle. The circumference of the obstacle

must be larger than the wavelength to sustain re-entry so that when the waveform completes its circuit around the obstacle, the upcoming region has recovered from the previous ERP. The spiral wave model describes re-entry around a functional core (which may be stable or meander), in which the wave rotates around the core circuitously.

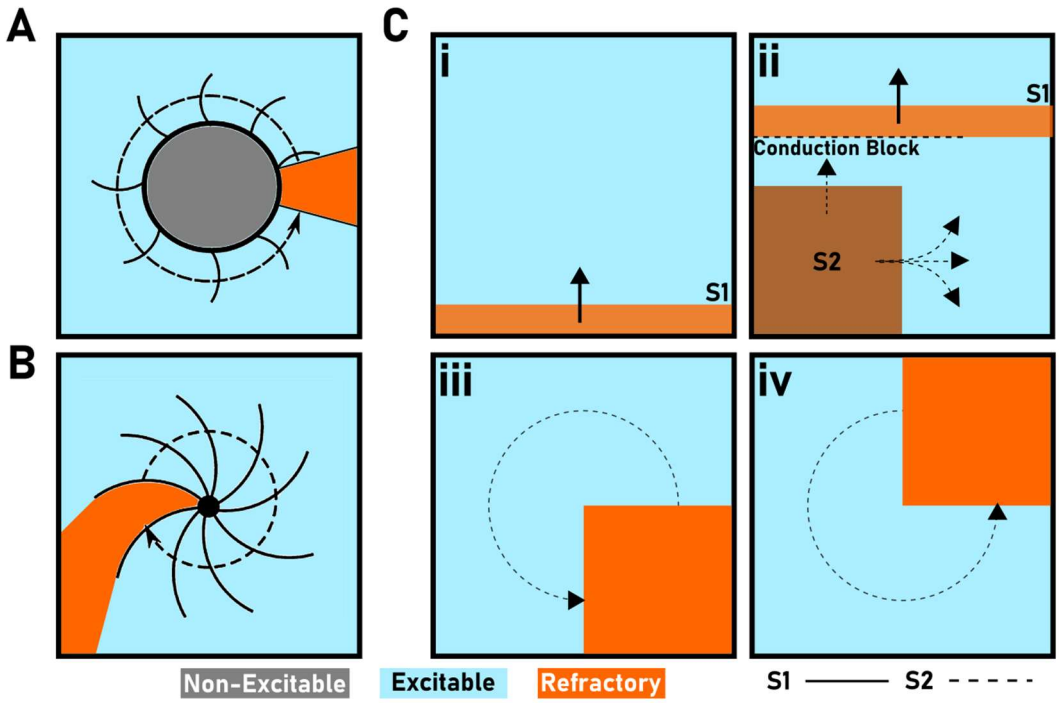

Figure 2.10 Mechanisms of re-entrant excitation

Illustration of several re-entry mechanisms. A – Leading circle theory of re-entry: excitation wavefront circulates an anatomic obstacle whose circumference is larger than the excitation wavelength. B – The spiral wave model: excitation wavefronts propagate outwards from a functional core, rotating around it. C – Spiral wave re-entry through S1-S2 stimulation in a 2D patch of tissue. (i) A stimulus (S1) is applied at the bottom edge of the tissue, stimulating an excitation wave propagating upwards; (ii) a secondary stimulus is applied in the bottom left quadrant of the tissue, inducing a unidirectional conduction block as the S2 wavefront cannot propagate through the region in the effective refractory period (ERP) following the S1 wavefront; (iii) S2 wavefront excites the upper portion of the tissue once it has recovered from S1 refractoriness; (iv) The S2 waveform continues circulating in the 2D tissue, exciting zones as they exit the ERP phase. Panels A and B based on Colman, 2014. [62]

An example of the spiral wave mechanism is illustrated in Figure 2.10C. In this example, a regular stimulus (S1) applied at the bottom of this tissue initiates an S1 waveform propagating uniformly from the bottom to the top (Figure 2.10Ci). The secondary stimulus (S2) is then applied to a local region of the tissue, propagating centripetally from its epicentre; when the S2 wavefront reaches the S1 wavelength, unidirectional conduction block parallel to the S1 waveform occurs, forcing the S2 wavefront to propagate perpendicularly, spreading outwards once the top of the tissue has repolarised (Figure 2.10Cii). The region S2 originated in has now repolarised, and so the wave circles back on itself, forming a self-sustaining spiral wave re-entry (Figure 2.10Ciii-iv).

2.2.8 Differences in Atrial and Ventricular Cells

The studies in this thesis utilise single-cell cardiomyocyte models of atrial and ventricular cells; hence it is important to understand some of the key electrophysiological differences between these cell types. Figure 2.11 illustrates example differences in atrial and ventricular AP morphology and their underlying ionic currents [95].

Prominent morphological differences in the atrial AP compared to a ventricular AP is a less prominent plateau phase due to an average reduction in Ca^{2+} influx and a shallow repolarisation phase caused by comparatively smaller repolarising K^+ currents, particularly I_{K1} (Figure 2.11) [96, 97]. There are additional currents present within the human atrial myocardium: the ultra-rapid delayed rectifier K^+ current, I_{Kur}, which has faster activation kinetics >2 orders of magnitude higher than the rapid-counterpart, I_{Kr} [98]; the acetylcholine-activated potassium current, I_{KACh} , which flows through a ligand-gated ionic channel which activates in the presence of acetylcholine [99]. I_{Kur} and I_{KACh} are considered promising therapeutic targets for developing anti-arrhythmic drugs as conventional K^+ blockers used in arrhythmia therapies may prevent AF but have pro-arrhythmic effects in the ventricles leading to morbid outcomes [100, 101].

The intracellular Ca^{2+} handling system of atrial cardiomyocytes also differs significantly from ventricular cardiomyocytes [102]. In atrial myocytes, during the AP, the systolic CaT rises initially at the cell surface and then propagates via CICR to the cell's interior as a wave. This pattern of peripheral to centre propagation is observed in de-tubulated ventricular myocytes [103] and de-tubulated

cardiomyocyte models [3], suggesting that the relative absence of t-tubules in atrial cardiomyocytes [85, 104] (though some studies note the presence and heterogeneity of the t-system in large mammalian species [75]) is responsible in part for the differences in Ca^{2+} handling machinery. Intracellular CaTs are observed to have a smaller magnitude in atrial cells [102], which decay more rapidly due to an increased rate of SR Ca^{2+} uptake by SERCA2a compared to ventricular cells.

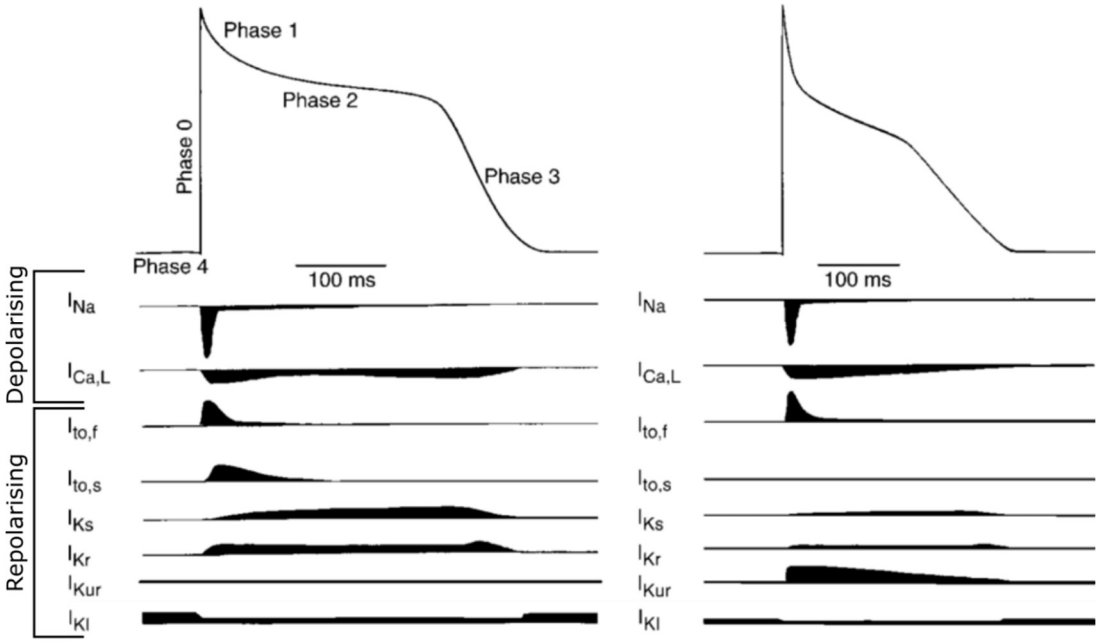

Figure 2.11 Comparing atrial and ventricular action potentials and ionic currents

Action potential (AP) waveforms and underlying ionic currents in adult human ventricular (left) and atrial (right) cardiomyocytes. Adapted from Nerbonne and Kass, 2005. [95]

2.2.9 Electrocardiogram

The electrical activity within the heart is powerful enough to be detected through electrodes placed on the body. An electrocardiogram (ECG) describes this heart's electrical activity at rest over time, measured through a series of electrodes, and has evolved into a vital diagnostic tool that forms the basis for much of modern clinical cardiology [61]. Interpreting established biomarkers on the ECG allows clinicians to analyse and diagnose cardiac disorders and arrhythmias using non-invasive methods. These methods continuously evolve, allowing clinicians to make more informed decisions and improve patient care [105, 106].

The ECG of a normal human heartbeat at rest (Figure 2.12) comprises distinct phases that represent the electrical activity of each stage of the heartbeat. The first phase, the p-wave, denotes atrial depolarisation, with the start of the P wave representing the initiation of the excitation waveform from the SAN. The QRS complex is tri-phasic and represents ventricular depolarisation. Due to the difference in magnitudes of the p-wave and QRS complex, atrial repolarisation is often masked and not visualised. Following the QRS complex is the T wave which represents ventricular repolarisation. The activity of the SAN and AVN pacemaker cells is not visible on the ECG due to the relative sizes of electrical activity but is implied through the presence of the distinct phases.

Established ECG characteristics allow clinicians to identify and diagnose rhythmic disorders and diseases in the heart. The PR interval (Figure 2.12) is the time-interval starting at the initiation of the p-wave (excitation initiated in the SAN) to the downwards deflection at Q (AVN conduction through to the ventricles) represents the time taken for the excitation waves to conduct through the AVN from initiation, and thus prolongation of the PR interval is thus indicative of AVN dysfunction. The prognosis of patients with long-term PR interval prolongation is associated with increased risks of developing atrial fibrillation [107]. The QRS complex describes the total activation time in the ventricles, and prolongation of the width of the QRS complex gives information about potential dysfunction in ventricular condition or the existence of arrhythmias [108]. The QT interval is defined as the period between the initial ventricular depolarisation and the complete repolarisation of the ventricles, thus indicating the total time of ventricular activation and recovery. Significant shortening or prolongation of the QT interval is known as short- or long-QT syndrome [109], respectively, which is associated with an increased predisposition to ventricular arrhythmias, and thus a significant risk of sudden cardiac death.

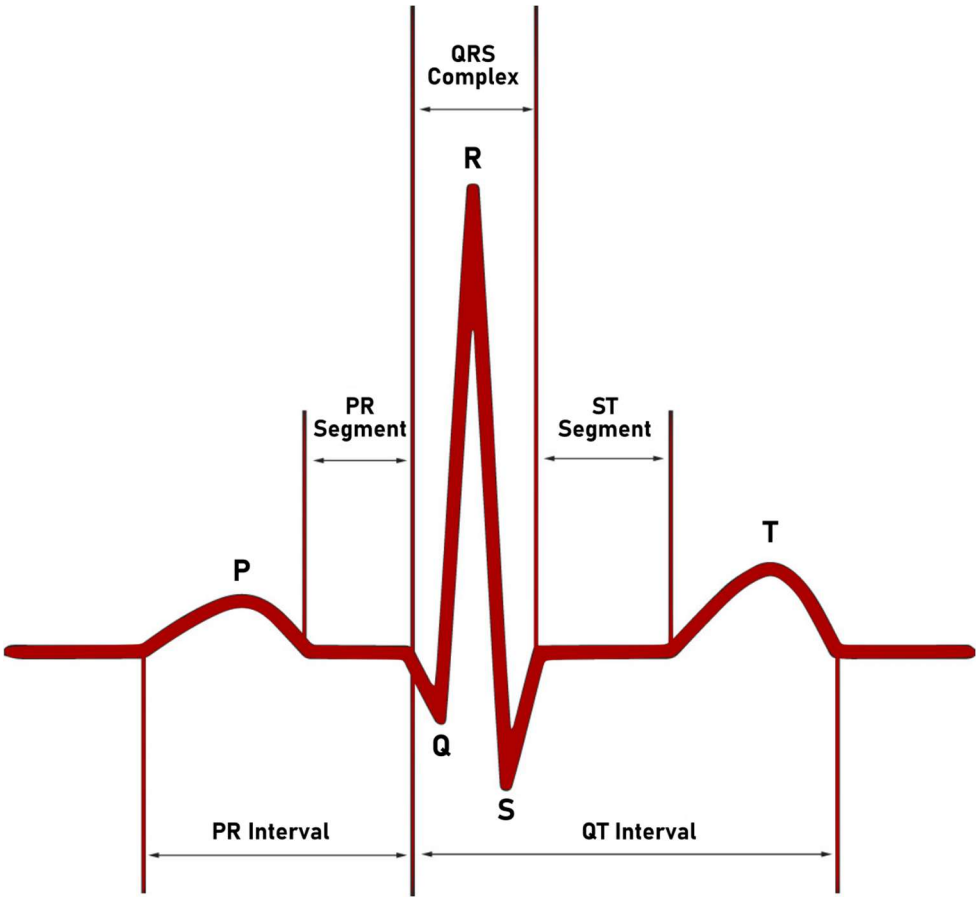

Figure 2.12 Electrocardiogram (ECG) waveform.

A diagram showing a typical electrocardiogram (ECG) waveform and the clinical biomarkers used to characterise ECGs. Adapted from Zheng et al. (2020) [105].

2.2.10 Voltage Clamping

It is difficult to accurately measure the net flux through the many ionic transporters within cardiomyocytes: many ion channels, for example, are voltage-gate, and thus the action of these channels varies in both space (along the membrane) and time (at some specific point on the membrane). The voltage clamp is an experimental method used to characterise these ionic currents by holding transmembrane potential at a set voltage, manipulated independently of the ionic currents, thus allowing the current-voltage (I-V) relationships of membrane channels to be studied.

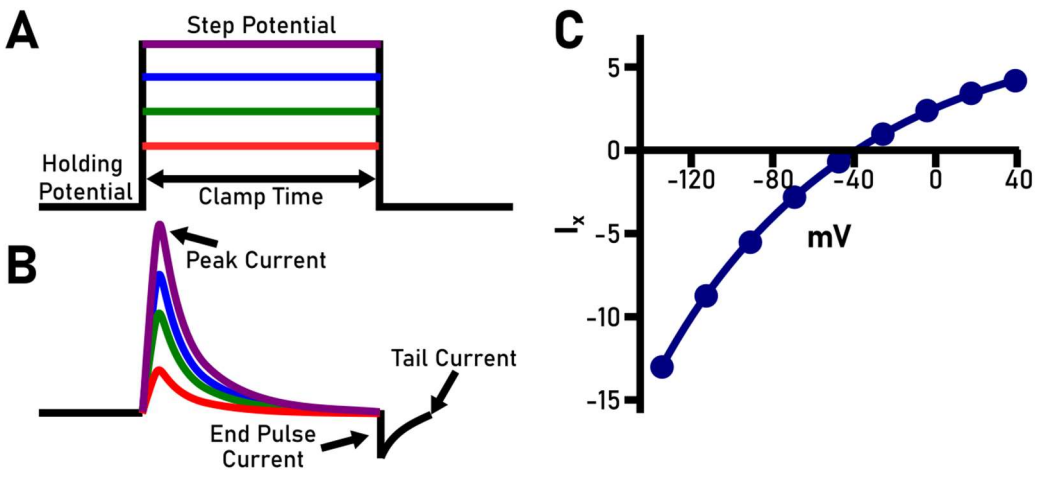

Figure 2.13 Voltage clamping protocol

A simple example of a voltage clamping protocol. Important features are labelled. A – Multi-step voltage clamp with four clamp-step functions. B – Current trace examples from the above voltage clamp, colours correspond to clamp-step in A. C – An example of a current-voltage (I-V) relationship. The voltage clamp current needed to hold a clamp step, I_xIs plotted against the step voltage (mV) for each clamp-step tested.

Voltage clamping is achieved through measuring currents at a series of "step-voltages" using intra- and extracellular electrodes to maintain a specific potential difference across the sarcolemma (Figure 2.13A). In a simple version of the voltage clamp, the cell membrane is set at a holding voltage and then instantaneously stepped to the step-voltage for some time (clamp time) held through applying an equal and opposite current to clamp the potential at this step-voltage (Figure 2.13B) [110]. The preparation is then returned to the holding voltage, and the process is repeated for a series of step-voltage, which encompass the physiological ranges of activation for the specific current being measured. An I-V relationship (Figure 2.13C) for a specific ion channel can thus be measured by plotting the specific current needed to equilibrate the transmembrane potential at each step-voltage, giving an indication of the voltages ranges a current is most active in, but not the value of the current, as most ion channel currents are time-dependent.

2.3 Cardiac Arrhythmias and Heart Failure

2.3.1 Arrhythmic Cardiovascular Diseases

Arrhythmia means ‘without rhythm’; thus, a cardiac arrhythmia is simply a variation from the normal heart rhythm, which is physiologically unjustified [111]. The heart contracts in a highly coordinated and effective manner in normal health and is robust enough to adjust to the body’s dynamic physiological demands in normal activities like exercise. Disruption to the heart’s normal rhythm, i.e., a cardiac arrhythmia, reduces cardiac output and is one of the most frequent causes of morbidity in patients living with CVDs; many CVDs are either a result of arrhythmias or lead to the development of arrhythmias. Thus, it is important to understand the prognosis and treatment of these arrhythmias and study the arrhythmogenic triggers underlying their development. Figure 2.14 illustrates the ECG patterns for common cardiac arrhythmic disorders [112].

2.3.1.1 Bradycardia

Bradycardia refers to abnormally slow heart rates, typically defined as a resting heart rate below 50 - 60 beats per minute [113, 114]. The lack of sufficient blood flow to the body can result in fatigue, dizziness and fainting in bradycardic patients and put additional strain on other organs. Severe bradycardias may result in cardiac arrest and sudden cardiac death without treatment. Typically, bradycardia is unresponsive to pharmacological interventions; however, it can be treated with the implantation of a pacemaker.

2.3.1.2 Tachycardia

Tachycardias refer to abnormally fast heart rates, typically defined as a resting heart rate above 100 beats per minute, although this varies throughout childhood development [115]. Tachycardia can be induced due to a fast-paced ectopic focus or the presence of re-entrant excitation. Like bradycardia, abnormally fast heart rates result in reduced cardiovascular output, with patients experiencing angina (pain and discomfort due to a lack of blood flow to the heart), palpitations, fainting. Sustained ventricular tachycardia is associated with an increased risk of sudden cardiac death [116] and is associated with the electrical and structural remodelling of cardiomyocytes, predisposing the heart to the development of fibrillation.

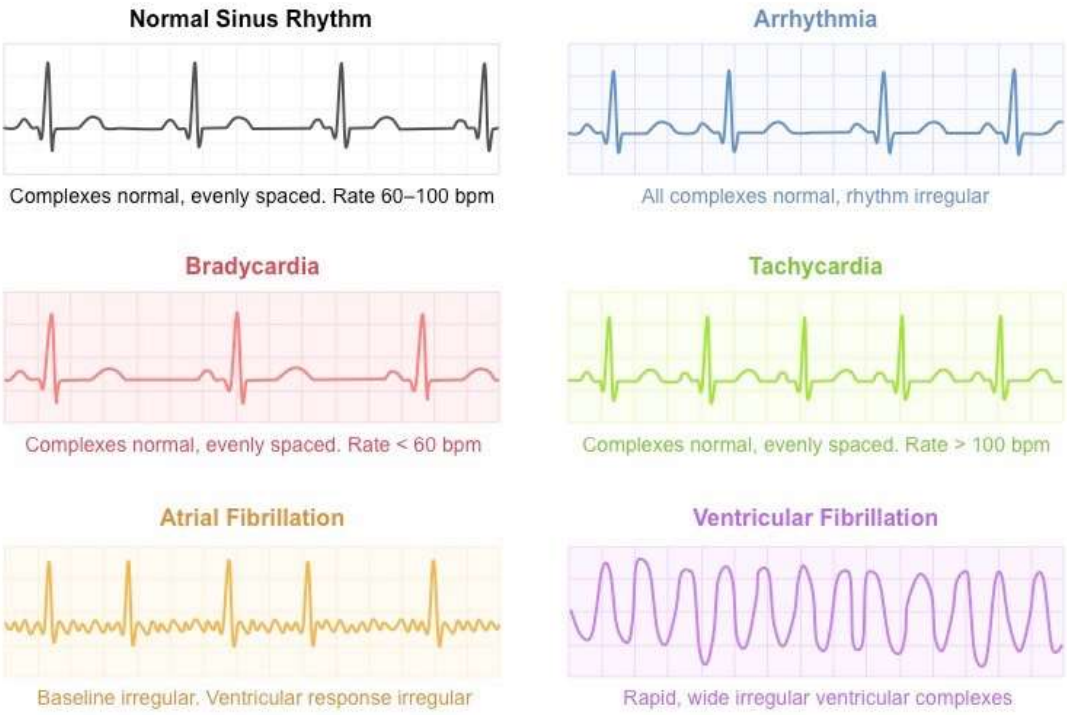

Figure 2.14 Examples of ECGs in normal sinus rhythm and arrhythmia

Illustrative ECGs display the visual differences between normal sinus rhythm and cardiac rhythmic disorders. Taken from [112].

2.3.1.3 Fibrillation

Fibrillation refers to fast and irregular activation of the heart, resulting in contractile dysfunction. Hearts undergoing fibrillatory activity are rapidly excited, inhibiting the hearts' ability to relax, and as such fibrillating hearts do not successfully contract. The distinction between fibrillation and tachycardia lies in its more irregular conduction patterns and ECG waveforms. Atrial fibrillation (AF) is the most common sustained cardiac arrhythmia [117] and may persist for long periods and cause potential complications such as heart attack (myocardial infarction), stroke and even sudden death [118]. In contrast, ventricular fibrillation (VF) almost immediately leads to a heart attack [119, 120].

AF is generally understood to be a progressive condition: it is paroxysmal if the episodes have a duration no longer than 7 days, persistent if the duration of fibrillatory activity exceeds 7 days [121], and permanent if the heart does not return to sinus rhythm. The progression of AF from short-term episodes to a permanent condition carries significant importance for treatments as some treatments, such as rhythm control therapy, are time-sensitive and most effective for paroxysmal AF

[122]. Limited pathophysiological understanding of the initiation, maintenance and progression of AF hinders pharmacological progress. Current management options, such as implanted defibrillators or catheter ablation, are invasive procedures with limited success rates [123].

2.3.1.4 Ischemia

Ischemia refers to the inadequate blood supply to a local region due to blockage of the blood vessels supplying that region [124]. Ischemic heart disease, also called coronary heart disease (CHD), is the term that encompasses cardiac problems stemming from the narrowing of the coronary arteries, which supply blood to the heart muscle, often through blood clots, vasoconstriction, or most commonly, a build-up of plaque (atherosclerosis) inside the coronary arteries. Sustained or severe inadequacies in blood supply to cardiac muscle may result in myocardial infarction (heart attack), where regions of the afflicted myocardium die and are replaced by scar tissue (ischemic scarring) [125]. The presence of ischemic scarring may reduce cardiac output, as dead cells cannot contract, and may also provide a structural obstruction to conduction pathways, leading to the breakup of the excitation waveform and re-entry [125, 126], predisposing the heart to arrhythmia.

2.3.2 Heart Failure

Heart failure (HF) is a clinical syndrome characterised by the heart's inability to pump sufficient blood to meet the body's metabolic demands, either through impairment of the ventricular filling with blood or blood ejection from the ventricles [127–129]. Impairment of these functions is a consequence of structural and functional defects in the myocardium and is classified as left ventricular, right ventricular or biventricular heart failure depending on the location of these defects [127]. These are further divided into two conditions depending on the preservation of ventricular ejection fraction – the ratio of blood within the ventricle to the blood ejected during contraction [127]. HF with a reduced ejection fraction, also known as a systolic failure, results from the ventricles inability to contract effectively and thus eject less blood. HF with a preserved ejection fraction, or diastolic failure, describes the inability for the ventricle to fill with blood during diastole, caused by dysfunction in the relaxation of the ventricle and stiffness. Right ventricular heart failure is a major cause of death in patients with pulmonary arterial hypertension

(pressure overload, PAH), characterised by high blood pressure in the lungs, generally caused by obstructions in the small arteries in the lungs [130].

The initiation of HF is typically caused by an initial event, such as a myocardial infarction (MI, commonly known as a heart attack) because of coronary heart disease, mechanical overload via high blood pressure, cardiac arrhythmias, cardiomyopathy, or valve malfunction. The progressive deterioration of cardiac function is complex and leads to cellular and subcellular maladaptation through compensatory responses such as hypertrophy or the formation of ischaemic scarring following an infarction, which may drive further deterioration [129, 131]. HF-associated remodelling of cellular and sub-cellular structures result in abnormalities in Ca^{2+} cycling [132, 133]; this is discussed in further detail in Section 2.3.

The prognosis for patients diagnosed with HF is poor – with 5 and 10-year survival estimates of 50% and 10%, respectively [134, 135]. Of these deaths, up to 50% are sudden cardiac deaths (also known as cardiac arrest) caused by the sudden loss of heart function [136]. Despite many advancements in treating the early stages of heart failure, there has been a lack of improvement in survival time [137]. Part of this is due to the prevalence of co-morbidities in chronic HF patients, which further impacts prognosis and highlights a need for the development of holistic treatment approaches.

2.3.3 Calcium Homeostasis Dysfunction and Remodelling in Disease

Cardiac remodelling refers to the molecular, cellular and tissue-level changes which manifest as changes in the morphology and function of the heart [132, 138]. In Section 2.2.3, the critical role of Ca^{2+} cycling in maintaining effective ECC is explained. Modulation of intracellular Ca^{2+} handling either through functional alteration in ionic transporters' activity or the structural remodelling of cardiomyocytes will influence the CaT and SR Ca^{2+} loading. This term covers physiological remodelling, such as in an athlete’s heart through exercise training [139], and pathological changes either through the impact of disease, injury, or maladaptation; this section discusses the latter. Conditions linked to an increased risk of cardiomyocyte remodelling include both cardiovascular (e.g., high blood pressure, heart failure) and non-cardiovascular (e.g., diabetes, obesity, age) conditions, which predisposes the development of heart failure, or arrhythmias [89, 122, 140, 141].

Ion channel remodelling and disruption to normal Ca^{2+} homeostasis are linked to contractile disfunction, such as in HF, and the development of pro-arrhythmic behaviour such as spontaneous Ca^{2+} release and alternans (discussed later in Section 2.3.4) [142, 143]. Expression of ionic currents, including I_{CaL} [144, 145], I_{CaT} [146], I_{Ks} [147, 148], I_{Kr} [147, 148], I_{K1} [140, 147, 149–151], I_{to} [148, 150–152] and I_{KACh} [153] have been observed to change in failing cardiomyocytes [154]. Cardiomyocytes from the failing heart also demonstrate disrupted ECC, associated with a loss of CICR gain [155, 156] and a general reduction in CaT magnitude associated with reduced SR-Ca^{2+} release [157, 158]. SR-Ca^{2+} uptake is consistently observed to decrease in HF [158, 158–163], which correlates with an increase in resting cytosolic Ca^{2+} levels [164, 165]. Increases in diastolic Ca^{2+} are additionally linked to an increase of intracellular [Na^{+}] in the failing myocardium [166], which may increase the Ca^{2+} influx of NCX during the plateau phase of the action potential.

SR-Ca^{2+} content has been observed to decrease [157, 167, 168] and increase [169, 170] in various cardiac pathologies. Increases in SR-Ca^{2+} content, despite a consistent decrease in SR-Ca^{2+} uptake, has been attributed to increased phosphorylation of phospholamban (PLB), a SERCA2a regulator [170–172]. In HF, observed reduced SR-Ca^{2+} content is associated with lower CaT magnitude and higher diastolic Ca^{2+} and increased SR-Ca^{2+} leak which promotes the incidence of spontaneous Ca^{2+} release events (SCRE) [163, 173, 174]. Increased SR-Ca^{2+} content combined with increased diastolic Ca^{2+} can generate asynchronous Ca^{2+} waves during diastole by activating NCX and producing afterdepolarisations in membrane potential [167].

Structural remodelling of the t-tubule system associated with HF [175–177] can decouple CICR through the increasing distance between LTCCs and RyRs [178–180] and leads to the formation of "orphaned" RyRs which are no longer co-localised with t-tubules. This remodelling causes a de-synchronisation of the CaT throughout the cardiomyocyte [76, 179, 181], promoting the emergence of CaT alternans. In addition to the t-system, observations of remodelling in the organisation of primary Ca^{2+} transporters (RyRs, SERCA2a, NCX) have been published [13, 176, 180, 182, 183], but research relating structural remodelling to Ca^{2+} channel organisation and modulation of Ca^{2+} handling is limited.

2.3.4 Arrhythmogenic Mechanisms

Clusters of RyR on the SR membrane can open spontaneously during diastole, generating local elevations in intracellular Ca^{2+} (Ca^{2+} sparks), which are limited in propagation [184, 185]. These elementary events occur frequently (50-5000 sparks per second per cell [185]), and the frequency of these sparks can vary from cell to cell and from species to species [186, 187]. In stimulated pacing, Ca^{2+} sparks are evoked by an influx of Ca^{2+} via voltage-gated LTCCs, but there exist conditions in which these elementary Ca^{2+} units can propagate and recruit neighbouring CRUs to release Ca^{2+} through CICR [188]. In the presence of higher SR Ca^{2+} content or increased RyR sensitivity, such as in HF [189], larger Ca^{2+} sparks can occur with the potential to recruit neighbouring CRUs without electrical stimulation, producing a propagating Ca^{2+} wave.

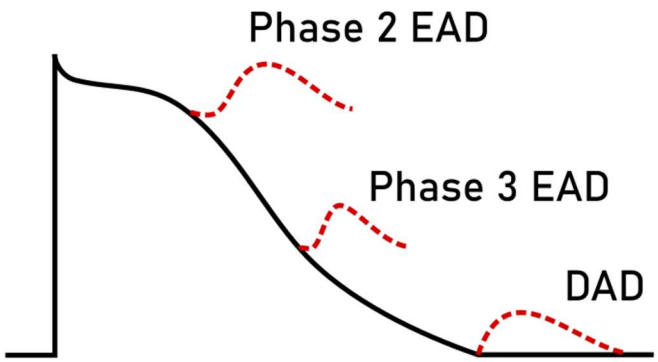

Figure 2.15 Early and delayed afterdepolarisations

An illustration of after-depolarisation events. Early after-depolarisations (EAD) occur during phase 2 or phase 3 of the action potential, whereas delayed after-depolarisations occur after the membrane has fully repolarised. Dotted red lines illustrate EADs and DADs.

Depolarisations in membrane potential caused by spontaneous activity are known as after-depolarisations (a slowing or reversal of normal repolarisation), which are categorised by two sub-types shown in Figure 2.15: early after-depolarisation (EAD), which occur during the plateau or repolarisation phases of the AP, and delayed after-depolarisation (DAD) which occur after the membrane has fully repolarised following an AP [111, 190, 191]. DADs result from elevated intracellular Ca^{2+} load and SCRE; local increases in intracellular Ca^{2+} activate NCX, producing an inward transient current which depolarises the membrane [17, 163,

192]. EADs are associated with a reduced repolarisation reserve, and a prolonged APD is produced either through the re-activation of LTCCs or spontaneous Ca^{2+} waves [190, 193]. Both EADs and DADs can exceed the transmembrane potential threshold to activate I_{Na} and trigger an action potential (known as a triggered activation (TA), or an ectopic beat). This ectopic firing disturbs normal cardiac rhythm but is considered normal and not indicative of any CVD by itself, but they occur more frequently in CVDs. By depolarising resting membrane potential in a region of the heart, DADs and triggered activations can cause conduction block and re-entry (described in Section 2.2.7).

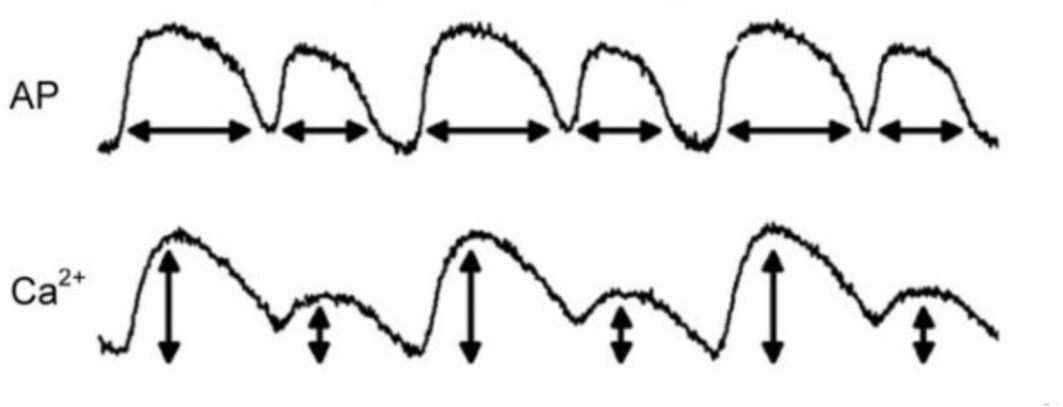

Figure 2.16 Alternans

Alternans as they appear in transmembrane action potential (AP) and intracellular Ca^{2+} transient (CaT). Alternans can be beat-to-beat alternations in magnitude and duration. Adapted from Zang and Xia (2014) [194].

Alternans are characterised by periodic beat-to-beat oscillations in magnitude and duration of the AP or CaT (Figure 2.16). There are two primary cellular mechanisms for the initiation of AP alternans. At high pacing rates or under pathological remodelling, alternans can originate from alternations in ion channel kinetics [195, 196]. Alternating properties of ion currents beat-to-beat produces alternating changes in AP morphology, which influences the dynamics of LTCCs, initiating CaT alternans. The second mechanism is Ca^{2+}-drive: Ca^{2+} handling instabilities lead to alternating CaT properties, which, if sufficiently large, result in AP alternans through the action of LTCCs and NCX [194]. A unified theory of Ca^{2+} alternans known as the '3R' theory of alternans is proposed [197, 198], which surmises that CaT alternans occurs as a result of instabilities in the relationship between three critical properties of Ca^{2+} sparks: the randomness of Ca^{2+} spark generation,

recruitment of sparks by neighbouring CRUs and the refractoriness of a CRU (the "3Rs") [92]. Ca^{2+} sparks occur spontaneously and randomly, and because of CICR, the spark from one CRU may propagate and elicit the release of secondary sparks from neighbouring CRUs – this is the basis of Ca^{2+} waves discussed above. Furthermore, after a CRU produces a Ca^{2+} spark, it remains refractory for a time in which another spark cannot be released. It is determined that the phase space for alternans exists when there is an intermediate amount of Ca^{2+} sparks, high inter-CRU coupling, which enable high levels of spark recruitment, and a high degree of refractoriness in CRUs throughout the cell [73].

Alternans can be either spatially concordant, where regions of heart tissue or cells undergo synchronous alternans, where all regions are in the same phase or spatially discordant, in which different regions of tissue or cells are dyssynchronous [199, 200]. Spatially discordant alternans in tissue are considered more arrhythmogenic than concordant alternans, favouring re-entry and facilitating the onset of arrhythmias.

2.4 Microscopy

There is no original microscopy work presented within this thesis; however, it is important to briefly introduce some basic microscopy concepts to better understand the datasets used. The main source of data utilised in Chapters 3 and 4 is confocal microscopy, which will be described briefly here – however, if the reader wishes to know more details about this technique or other optical microscopy methods, Thorn's quick guide to light microscopy is recommended [201].

Traditional light microscopes create a magnified image through the use of a series of glass lenses. A beam of light is focused onto or through an object, and then a convex objective lens enlarges the image formed by diffracting the light pattern [202]. The underlying principle here is the diffraction of photons, an elementary particle or "quantum" of electromagnetic radiation [203]. It is impossible to focus light onto an infinitely small point; thus, the electromagnetic waves converge and interfere at the focal point. The resulting diffraction pattern is the point spread function (PSF; Figure 2.17): concentric circles radiating out from a central disc of high intensity.

Resolving sub-wavelength structures with optical microscopes is challenging because of the diffraction limit. The minimal distance between two objects, d, which

can be resolved separately is given by Rayleigh criterion for resolution (Figure 2.17A) [204]:

$$\theta_{min} = 1.22\frac{\lambda}{D} \tag{2.1}$$

Where D is the diameter of the aperture, λ is the wavelength of light and θ_{min} is the critical angle which below, no two objects can be resolved. For two illuminated objects, this gives the minimal distance of separation, d, for these objects to be separately resolvable as [201]:

$$d = 0.61\frac{\lambda}{NA} \tag{2.2}$$

where NA relates to the numerical aperture of the objective lens. The minimal resolvable distance, d, is also described as the resolution of an image.

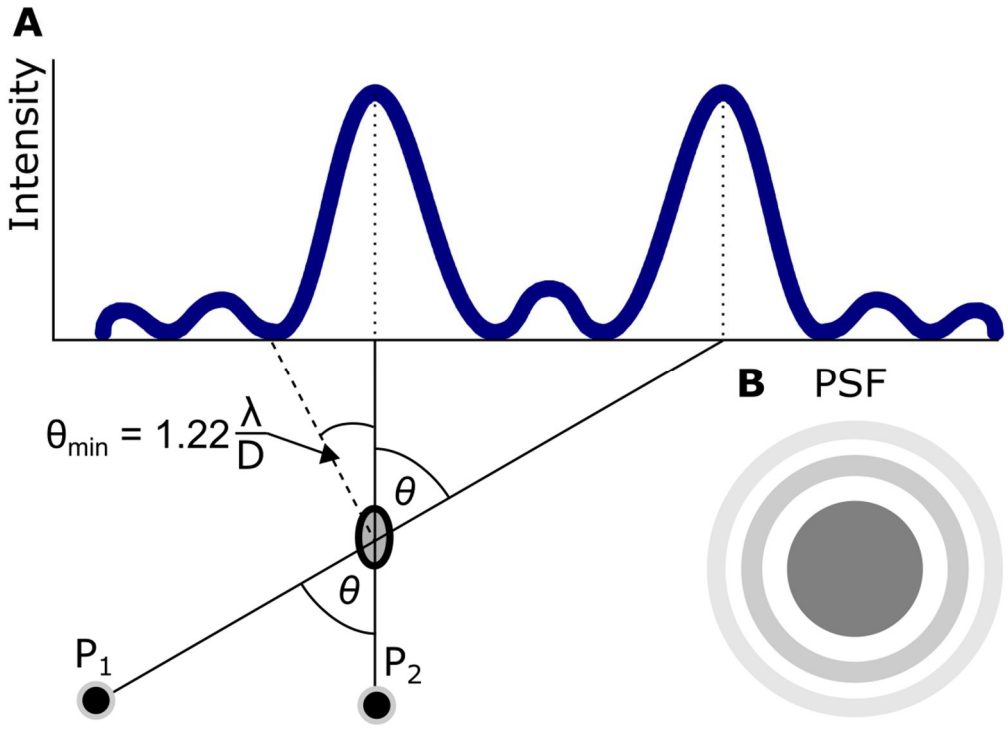

Figure 2.17 Rayleigh criterion of resolution and point spread function

A – The Rayleigh criterion for resolution. Two point light sources, P_1 and P_2 can be resolved separately if the angle $\theta > \theta_{min}$. B – Illustration of the point spread function (PSF) of point diffusion through a circulatory aperture.

The data used within this thesis is produced using fluorescence microscopy techniques. That is, the application of fluorescent dyes (or fluorophores) to label

specific targets of interest. Fluorophores are molecules that absorb an incoming wavelength of light (excitation wavelength), absorb some of the energy from that wavelength, then emit a longer wavelength (emission wavelength) [201]. These fluorescent dyes are often attached by binding a fluorescently labelled antibody to the protein of interest. Multiple fluorophores can be bound to a cardiomyocyte simultaneously to allow for imaging multiple targets simultaneously to produce multi-channel images.

Conventional fluorescence microscopy has a significant limitation in that illuminating light excites fluorophores throughout the sample. Confocal microscopy addresses this limitation and instead illuminates the sample using a focused laser beam at a single point within the focal plane of the sample [201]. This light is then detected using a pinhole, which blocks light from out-of-focus planes, and then uses this data to build up an image point by point. Variations of this technique exist, such as spinning confocal microscopy, which utilises a disk of pinholes that sweep across the sample, scanning over every point of the sample during a single revolution. This technique combines ease of use, high sensitivity and the ability to capture hundreds of frames per second; thus, it is commonly used in cardiac imaging studies [13, 74, 205–207].

2.5 Animal Models

It is important to clarify that there is no one “ideal” animal model for cardiovascular research. The hearts of laboratory species evolved to meet their unique physiological demands to survive in their respective environments, and these adaptations result in different electrophysiological behaviours. This thesis has utilised two animal models: the rabbit model to study Ca^{2+} variability and a well-established rat model of monocrotaline-induced right-ventricular heart failure. These models will be discussed, followed by the ethical implications of using animal models in research.

2.5.1 Rabbit Model for Cardiac Research

Rabbit models provide an intermediary model in terms of financial cost, being significantly cheaper than larger species, requiring less housing space, cheaper nutrition and care than larger laboratory species such as dogs, sheep and pigs [26–28], but more expensive than rodents. The availability of rabbits for in vivo experiments and moderately fast generation times [208] has resulted in a plethora of

well documented and commonly performed quantitative and imaging techniques such as echocardiography, electrocardiography, hemodynamic cardiac catheterization and cardiac magnetic resonance imaging [26].

The rabbit myocardium exhibits remarkable similarities in cardiac electrophysiology to the human myocardium compared to other small animal models [25]. Potassium repolarisation currents (I_{to}, I_{Kr}, I_{Ks}) in rabbit atrial models have similar dynamics to the human atria [209, 210], although I_{to} is approximately three times larger in rabbit than human [33]. Both rabbit and human models demonstrate a positive relationship force-frequency relationship, i.e., increasing stimulation rate in rabbits and humans in vitro muscle results in a similar increase in contractile force [26, 28, 184]. The role of extruding intracellular Ca^{2+} following cellular contraction is similarly distributed between SERCA2a (70-74%, rabbit; ~75%, human) and NCX (23-28%, rabbit; 18-19%, human) [26, 208], though SR-Ca^{2+} uptake is approximately 50% faster in rabbit models than in human [211]. The effective size of rabbit cardiac tissue compared to excitation wavelength is similar to humans [212], which is important for studying re-entry, AF and VF. Unlike humans, rabbits' resting in vivo heart rates is measured at 130 – 300 bpm [26], which is much higher than ~50 – 90 bpm in humans. This is significantly closer to human than rodent heart rates (mouse, 310 – 840 bpm; rats, 250 – 493 bpm) but still renders rabbit models a less-than-ideal choice for exercise-based studies.

Overall, rabbit models offer a compromise between larger mammals with more similar electrophysiology and smaller, cheaper animal models. Similar electrophysiology and Ca^{2+} handling (with some caveats) make rabbit models suitable for basic research or as an intermediary step between rodent models and human applications [23, 25, 26]. However, longer generation times and higher associated costs than rodents mean that they are less suitable for longer studies which require generations of a species.

2.5.2 Monocrotaline Rat Model of Right Ventricular Heart Failure

A useful animal model to study RV HF is the monocrotaline (MCT) rat model, a well-established protocol for MCT-induced pulmonary arterial hypertension (PAH) [12, 154, 213, 214]. This model involves a single intraperitoneal injection of monocrotaline, which is then activated by the liver into a reactive metabolite before being pumped into the pulmonary veins via red blood cells, causing injury to the endothelium. Several weeks after MCT is administered, rats develop PAH, leading

to increased pulmonary vascular resistance, compensatory RV hypertrophy and finally RV HF [214]. Recent studies indicate that PAH also induces LV atrophy as a compensatory response: the LV experiences reduced filling and mechanical loading, leading to atrophic remodelling [215, 216].

Specific details of the experimental procedure others used to produce the relevant data in this thesis are specified in Chapter 4, and the experimental results of this remodelling are given when appropriate to compare with the present studies.

2.5.3 Ethical Issues in Using Animal Models

The most important disadvantage of using animal models in scientific research is the ethical problem of inflicting distress through confinement, pain, and disease on the animals themselves. The necessity of using animal models often comes at the expense of these animals' death, so it is of utmost importance to ensure that the increase in knowledge gained from these animal models outweighs their sacrifice and ensure that the animals have the minimal harm inflicted upon them. This idea led to Russell and Burch's proposal of the 3R principles for humane experimentation in 1959 [217]. The 3Rs stand for reduction, replacement and refinement – that is, the reduction of the number of animals used in experimental set-ups, the replacement of conscious living higher animals for insentient material, and the refinement of experimental procedures to minimise the severity of inhumane procedures applied to those animals, if an alternative is not possible [218]. The implementation of these principles often improves the quality of animal studies by enforcing the development of more sophisticated practices [219]. Today, these principles have been embedded in law following the UK Animals (Scientific Procedures) Act 1986 [220] and EU Directive 2010/63/EU [221]. The establishment of the National Centre for the Replacement, Refinement and Reduction of Animals in Research (NC3Rs) [222] in the UK drives forward the development and uptake of 3Rs approaches, bringing a greater focus on the ethical need to develop alternative methodologies which minimise the suffering and use of animals. One such approach to achieve this is the development of physiologically detailed mathematical and computational models of cardiac electrophysiology to supplement and inform experimental studies.

2.6 Mathematical Modelling of Cardiac Electrophysiology

In order to develop computational models of cardiomyocytes, cardiac tissue and cardiac electrophysiology, the behaviour of ion channels and processes underlying the AP and CaT must be mathematically formalised. This section covers the mathematical formalism necessary to understand and produce single-cell models of cardiomyocytes and the development of these formulations. The reader is referred to three comprehensive reviews of these techniques and others pertaining to tissue and organ-level modelling by Rudy and Silva (2006) [11], Qu et al. (2014) [29] and the Leeds computational electrophysiology lab by Benson et al. (2021) [77].

2.6.1 Ionic Gradients and Reversal Potential

It was previously established that ions in the intra- and extracellular spaces flow through ion channels in the direction of an electrochemical gradient. Thus, the flow of an ion across an ion channel is dependent on the relative intra-, and extracellular concentrations of that ionic species (the concentration gradient) and the membrane potential (the electrical gradient) as cardiomyocytes cycle multiple ionic species.

Consider a two-ion system, as illustrated in Figure 2.18, with two ions, a positively charged ion a and a negatively charged ion b, separated by a semi-permeable membrane with a transport channel selective to ion a. Positively charged ions (ion a) flow across a chemical gradient from one chamber to another through a selective ion a channel, however, ion b cannot move across, resulting in an accumulation of negative charge in the chamber with ion b. This opposes the chemical gradient by providing an attractive electromagnetic force on ion a, which grows as the charge in the chamber becomes more negative. The sum of the chemical and electrical gradients is the electrochemical gradient, which determines the direction of movement. Once the chemical and electrical gradients are equal and opposite, the electrochemical gradient is zero, and the ion no longer moves through the ion channel.

The balance between electrical and chemical forces can be described using a quantity known as Gibb's free energy, G [6]. The free energy change associated with moving a mole of ion X from chamber 1 with a higher concentration of X, across a plasma membrane to chamber 2 with a lower concentration of X is given by

$$\Delta\, G_{conc} = RT\ \ln\frac{[X]_{C1}}{[X]_{C2}} \tag{2.3}$$

where $R = 8.314\ J.K^{-1}.mol^{-1}$ is the ideal gas constant and T is the absolute temperature in kelvin (K).

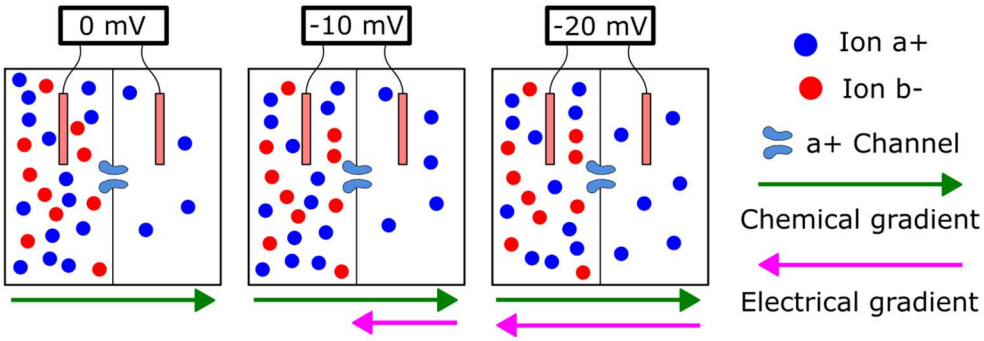

Figure 2.18 Electrochemical gradient diagram

A simplified illustration of electrochemical gradients across a cell membrane. The activated a+ channel allows +ve a ions to flow across the membrane in the direction of the chemical gradient from the left to the right chamber, and -ve b ions do not move. Charge accumulates as these ions move across the chemical gradient, resulting in an electrical gradient opposing ion movement. When chemical and electrical gradients are equal and opposite, the system reaches equilibrium.

The free energy change associated with moving a mol of a charged particle with valence z across an electric potential, $E\,(V)$, is given by

$$\Delta G_{elect} = zFE \tag{2.4}$$

where $F = 96485\ C.mol^{-1}$ is the Faraday constant.

When the electrical and chemical gradients balance, the free energy equations balance

$$\Delta G_{conc} = \Delta G_{elect} \tag{2.5}$$

$$RT\ \ln\frac{[X]_{C1}}{[X]_{C2}} = zFE \tag{2.6}$$

By rearranging this equation, we can obtain a value for the reversal potential, E_{rev}, at which the net movement of an ionic species, X, across a cell membrane is zero:

$$E_X = \frac{RT}{zF} \ln \frac{[X]_1}{[X]_2} \tag{2.7}$$

This equation (Eqn. 2.7) is known as the Nernst equation, and E_x is also known as the Nernst potential for some ion x [6], giving the transmembrane potential at which a specific ionic species is at equilibrium. This may also be referred to as the reversal potential, E_{rev} – any change in membrane potential across this equilibrium point will reverse the direction of ion flux across an ion channel. As cardiomyocytes are multi-ion systems, other ionic species will still be transported through other ionic channels. For channels that are permeable to multiple ionic species, a modification of the Nernst equation known as the Goldman-Hodgkin-Katz (GHK) equation exists to calculate the Nernst potential where multiple ionic species are involved [6, 77]:

$$E_{rev} = \frac{RT}{F} \ln \left(\frac{\sum_i^n P_{X_i^+} [X_i^+]_o + \sum_i^n P_{Y_i^-} [Y_i^-]_o}{\sum_i^n P_{X_i^+} [X_i^+]_i + \sum_i^n P_{Y_i^-} [Y_i^-]_i} \right) \tag{2.8}$$

where P_{ion} is the permeability of the channel to that ion and X^+ and Y^- are some monovalent positive or negative ionic species. The GHK equation (Eqn. 2.6) can be used to determine the movement of transmembrane potential, as it will tend towards the E_{rev} of the ionic species whose permeability is greatest at some membrane potential and can be used to determine the resting potential of a cardiomyocyte.

2.6.2 The Electric Circuit Model of the Cell Membrane

As aforementioned in Section 2.2.1, the cell membrane of a cardiomyocyte can be modelled as an electric circuit (Figure 2.5) considered as a capacitor, with capacitance $C_m$with embedded ionic channels, pumps and exchangers acting as voltage-dependent and time-dependent variable resistors. Due to their selective permeability to one (or more) ionic species, these ion channels are modelled in parallel. Current can flow across this simple circuit by going through the variable resistors (ions flowing through ionic channels) or by charging the membrane capacitance (the capacitive current, I_C) [6, 29, 77]. The electrochemical gradient that directs ions' net flow through ion channels provides the electromotive force, V, are modelled as batteries coupled to the variable resistor of the same ionic species (Figure 2.19).

The charge across the capacitor (the membrane) is given by the capacitor relation, $Q = C_m V$. With a constant capacitance, this gives the capacitive current, I_C as the time-derivative of this capacitance relation [6, 77]:

$$I_C = \frac{dQ}{dt} = C_m \frac{dV}{dt} \tag{2.9}$$

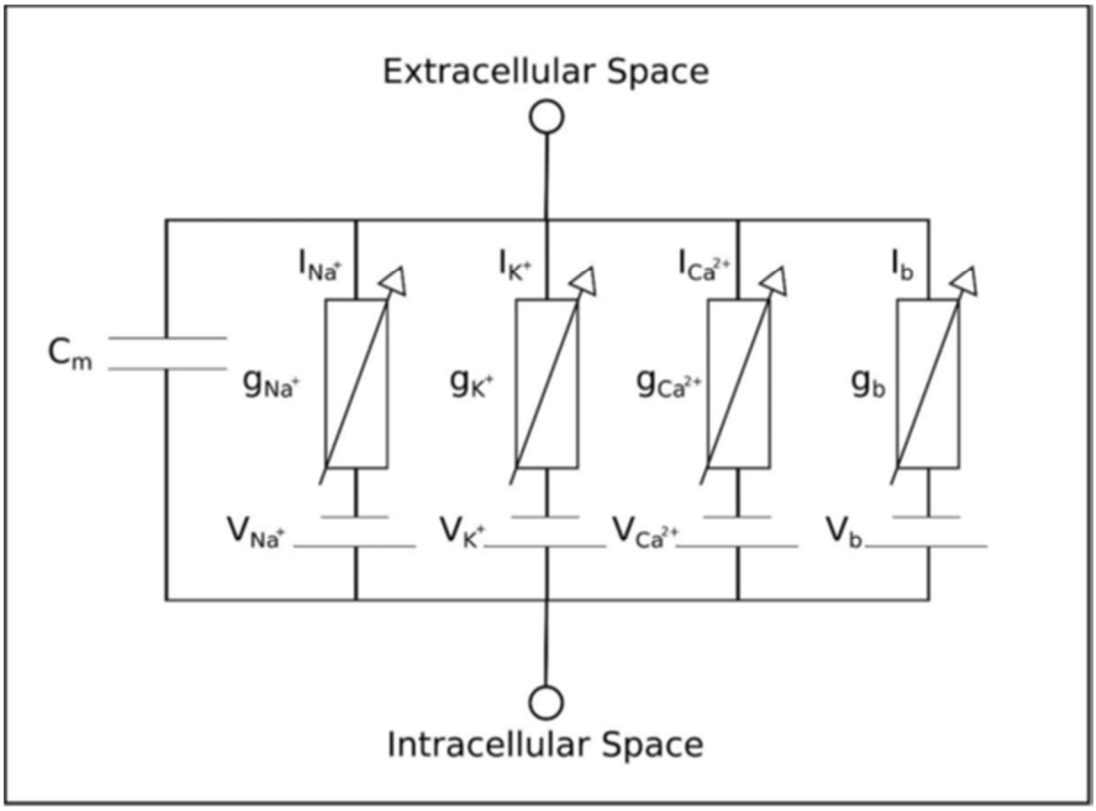

Figure 2.19 The electric circuit model of the cell membrane

Schematic illustrating the basic framework of the electric circuit model of cell membranes. Ionic channels, for Na^+, K^+, Ca^{2+} and background currents, I_x, are modelled in parallel as variable resistors with conductance g_x, coupled with batteries representing the electrochemical gradient V_x, the electromotive force driving current flow. The cell membrane is modelled as a capacitor with membrane capacitance C_m.

Kirchhoff's first law of circuits, the "junction rule", states that for any point in an electric circuit, the algebraic sum of currents flowing into that juncture must be equal to the sum of currents flowing out of it, thus the sum of all ionic currents, I_{ion}, and the capacitive current must be equal and opposite:

$$I_{ion} = -I_C \tag{2.10}$$

$$I_{ion} = -C_m \frac{dV}{dt} \tag{2.11}$$

From here, it is simple to re-arrange to find that the rate of change of membrane potential is determined by the sum of all ionic currents and membrane capacitance:

$$\frac{dV}{dT} = -\frac{I_{ion}}{C_m} \tag{2.12}$$

Using Ohm's law, $V = IR$, we can model the current through ion channels. For some ionic current, I_x, permeable to ion x:

$$I_x = g_x(V_m - E_x) \tag{2.13}$$

where g_x is the conductance of current I_x, and $V_m - E_x$ is the electrochemical gradient of ion x. Different approaches can be taken in modelling ionic currents through different formulations of conductance; the most common methods of modelling this conductance are Hodgkin-Huxley formulations (described in Section 2.6.3) and Markov chain models (described in Section 2.6.4).

2.6.3 Hodgkin-Huxley Formulations

In 1952, Hodgkin and Huxley published the first mathematical description of an action potential in a series of five papers detailing the components of membrane conductance [223, 224], ionic currents carried by Na^+ and K^+ ions [225], I-V relationships [226] and membrane potential [227] in the giant squid axon. This model consisted of two time and voltage-dependent currents (Na^+ and K^+) and one time-independent leak current formulated as non-linear ordinary differential equations, describing the movement of ions through voltage-gated ion channels. These so-called Hodgkin-Huxley (H-H) formulations used to describe a standard, two-gate voltage-gated ion channel will be given here.

As discussed in Section 2.2.1, ion channels exist in multiple conformational states, enabling or disabling the passage of select ionic species along the electrochemical gradient. For a given ion channel permeable to an ionic species x, the general form for a H-H two-gated current is given by the formula:

$$g_x = \overline{g_x} m^a h^b (V - E_x) \tag{2.14}$$

where $\overline{g_x}$ is the maximal conductance of the population of ion channels, m and h are the activation and inactivation variables, dimensionless variables representing the activation and inactivation gates. a and b represent the number of independent

activation and inactivation gates. The activation variable describes the proportion of activated ion channels, and the inactivation variable describes the proportion of ion channels that are not inactivated; Thus, they take on a value between 0 and 1. For an ion channel with one activation and one inactivation gate, if all gates are in the open state, $m = h = 1$ the conductance will be equivalent to that ion channel populations' maximal conductance, $g_x = \overline{g_x}$.

The proportion of channels in the open activation state is given by m, and thus the proportion of channels in the closed activation state is $1 - m$. The channel moves between these two states with voltage-dependent rate constants α and β, for opening and closing and activation gate [77]:

$$(1 - m) \underset{\beta_m(V)}{\overset{\alpha_m(V)}{\rightleftharpoons}} m \tag{2.15}$$

Similarly, for the inactivation gate

$$h \underset{\beta_h(V)}{\overset{\alpha_h(V)}{\rightleftharpoons}} (1 - h) \tag{2.16}$$

Hence, the rates of change of the proportion of channels in either state is given by:

$$\frac{dm}{dt} = \alpha_m(1 - m) - \beta_m m \tag{2.17}$$

for activation gates and:

$$\frac{dh}{dt} = \alpha_h(1 - h) - \beta_h h \tag{2.18}$$

for inactivation gates.

These differential equations (Eqn 2.17 and 2.18) describe the gating mechanism. Assuming that the membrane potential is at some voltage V_0, and the gating variables, m and h are at steady-state values m_0 and h_0 appropriate to V_0 and the rate coefficients $\alpha_m, \alpha_h, \beta_m, \beta_h$ also have values appropriate to V_0. If V_0 is changed to a new voltage then the rate coefficients instantly take on a new value appropriate to the new voltage. The differential equations (Eqns 2.17 and 2.18), determine how m_0 and h_0 approach their new values, m_∞ and h_∞, and are solved as follows:

$$m = m_\infty - (m_\infty - m_0) \exp\left(-\frac{t}{\tau_m}\right) \tag{2.19}$$

$$h = h_\infty - (h_\infty - h_0)\exp(-\frac{t}{\tau_h}) \tag{2.20}$$

where m_∞ and h_∞ are the activation and inactivation steady-states which a gating variable tends towards at the new voltage given by:

$$m_\infty = \frac{\alpha_m}{\alpha_m + \beta_m}, \qquad h_\infty = \frac{\alpha_h}{\alpha_h + \beta_h} \tag{2.21, 2.22}$$

The time constants, τ_m and τ_h, for this change are given by

$$\tau_m = \frac{1}{\alpha_m + \beta_m} \tag{2.23}$$

$$\tau_h = \frac{1}{\alpha_h + \beta_m} \tag{2.24}$$

Substituting the equations for steady-state and time constants into Eqns. 2.15 and 2.16 give the differential equations by which Hodgkin-Huxley ion gating variables evolve:

$$\frac{dm}{dt} = \frac{m_\infty - m}{\tau_m} \tag{2.25}$$

$$\frac{dh}{dt} = \frac{h_\infty - h}{\tau_h} \tag{2.26}$$

Assuming that over the time-step considered that voltage is time-independent (see Section 2.7), the time course of the gating variable can be obtained by solving Eqns. 2.15 and 2.16 giving:

$$m = m_\infty - (m_\infty - m_0)\exp\left(-\frac{t}{\tau_m}\right) \tag{2.27}$$

$$h = h_\infty - (h_\infty - h_0)\exp\left(-\frac{t}{\tau_h}\right) \tag{2.28}$$

where m_∞ and h_∞ are given by Eqns. 2.21 and 2.22, τ_m and τ_h are given by Eqns. 2.23 and 2.24, and m_0, h_0 are the initial values of m and h.

Solving these equations iteratively and substituting them into Eqn. 2.14 gives the current flowing through some ion channel, with experimentally determined values for the maximal conductance, $\overline{g_x}$, steady-state and time-course kinetics of the current. These can be obtained through voltage-clamping experiments, to fit suitable formulations describing the steady-state and time constants of activation and

inactivation. Methods of solving these equations iteratively are discussed in Section 2.7.

The formulations describing steady-state conductance and time constants are often fit directly to this experimental data (this model-fitting is performed in Chapter 5). Steady-state gating variables are often fitted using a logistic sigmoid function, $S(x)$, which have a general form:

$$S(x) = \frac{1}{1 + e^{-x}} = \frac{e^{x}}{e^{x} + 1} = 1 - S(-x). \tag{2.29}$$

where $S(x)$ can take the value of any real number between 0 and 1, representing the full closing or full opening of activation/inactivation gates in ion channels. Sigmoid curves are generally monotonically increasing (activation functions) or decreasing (inactivation functions), well suited to the voltage-dependent steady-state functions representing cumulative activation/inactivation. Often, these sigmoid functions take the general form:

$$y_{\infty} = \frac{1}{1 + \exp\left(V_m - \frac{V_{1/2}}{k}\right)} \tag{2.30}$$

where $V_{1/2}$ is the voltage of half activation (e.g. the membrane potential when the steady state gating variable, $y_{\infty} = 0.5$) and k is the gradient or slope of activation. The values of the rate coefficients α and β can be determined from the steady-state and time constants, obtained experimentally using:

$$\alpha_m = \frac{m_{\infty}}{\tau_m}, \qquad \beta_m = \frac{1 - m_{\infty}}{\tau_m} \tag{2.31, 2.32}$$

$$\alpha_h = \frac{h_{\infty}}{\tau_h}, \qquad \beta_h = \frac{1 - h_{\infty}}{\tau_h} \tag{2.33, 2.34}$$

It should be stated that there is no reason why there must be two types of gates present [62]. Variations to this twin-gated model include single-gated models, such as I_{Ks}, which only has activation gate kinetics [37] and currents which activate or inactivate over multiple time-courses, such as I_{KACh} [99]. Regardless, the basic framework of the H-H formulations remains the same and can be slightly modified to model these variations. The disadvantages of H-H formulations are that they over-simplify the conformational changes occurring at the protein level, rendering them

unable to accurately model the complexities in transitioning between these conformational states.

2.6.4 Markov Chain Models and Stochasticity

Another common form of modelling ion channels is using Markovian formulations to model the equivalent of activation/inactivation parameters via a transitional probability that an ion channel changes between conformational states [11, 62, 77]. Unlike H-H formulations, these gating variables are co-dependent. The inclusion of dependence between transition states (i.e., the occupancy of one state partially determines the probability of transition to another state) increases the complexity of these formulations compared to H-H but are superior in modelling accurate ion channel kinetics [11]. The overall formulation for the current flowing through some ionic channel, x, for a Markovian model is given by:

$$g_x = \overline{g_x} O(V - E_x) \tag{2.35}$$

where O is the collective total open state occupancy, the proportion of channels which occupy the open state in which an ion current can flow through, which can also be considered the possibility that any single ion channel occupies the open state (refer to Section 2.2.1, Figure 2.5 for an explanation of ion channel conformational states). A Markov chain model equivalent to a two-gate H-H formulation [11] is illustrated in Figure 2.20 and described below.

In this example, four states exist (Figure 2.5, 2.20): O, the open state; C, the closed state; I_C, the closed inactivated state; and I_O, the inactivated open state. Of these conformational states, current may only flow through ion channels in the open state. Voltage-based transition rates (for individual channels) between these states are denoted by α, β, δ and γ (ms^{-1}) indicating the direction of movement in the Markov diagram (α, right; β, left; δ, up; γ, down), for a population of ion channels, this may be considered the transitional probability. The following ODEs describe the rate of change for each of these four conformational states:

$$\frac{dC}{dt} = \beta O + \delta I_C - (\alpha + \gamma) C \tag{2.36}$$

$$\frac{dO}{dT} = \alpha C + \delta I_O - (\beta + \gamma) O \tag{2.37}$$

$$\frac{dI_C}{dt} = \beta I_O + \gamma C - (\alpha + \delta) I_C \tag{2.38}$$

$$\frac{dI_O}{dt} = \alpha I_C + \gamma O - (\beta + \delta) I_O \tag{2.39}$$

The Markovian approach provides a mechanistic link between the AP morphology and ion channels' structural and functional properties. Conformational states and the transitions between them can be studied by measuring the occupancy of each state throughout the action potential, which is particularly useful in studying gene mutations that impair the activation or inactivation kinetics of a specific channel [11, 77].

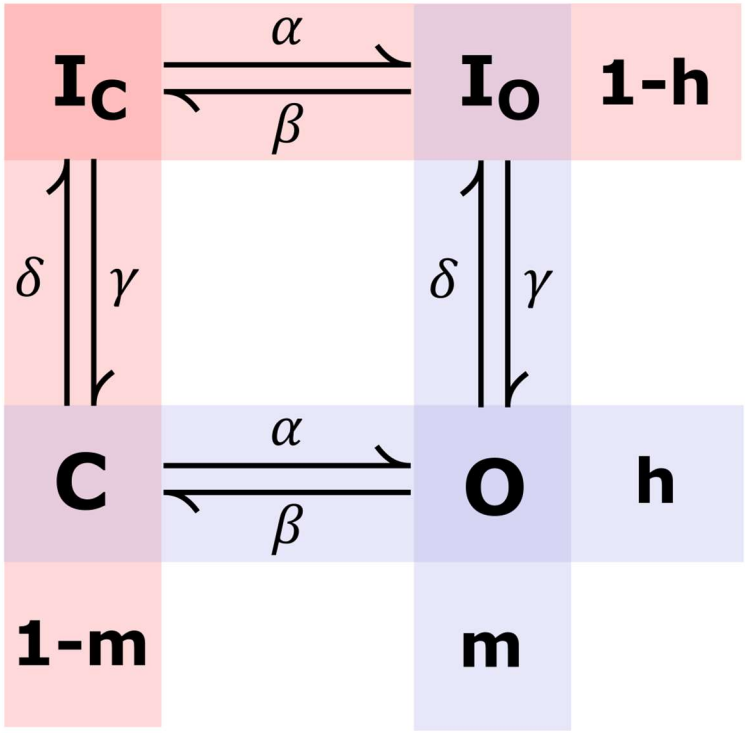

Figure 2.20 Four-state Markov chain model

Schematic of a simple four-state Markov chain model, analogous to a two-gated Hodgkin-Huxley (H-H) formulation. Four states are possible: O, open state; C, closed state; I_O, inactivated open state; I_C, Inactivated closed state. Current may only flow in the open state. Transition rates are given by α, β, δ and γ. Configuration space analogous to the H-H gating variables (m, h) are highlighted in blue (open activation conditions) and red (open inactivation conditions). Based on Rudy and Silva (2006) [11]

Markov chains can also be used to model the opening and closing of individual ion channels as stochastic processes [29], processes involving random variables dependent on some variable parameter such as time. Eqn. 2.35 can be modified to

instead describe the flow of ionic current across a collection of ion channels by replacing the maximal conductance parameter, $\overline{g_x}$, with the maximal conductance parameter for a single ionic channel, $\overline{g_{sc,x}}$, and replacing the collective proportion of channels in the open state, O, with the number of channels in the open state, N_O:

$$I_x = \overline{g_{sc,x}} N_O (V - E_x) \tag{2.40}$$

Consider a single ionic channel with two states, the open state, O, and the closed state, C. At some time, t, this channel is in the open state, and assume that at some time, $t + \Delta t$, there is a probability that this channel has transitioned into the closed state which can be given as a function of probability and time, $P_C \Delta t$. Thus, the probability that the channel remains in the open state at $t + \Delta t$ is given by $(1 - P_C)\Delta t$. For any ion channel, generating a random number, r, between 0 and 1 to determine whether the state of this ion channel transitions from the open state to the closed state gives the channel's activation as a stochastic process. If $0 \leq r \leq P_C \Delta t$, the channel will transition to the closed state; otherwise, it remains open. This can be applied to each channel in the collection of channels, N_O, to model transitional probability stochastically in a cardiomyocyte. This is inherently a computationally intensive method; complexity grows with the number of conformational states and the number of stochastic channels.

Combining these models with a cell or tissue electrophysiology model provides an effective method of studying single-channel mutations on whole-cell electrophysiology [77]. Stochastic Markovian formulations have been incorporated into computational models of intracellular Ca^{2+} handling, used to model state transitions of LTCCs and RyRs [49, 228–230] to simulate the physiological randomness associated with Ca^{2+} spark initiation and recruitment. However, Markov chains are more complex and require a larger set of equations to solve than H-H formulations, significantly increasing computation time and thus are often only used when a H-H formulation is not suitable for the purpose of a study [62].

2.6.5 Modelling Intracellular Ca^{2+}

The intracellular calcium system is of critical importance to normal electrophysiology in cardiomyocytes. An accurate mathematical description of this system is necessary to study intra- and intercellular variability and many cardiac pathologies. Most cardiac models since the development of the Beeler-Reuter model

in 1977 have included at least some basic calcium system dynamics [88]. Recent models incorporate the mechanisms of ECC and CICR (described in detail in Section 2.2.3), including modelling the SR calcium channels to reproduce the dynamics of CICR and calcium re-uptake into the SR [39], stochastic modelling of LTCCs and RyRs [49, 228–230] (Section 2.6.4), diffusion across intra-cellular domains [49, 51, 52, 231, 232], and the heterogeneous structures of t-tubule systems in different types of cardiac cell [3, 76, 233]. Detailed spatio-temporal models of Ca^{2+} dynamics are required for fibrillatory studies in order to produce spatial arrhythmic phenomena, such as SCRE [185, 234, 235] and spatially concordant/discordant alternans [52, 76, 236] (refer to Section 2.3.4 for details). A detailed description of an idealised spatio-temporal Ca^{2+} handling model developed in our laboratory (by Colman [1, 49, 50, 237]) is given in Section 2.8.2.

2.7 Numerical Methods

As discussed in Section 2.6, mathematical models of cardiac electrophysiology are comprised of systems of non-linear ODES, which require integrative methods to approximate a solution. The methods in which these ODEs are discretised and solved over time-steps are known as numerical methods. In this section, several common iterative methods will be discussed. The reader is once again referred to Benson et al. (2021) [77] for a comprehensive discussion of numerical methods which extends beyond the scope of this thesis, detailing electrical propagation in tissue models.

2.7.1 Forward Euler Method

Hodgkin-Huxley ODEs describing gating variables and membrane potential can be solved using simple finite difference methods, such as the forward Euler method (or explicit Euler) [62, 77]. The forward Euler method is one of the most basic algorithms for solving ODEs with a given initial value. Consider a function with the following form (similar to Eqn. 2.8):

$$\frac{du}{dt} = f(u, t) \tag{2.41}$$

And let $u_0 = u(t_0)$, the value of u when $t = t_0$. The limit as the time step approaches zero, $\Delta t \to 0$, cannot be numerically evaluated:

$$\frac{du}{dt} = \lim_{h \to 0} \frac{u(t + \Delta t) - u(t)}{\Delta t} \tag{2.42}$$

though for any small, positive timestep Δt, the finite difference can be evaluated. The forward Euler method is convergent (the numerical solution approaches the true solution as the time-step approaches zero), and thus, it is assumed that for any sufficiently small time step Δt, the function $f(u, t)$ remains constant [238]. Thus, the time-derivative of u can be approximated through:

$$\frac{u(t + \Delta t) - u(t)}{\Delta t} = f(u, t) \tag{2.43}$$

given u at some time t, the value of u at some time $t + \Delta t$ can be computed by solving the difference equation:

$$u(t + \Delta t) = u(t) + f(u, t)\Delta t \tag{2.44}$$

This is a single time-step of the forward Euler method. The general form for this iterative solution is given as:

$$u_{n+1} = u_n + f(u_n, t_n)\Delta t \tag{2.45}$$

where n is the timestep and $n + 1$ is the next timestep. The simplicity of the forward Euler method makes it computationally efficient; however, depending on the problem at hand, it may require a very small time-step (<< 1ms) for numerical stability, as the error per each timestep is proportional to the square of the size of the timestep.

More accurate exist such as the fourth-order Runge-Kutta method (or RK4) [238], which takes the average of four incremental estimations to solve each timestep, rather than the single estimation in the forward Euler method. These methods are better suited to highly stiff equations (such as those describing systems where variables change with different time scales, such as gating variables) and allow larger time-steps to be used without a loss of accurately. Despite an increase in computational expense per time-step, these methods may reduce computational expense. The very fast action of the I_{Na} fast activation gate constrains the time-step to the bounds in which the FE method is appropriate, however, and it is for this reason which FE is the most commonly used method in cardiac modelling.

2.7.2 Rush-Larsen Method for Gating Variables

A typical method for solving Hodgkin-Huxley gating variables is the Rush-Larsen method [239, 240], popular due to its improved stability over the forward Euler method and a simple implementation [241]. The general equation for a typical gating variable, y, can be given as:

$$\frac{dy}{dt} = \alpha_y(V_m)(1 - y) - \beta_y(V_m)y \tag{2.46}$$

The Rush-Larsen method assumes that membrane potential, V_m, remains constant over each timestep, such that the rate coefficients α and β are constant over some sufficiently small timestep Δt. This allows Eqn. 2.46 to be treated as a linear ODE with an exact solution given by:

$$y_n = y_\infty(V_m) + \left(y_{n+1} - n_\infty(V_m)\right) \exp\left(-\frac{\Delta t_n}{\tau_y}\right) \tag{2.47}$$

The Rush-Larsen method is more accurate than solving Eqn. 2.46 with the forward Euler method as it only dependent on the membrane potential, V_m, and is not dependent on any derivatives of the gating variable, y.

2.8 Computational Models

This thesis uses previously developed computational models of cardiac AP and intracellular Ca^{2+} handling for different purposes. In Chapters 3 and 4, a simplified version of the O'Hara-Rudy dynamic human ventricular model [46, 50, 237] and the Colman Multi-Scale Cardiac Simulation Framework (MSCSF) compartmentalised spatio-temporal Ca^{2+} dynamics model [1, 49, 50, 237] are used to achieve the second objective of this thesis (see Section 1.3). The third objective of this thesis (development of a novel congruent rabbit electrophysiology model) is done using components from the Aslanidi et al. (2009) rabbit atrial model [242, 243], which itself is an update to the Lindblad et al. (1996) rabbit atrial model [36], and an implementation of the Grandi-Bers human atrial Ca^{2+} handling model [44, 54]. These models will be described in brief detail in this section in order of appearance.

2.8.1 O'Hara-Rudy Dynamic Human Ventricular Model

The O'Hara-Rudy Dynamic Human Ventricular Model [46] (Figure 2.21), often referred to simply as the ORd model, was published in 2011 with the objective of

developing a novel model of the human ventricle able to reproduce a broad range of physiological behaviours accurately. In the decade since publication, the ORd model is considered the "gold standard" for in silico human ventricular electrophysiology [244–246] and has been well-documented and commonly used in many in silico studies in the last decade.

O'Hara reformulated detailed and accurate kinetics for I_{to}, I_{NCX}, I_{K1}, I_{Kr} and I_{Na} using new experimental data collected from more than 100 undiseased human hearts [245], producing an electrophysiological model capable of accurately reproducing electrophysiological biomarkers (APD, APD restitution) observed in experimental data. Extensive validation, electrophysical stability, and the ability to reproduce cellular arrhythmogenic phenomenon (EADs, AP and CaT alternans) make this an attractive model to use for studies on Ca^{2+} dynamic variabilities and simulating drug effects on cardiac cells.

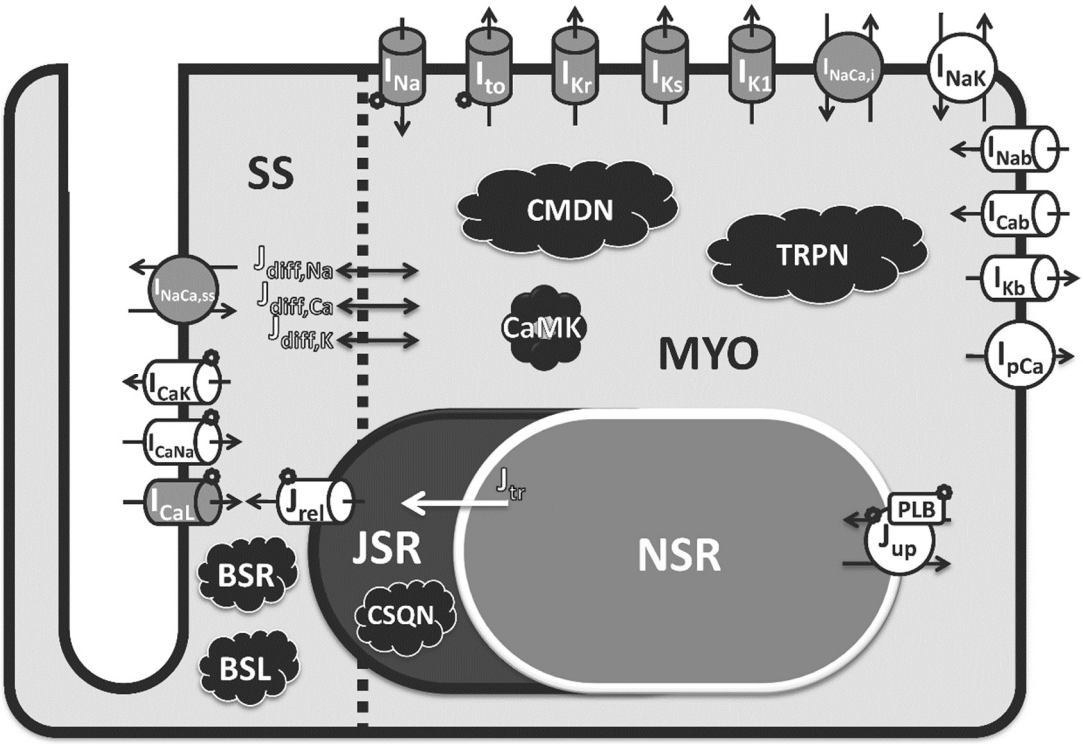

Figure 2.21 ORd human ventricular model schematic

A schematic for the complete O'Hara Rudy Dynamic (ORd) human ventricular model. Formulations for all currents and fluxes were based either directly (grey) or indirectly (white) on undiseased or non-failing human experimental data. Taken from O'Hara et al. (2011) [46].

Limitations of this model include limited sensitivity of I_{CaL} to extra-cellular Ca^{2+}, some deviation from the experimental I-V relationship for I_{CaL} at positive membrane potentials and an inability to produce DADs due to a direct dependence of SR-Ca^{2+} release flux, J_{rel} (via RyR-sensitive channels) on LTCCs [46, 244].

2.8.2 Colman MSCSF Compartmentalised Ca^{2+} Dynamics Model

The Leeds Computational Physiology Labs' Multi-Scale Cardiac Simulation Framework, primarily developed by Michael Colman, is an open-source project, providing a comprehensive framework of biophysically detailed cell models to study cardiac arrhythmias in cardiomyocytes and tissue within a maintained, frequently-updated and consistent framework [50]. The MSCSF contains two 3D spatial-temporal models with different approaches to modelling intracellular Ca^{2+} dynamics: a coarse-grained discretised approach termed the "compartmentalised" model (Figure 2.22) and a higher-resolution free-diffusion model. This section will describe the fundamental structure and dynamics of the compartmentalised model used in Chapters 3 and 4. Full equations, parameters and descriptions for both approaches can be found in [1, 49, 50, 237].

The idealised, compartmentalised model is discretised into a grid of 19500 CRUs (15 x 20 x 65) at a resolution of approximately ~1-2 μm. Each of these CRUs contains five compartments, as is common across Ca^{2+} models [1]: the bulk intracellular space (or bulk cytoplasm), is the largest compartment, taking up approximately $\sim 88\%$ of the volume in each CRU; the SR, which is split into the network and junctional SR (nSR and jSR, $\sim 8.8\%$ and $\sim 1.3\%$ of volume respectively); the sub-space, the space near the t-tubules ($\sim 1.5\%$ volume); and the dyadic cleft, the tightly coupled region containing LTCCs and RyRs ($\sim 0.1\%$ volume). In the dyadic space of each CRU, the number of LTCCs and RYRs is spatially heterogeneous, with a mean of 100 RyRs ($\pm$ 40) and 13 LTCCs ($\pm$ 28%) per CRU by default. LTCC and RyR activation are stochastically modelled using Markovian formulations to capture the random nature of CICR [49].

The bulk cytoplasm, nSR and sub-space can be spatially coupled to neighbouring CRUs, but the jSR and dyadic spaces are isolated and only transfer between compartments in their CRU. The Ca^{2+} concentrations in each of these five compartments are described by a set of homeostatic equations [1]:

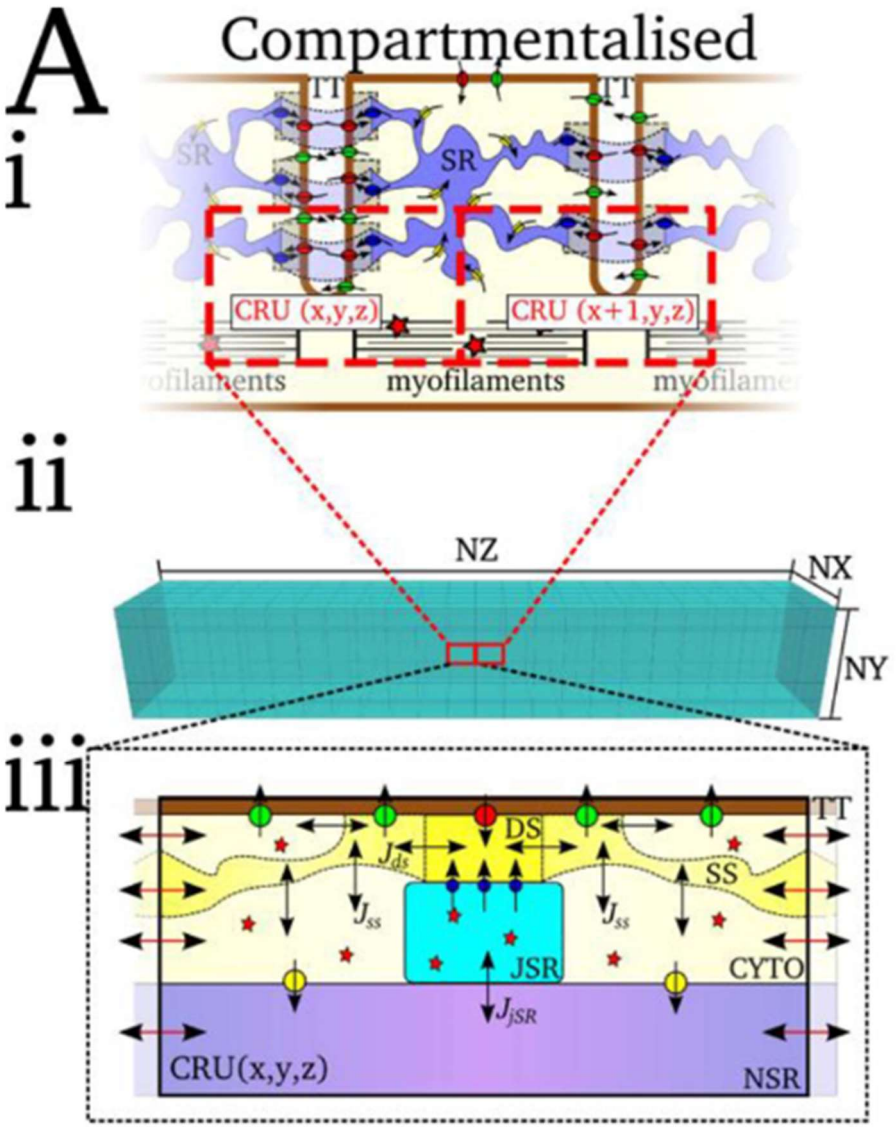

Figure 2.22 MSCSF compartmentalised Ca^{2+} dynamics model

A schematic of the compartmentalised 3D spatio-temporal Ca^{2+} dynamics within the MSCSF framework. The compartmentalised model is discretised using the volumes associated with a dyad (or Ca^{2+}-release unit, CRU) (i). These CRUs are arranged in a 3D matrix to form the cell (ii). Each CRU contains a t-tubule, TT, and five compartments: the dyadic cleft space, DS; sub-space, SS; bulk cytoplasm, CYTO; network SR, NSR; and junctional SR, JSR. Fluxes between these are illustrated by arrows. Adapted from Colman et al. (2020) [225].

$$\frac{d[Ca^{2+}]_{cyto}}{dt} = \beta_{\text{cyto}}\left(\boldsymbol{D}\nabla^2[Ca^{2+}]_{cyto} + \phi_{\text{cyto}} + \left(\frac{v_{ss}}{V_{cyto}}\right)J_{ss}\right) \quad (2.48)$$

$$\frac{d[Ca^{2+}]_{ss}}{dt} = \beta_{ss}\left(\boldsymbol{D}\nabla^2[Ca^{2+}]_{ss} + \phi_{ss} + \left(\frac{v_{ds}}{V_{ss}}\right)J_{ds}\right) \quad (2.49)$$

$$\frac{d[Ca^{2+}]_{nSR}}{dt} = \beta_{\text{nSR}}\left(\boldsymbol{D}\nabla^2[Ca^{2+}]_{nSR} + \phi_{nSR} + \left(\frac{v_{jSR}}{V_{nSR}}\right)J_{jSR}\right) \quad (2.50)$$

$$\frac{d[Ca^{2+}]_{ds}}{dt} = \phi_{ds} - J_{ds} \quad (2.51)$$

$$\frac{d[Ca^{2+}]_{jSR}}{dt} = \beta_{jSR}(\phi_{jSR} + J_{jSR}) \quad (2.52)$$

Where $\boldsymbol{D}$ is the diffusion coefficient, ∇^2 is the 3D spatial Laplacian operator (also called the vector Laplacian), which determines diffusion between compartments, β are instantaneous buffering terms, v refers to volumes of the compartments. Ca^{2+} flux between each compartment, J, is given by the following set of equations:

$$J_{ss} = \left([Ca^{2+}]_{ss} - [Ca^{2+}]_{cyto}\right)\tau_{ss}^{-1} \quad (2.53)$$

$$J_{ds} = \left([Ca^{2+}]_{ds} - [Ca^{2+}]_{ss}\right)\tau_{ds}^{-1} \quad (2.54)$$

$$J_{jSR} = \left([Ca^{2+}]_{nsR} - [Ca^{2+}]_{jSR}\right)\tau_{jSR}^{-1} \quad (2.55)$$

where τ are the time-constants of diffusion for each compartment, and finally the reaction terms, ϕ, which are given by the following set of equations:

$$\phi_{cyto} = J_{NCX} + J_{CaP} + J_{CaB} - \left(J_{up} - J_{leak}\right) - J_{trpn} \quad (2.56)$$

$$\phi_{nSR} = \left(J_{up} - J_{leak}\right)\left(\frac{v_{cyto}}{v_{nSR}}\right) \quad (2.57)$$

$$\phi_{ss} = \left(J_{NCX,ss} + J_{CaP,ss} + J_{CaB,ss}\right) \quad (2.58)$$

$$\phi_{ds} = J_{rel} + J_{CaL} \quad (2.59)$$

$$\phi_{jSR} = -J_{rel}\left(\frac{v_{ds}}{v_{jSR}}\right) \quad (2.60)$$

The spatial Laplacian operator, ∇^2, describing spatial diffusion in Equations 2.47 - 2.49 is approximated for some voxel, $n \in N_{cyto}$, by coupling the cytoplasm, sub-space and nSR to the voxel's 6 closest neighbours (located +x, -x, +y, -y, +z, -z

spatially in the matrix relative to n) using a 6-node nearest neighbour finite distance approximation:

$$\boldsymbol{D}\nabla^2[Ca^{2+}]_{x=cyto,ss,nSR} \approx J_{Ca\_diff\_x} \tag{2.61}$$

$$J_{Ca\_diff\_x} = \sum_{i=1}^{i=3}\left(\frac{^{e_i+1}[Ca^{2+}]_x + {}^{e_i-1}[Ca^{2+}]_x - 2\,{}^{e_i}[Ca^{2+}]_x}{\tau_{x,e_i}}\right) \tag{2.62}$$

Where e_i refers to the three spatial dimensions (x, y, z) and τ_{x,e_i} is the spatial discrepancy step.

2.8.3 Aslanidi Rabbit Atrial Model

Aslanidi et al. (2009) published a novel rabbit atrial electrophysiological model of right atrial cells [242], improving upon the previously published Lindblad et al. (1996) model [36] by replacing currents formulated from hybrid datasets (different cell types, different animals) with novel formulations for I_{Na}, I_{CaL}, I_{to} and I_{sus} based on rabbit atrial experimental data provided by Yamashita et al. (1995) [247] and Ko et al. (2006) [248]. This model inherited the qualitative Ca^{2+} handling system from the Lindblad model and thus can only qualitatively reproduce the CaT, as the limited available data did not provide sufficient information to model Ca^{2+} handling mechanisms in the rabbit atria quantitatively.

The Aslanidi et al. (2009) model [242] comprises of a family of cell models which describe the electrophysiological properties of cell types present within the rabbit atrium, including left and right atrial cells, crista terminalis and pectoral muscle cells [37, 38, 242]. Derivations from these models are presently used in rabbit atrial model studies, combined with contemporary models of non-rabbit specific Ca^{2+} handling, which mitigate the shortcomings of the qualitative Ca^{2+} handling system. [3, 48, 242]. Aslanidi et al. (2009) produced a model variant incorporating a modified version of the Shannon-Bers rabbit ventricular Ca^{2+} model [39]. SR-Ca^{2+} uptake and release was rescaled to produce shorter CaT (~100ms) characteristic of rabbit atrial myocytes [249, 250] and had their rate constants increased significantly, along with a ~50% reduction in cell volume parameters. Unfortunately, several hybrid currents remain in the Aslanidi model due to limited experimental data.

2.8.4 Grandi-Bers Human Atrial Ca^{2+} Handling Model

The Grandi-Bers human atrial AP and Ca^{2+} model [44] was the first model to focus on human atrial Ca^{2+} handling, developed from their labs' human ventricular model (Grandi et al. (2010) [54]) which itself is a derivation from a rabbit ventricular model produced in the same lab (Shannon et al. (2004) [39]). Ionic currents and Ca^{2+} dynamics were modified from the human ventricular myocyte by implementing experimentally observed structural and ionic differences between atrial and ventricular myocytes [251]. Included within these changes were reformulations of I_{CaL} magnitudes and kinetics; reduction of I_{NCX} and I_{K1}; addition of atrial-specific I_{Kur}; modification of I_{to} to only include fast kinetics; and doubling the cytoplasmic constant of J_{up}. This model inherited the multi-compartmental structure described in Shannon et al. (2004) [39], along with the first computational description of the dyadic cleft. These compartments are illustrated and described in further detail in Section 5.2, where this Ca^{2+} model is used in the development of a novel rabbit atrial electrophysiology model. The Grandi-Bers model is widely utilised in simulation studies [43, 252, 253] and accounts for electrophysiology and Ca^{2+} handling properties in atrial cells under control and AF conditions, making it a suitable framework for studying Ca^{2+} variability.

3

A Novel Method of Quantifying Spatial Heterogeneity in Sub-Cellular Structural Microscopy Images

3.1 Introduction

3.1.1 Importance of Sub-Cellular Structure

The periodic cycling of Ca^{2+} ions in cardiac cells couples electrical excitation to the mechanical contraction of cardiac tissue [16] (refer to Section 2.2.3 for a full description of ECC). The delicate equilibrium of Ca^{2+} fluxes maintains the homeostasis of this system through specialised ionic transports, fluxes that must be tightly regulated to ensure a stable, sufficient cardiac output to meet the body's dynamic physiological demands [14, 17]. Disruption to this balance is linked to the development of pro-arrhythmic cellular phenomena [15, 17, 254]. Investigating the complex, multi-scale mechanisms by which aberrations in Ca^{2+} homeostasis develop into arrhythmic behaviours is therefore critical to achieving a fundamental understanding of the heart's electro-mechanical system; and to the clinical motivations of treating common cardiac conditions such as atrial fibrillation and heart failure (HF) by which these mechanisms underlie [255, 256].

In Section 2.3.3, remodelling of cellular structure and function of cardiomyocytes under cardiac disease was described, and the presence of heterogeneity in intracellular Ca^{2+} cycling. Recent advances in super-resolution imaging, including the development of techniques such as dSTORM, DNA-PAINT and expansion microscopy [12], have provided insight into the structure of individual RyR clusters [12], the t-system [76, 182], SR membranes [182] and the co-localisation of the Na^{+}-Ca^{2+} exchanger (NCX) and dyads [13]. As discussed prior, there is significant evidence that cellular remodelling of the organisation of these channels is associated with cardiac disease [13, 176, 180, 182, 183].

Experimental Ca^{2+} imaging studies reveal significant spatial variation in the upstroke and decay phase of the intracellular CaT [257], indicating a dependence on underlying sub-cellular structure and the spatially non-uniform distribution of Ca^{2+} channels. Thus, it follows that this observed heterogeneity in channel expression

must have functional ramifications on intracellular Ca^{2+} homeostasis and consequently influence the dynamics associated with the generation of arrhythmic phenomena at the cellular level. While the extent of variation in the number of RyRs present across clusters has been recently described by Sheard et al. (2019) [12], quantification of the magnitude of heterogeneity in health and pathology has yet to be performed in other key Ca^{2+} channels, including NCX and SERCA2a. Moreover, the non-uniform spatial profile of these channels (including RyRs) has not been quantified, including correlation in expression individually and concomitantly of these channels. A full characterisation of this spatial heterogeneity would provide substantial insight into the role of spatial structures in ECC.

3.1.2 Correlating Heterogeneous Structure and Function

A comprehensive analysis of the structure-function dynamics of sub-cellular expression heterogeneity and the intracellular Ca^{2+} handling system would elucidate the mechanisms by which Ca^{2+} cycling controls the heartbeat in control and disease. However, correlating underlying structure to function presents a significant research challenge. Due to the role of diffusive coupling between different sub-cellular regions, Ca^{2+} heterogeneity does not follow linearly or trivially from channel expression, and thus it is necessary to perform both structural imaging and Ca^{2+} imaging on the same cells. Hurley et al. (2021) [205] presents the only contemporary experimental strategy for co-localising Ca^{2+} sparks and underlying RyR structure; however, Ca^{2+} imaging is limited by resolution, detection sensitivity, and sensory limitations. Therefore, it is difficult to relate measured whole-cell spatial Ca^{2+} profiles to underlying channel expression and dissect the relative roles and importance of heterogeneities in different channels experimentally.

Computational modelling is a powerful tool to supplement experimental studies and dissect the mechanisms underlying cardiac function and disease [30, 31]. Developing accurate and physiologically detailed models presents many challenges (refer to Section 1.2) in formulating the mathematical descriptions of complex physiological mechanisms and incorporating experimental data. Realistic image-based modelling presents further unique challenges that disjoint experiments and simulations. Current high-resolution, detailed models are computationally intensive, and while possible for focused investigations [49, 258], are unsuitable for systematic studies requiring larger numbers of simulations on a range of structures and limited

to available structural data. Thus, developing a scalable image-based modelling method suitable for larger-scale comprehensive investigations relating the underlying subcellular structure to cellular function has considerable merit.

3.1.2 Aims

This chapter addresses current barriers in characterising spatial heterogeneity in channel expression and correlating this underlying structure to function. A novel method is developed to quantify underlying the correlation, organisation, and variance in expression in confocal fluorescent microscopy data using pre-existing data. A new marker, correlation length scale, is then used as the basis of a novel, scalable image-based computational modelling approach which uses Gaussian random fields to reproduce the observed correlation, variation and expression quantified using the novel method in an expression map. An open-source toolkit that contains implementations of the above methods is described, and finally, an example application of these methods is provided in a proof-of-concept study which demonstrates the value of these methods is given. To summarise, the objectives of this chapter are as follows:

1. To develop a novel method to quantify the spatial heterogeneity of existing structural microscopy datasets.
2. To bridge the gap between experiment and simulation by developing a scalable image-based modelling technique utilising the markers quantified by the novel method.
3. To develop an open-source software containing implementations necessary to replicate this protocol.

3.1.3 The Sub-cellular Heterogeneity Analysis Toolkit

The software developed as part of this thesis is available with documentation on our lab's GitHub page (https://www.github.com/michaelcolman) and through our group's website (http://physicsoftheheart.com). The version of the toolkit described in this thesis is the most up to date version at thesis submission. However, this may have been updated to ensure compatibility with required packages as they update in the future.

The user requires Python 3.6.0 or higher (ideally the most recent version) to run this toolkit and a Microsoft Windows, macOS or Unix-based system. An executable

labelled “Setup” is provided to install all dependencies, and there are several examples of how to use this software, including example data and a full set of documentation.

3.2 Method Development

3.2.1 Ethical Considerations

The animal data used in this chapter were either previously published [13] or produced for non-related research at the time of writing and not produced for this study. All non-published animal data was generated at the University of Leeds under various historic licenses.

In line with the 3Rs principles, this work aims to replace animal research with an appropriate, validated in silico model, and this project was able to reduce the number of animals required through the recycled use of these banked historical samples, both published and unpublished images.

All animal experiments were conducted according to the UK Animals (Scientific Procedures) Act of 1986 under the EU Directive 2010/63/EU with UK Home Office and local ethical approval.

3.2.2 Experimental Datasets

This method was developed using high-resolution confocal microscopy datasets obtained from healthy rat ventricular myocytes at resolutions of between 0.4 and 0.9 μM per pixel, with fluorescently stained SERCA2a, RyR or NCX.

The imaging data utilised with this chapter (and, by extension, Chapter 4) were not obtained by the author of this thesis. Instead, all experimental imaging data was donated from the co-authors of the relevant publications (Colman et al. (2020) [1], and Holmes et al. (2021) [2]; related conference abstract: [259]): Izzy Jayasinghe, Miriam Hurley and Thomas Sheard of Leeds University (at the time this work was produced). The following subsections (3.2.2.1 – 3.2.2.4) contain information that describes how these data were obtained; credit goes to Miriam Hurley for putting together the information in these subsections.

3.2.2.1 Cell Isolation

Ventricular cardiomyocytes from adult male Wistar rats were obtained from enzymatic isolation upon the Langendorff apparatus. The whole heart was quickly excised upon the animal reaching its endpoint and cannulated to a Langendorff apparatus at the aorta. Retrograde perfusion of isolation solution (IS) consisting of (in mM): 130 NaCl, 1.4 $MgCl_2$, 5.4 KCl, 0.4 NaH_2PO_4, 5 HEPES, 10 Glucose, 20 Taurine, 10 Creatine at pH 7.4; 37°C with added 0.75 mM $CaCl_2$ was started at a steady 7 mL/min to clear the heart's coronary circulation. The following protocol was then implemented to enzymatically isolate left and right ventricular cardiomyocytes. For 4 minutes, IS with added 0.1 mM EGTA (Sigma-Aldrich, USA) and 0 mM $CaCl_2$ was perfused to remove Ca^{2+} from the heart. Next, a 7-minute perfusion of IS with 0 mM $CaCl_2$, 1 mg/mL Collagenase Type II (Worthington Biochemicals, USA) and 0.8 mg/mL protease (Sigma-Aldrich, USA) occurred to enzymatically digest the heart. The whole heart was removed from the Langendorff apparatus and weighed. Atria and vasculature were dissected away, and the heart weighed again before the dissection and weighing of the left and right ventricle. The RV and LV tissue were placed in separate conical flasks with collagenase solution. The conical flasks were shaken using a rotary shaker for 5 minutes, within a 37°C water bath prior to filtering enzyme solution through a 200 μm^2 nylon mesh gauze. Collected cardiomyocytes were centrifuged (50 rpm; 45 s), the supernatant removed, and cardiomyocytes re-suspended within 750 mM $CaCl_2$ containing IS. The remaining tissue was shaken again for 5 minutes, with the above steps repeated until no cell-rich tissue remained. LV and RV cardiomyocytes were separately re-suspended with Tyrode's solution, which constituted of (in mM): 140 NaCl, 4 $MgCl_2$, 1 KCl, 10 HEPES, 10 Glucose, 0.75 $CaCl_2$ at pH 7.4 and kept at room temperature (RT) until required for experiments.

3.2.2.2 Fixation

Cardiomyocytes for immunofluorescence staining were incubated for 2 hours at 37°C upon an 11.9 ug/mL laminin-coated coverslip (#1.5) prior to fixation in situ with 2% PFA followed by PBS washes.

3.2.2.3 Immunofluorescence Staining

Ventricular cardiomyocytes were permeabilised with 0.1% Triton X-100 (Sigma-Aldrich, USA) in PBS for 10 minutes at RT. Subsequently, cells were blocked for 60 minutes at RT with PBS with 10% normal goat serum (NGS; ThermoFisher Scientific, UK). A primary antibody was used to label the protein of interest. The primary antibody was diluted in incubation solution to its required working concentration. Incubation solution consists of the following (w/v or v/v); 0.05% NaN_3, 2% NGS and 0.05% Triton X-100 dissolved in PBS. Cells were incubated overnight at 4°C and then washed three times in PBS for 20 minutes each.

Standard Alexa fluorophore dyes were used to undertake diffraction-limited confocal microscopy. These secondary antibodies were applied to cells for 2 hours at RT. Cells were washed three times in PBS for 20 minutes each prior to storage at 4°C until imaged.

Primary antibodies: SERCA (mouse) Abcam 1:200 AB2861, Anti-Mouse Alexa 488 Invitrogen 1:200 A11001, Anti-Mouse Alexa 647 Invitrogen A21235.

3.2.2.4 Confocal Microscopy

Images were obtained using an LSM880 inverted microscope (Carl Zeiss, Jena), with a Plan-Aprochromat 63x 1.4 NA objective and an approximate 0.7 airy unit pinhole. 633 nm or 488 nm laser excitation with emission bands were selected using in-built software. Images acquired using the ZEN software.

3.2.3 Quantifying Spatial Variation using Variograms

Quantifying spatial heterogeneity within a dataset requires measurements of the direction and magnitude of variation at each point within the data. One common approach to measuring this variation in spatial data is using variograms, statistical functions that describe a dataset's spatial continuity. An example of an empirical variogram is presented in Figure 3.1 and is estimated using an algorithm calculating the following equation:

$$\gamma(r_k) = \frac{1}{2N(r_k)} \sum_{i=1}^{N(r_k)} \left(z(x_i) - z(x_i')\right)^2 \tag{3.1}$$

where γ is the semi-variance, a measurement of the spatial dependency between all sets of two points (x, x') at some distance r, and the bins are given by $r_k \leq$

$\|x_i - x_i'\| < r_{k+1}$. The estimated variogram is then fitted using some covariance function that determines the specific variables estimated in this fitting procedure [260], given by the general formula:

$$\gamma(r) = \sigma^2 \cdot \big(1 - cor(r)\big) + C_0 \tag{3.2}$$

where σ^2 is variance, and C_0 is the nugget, the height of discontinuity at the origin, representing a non-zero variance at $r = 1$ (Figure 1 Bii) and $cor(r)$ is some correlation function.

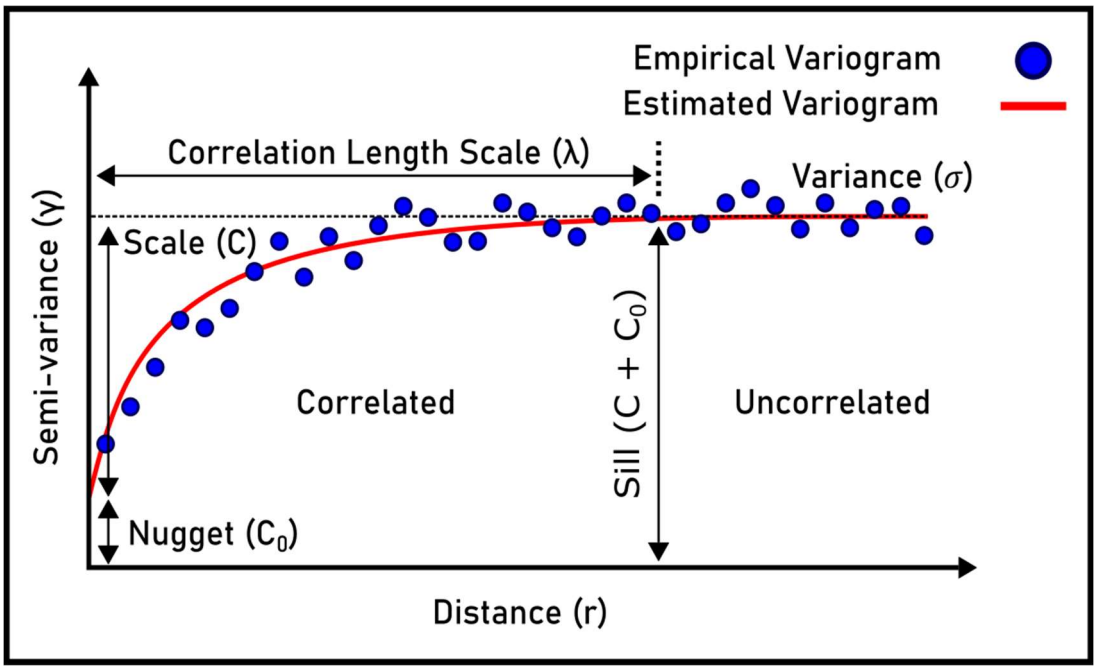

Figure 3.1 The empirical variogram.

The semi-variance of a dataset is plotted as a function of distance, r , and used to fit an empirical variogram using some pre-specified covariance function. The covariance function selected determines the specific parameters measured; common parameters include the variance, σ, correlation length scale, λ, and the nugget, C_0.

The specific covariance function selected to measure the spatial profile of a dataset must consider the form of that dataset. A suitable covariance function to analyse imaging data is the squared exponential covariance function (also known as the Gaussian or SE kernel); it is well suited to imaging studies due to its stationarity and simplicity. The Gaussian Kernel, k_{SE}, is given by:

$$cov(r) = k_{SE}(x, x') = \sigma^2 e^{-\frac{(x-x')^2}{2\lambda^2}} \quad (3.3)$$

where this expression replaces $\sigma^2 \cdot \big(1 - cor(r)\big)$ in Eqn. 3.2, and λ is the correlation length scale; the distance over which data is spatially correlated (i.e., it is impossible to extrapolate data more than λ units away from any point). The correlation length scale implies the spatial smoothness of data, e.g., how ion channel expression in a cardiomyocyte correlates along its axes. The Gaussian kernel requires a smooth sample path to estimate this length scale reliably; thus, this approach may require down-sampling the data to lower resolutions. This method, if successful, estimates the variation, correlation length scale and anisotropy of the dataset (through measurements of the former parameters in only orthogonal directions). Along with a measurement of the mean whole-cell expression, which is trivial, this provides all the information needed to characterise the spatial heterogeneity within imaging data.

Variograms are often used alongside spatial random fields (SRFs) in field-based imaging studies [1, 261, 262]. By definition, a random field, $F(x)$, is a random function over some arbitrary, usually multi-dimensional system which can be described as a set of continuously indexed variables $x \in \Omega$ where Ω is an open set of real numbers which describe the geometry of the system [263, 264]. SRFs can be analysed using variograms in the method described above and produced using the parameters extracted from the empirical variogram using covariance functions. Therefore, SRFs provide an opportunity to model and validate methods involving spatial heterogeneity or variogram analyses – which will be utilised later in the chapter.

3.2.4 Image Processing

The confocal microscopy datasets must be suitably processed to ensure the variogram fitting protocol described in Section 3.2.3 produces accurate and meaningful results. The processing procedure for a single x-y slice of a confocal dataset is presented in Figure 3.2.

To recap, the variogram fitting procedure using a Gaussian kernel will quantify the isotropic and directional correlation length scale and variance in a dataset. In order to obtain directional length scales, the image must be rotated such that the

longitudinal and transversal axes of the cell are in alignment with the x and y axes of the image (Figure 3.2A), and this alignment must remain consistent in order to compare different cells. A smooth sample path is required to use the Gaussian kernel (Eqn. 3.3), and as such, any region outside of the boundaries of the cell must be removed, as well as any internal cell structures (such as a nucleus) which would perturb this. Thus, the image should be cropped to obtain the largest region possible that meets these criteria (Figure 3.2A).

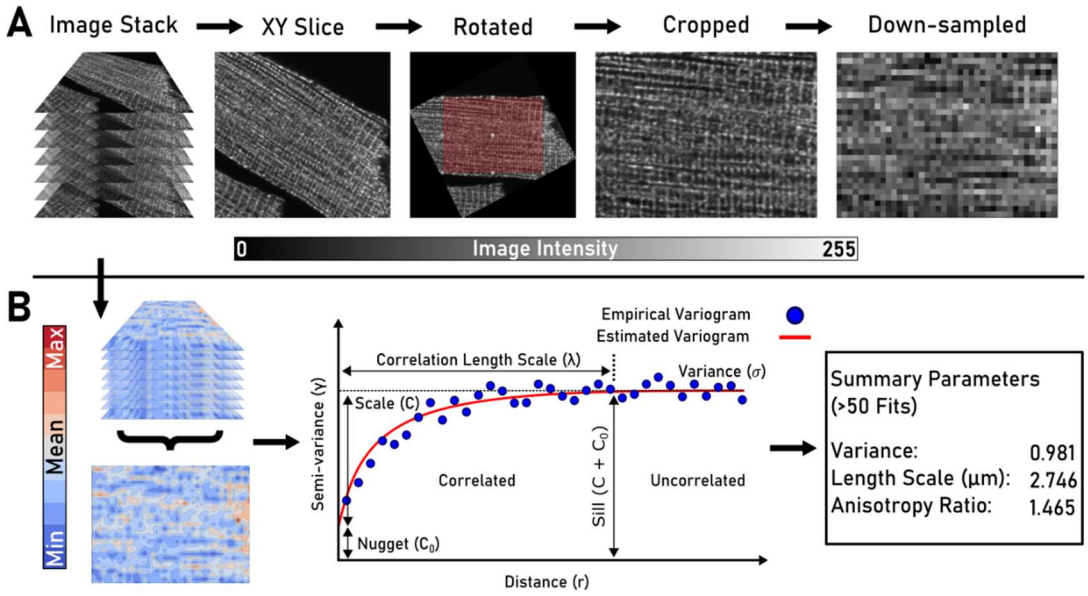

Figure 3.2 Confocal image processing and analysis

A – Illustration of the processing required to render an image suitable to fit an empirical variogram and extract correlation length scales from confocal microscopy imaging data. In this example, a rat ventricular myocyte with immunofluorescence stained SERCA2a is analysed. B – The semi-variance across pairs of points in the integrated 2D dataset is plotted as a function of distance, then fitted by an estimated variogram with a Gaussian covariance function to measure correlation length scales, λ, in the spatial data. Outputs are a statistical summary of > 50 successful fits.

In addition to cropping out extracellular space and large interior organelles, the image data requires down-sampling to a resolution, resulting in continuous data by removing the influence of the underlying membrane structure. Super-resolution confocal images are large datasets that can be substantially manipulated; however, the resulting dataset must contain a large quantity of data to obtain meaningful

values of the longitudinal and transversal correlation length scales; though, it is possible to obtain a reasonable approximation of isotropic correlation length scale with fewer data points. Thus, maximising the amount of data within the processed dataset while ensuring the removal of underlying structures and cellular obstructions is paramount during image processing.

For 3D datasets, this process is repeated for all suitable x-y slices within the z-stack of images to ensure identical dimensions in the final dataset. The x-y slices are then integrated over the z-axis, incorporating the spatial information for a 2D variogram fitting (Figure 3.2B).

3.2.5 Empirical Variogram Fitting Procedure

Once processed, the image data is used to produce an unstructured mesh grid, used for an initial estimation of isotropic variation and correlation, followed by a structured mesh grid using the initial isotropic estimations as a starting point to determine estimations in the longitudinal and transversal parameters. Unstructured grids are suitable to estimate isotropic properties as connectivity is based upon the variation of the dataset, as opposed to the structured grid, which contains information on direction and variation using the connectivity of the original dataset on an equidistance Cartesian grid.

Each of these estimations is obtained by calculating a semi-variogram for the dataset using the following equation [261]:

$$\gamma(r_k) = \frac{1}{2N}\sum_{i=1}^{N}\left(z(x_i) - z(x_i')\right)^2 , \qquad r_k \leq \|x_i - x_i'\| < r_{k+1} \tag{3.4}$$

where γ is the estimated semi-variogram, and r_k is the distance between points x_i, x_i'. Once γ_i has been calculated for the isotropic, longitudinal, and transversal directions; these are used to fit an empirical variogram (Figure 3.1, 3.2B). The calculations necessary to perform this analysis were performed in Python using the GeoStatTools package [260]. The specific function also requires pre-specified binning parameters and calls the SciPy [265] least-squares fitting algorithm to iteratively fit the estimated variogram function to the dataset (Figure 3.1). This process produces outputs for physical values of variation, correlation length scales and anisotropy, which can then be used to produce spatial random fields using some

complementary covariance function. Each cell was analysed a minimum of 50 times to ensure that any outputs were reliable.

3.2.6 Validation of Image Analysis Method

Variograms and spatial random fields are familiar tools in imaging studies; however, their use in quantifying correlation length scale and variation in sub-cellular structural image data is a novel application and must be validated. Firstly, the method must be shown to produce consistent measurements isotropic and directional correlation length scales (Figure 3.3), and secondly, the method must accurately estimate the spatial parameters for a dataset with known correlation length scales (Figure 3.4).

A total of five cellular imaging datasets from different cell types were analysed using the discussed methodology (Figure 3.3A). Images were rotated to the correct alignment, cropped to remove background and large internal structures and down-sampled to a resolution of 1 – 1.5 μm^2 to produce a smooth sample path. These processed datasets were then analysed using the variogram method in their correct orientation and then analysed again after a quarter-rotation clockwise - aligning the x-axis of the myocyte with the y-axis of the image (Figure 3.3B). After processing, these datasets had dimensions of between 25-35 px in the x- and y-directions – reducing the dimensions of the original datasets considerably.

Cells 1 and 2 produce identical fits in all directions, while Cells 3-5 produce similar isotropic fits but show small differences in directional fitting (Figure 3.3B); the x- and y- directional fits are swapped as expected after the rotation but vary due to the difficulties of fitting variograms to smaller datasets. Isotropic fits are generally more similar than directional fits after rotation, with only cell 5 displaying a visible difference. Thus, for cellular imaging data, we can infer that this method is suitable for estimating correlation length scales in the isotropic, transversal, and longitudinal directions, with some difficulties in estimating directional correlation in smaller datasets.

In Figure 3.4, large Gaussian random fields (GRFs: i.e., SRFs produced using the Gaussian covariance function used to analyse the confocal microscopy images) were constructed to ensure that the variogram analysis method correctly estimated the correlation length scales of normalised images. Two isotropic and two anisotropic maps were produced with dimensions of 250 x 250 pixels, normalised such that each

value in the field was between 0 and 2, and the mean of each GRF was kept identical.

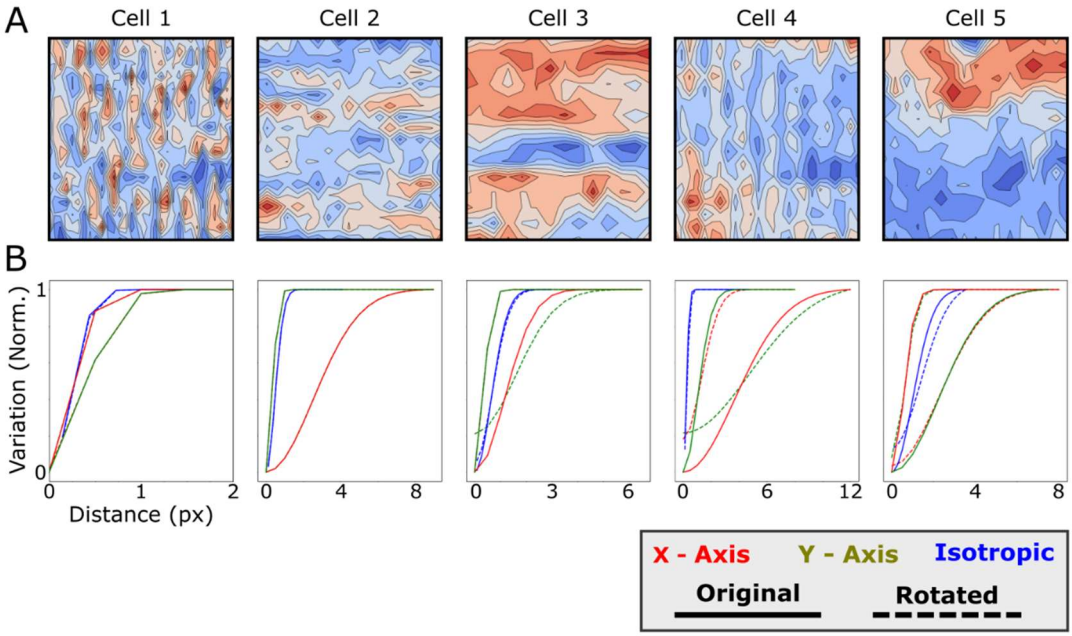

Figure 3.3 Validating the consistency of the isotropic and directional variogram fitting procedure

A) Contour maps of confocal microscopy datasets from 5 different rat ventricular myocytes, post-processing. Maps are scaled for visual purposes; actual data sizes range from 20-35 px in x- and y- directions. B) Normalised variogram fitting in the isotropic (blue), x- (red) and y- (green) directions for the corresponding cells above. Each cell was fitted in its regular orientation (full lines) and after a 90-degree rotation clockwise (dashed lines)

All GRF expression maps, when analysed, reproduced estimations of correlation length scales congruent with the values from which they were generated. Any minor variation in this estimation can be attributed to the inherent randomness of field generation at these scales. Thus, it can be concluded that the variogram analysis method is suitable for analysing both confocal microscopy datasets and GRFs generated from the variogram analysis outputs.

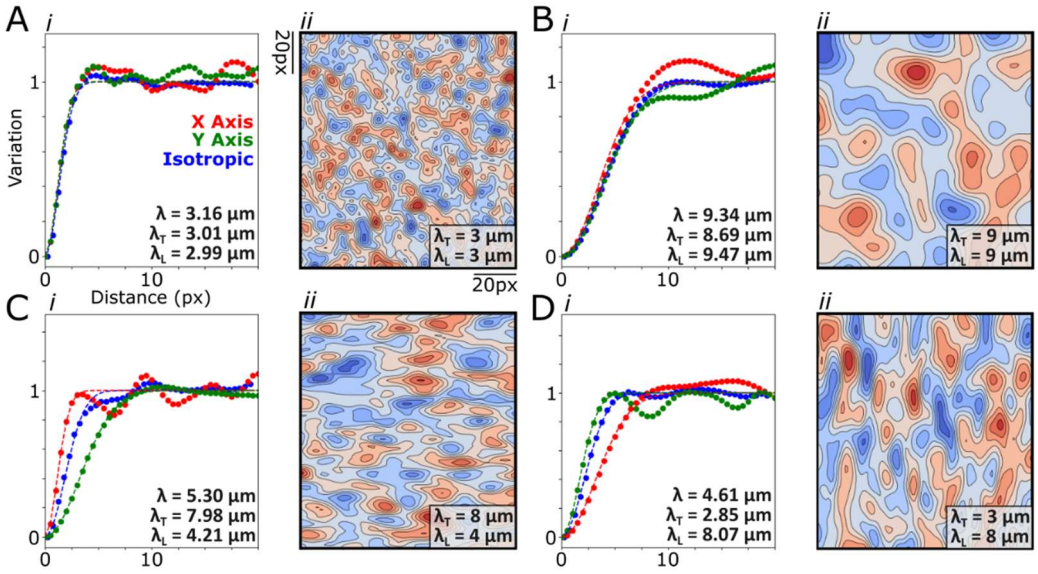

Figure 3.4 Validating the accuracy of the isotropic and directional variogram fitting procedure

Large isotropic (A, B) and anisotropic (C, D) Gaussian random fields (GRFs) were generated with dimensions of 250 x 250 px. For each map A, B, C, D: i – Empirical variogram fitting (dashed lines) for isotropic (blue), x- (red) and y- (green) directions, fitted to the semi-variogram of each GRF (markers, coloured) to determine variation and correlation length scale, λ; ii – Contour maps displaying 100 x 100 px regions of the generated GRFs. X-axis is transversal, λ_t; Y-axis is longitudinal, λ_L.

3.3 Image-Based GRF Modelling Approach

3.3.1 Practical Approaches to Modelling Spatial Heterogeneity

Producing expression maps to model spatial heterogeneity on the resolution of the compartmentalised Ca^{2+} handling model enables a comprehensive investigation into the functional impact of a range of spatial expression structures. However, producing an expression map at this resolution that captures sufficient spatial information from the experimental imaging data, but remains suitable for large-scale systematic studies, is challenging,

A very trivial and crude approach to constructing such an expression map would be to use a random number generator or a Gaussian distribution to populate the values of some 3D domain with values within physiological constraints (Figure 3.5A).

Such an approach would only require a physiologically suitable variance and some understanding of total-whole cell expression variability. This, however, is an unsuitable approach to study sub-cellular heterogeneity comprehensively. Random generation of values does not capture the spatial organisation inherent within cardiomyocytes, nor is it realistic to produce a range of maps suitable for studying the impact of the spatial organisation of expression using this method.

A second approach could be to produce a patch-based expression map generated using an algorithm, specifying regions of differing expression and the volume and shape of the patches (Figure 3.5B). This approach may be suitable to study larger structures, such as transverse-tubule organisation [3], which have the binary options of being present or absent from some region of a cell, but it is not suitable for studies in which there is a gradient of expression between all voxels of the cell. To simulate sub-cellular structure to a reasonable approximation at the discretisation of the compartmentalised model, variation in the expression gradient is an important factor in describing heterogeneity.

An ideal method is by using spatial random fields (SRFs) in conjunction with an appropriate distribution function (Figure 3.5C). SRFs have been utilised in cardiovascular modelling studies previously: modelling the effects of fibrosis and vulnerability to re-entry in human atrial tissue [266]; modelling uncertainty in the orientation of cardiac myofiber orientation using random fields [267]; 3D reconstruction of the left ventricle in cardiac angiography [268]. Additionally, they are a well-documented tool for image-based studies in other research fields such as cosmology, used in spatial field reconstruction to aid in creating synthetic images of galaxy properties from noisy data [269] and dark matter mass mapping from weak gravitational lensing measurements [270].

SRFs are constructed using distribution functions that account for the variation, correlation, and anisotropy in a variable; applied to channel expression, this would ensure that the expression value in each CRU is not independent of that in its neighbours, which would ensure no unphysiological extremes in the gradient of expression throughout the cell (Figure 3.6). Using a suitable distribution function such as the Gaussian function allows the application of constraints that impose physiological values obtained from the microscopy data.

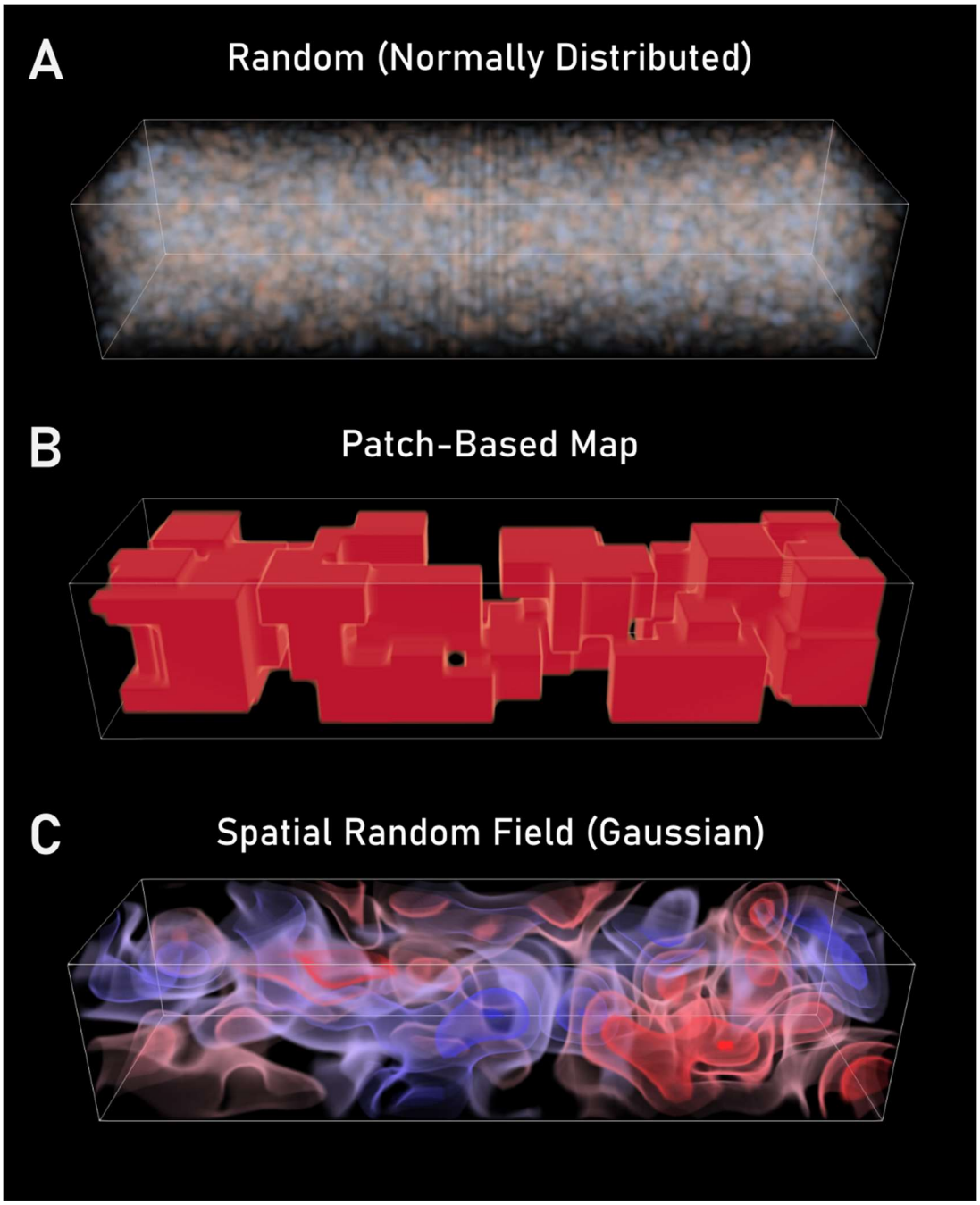

Figure 3.5 Types of heterogeneous expression map.

Three examples of heterogeneous, 3D expression maps. A – A normally distributed random population map. Each value is taken randomly from a Gaussian distribution with no constraints. B – A Patch-based map generated using a random algorithm, as performed in [3]. C – Gaussian random field (GRF) generated using a Gaussian covariance function.

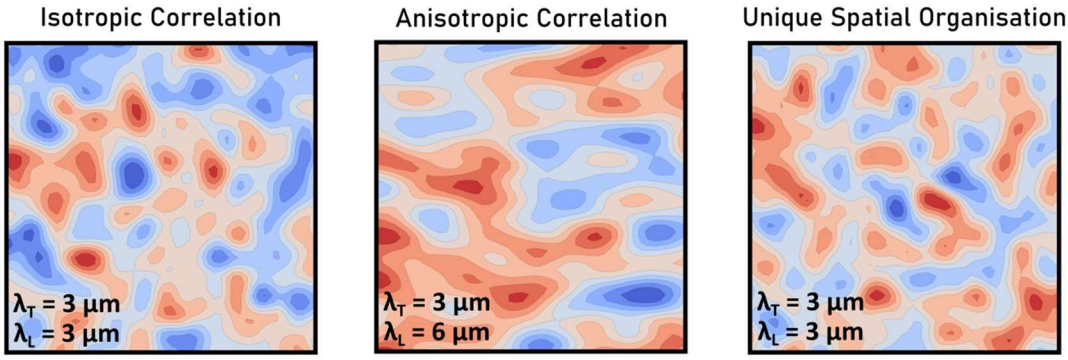

Figure 3.6 Illustration of GRF Properties

Gaussian random fields (GRFs) have several properties which make them ideal for modelling heterogeneity. Correlation length scales can be isotropic (left) or anisotropic (middle). Using the same set of input parameters (right), it is possible to produce unique maps with the same correlation, mean expression and variation but a unique spatial organisation.

It has been demonstrated that mean expression, variance, and correlation length scales can be accurately determined using the novel variogram approach detailed in Section 3.2. Therefore, it is possible to use Gaussian random fields to produce a range of expression maps representing the full range of experimentally observed correlation length scales. Moreover, the ability to generate maps with a unique spatial organisation from the same input parameters allows for the study of spatial organisation in isolation; thus, making GRF expression maps an attractive choice for modelling correlation length scales.

3.3.2 Image-Based Modelling using the Multi-Scale Cardiac Simulation Framework

The GRF expression maps can be generated with any dimensions to be suitable for use in computational models. This chapter uses a simplified version of the O'Hara Rudy dynamic human ventricle AP model, detailed in Section 2.8.1 (Figure 3.7A), combined with the compartmentalised spatiotemporal stochastic model of intracellular Ca^{2+} handling within the MSCSF [49] described in detail in Section 2.8.2 (Figure 3.7B). The O'Hara Rudy AP model was chosen as it is stable, well-used and well documented (examples of recent studies using this model, including for regulatory purposes [245, 246, 271]), and previously integrated into the MSCSF by Colman [50] for this reason.

This coarse-grained idealised model is an effective discretisation of the whole cell, divided up into 19500 Ca^{2+} release units (CRUs) comprised of multiple intracellular and SR compartments (Figure 3.7B, Ci). This discretisation corresponds to a resolution of approximately 1-2 μm, which is a suitable discretisation due to the requirement of down-sampling confocal microscopy data (see Section 3.2.4) to similar resolutions to produce continuous data.

The MSCSF includes the functionality to load expression maps to this matrix, individually modulating the specified parameter (such as scaling SERCA2a function, used in Chapter 4) by setting local flux scale factors as the correlating spatial value in the expression map. For example, for some CRU in the model, with co-ordinate (x, y, z), using an expression map of SERCA2a heterogeneity, the SR-Ca^{2+} uptake flux, J_{up}, would be scaled by:

$$^{x,y,z}J_{up} = {}^{x,y,z}G_{up} \cdot f([Ca^{2+}]) \tag{3.5}$$

where the value of $^{x,y,z}J_{up}$ in each voxel, (x, y, z), is multiplied by the local flux scale factor, $^{x,y,z}G_{up}$.

Therefore, discretising structural image data to the model's resolution reproduces representative expression structure in the computational model by modulating the associated parameters producing a pseudo-structure through these local-scale factors. Any number of GRFs may be generated using a range of correlation length scale parameters (Figure 3.7Cii) representing the range of experimental observations or be directly produced from experimentally obtained parameters to reproduce the heterogeneity of a specific cell.

It should be stated that while this chapter discusses the use of the MSCSF, it is entirely practicable to use the same general methods for introducing subcellular heterogeneity in other existing contemporary spatial cell models with any stable AP model.

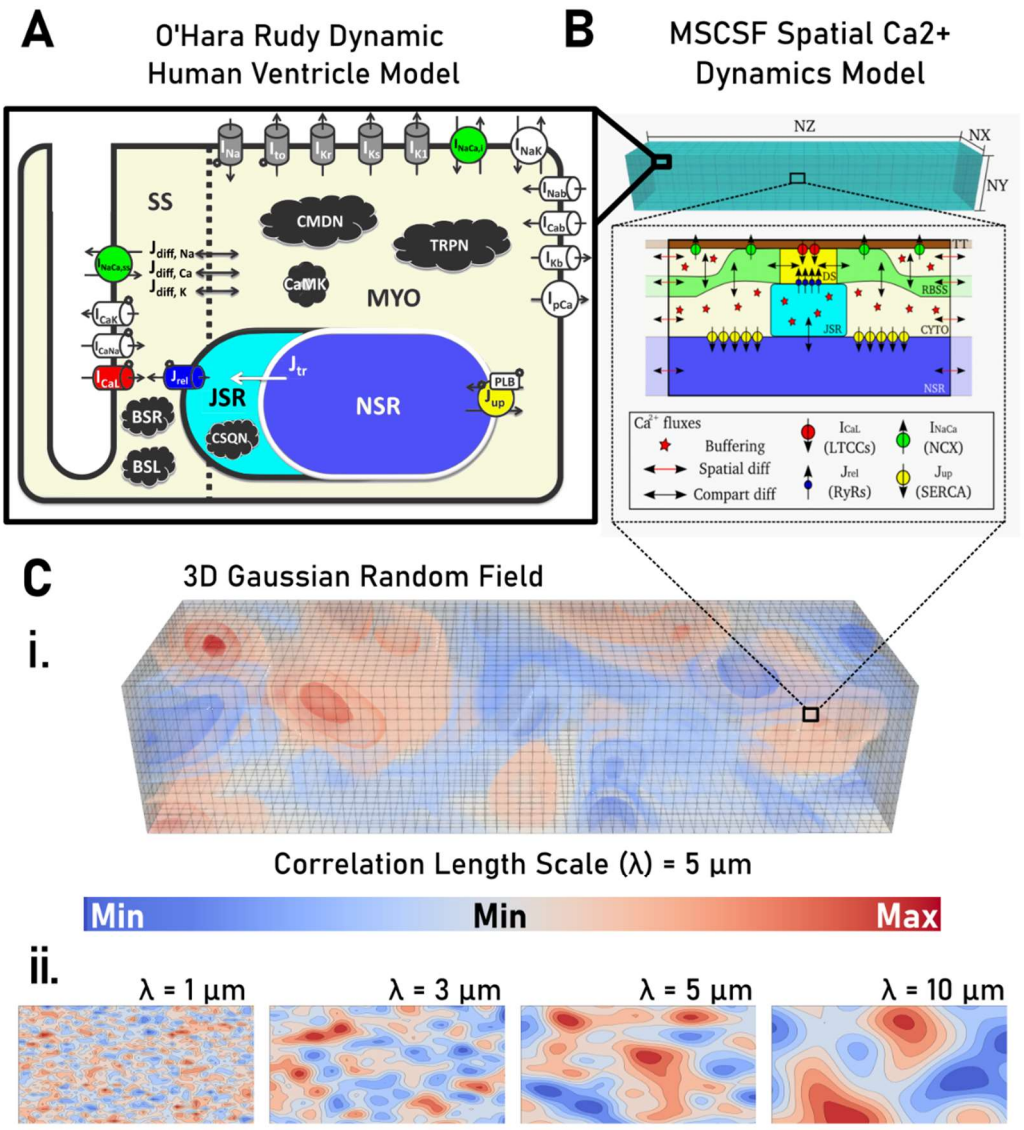

Figure 3.7 Image-Based Simulation Framework

The novel GRF image-based simulation framework used in the MSCSF. A - Electrophysiology Schematic of the O'Hara Rudy Dynamic Human Ventricle Model, adapted from [46] and coloured to correlate with panel B. B – Fundamental structure of the 3D spatiotemporal Ca^{2+} handling model in the MSCSF, illustrating the compartments for each Ca^{2+} release unit (CRU), as well as the primary Ca^{2+} fluxes. Taken from [1]. C – i) Example of a 3D Gaussian Random Field (GRF) expression map and ii) examples of 2D GRFs produced at different length scales.

3.4 Development of an Open-Source Toolkit to Analyse Sub-cellular Structural Microscopy Images

To simplify the complex process of analysing structural microscopy images and make the method widely available, the Sub-Cellular Heterogeneity Analysis Toolkit was developed to implement the methods outlined in Sections 3.2 and 3.3. This toolkit semi-automatically processes structural cellular imaging data to ensure suitability for an empirical variogram fitting procedure, then quantifies the spatial heterogeneity in the dataset – extracting measurements of the variation, mean whole-cell expression, and correlation length scale of the data. These parameters can then be used to produce any number of Gaussian random fields, which reproduce the spatial properties of the analysed dataset and can be used in computational simulation studies. This section outlines the development of this toolkit, describing its functionality in detail and how these implementations improve the usability of these novel methods.

3.4.1 Data and Technologies

Cardiomyocyte imaging studies are done utilising different imaging modalities, resolutions, and microscopes, resulting in variation in image quality, file size, dimensions, and metadata that must be considered when analysing them. The development of this toolkit utilised only confocal microscopy data previously described in Section 3.2.2; however, to enable wider use of this heterogeneity analysis technique, other modalities (such as super-resolution data donated by Thomas Sheard (Sheard et al. (2019) [12]) were taken into consideration when designing this toolkit. In addition, several accessible technologies were used to develop this toolkit which are described in the following sections.

X.4.2.1 Qt

A graphical user interface (GUI) was developed for this toolkit to increase its accessibility to those unfamiliar with using the command line. Additionally, it provides visualisation tools to aid with the selection and processing of data. The Qt technology [272, 273] was utilised to do this, as it was a well-supported platform for developing GUIs. These tools allowed for the development of a simple, robust, cross-platform GUI which would work without making version changes for different operating systems, and hence was well suited for this project.

X.4.2.2 Python 3

The Sub-cellular Heterogeneity Analysis Toolkit was developed in Python 3 (ver. 3.9) [274], which has a robust and well-supported library of built-in packages which are well documented and well used within the scientific community. Additionally, Python 3 has a modern built-in implementation of the Qt GUI cross-platform framework, PyQT5 [273], which was utilised to build a portable GUI wrapper for these tools.

The Python Imaging Library, Pillow (or PIL) [275], was used to handle the loading and pre-processing of image data. PIL was specifically selected as it provides extensive file format support, powerful image processing capabilities and is well documented and supported. MatPlotLib [276] is used for the visualisation of the datasets and to provide interactive tools in the GUI to make processing images easier. The renowned Numpy [264] and Pandas [265] packages were utilised for their comprehensive mathematical functions and powerful array manipulation features to transform and handle large image data arrays.

X.4.2.3 GeoStat Framework

GeoStatTools is a Python 3 library that provides geostatistical tools including kriging, random field generation, variogram estimation and covariance models, produced and is maintained by Sebastian Müller and Lennart Schüler [260, 261]. The functions in this package were adapted and used to perform the variogram analysis and spatial random field generation on the structural microscopy image datasets.

3.4.2 Toolkit: Data Handling

The Sub-cellular Heterogeneity Toolkit was designed to take in experimental imaging data, and process that into a form suitable for a variogram analysis and then quantify the spatial information in that dataset to extract parameters describing its heterogeneous structure. The first tab which appears upon launching the toolkit is shown in Figure 3.8, and each tab can be navigated using the tabs at the top of the window (Figure 3.8A). Information on the Leeds Computational Physiology lab is provided, including a web address for the documentation and a way to contact the lab.

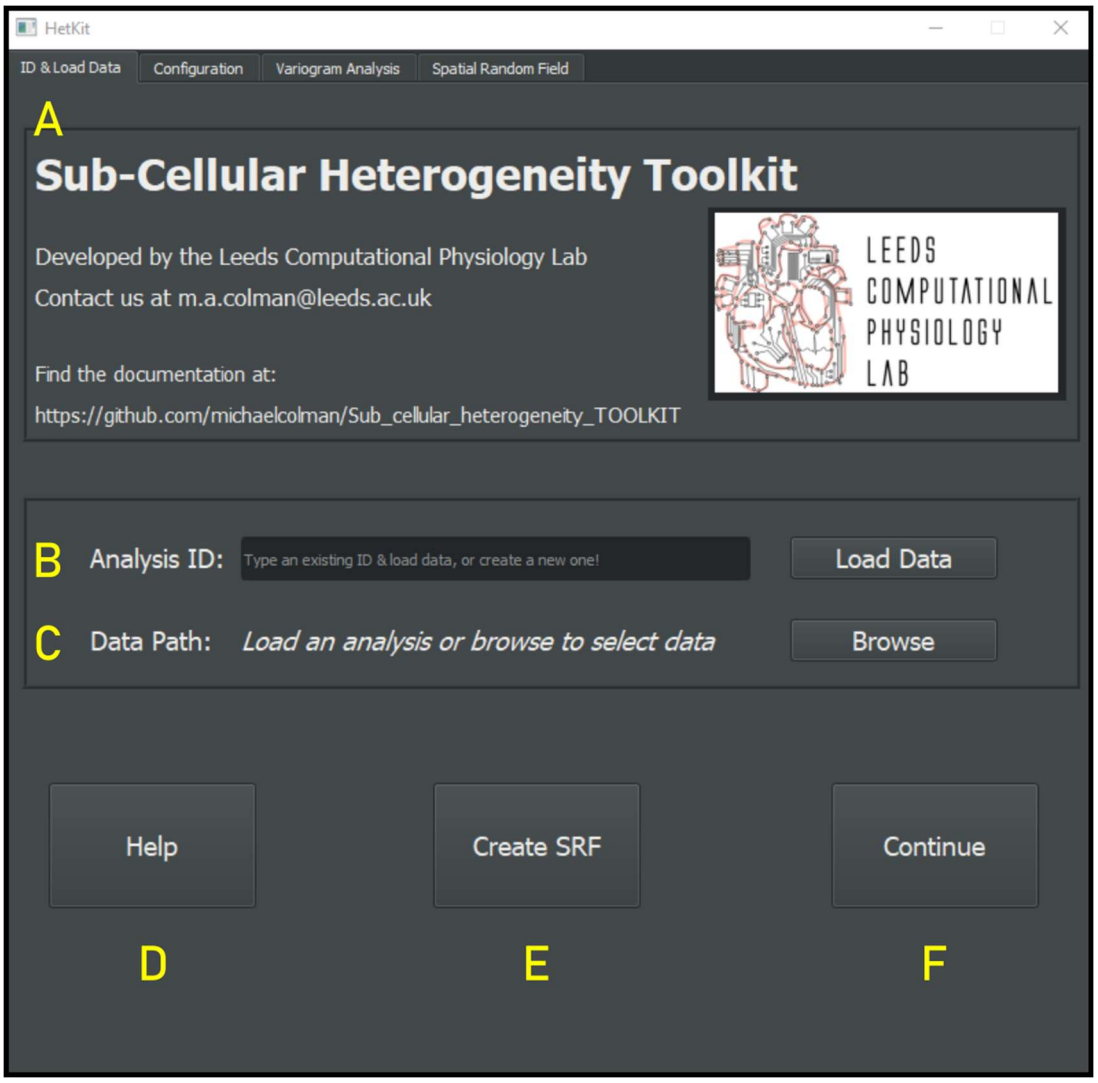

Figure 3.8 Sub-cellular Heterogeneity Toolkit: ID & Load Image Tab.

This tab contains the following functionality: A- Tab-based Navigation to other parts of the toolkit. B – Entry field for an ID for the current analysis or load data from a previous analysis using the specific ID. C – Data Path display and a button to open the file explorer to navigate to a dataset. D – Help button, which links to a GitHub repository with the codebase, and documentation. E – Create SRF button, which links to the Spatial Random Field Tab. F – Continue button, which saves current settings and moves to the next tab, Configuration.

To cater for analysing multiple sets of data, or the same set of data in multiple ways, an ID system was chosen in combination with an easy to read and access JSON database where the user can save and load analysis parameters to create new studies or re-visit and edit old studies. JSON was selected, as this file format is formatted for readability, and a user may go into the database themselves to quickly find

information without needing to reload data. An analysis ID can be entered in the text field (Figure 3.8B) and then using the “load data” button, either a new analysis is created or an old one with a matching ID is loaded. A pop-up will ask the user to confirm this action. The path to the image data can be selected using the “Browse” button (Figure 3.8C) and is displayed in the text field next to it. Multiple images can be selected for analysis and should be done so in order of the z-axis.

The help button (Figure 3.8D) opens this link to the codebase available on GitHub and the accompanying documentation. The “Create SRF” button brings the user to the final tab of the toolkit, labelled “Spatial Random Field”, which contains all the tools needed to produce a spatial random field, and can be done after loading a previous analysis. The continue button saves inputs and data paths, bringing the user to the next section of the toolkit – configuration.

3.4.3 Toolkit: Configuration

To perform a successful variogram fitting, there are several criteria that the selected image data must fill for the analysis to produce reasonable, meaningful results. This configuration can be performed in the “Configuration” tab (Figure 3.9).

The correct channel must be selected (Figure 3.9A) to isolate the selected stain when analysing multi-channel images. It is possible to perform the same analysis on multiple channels, but these must be done separately. The data must be in the correct axial orientation to produce meaningful transversal and longitudinal correlation length scales. To do this, the image data should be rotated such that the x and y axes of the cell align with the plot's x- and y- axes and can be done using the rotation tool. (Figure 3.9B, F).

As previously stated in 3.2.4, it is recommended that the image be cropped to remove regions outside the cell boundaries and avoid the inclusion of large organelles. To facilitate this sensitive cropping procedure, a mouse-based click-and-drag tool has been included in the toolkit used by drag-selecting a region on the plot and adjusting the region afterwards, the coordinates of which will be displayed. (Figure 3.9C, F)

The toolkit includes functionality to down-sample the image to a specified resolution (Figure 3.9D). This allows the user to down-sample imaging data with different resolutions, obtain a suitable down-sampling resolution to ensure

continuity of the dataset, and customise the down-sampling protocol to produce a resolution suitable for the purpose of the study.

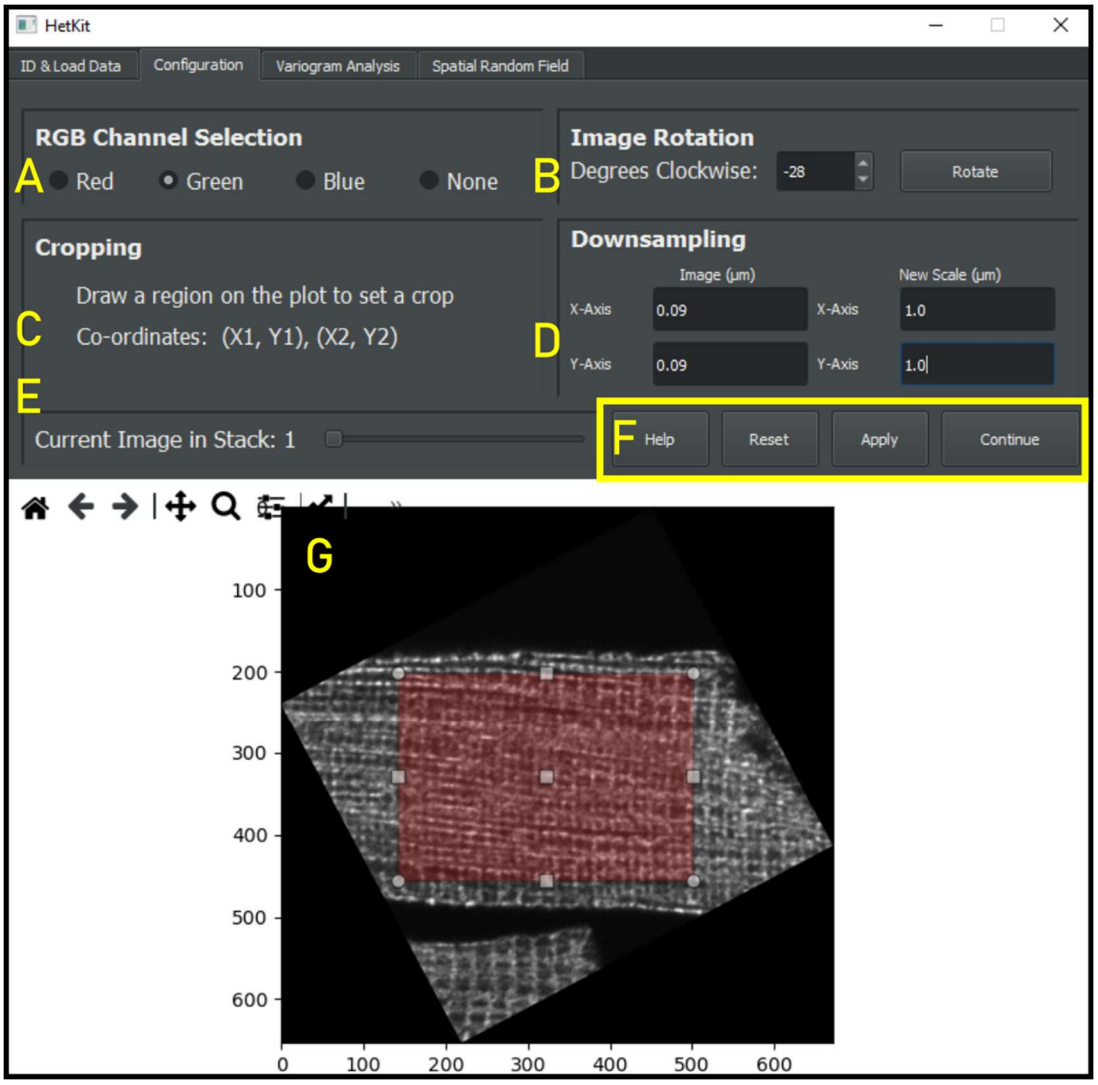

Figure 3.9 Sub-cellular Heterogeneity Toolkit: Configuration Tab.

This tab contains the following functionality: A – RGB channel selection options to isolate stained targets. B – Image rotation function. A degree can be entered into the field or selected using the arrows, and the rotate button will perform the rotation and display it. C – Cropping functions, a region of the image can be selected using a click-and-drag method (see G). D – Down-sampling function, the scale of the x- and y-axes of the image can be altered to decrease resolution. E – Image selection slider; changing this will display another of the loaded images if applicable. F – Help, Reset, Apply and Continue Buttons. G – A MatPlotLib canvas displaying the current state of the data being processed. Note: changing this does NOT change the original files.

Scales of the original image and the desired resolution are entered into the fields (metadata formats vary with file type, so this is best done manually rather than attempting to extract it from metadata.)

The Sub-cellular Heterogeneity Toolkit can analyse stacks of images, which is often the case in structural microscopy, with multiple x-y slices through the Z-axis (depth) comprising the dataset. To perform the variogram fitting successfully, each image in the stack must have equal dimensions, and as such, the same processing will be applied to every image selected. The image-slider (Figure 5.9E) allows the user to load each image and check that the chosen configuration is suitable for all images in the display (Figure 3.9F).

3.4.4 Toolkit: Variogram Analysis

Once the selected datasets are configured to be suitable for a variogram fitting, the "Variogram Analysis" tab (Figure 3.10) contains functionality to customise the binning parameters used in the process and to load a VTK file instead of using the analysed data (Figure 3.10A), and the outputs given (Figure 3.10B). The binning parameters "Bin Count" and "Bin Range" are the number of bins and the range of the bins used to fit the variogram. It is recommended to use a range of these parameters at the same magnitude as the dimensionality of the processed datasets - the toolkit will perform a variogram fitting for each combination of binning parameters and use these results to produce a mean value and error from successful fits. Variogram fitting protocols are performed using functions from the GeoStatTools Python package [260]. A VTK file may be loaded instead, including one produced from the toolkit, to analyse that instead.

The outputs include rotated, cropped and down-sampled versions of the selected image data, histograms of the variogram fitting process, and the variogram plots themselves for each fit. These are labelled with the parameters used for each.

A contour plot of the processed data from the "Configuration" tab is displayed (Figure 3.10C) above the button used to start the variogram analysis process (Figure 3.10D). A progress bar will start to fill, informing the user of the current progress. Once completed, the user can access the outputs by using the "Analysis Results" button (Figure 3.10F), which opens the directory of the outputs in file explorer, or the user can click the "Continue" button to advance onwards to the SRF generation functions.

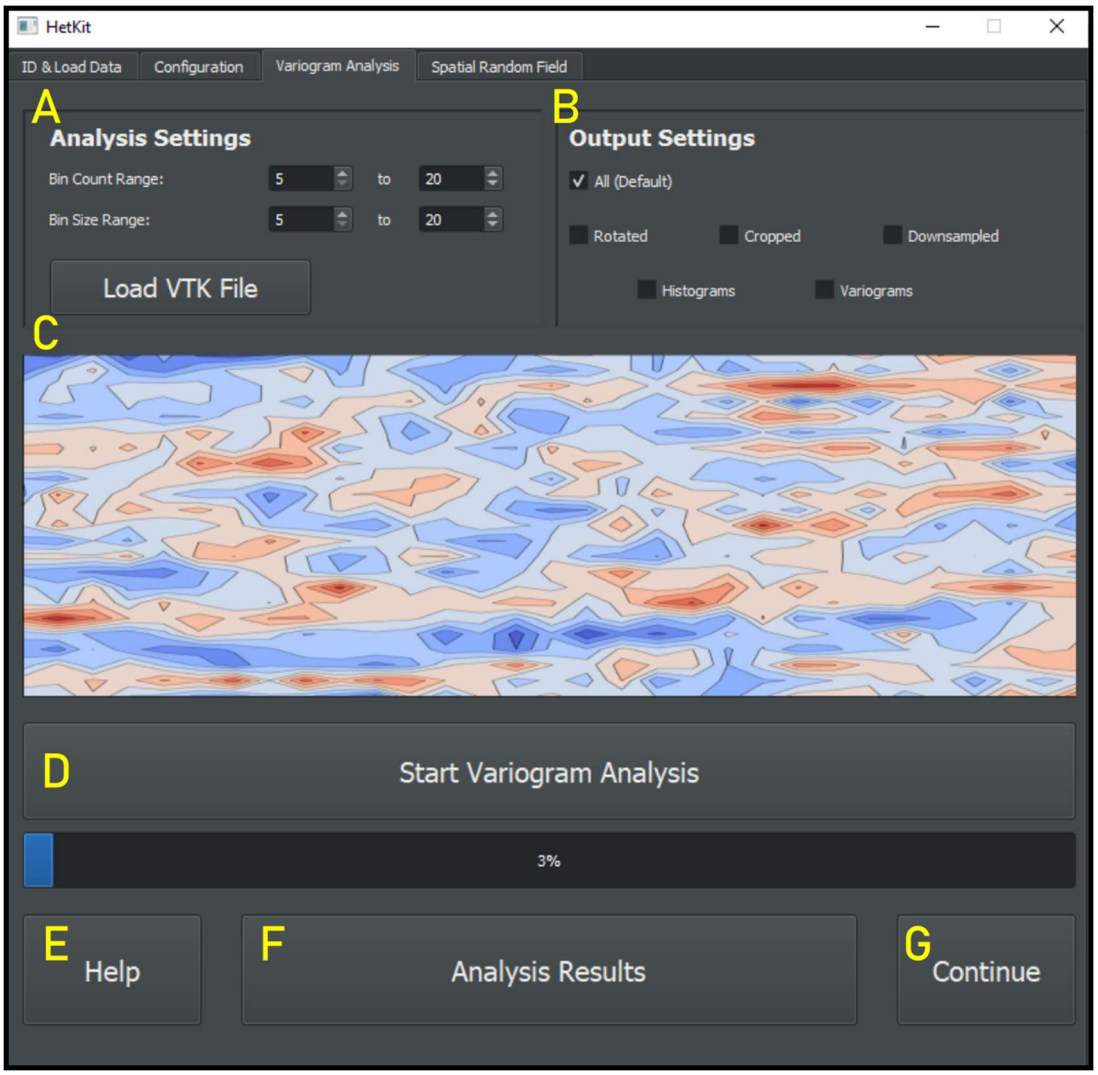

Figure 3.10 Sub-cellular Heterogeneity Analysis Toolkit: Variogram Analysis Tab.

This tab includes the following functionality: A – Analysis Settings changing the binning parameters used within the analysis. These should reflect the size of the dataset. B – Output settings, which allow the user to select which outputs are produced for each analysis. C – A panel displaying the contour plot of the analysed images (if continue was selected). D – A button that begins the variogram analysis with the chosen settings. The bar below this button displays the progress. E – Help button, which opens the GitHub repository with the code and documentation. F – Analysis Results, once the progress bar indicates the analysis is complete, this button will open the file location of the results files for this ID. G – Continue, saves current results and proceeds to the Spatial Random Field tab.

3.4.5 Toolkit: Spatial Random Field Generation

The final section of the toolkit, the “Spatial Random Field” tab (Figure 3.11), handles the generation of spatial random fields, which can be performed directly from the analysis results of the selected dataset or can be done separately using custom inputs. The user may choose a filename for the Gaussian Random Field (Figure 3.11A) and the number of SRFs they wish to produce (if the name of the SRF is “Test”, then each file will be labelled “<ID>_Test_1_VTK”, “<ID>_Test_2_VTK”, etc.).

The mean expression of the GRF and the variance as a proportion of that mean expression can be set directly, as can the transverse and longitudinal correlation length scales (Figure 3.11B) – or can be loaded directly from the analysis if successful. Additionally, the dimensions of the SRF can be set manually to any size up to 1000 x 1000. (Figure 3.11C). To improve compatibility with the Multi-Scale Cardiac Simulation Framework (MSCSF), default settings for the “Full” cell size and “Part” cell size are included and can be quickly selected to produce an SRF the correct size as the compartmentalised CRU model used in this thesis [49].

There is the option of previewing an SRF using the selected correlation length scales (Figure 3.11D) before generating them using the “Generate Spatial Random Fields” button (Figure 3.11E). A progress bar shows the current progress, and the SRF directory can be opened in file explorer by pressing the “Open SRF Location” button.

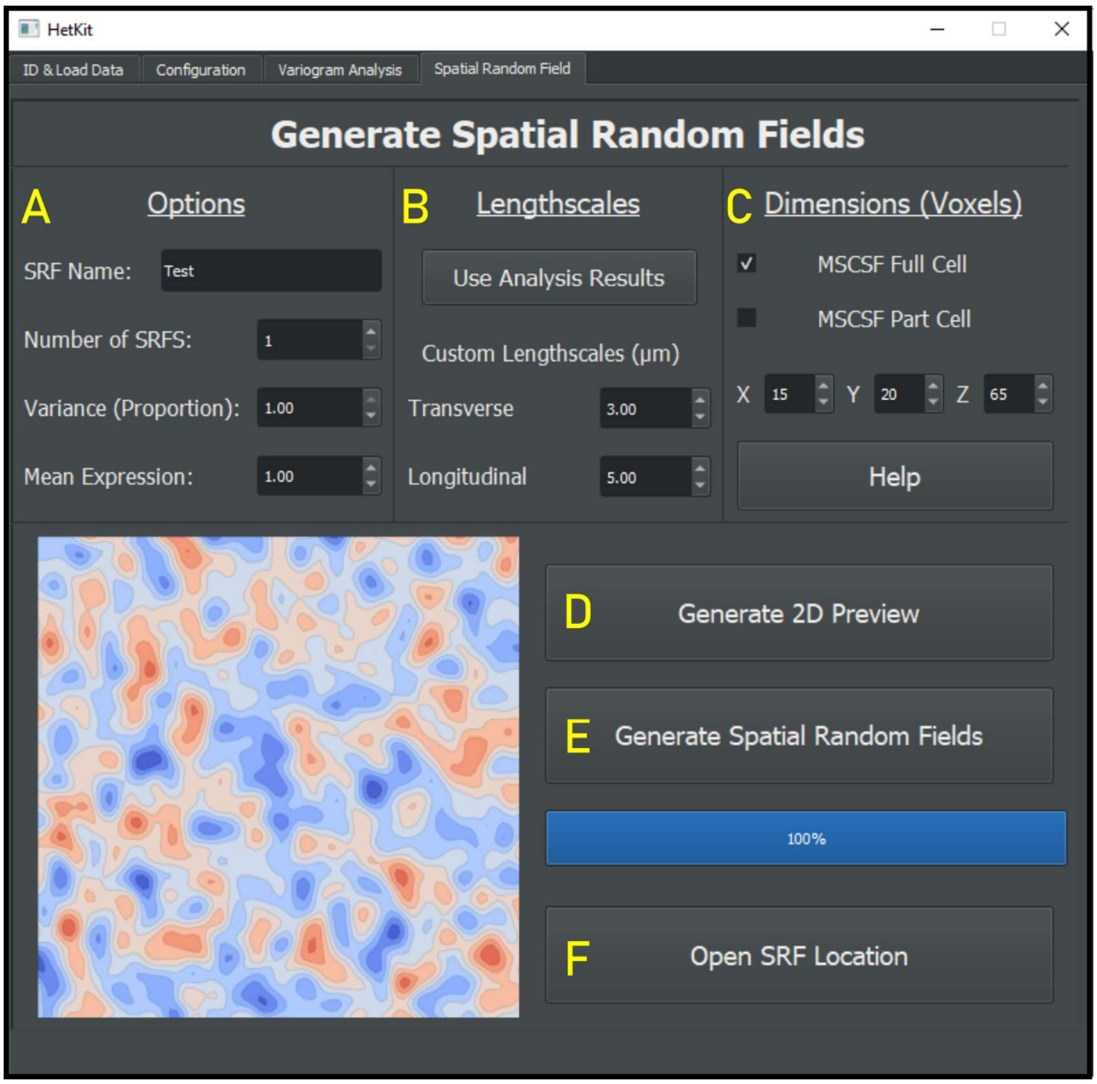

Figure 3.11 Sub-cellular Heterogeneity Analysis Toolkit: Spatial Random Field Tab.

This tab includes functionality to produce Gaussian Random Fields (GRFs) using user-inputted initial settings. A – Options for the name, number, variance, and mean expression of the GRFs. B – Options for the transverse and longitudinal length scale of the GRFs, either directly from the analysis results (button) or custom using the entry fields. C – Options for the dimensions of the spatial random fields, including defaults for the MSCSF full cell and part cell sizes. D – Generates a 2D Preview (see left of button) using the chosen correlation length scales. E – Generate GRFs of the specified number to the specified parameters. F – Opens the location of the generated GRFs in the file explorer.

3.5 Proof-of-Concept Application: Characterization of Sub-cellular Heterogeneity and its impact on ECC.

This semi-automatic toolkit was designed to extract spatial information on heterogeneous expression from cellular imaging data and produce suitable expression maps to use with the MSCSF to investigate the functional impacts of heterogeneous channel expression comprehensively. As a proof-of-concept for the viability of this modelling method to study the relationship between sub-cellular structure and function, a preliminary study into whole-cell means expression and correlation length-scale was performed to understand how these parameters vary across healthy ventricular cells. Following this quantification, GRFs were generated at a range of correlation length scales to investigate how introducing heterogeneous expression of RyRs, SERCA2a and NCX in isolation and concomitantly impacted CaTs. Our lab published this method in Methods [1], and part of this preliminary study was presented in that publication.

3.5.1 Characterisation of Sub-cellular Channel Expression Heterogeneity

Pre-existing cellular imaging data from rat ventricular myocytes, as described in Section 3.2.2, was analysed using the Sub-cellular Heterogeneity Analysis Toolkit. The image selection contained confocal microscopy images from 10 different cardiomyocytes with immunofluorescent staining of SERCA2a (5 cells) or RyR (5 cells) (Figure 3.12). The processing method outlined in Figure 3.2 was used as implemented within the toolkit for both groups of cells (Figure 3.12Ai-iii; Bi-iii).

SERCA2a expression demonstrated a Gaussian distribution across all cells studied, with local expression ranging from ~10% to ~220% of mean whole-cell expression (Figure 3.12Aiv). RyR expression followed a lognormal skewed distribution, skewing from 0% to 500% of the mean expression (Figure 3.12Biv). Transversal variogram fits were less varied and shorter than longitudinal fits across both SERCA2a and RyR cells (Figur 3.12C, D), which indicates less correlation in this direction – however, the limitation of this method when analysing small datasets (including the shorter transversal axis) must be considered. Isotropic fits varied between transversal and longitudinal fits in variability, which is expected, as the isotropic length scale should exist between the two directional variations.

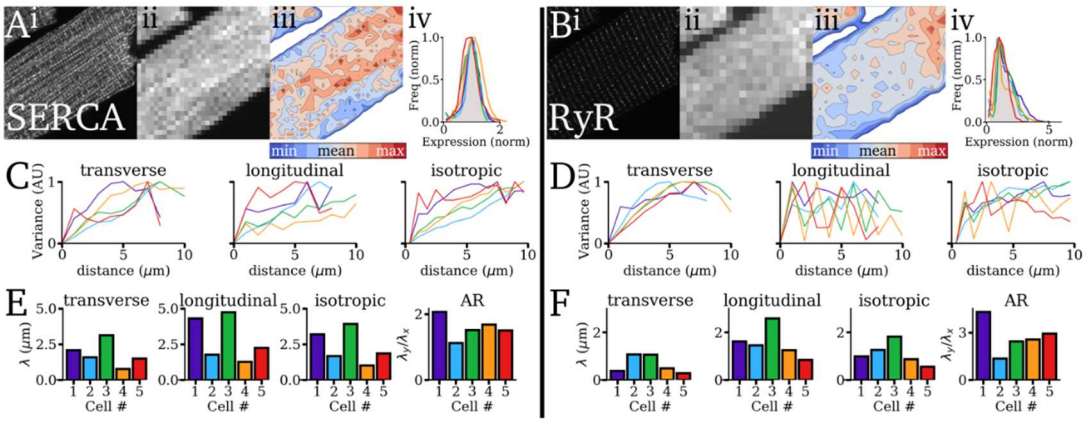

Figure 3.12 Characterising sub-cellular heterogeneity using variograms.

Examples of 2D slice imaging data for A – SERCA2a and B – RyR2: (i) – Original image; (ii) – down-sampled image; (iii) – visualisation as a heterogeneity contour map; (iv) – histograms of normalised expression. C-D – Variograms in the transverse and longitudinal directions and the isotropic variogram for five individual cells (coloured lines). E-F – Estimates of the anisotropic and isotropic correlation length scales (λ) and anisotropy ratio (AR) for the five cells.

This analysis reveals correlation length scales in the range $\lambda = 1 - 5$ μm for SERCA2a (Figure 3.12E), and in between $\lambda = 1 - 3$ μm for RyR (Figure 3.12F). Both proteins display expression which is generally anisotropic between the longitudinal and transversal directions and a larger correlation length scale in the longitudinal axis. Shorter correlation length scales in RyR suggests they have a more randomised distribution in comparison to SERCA2a. Generally, there is larger inter-cellular variability in length scales than relative expression variation (Figure 3.12A-B, iv).

A correlation length scale equal to the resolution of the dataset indicates no correlation between neighbouring pixels; however, this is unlikely to occur due to noise in the data. It should be noted that while this analysis may produce a correlation length scale smaller than the resolution of the dataset, this has no additional physical meaning and is also treated as no correlation. Longer correlation length scales represent a larger correlation on that axis, i.e. longer, smoother inter-pixel variation.

3.5.2 Functional Assessment of the Impact of Sub-cellular Heterogeneity on ECC

The idealised, compartmentalised MSCSF spatial-temporal model of Ca^{2+} handling [49] provides a powerful tool to perform simulations using structural expression maps directly relating to the experimental data. The GRF image-based modelling method detailed in Section 3.3.2 was used to study the functional impact of introducing heterogeneous RyR, SERCA and NCX expression on the CaT. The toolkit was used to produce Gaussian Random Fields (GRFs) at correlation length scales ranging between 1 – 10 μm for each protein (Figure 3.13A), with constant whole-cell mean expression and variance. Thus, this preliminary study focuses on the importance of correlation length scale, λ, in RyR, NCX and SERCA2a, and the importance of the correlation (or anti-correlation between these targets (Figure 3.13B). These simulations were performed at a pacing rate of 1 Hz under control conditions.

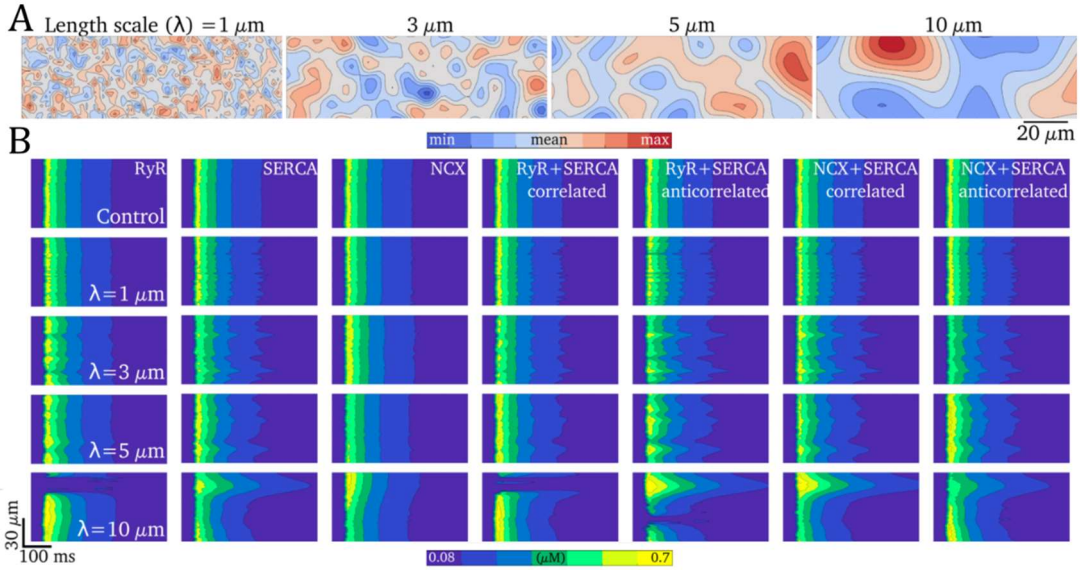

Figure 3.13 Intracellular CaT linescans under isotropic heterogeneous expression of RyR, SERCA2a and NCX.

A – Isotropic maps produced by Gaussian Random Fields (GRFs) at varying correlation length scales (λ). B – Intracellular Ca^{2+} z-axis linescans at normal pacing (1 Hz) produced in homogeneous conditions (control) and isotropic heterogeneous conditions at different correlation length scales for RyR, SERCA2a, NCX and combinations of these either correlated or anti-correlated. Adapted from Colman et al. (2020) [1].

The introduction of RyR and SERCA2a heterogeneity resulted in more spatially disordered CaTs in both the upstroke and decay phase, compared to the homogeneous cell model and heterogeneity in NCX, which primarily affected CaT decay (Figure 3.13B). The control homogeneous cell model produced CaTs that were more spatially homogeneous than those measured experimentally [257]. Length scales of 1-5 μm, corresponding to the range measured in healthy rat ventricular myocytes, produced spatial CaTs more closely matched experimental observations. Length scales of 10 μm produced heterogeneity larger than is generally observed in healthy cells. The correlation of targets when two were simultaneously varied was revealed to be an important determinant of the transient properties, potentially enhancing or inhibiting local regions of large heterogeneity (Figure 3.13B).

Additional simulations on control and heterogeneous GRF expression maps were performed at a higher pacing rate of 2 Hz (Figure 3.14A) and with enhanced subspace diffusion ("medium" and "fast" settings in the MSCSF [1]) to promote spontaneous Ca^{2+} release events (SCRE) (Figure 3.14B). Under identical conditions, heterogeneous expression maps of RyR, SERCA2a and NCX were all shown to promote CaT alternans (Figure 3.14A) and spontaneous Ca^{2+} release events (SCRE) (Figure 3.14B). Correlation length scales observed in healthy rat ventricular myocytes (λ = 1 – 5 μm) produced CaT alternans for RyR, SERCA2a and NCX simulations, while higher length scales produced Ca^{2+} waves that failed to propagate in the SERCA expression maps (Figure 3.14B). Differences in CaT alternan behaviour are observed between different length scales of NCX expression. The introduction of heterogeneous SERCA2a, NCX, and RyR expression promoted SCRE with medium diffusion time constants where none was present in the homogeneous condition. Heterogeneous NCX and RyR significantly increased this, while heterogeneous SERCA2a expression produced only a few SCREs. All heterogeneous conditions displayed enhanced SCRE compared to the homogeneous condition under fast subspace diffusion.

This analysis, combined with previous studies on RyR location and T-system density and structure [49, 277, 278], highlights the importance of expression heterogeneity, correlation length scale and inter-channel correlations on ECC.

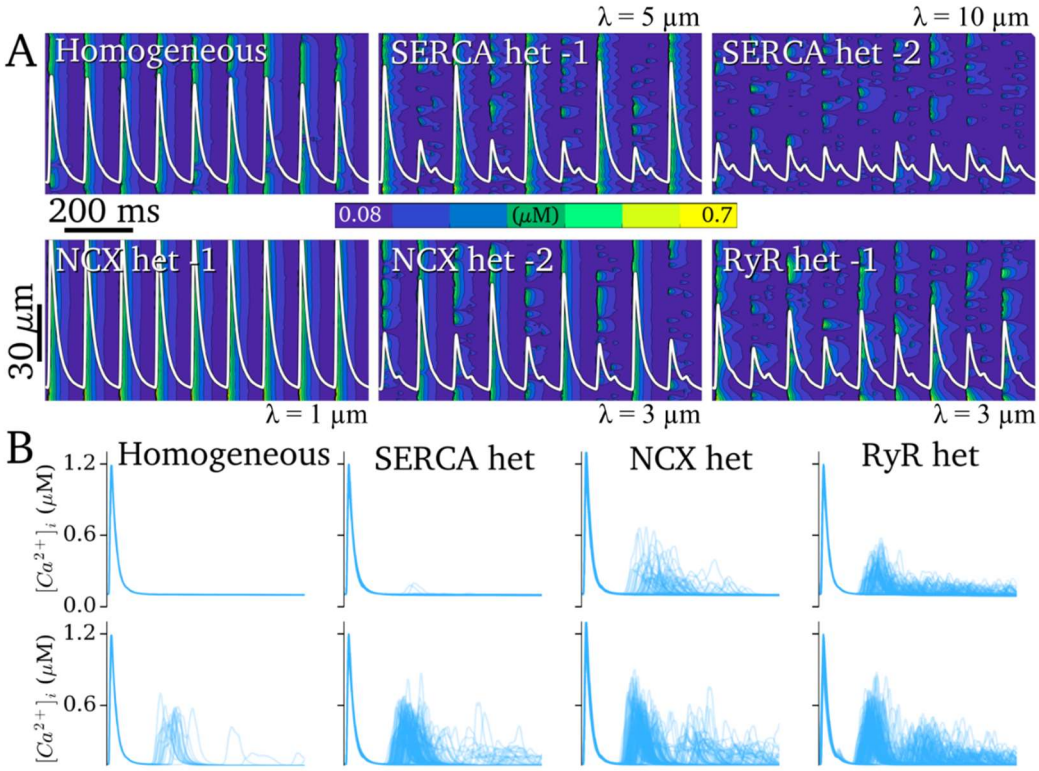

Figure 3.14 Alternans and SCRE under isotropic heterogeneous expression of RyR, SERCA and NCX.

A – Intracellular Ca^{2+} z-axis linescans at enhanced pacing (2 Hz) and enhanced subspace diffusion ("medium" in MSCSF) produced in homogeneous conditions (control) for homogeneous and heterogeneous conditions (labelled). B – Overlapped Ca^{2+} transients (CaTs) for 100 simulated runs of different isotropic heterogeneity expression maps with "medium" (upper) and "fast" (lower) subspace diffusion time constants.

3.6 Discussion

3.6.1 Summary

This chapter presents a novel methodology to quantify the spatial profile of sub-cellular heterogeneous expression in structural immunofluorescence microscopy datasets. Variograms are used to characterise the spatial distribution of a stained target to provide reliable estimations of isotropic and directional correlation length scales, variance and whole-cell mean expression distributions (Figures 3.1-3.4). Following this, a novel image-based computational modelling method was

introduced utilising Gaussian random fields, which reproduce the observed spatial properties of heterogeneity obtained using the novel variogram approach (Figures 3.5-3.7). The image processing, variogram fitting and GRF generation protocols were implemented into a semi-automatic, open-source toolkit in Python 3– the "Sub-cellular Heterogeneity Analysis Toolkit (Figures 5.8-5.11). These approaches were then applied in a proof-of-concept study that characterised the spatial distributions of SERCA2a and RyRs in multiple rat ventricular cardiomyocytes (Figure 5.12), followed by an application of the GRF image-based computational modelling. The functional effects of introducing heterogeneous expressions of SERCA2a, RyR and NCX in isolation and (anti-)correlation on the CaT were analysed in control conditions (Figure 5.13). Additionally, the impact of introducing heterogeneity in these parameters in isolation was investigated under proarrhythmic model conditions (Figure 5.14).

3.6.2 Relevance of Experimental Quantification Method

Variation in the function (through either expression or modulation) of ionic channels and primary Ca^{2+}-handling proteins can significantly change Ca^{2+} cycling within a cardiomyocyte (see Section 2.3.3). Cardiac remodelling due to various pathologies has been well studied, and it is understood that the expression or distribution of many channel proteins is remodelled in various cardiac pathologies [13, 144–153, 176, 180, 182, 183]. Despite this, there is a lack of study into the magnitude of expression heterogeneity of some primary Ca^{2+} handling channels. Jayasinghe et al. (2018) [10] and Sheard et al. (2019) [12] both provide data on the localisation and localised expression of RyRs across clusters in rat ventricular myocytes; such a study has not been performed for SERCA2a or NCX. A study of how channel expressions correlate in the sub-cellular structure had not been performed in cardiomyocytes.

The novel method and the associated toolkit developed in this chapter provides a way to characterise the spatial profile of heterogeneous expression in immunofluorescent microscopy data using a new marker, the correlation length scale (λ) of expression. In addition to providing a novel analysis technique, it was developed using pre-existing datasets; thus, there is no requirement to produce new data in order to utilise this method, making it a cost-effective method of characterising spatial correlation in subcellular expression.

Applications of this method include characterising the variation and correlation of expression for stained targets and comparing the spatial profile of specific targets across cell types, species or pathologies. A comprehensive analysis of spatial heterogeneity of key ionic and flux handling channels in healthy and diseased cardiomyocytes may reveal novel insights into the progression of cardiac remodelling in disease. This analysis may be used in conjunction with combined confocal and Ca^{2+} imaging approaches such as described by Hurley et al. (2021) [205] to correlate Ca^{2+} activity with relative changes of expression of relevant channels throughout a cell. However, it remains challenging to provide a comprehensive investigation of these structure-function dynamics experimentally. This method provides an image-analysis approach that can inform image-based modelling techniques by analysing pre-existing datasets (Sections 3.3, 3.5, and Chapter 4).

3.6.3 Comparison to Previous Spatial Image-Based Modelling Approaches

Image-based computational modelling provides a viable approach to study the relationship between sub-cellular structure and function on a cellular level, which is difficult to do with confidence experimentally. However, contemporary cellular computational models have been limited in the imaging data they incorporate. This chapter provides, along with the novel image-analysis method, a novel image-based modelling approach utilising GRFs to quantitatively reproduce experimentally observed mean-cell expression, sub-cellular variance and correlation of an ionic channel.

Colman (2019) [50] developed a detailed free-diffusion model of intracellular Ca^{2+} handling, which incorporated electron microscopy super-resolution structural data ($O(10^2)$ nm) to reconstruct realistic t-system and SR structure. This highly-detailed model demonstrated that the spatial distribution of dyads, t-system and SR structures tightly regulated abnormal Ca^{2+} cycling. While an effective method, this is not suitable for larger-scale comprehensive studies; this method only implemented a detailed reconstruction of a single cardiomyocyte, requires extensive 3D structural data and is computationally expensive to run. The method detailed in this chapter addresses the above by using an idealised, discretised structure (Figure 3.7B) and expression maps that create a pseudo-structure through modulating local scale

factors that model the expression of a specific channel. This approach is significantly less costly to simulate and is suitable for larger-scale studies. However, this idealised approach offers significantly less detail ($O(10^0)$ μm), and does not simulate structure-function dynamics at the super-resolution scales.

Sutanto et al. (2018) [258] provide an approach that uses RyR imaging data in a similar way to this chapter, with some important caveats. RyR x-y slices are down-sampled to a resolution of 1 μm^2, then stretched over a pre-defined model grid in 2D and used to modulate local RyR expression using the normalised, relative intensity of each pixel. Depending on the grid size used, this approach is sufficiently detailed to capture inter-band RyR structure, which in the novel approach discussed in this chapter is not explicitly modelled separately but included within the down-sampling. Sutanto et al. (2018) [258] only consider a 2D representation of a cardiomyocyte and thus cannot simulate 3-D Ca^{2+} wave propagation. Additionally, this approach is limited to directly using imaging data, whereas the novel approach may directly use quantitative imaging data (the GRF produced directly from an analysed cell) or indirectly through the construction of maps representing the range of observations.

Song et al. (2018) [76] used a qualitative approach, constructing t-tubule structures similar to those experimentally observed using a selection of algorithms ranging from simplistic to complex organisations. This approach is scalable to investigate how the spatial organisation of the t-structure, including its presence (or lack thereof), is restricted to t-tubules only. The GRF-based approach is unsuitable for modelling the t-tubule structure directly, as the rigid structure of the t-system is not captured in random fields. The combination of these approaches, for example, the generation of a GRF complementary to a qualitative t-system or, indeed, the super-resolution reconstruction presented by Colman (2019) [50], may provide an approach to studying and relating the impacts of t-system and SR structure, and correlative measurements of channel expression simultaneously.

In addition to the advantages discussed above, the image-modelling approach outlined in this chapter allows for the use of multiple GRFs to correlate the expression of multiple variables simultaneously. For example, using a Ca^{2+} handling framework with detailed descriptions of regulatory complexes, such as the phospholamban-SERCA2a complex, allows the study of how heterogeneous co-localisation of these complexes impacts function.

3.6.4 Characterisation and Role of Heterogeneous SERCA2a and RyR Expression

A preliminary application of the novel toolkit, analysing SERCA2a and RyR expression in healthy rat ventricular myocytes revealed correlation length scales in the range $\lambda = 1 - 3$ μm for RyR and $\lambda = 1 - 5$ μm for SERCA2a. Correlation length scales in these proteins were observed to be generally anisotropic, with larger length scales existing in the primary axis (longitudinal) of the cardiomyocyte (Figure 3.12).

In general, larger inter-cellular variability in correlation length scales than in relative whole-cell expression was observed across both SERCA2a and RyR. To the author's knowledge, there is no published experimental data detailing SERCA2a expression distributions; however, the lognormal distribution of RyRs is congruent with recent experimental findings by Jayasinghe et al. (2018) [10] and Sheard et al. (2019) [12].

These findings were used to produce a set of isotropic GRFs for use in a simulation study into the functional effects of the heterogeneous expression of RyR, SERCA2a and NCX using isotropic GRF expression maps. Correlation length scales in the range observed in healthy rat ventricular myocytes produced CaTs more closely matched with experimental observations [257] than homogeneous models (Figure 3.13), whereas larger correlation length scales resulted in heterogeneity in the CaT larger than observed experimentally. The correlation and anti-correlation of expression in multiple channels simultaneously was observed to promote or inhibit CaT propagation in localised regions.

Under pro-arrhythmic conditions, the introduction of heterogeneity promoted CaT alternans and SCRE compared to a homogeneous model in control and HF-associated remodelling (Figure 3.14). The promotion of these behaviours varied with different length scales, suggesting a complex underlying structure-function relationship between heterogeneous channel expression and the development of cell-level cardiac dysfunction. These results and previous observations infer that sub-cellular heterogeneity of sub-cellular structure and channel expression play a critical role in determining the spatial profile of the CaT. Variation in the spatial profile of the CaT manifests as variability in local and whole-cell ECC.

3.6.5 Limitations

The novel image-analysis technique was developed to re-analyse existing high-resolution confocal immunofluorescent imaging data. While an effort was made to consider other imaging modalities when developing the toolkit, the toolkit is mostly catered to analyse confocal datasets. Thus, modifications may be necessary to utilise other imaging modalities, formats or techniques – such as an additional processing step. The toolkit provides functionality to manually input resolution sizes and select suitable regions for the full image stack, but this may not be sufficient depending on the data used.

Multi-image datasets were integrated over the z-axis due to differences in how some cells are imaged and the availability of data during development. This choice leads to a loss of information, as heterogeneity is highly likely to exist in all dimensions, but the z-axis presents significant challenges to analyse with little gain. Not all images in a stack are suitable for the same analysis due to processing constraints (e.g., complex membrane structure, organelles), and few utilised datasets have enough slices to perform a z-axis directional variogram fit. Attempting a 3D variogram analysis on a dataset without a sufficient number of slices would affect the reliability of isotropic fitting; thus, the images are integrated over the depth axis.

Due to the pre-requisites for using the Gaussian covariance function, processing confocal microscopy datasets may result in datasets too small to perform a reliable directional variogram fitting – only rendering an isotropic length scale. This criterion puts physical limitations on the target being analysed; smaller or sparse datasets may require downsampling that exceeds the limit to produce reliable measures. Additionally, there are sources of error present within each dataset due to differences in imaging technique or fragments appearing in the images. To mitigate the impact of these issues, the toolkit includes functionality to perform variogram fittings over a range of binning parameters and provide estimations of measurement error for successful parameter combinations, thus enabling the analysis of smaller or trickier datasets. However, smaller confocal datasets may only yield a successful isotropic correlation length scale despite these mitigation strategies.

The GRF image-based computational modelling method was discussed compared to other models in Section 3.6.3, and the limitations which arose are discussed here. The discretisation of the idealised model is not sufficiently high-resolution to

capture the super-resolution structure of the t-tubules or SR, unlike the super-resolution models presented by Colman (2019) [1, 50] and Song et al. (2018) [76], and thus analysing the functional implications of heterogeneous distribution around these structures is not possible using this model. Additionally, micro-structures present within the data (such as sparse inter-band RyR captured by the approach presented by Sutanto et al. (2018) [258]) are not directly incorporated. Finally, the GRF approach is valid for approximately Gaussian expression distributions; however, other covariance functions may better suit other channels.

Future challenges not addressed by these novel methods include quantification of SERCA2a heterogeneity and the SR structure at higher resolutions where it would not be continuous outside of the SR structure itself and quantification of the correlation length scales of various channels proteins existing in sarcolemmal invaginations. Both of these challenges may involve further developments building from this approach.

3.7 Conclusion

This chapter discusses the development of a set of complementary image-analysis and image-based modelling methods. The novel image-analysis method enables the quantification of the spatial profile of heterogeneity and presents a novel marker in which to compare the expression of a target between cells, the correlation length scale. The image-based modelling method bridges the gap between experimental observations of spatial variation in the CaT and the underlying structure, providing a method of confidently relating whole-cell spatial Ca^{2+} profiles to underlying channel expression and dissecting the relative roles and importance of subcellular heterogeneity in Ca^{2+} handling channels. A preliminary study demonstrated the importance of sub-cellular heterogeneity of Ca^{2+} handling channels on determining intracellular Ca^{2+} variability both locally and globally within the cell and in the development of pro-arrhythmic cellular phenomenon. Implementations of these methods have been collected into an open-source toolkit made available in the corresponding publication (Colman et al. (2020) [1]).

4

Characterising the Spatial Profile and Role of SERCA2a Heterogeneity in Control and Right Ventricular Heart Failure

4.1 Introduction

4.1.1 The Role of SERCA2a in Health and Disease

Within cardiomyocytes, the SR acts as a reservoir for Ca^{2+}, mediating the cyclical uptake and release of Ca^{2+} during relaxation and cellular contraction through the process of CICR [279] (see Section 2.2.3). SERCA2a enables muscular relaxation by removing Ca^{2+} from the cytosol, promoting unbinding of Ca^{2+} to troponin. In turn, this refills the SR Ca^{2+} reservoir, which enables the next contraction [159, 167]. In humans, SERCA2a (J_{up}) is responsible for extruding the Ca^{2+} released from the SR during CICR (J_{rel}), approximately 70-75% of the CaT, while NCX (I_{NCX}) is mostly responsible for removing the extracellular Ca^{2+} brought in through the action of LTCCs (I_{CaL}), with a small contribution from sarcolemmal Ca^{2+} ATPase, I_{CaP} [280, 281]. Thus, it is important that the relative contributions of SERCA2a and NCX balance these cytosolic influxes.

Despite its importance in ECC, our understanding of the expression and activity of SERCA2a in health and HF remains incomplete. There is a consensus that SR-Ca^{2+} uptake is impaired in the failing heart [160, 163, 282, 283]; however, studies disagree on whether SERCA2a expression is depressed in the failing myocardium. Many studies observe that SERCA2a expression decreases in the failing myocardium in both human and animal models [90, 159–162, 165, 283–287]; other studies report no change in expression despite a decrease in J_{up} [288–290]. Most findings also suggest that the expression of phospholamban (PLB), a micropeptide protein which acts to inhibit SERCA2a in its unphosphorylated state, is also unchanged in HF [291]. It has been suggested that in HF, SR-Ca^{2+} activity is reduced through the relative increase in PLB:SERCA2a, or through decreases in PLB phosphorylation [292]. The net effect of this remodelling, however, consistently shows a reduction in the rate of SR-Ca^{2+} uptake.

This reduction of SERCA2a activity correlates with increases in diastolic intracellular Ca^{2+} [164, 165] and decreases in the magnitude of the CaT [14, 16]. SR-Ca^{2+} content has been observed to decrease [157, 167, 168] and increase [169, 170] in some models of heart failure. Additionally, reduced expression and activity of SERCA2a have been observed in advanced age in both animal models [293] and the human myocardium [294, 295]. Thus, there is an incomplete understanding of the function and role of SERCA2a in pathology and ageing.

SERCA2a is a commonly discussed therapeutic target; upregulation of SERCA2a activity has been studied for many years as a method to attenuate the symptoms of HF [167, 296, 297], including improving systolic and diastolic function and diminishing the occurrence of arrhythmias. Additionally, the overexpression of SERCA2a (and thus, an increase in whole-cell activity) via gene therapy in a series of animal [298–300] and human [301, 302] models has been shown to improve cardiac function in HF.

A complete understanding of the role of SERCA2a in both health and disease is critically important to understand the development of cardiac dysfunction and develop actionable clinical responses to stabilise cardiac function in the failing myocardium.

4.1.2 Heterogeneous SERCA2a Expression

The previous chapter (Section 3.1) discussed the lack of information on the heterogeneity in the magnitude and spatial organisation of expression of Ca^{2+} handling proteins, such as SERCA2a. Moreover, there exists little data detailing the subcellular localisation of SERCA2a, by extension, the SERCA2a inhibitor, PLB [303–305]. Existing studies all concur that SERCA2a is concentrated along the z-lines of the sarcomere, with smaller proportions existing between these z-lines (see Section 2.2.1 for more information on cardiomyocyte structure) with visible heterogeneity throughout the cell. PLB is observed to be co-localised with SERCA2a following a similar distribution.

Quantification of heterogeneous expression in SERCA2a has not been performed in either healthy or remodelled cardiac cells; however, evidence suggests there is remodelling of SERCA2a distribution in HF. The expression of many Ca^{2+} channels and the underlying sub-cellular structure is observed to be remodelled in HF [13, 145, 176, 180, 183]. This remodelling affects the structure of the t-tubule system

and, critically, the SR in which SERCA2a channels are located [170, 216]. It is understood that CICR is critically dependent on spatial heterogeneity and the relative physical arrangement of Ca^{2+} channels to one another [306]. Despite this, there is a significant gap in our understanding of the sub-cellular distribution of SERCA2a, and moreover, there is no quantification as to the extent HF-associated remodelling impacts the spatial profile of SERCA2a.

4.1.3 Aims

This chapter aims to address the described gaps in the literature by utilising the novel image-analysis method developed and described in the previous chapter to quantify the spatial heterogeneity of SERCA2a expression in healthy and in the well-established monocrotaline (MCT) model of right ventricular heart failure in rat ventricular myocytes. Following this, the GRF image-based modelling approach, also developed and described in the previous chapter, is utilised to systematically assess the structure-function relationships and their modulation associated with heart failure. This joint experimental-computational approach will characterise the spatial profile of SERCA2a and elucidate the role and importance of SERCA2a heterogeneity in determining Ca^{2+} variability. Furthermore, SERCA2a heterogeneity will be introduced in pro-arrhythmic conditions to assess the importance and role this heterogeneity plays in promoting or inhibiting arrhythmic cellular phenomena.

To summarise, this chapter aims to achieve the following objectives:

1. To characterise and quantify the spatial profile of SERCA2a and its intracellular variability in healthy rat ventricular myocytes.
2. To characterise and quantify the remodelling of the spatial profile of SERCA2a in HF compared to control cells.
3. To investigate the functional implications of introducing heterogeneous and variable SERCA2a expression on the CaT in health and under HF-associated remodelling; and thus, determine if heterogeneous SERCA2a expression explains, or contributes to, reduced CICR in HF.
4. To investigate the impact of heterogeneous SERCA2a expression under pro-arrhythmogenic conditions and whether this heterogeneity explains or contributes to the observed increase in pro-arrhythmic phenomenon in HF.

The work that forms this chapter has been provisionally accepted for publication in a special issue of the Philosophical Transactions of the Royal Society B under the title

"Increased SERCA2a sub-cellular heterogeneity in right-ventricular heart failure modulates excitation-contraction coupling and arrhythmogenic dynamics" (see "Author Publications" for a breakdown of relative contributions).

4.2 Methods

4.2.1 Ethical Considerations

The animal data used in this study was part of the same dataset contributed by Izzy Jayasinghe, Miriam Hurley and Thomas Sheard as used in Chapter 3. Different cardiomyocytes were used in this study than in developing the toolkit described in Chapter 3. The animal data used in this study were either previously published [13] or produced for non-related research at the time of writing and not produced for this study. All non-published animal data was generated at the University of Leeds under various historic licenses.

In line with the 3Rs principles, this work aims to replace animal research with an appropriate, validated in silico model, and this project was able to reduce the number of animals required through the recycled use of these banked historical samples, both published and unpublished images.

All animal experiments were conducted according to the UK Animals (Scientific Procedures) Act of 1986 under the EU Directive 2010/63/EU with UK Home Office and local ethical approval.

4.2.2 Summary of Experimental Datasets

Previously-published [13] and unpublished confocal resolution microscopy images (Figure 4.1) of SERCA2a expression in rat ventricular myocytes were analysed. The author of this thesis did not carry out the animal experiments in this section; instead, they were carried out by the co-authors of the accompanying manuscript: Izzy Jayasinghe, Miriam Hurley, and Thomas Sheard. The information regarding the MCT model discussed in Section 4.2.2.1 was contributed by Thomas Sheard and is not the work of the Author. The described MCT model of RV HF follows those previously described within the literature [12, 154, 170, 213, 216].

4.2.2.1 Monocrotaline Model of Right Ventricular Heart Failure

Adult male Wistar rats (180–215g) had an intraperitoneal injection using a 26G needle of either 60 mg/kg MCT (Sigma-Aldrich, USA) to induce acute RV HF or an equivalent volume of 140 mM NaCl saline as a control. These two groups of animals will be referred to as Fail and Control, respectively. The 60 mg/kg MCT solution, within a 140 mM NaCl buffer, was prepared fresh on the day of injection. Initially, MCT was dissolved in 1 M HCl before being corrected to pH 7.4 within the NaCl buffer. Post-injection, animals were weighed and observed three times weekly for three weeks before being weighed and observed daily. Throughout this time, animals were monitored for visual signs of RV HF with an endpoint established upon a; 10 g weight loss within 24 hours, weight loss over two consecutive days or an overall weight loss of 20 g. Signs of a cold extremity, lethargy, dyspnoea and piloerection were also monitored to denote the severity of RV HF development. Upon the presentation of RV HF, animals were euthanised by concussion followed by cervical dislocation. Control animals were age-matched regarding the number of days post-injection in which the Fail animals reached their pre-described endpoint.

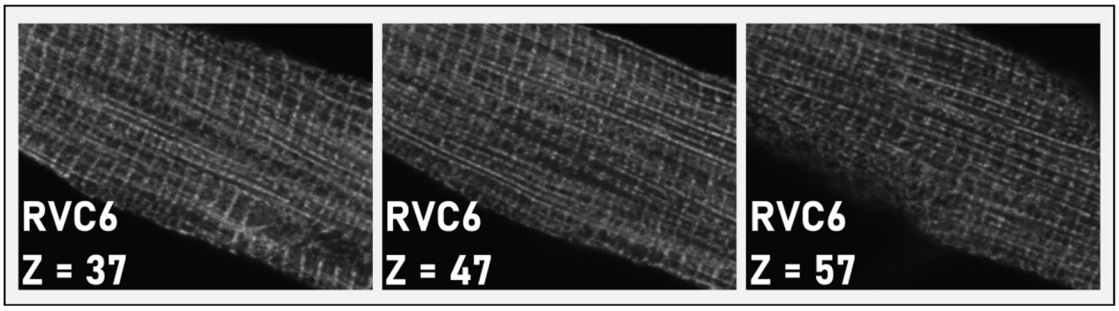

Figure 4.1 Example image stack of confocal SERCA2a microscopy image data

Three x-y slices from RVC6 (Right Ventricular Control cell #6) at z-axis depths of 37, 47 and 57.

4.2.3 Image Analysis

Correlation length scales, λ , and variance, σ, were measured in the expression of SERCA2a in immunofluorescence-stained confocal microscopy data using the Sub-Cellular Heterogeneity Analysis Toolkit developed in Chapter 3, using the method

described in that same chapter, and published in [1]. This method is briefly restated below to include adaptations for this study.

Only confocal microscopy data is utilised in this analysis to minimise additional sources of variation. Images are semi-automatically processed into a form suitable for the variogram analysis protocol before being plotted as an empirical variogram (Figure 3.2). Each cell was correctly processed as outlined in Section 3.2.4 before being down-sampled to a resolution of 1 μm^2. The variogram process was applied to each x-y slice in each image dataset before integrating over the depth axis. Three regions of each cell were analysed more than 50 times successfully to produce a statistical mean and error for each cell's isotropic correlation length scale, λ.

In total, 29 datasets were analysed, including stacks and single images from both left ventricular (LV) and right ventricular (RV) rat cardiomyocytes taken from animals that underwent the control (saline injection; N = 5 LV and 11 RV) and monocrotaline (MCT; N = 6 LV and 7 RV) treatment. In this study, 12 of the cardiomyocytes had single image datasets, 17 cardiomyocytes had 6 or more images, and 6 cardiomyocytes had 20 or more images. The two groups of cells will be referred to as the “control” group and the “HF” group from this point.

4.2.4 Computational Models

The computational portion of this chapter was performed using the GRF image-based computational modelling method developed and discussed in Chapter 3 and is briefly restated here. A simplified version of the O'Hara-Rudy Dynamic Human Ventricular model [46, 50, 237] (Figure 3.7A) was integrated into the Multi-Scale Cardiac Simulation Framework (MSCSF) compartmentalised Ca^{2+} dynamics model [50] (Figure 3.7B). Further details on each of these models can be found in Section 2.8, and the full image-based modelling method is described in Section 3.3.

These GRFs were generated at a discretisation resolution corresponding to the full-sized MSCSF matrix (19500 CRUs; 15 × 20 × 65). Each voxel of the GRF represents one CRU and scales local J_{up}^{max} by some value between 0 – 2. In the application study in Chapter 3, whilst some slight inter-cell variation in relative whole-cell SERCA2a expression was present, correlation length scales varied much more from cell to cell (Figure 3.12). Isotropic maps were generated with identical whole-cell mean SERCA2a expression and whole-cell variance, $\sigma = 1$, at four correlation length scales ($\lambda = 1, 3, 5, 10\ \mu m$; e.g., Figure 3.7C ii) encompassing the

range of experimentally observed length scales (see Section 4.3) and isolating the impact to that of correlation length scale only.

4.2.5 Experimental and Simulation Protocols

In this study, the correlation length scales describing the sub-cellular distribution of SERCA2a in rat healthy and right-ventricular-failure myocytes are quantified as described in Section 4.2.3. Following this, simulations were performed to access the impact of different correlation length scales on whole-cell Ca^{2+} dynamics under normal pacing and pro-arrhythmic conditions, corresponding to CaT alternans and spontaneous Ca^{2+} release events.

This work was undertaken using ARC4, part of the High-Performance Computing (HPC) facilities at the University of Leeds.

4.2.5.1 Normal Pacing and Rate Dependence

Expression maps were loaded into the MSCSF and paced for 60 beats at a steady-state at rates of 60, 75, 120, 133 and 150 beats per minute (bpm). At each of the selected correlation length scales ($\lambda = 1$, 3, 5 and 10 μm), three maps were used for a total of 12 heterogeneous maps, with a homogeneous control.

4.2.5.2 Alternans

CaT alternans were studied by applying rapid pacing (120 bpm) under multiple parameter combinations, known to promote alternans [233, 307, 308]. These involved reductions in the activity of the L-type Ca^{2+} channels (LTCCs) through either a reduction to channel expression, corresponding to the number of channels per dyad, N_{LTCC}, or a reduction to the channel open transition rate, $LTCC_{PO}$, or reductions in the activity of SERCA2a through reducing the whole-cell average of J_{up}^{max}. These modulations were applied individually and in combination. Global changes were applied consistently to homogeneous and heterogeneous sub-cellular SERCA2a expression maps.

4.2.5.3 Rapid Pacing, SR-Loading and SCRE

An additional set of 10 heterogeneous expression maps at each correlation length scale ($\lambda = 1$, 3, 5 and 10 μm) were generated to study spontaneous Ca^{2+} release dynamics (SCRE). To induce SR-Ca^{2+} loading, which promotes the emergence of SCRE, rapid pacing (150 bpm) was applied in combination with a functional model

of isoprenaline (ISO), which comprises enhanced LTCC activity (x2) and SERCA2a activity (x1.75) as well as enhanced K^+ currents to maintain action potential duration (APD). A second condition was introduced, further up-regulating SERCA2a by a factor of 1.5 to enhance SR-Ca^{2+} loading, covering for the uncertainty in the degree of enhanced activity due to ISO. 20 simulations were performed for each of the 10 heterogeneous maps for each condition (for a total of 200 runs at each correlation length scale), and 50 simulations were performed with the homogeneous control map to enable statistical analysis,

4.3 Results

4.3.1 Correlation Length Scale of SERCA2a Heterogeneity Increases in Right-Ventricular Heart Failure

In the analysed rat ventricular cardiomyocytes, the correlation length scale of expression was observed to range between $\lambda = 1 - 4$ μm in the control group (mean = 2.277 $\pm$ 0.143 μm) and between $\lambda = 2 - 11$ μm in the HF group (mean = 4.930 $\pm$ 0.588 μm) (Figure 4.2A, C). Differences in correlation length scale can be visualised in contour maps of SERCA2a expression in processed cardiomyocytes (Figure 4.2B). The control group cells are more structurally similar at their minimum and maximum correlation length scales than the HF group.

A significant difference in the mean correlation length scales of these two groups was found (Figure 4.2C; $p < 0.001$), thus, cardiac remodelling in the MCT model of RV-HF is observed to increase the spatial correlation of SERCA2a in the sub-cellular volume (larger correlation length scales) and increase the inter-cellular variability of spatial correlation (larger range of length scales). This significance is also present when isolating LV and RV cardiomyocyte populations (Figure 4.2C, right panel). RV cells are observed to have longer correlation length scales in both control and RV-HF remodelling (Control: mean = 2.476 ± 0.176 μm; MCT: mean = 5.214 ± 0.864 μm; $p < 0.001$) than in LV cells (Control: mean = 1.848 ± 0.155 μm; MCT: mean = 4.598 ± 0.864 μm; $p < 0.01$). Additionally, there was a small significant difference found in the correlation length scales in the control LV and RV groups ($p < 0.05$). Therefore, both LV and RV rat ventricular myocytes display a significant increase in spatial correlation in the MCT model of RV HF [12, 154,

213, 216], congruent with observations that the left ventricle atrophies in RV-HF as a compensatory response [215, 216].

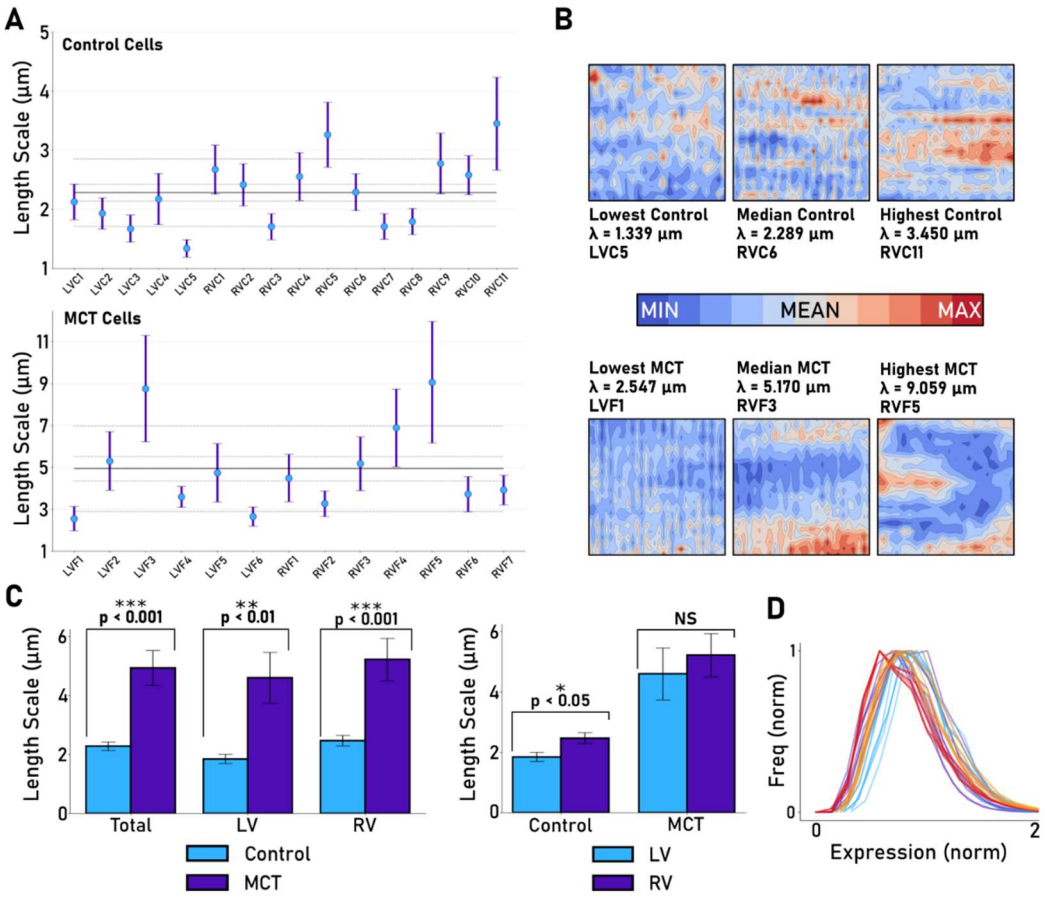

Figure 4.2 SERCA2a heterogeneity in control and RV-HF models of rat ventricular myocytes.

A – Comparison of cell-average correlation length scales, λ, in control (saline-treated) cells and monocrotaline (MCT) treated rat ventricular myocytes (Control: N = 16 cells; MCT: N = 13 cells). Horizontal lines represent the overall mean (full line) and standard deviations (1 and 2 standard deviations, dotted lines) for control and MCT cells. Error bars are 95% confidence intervals. B – Contour maps of sections of analysed cells. C – Comparison of mean λ in control and MCT-treated cells (left) and in left ventricular (LV) and right ventricular (RV) cells. D – Normalised SERCA2a expression distribution in analysed cells. Expression is measured via pixel intensity; each line represents one cell.

In the larger population of rat ventricular myocytes analysed in this chapter, the same Gaussian distribution of expression (Figure 4.2D) is observed as previously observed in the preliminary study in Chapter 3 (Figure 3.12Aiv).

4.3.2 SERCA2a Heterogeneity Reduces CaT Magnitude, SR-Ca^{2+} Load and Increases Spatial Variation in Intracellular Ca^{2+}

The SERCA2a expression distributions observed in both image analysis studies (Figure 3.12; Figure 4.2) are Gaussian. Therefore, it is an appropriate choice to model SERCA2a expression using GRFs. The isotropic, 3D GRF expression maps were generated using the range of correlation length scales observed across control and HF myocytes. It is observed that the GRF contour maps (Figure 3.7) are visually similar to the contour maps of SERCA2a expression (Figure 4.2B) at the corresponding correlation length scales. From this point, maps are referred to by their correlation length scale and map number (e.g., λ = 3 μm, map 2 refers to the 2nd of three maps at the correlation length scale of 3 μm).

At control pacing, peak CaT magnitude (obtained by averaging the local concentrations in each CRU throughout the cell) decreases in all heterogeneous conditions compared to the homogeneous control (Figure 4.3Ai). The magnitude of this reduction increased as the correlation length scale increased (Figure 4.3Bi), despite a maintained whole-cell average expression of SERCA2a across all maps. Additionally, the inter-map variation (the difference in value between maps of the same correlation length scale) is largest at the longest correlation length scales with a maximum reduction of 0.141 μM (22.9%) on λ = 10 μm, map 2. Diastolic [Ca^{2+}] was also observed to reduce under heterogeneous SERCA2a expression slightly (Figure 4.3Bii), with a maximal reduction of ~ 0.003 μM (~3.75%, λ = 10 μm, map 2).

The reduction in CaT magnitude correlates with a smaller but significant reduction in diastolic SR-Ca^{2+} load (Figure 4.3Aii, Biii) in all heterogeneous conditions, compared to the homogeneous condition. This reduction generally increased with longer correlation length scales with a maximal reduction of ~ 10% (λ = 10 μm, map 3), congruent with decreased SR Ca^{2+} content observations in HF [157, 167, 168]. The proportion of activated RyRs (Figure 4.3C) in normal pacing also decreased in all heterogeneous conditions, corresponding to the decreases in CaT magnitude with increasing reduction and inter-cellular variability at larger correlation length scales.

Minor increases in transmembrane action potential (AP, Figure 4.3D) after rapid depolarisation are observed in heterogeneous models compared to the homogeneous control, with a maximum effect of 2.3 mV (λ = 10 µm, Map 2). Action potential duration (APD) remains consistent across all maps, and the remaining morphology remains largely unchanged.

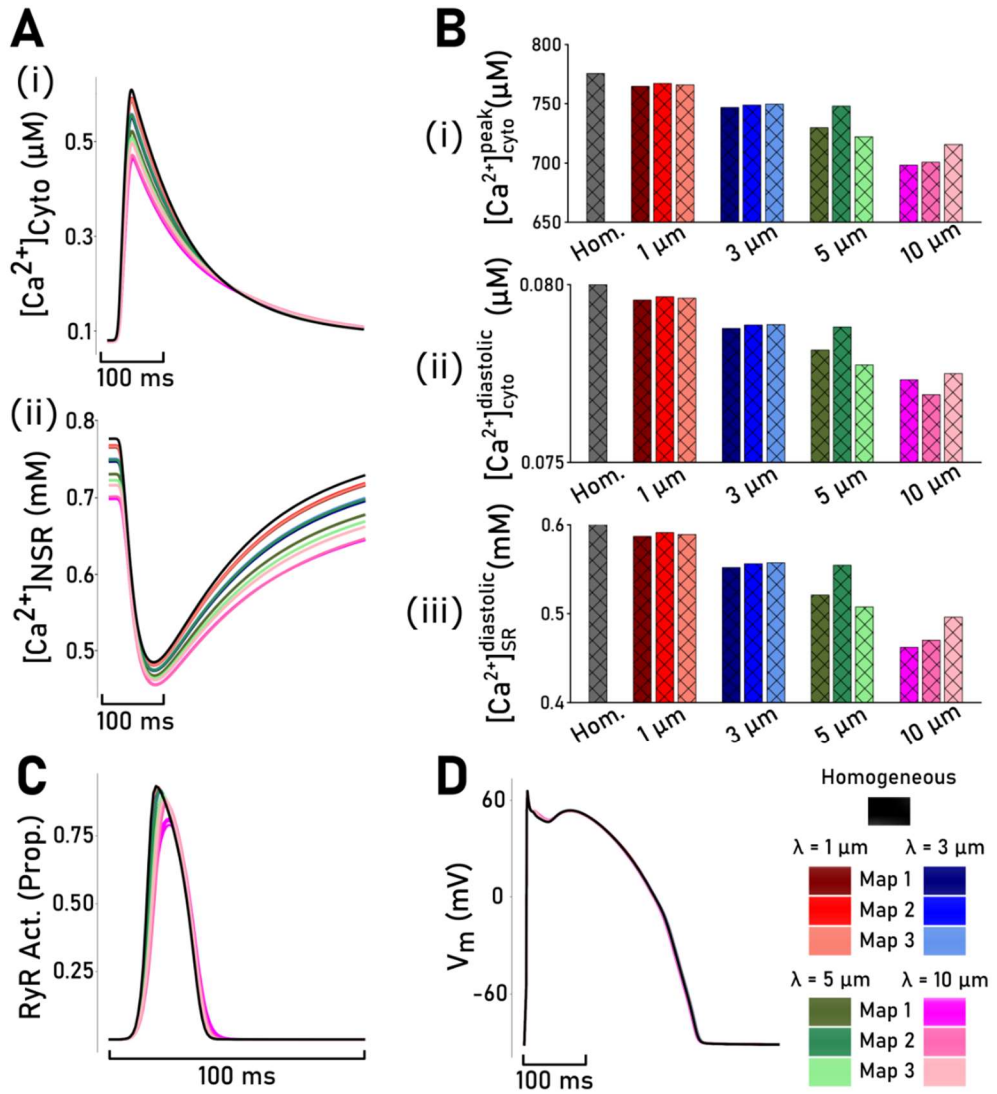

Figure 4.3 Whole-cell AP and Ca^{2+} dynamics at control pacing

Whole-cell dynamics for one cycle at steady-state under homogeneous and heterogeneous SERCA2a conditions at normal pacing, coloured by correlation length scale, λ (legend bottom right). A – Whole-cell averaged Ca^{2+} transient (CaT) and SR-Ca^{2+} for each condition. B – Summary of peak CaT magnitude, diastolic Ca^{2+} concentration and diastolic SR-Ca^{2+} load during normal pacing (corresponding to A). C – Proportion of RyR activated. D – Transmembrane action potential (AP). Time scales below plots in ms.

The reduction in CaT magnitude associated with longer length scales is accompanied by an increase in the spatial variation of the CaT throughout the cell (Figure 4.4) as a direct consequence of local SERCA2a function. Regions with higher SERCA2a expression (see SERCA2a scale bars in Figure 4.4) produce more rapid local CaT decay in that region, which is expected, as SERCA2a expression directly impacts the rate of SR-Ca^{2+} uptake [280, 281]. Slower CaT decay is spatially correlated with regions of lower SERCA2a expression. These factors result in large variabilities in the CaT with neighbouring regions of rapid and slow SR-Ca^{2+} uptake producing large regional differences.

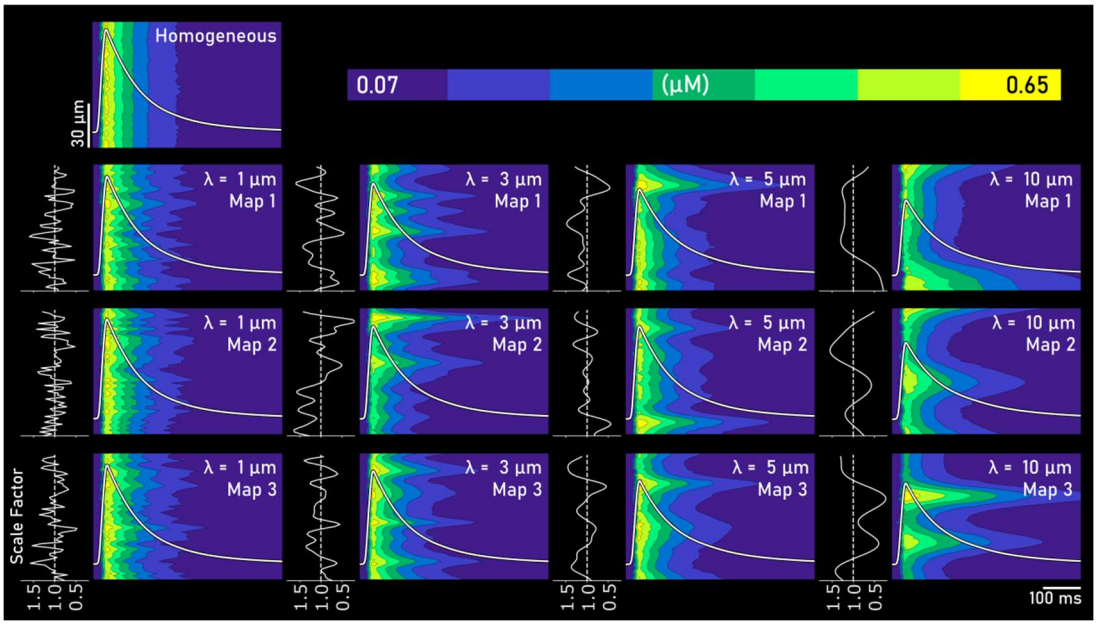

Figure 4.4 Spatial variation in Ca^{2+} transients due to SERCA2a expression heterogeneity

Space-time images of the Ca^{2+} transient (CaT) in the central longitudinal axis of the cell in the homogeneous and all heterogeneous conditions, corresponding to the conditions in Figure 4.3. Whole-cell average CaTs are overlayed in white. Each panel is accompanied by a plot showing the SERCA2a scale factor (left) along the same longitudinal axis.

This spatial variation and its inter-cellular variability increase with the correlation length scale. There is a more uniform whole-cell transition from systolic to diastolic intracellular Ca^{2+} concentration in the homogeneous and control-associated length scale models than the larger length scales. Smaller correlation length scales associated with control cells (λ = 1, 3 µm) have smaller localised regions of

enhanced or depressed SERCA2a expression; thus, resulting in smaller, less correlated changes in local CaT, while larger length scales (λ = 5, 10 μm) feature smoother, larger transitions.

4.3.3 Effects of Heterogeneous SERCA2a expression on Rate-Dependence

Between 60bpm and 150bpm, the introduction of SERCA2a heterogeneity at all correlation length scales yielded negligible differences in APD90 restitution (between ~ 5-10ms; Figure 4.5A); morphological differences (Figure 4.5B) were determined to be a consequence of differences in CaT magnitude (Figure 4.5C) and converged to the homogeneous morphology at all length scales within 100-150 ms. The largest potential differences to control were 2.3mV at 60 bpm, 6.3mV at 120 bpm, and 11.6mV at 150 bpm, all occurring on λ = 10 μm, Map 2.

Properties of the intracellular Ca^{2+} handling system were more substantially affected by increased pacing rate, generally amplifying differences between homogeneous and heterogeneous conditions at more rapid pacing rates compared to slower pacing rates. Heterogeneous conditions are observed to yield lower CaT peak magnitudes than the homogeneous control, further decreasing as the pacing rate increases from 60 to 150 bpm (Figure 4.5Ci). Higher pacing rates (120 bpm and above) observe a longer stimulus-peak time delay of the CaT under all heterogeneous conditions (Figure 4.5Cii) which is not prominent at control pacing. CaT peak delay is observed to increase at longer correlation length scales; despite relatively minor impact (~30% increase in time delay at 120 bpm, λ = 10 μm), this feature may be important in determining the behaviour of alternans [307]. Inter-map variation in CaT magnitude and stimulus-peak time delay increases with longer correlation length scales. Cardiomyocytes from failing hearts show defective CICR characterised by decreased CaT magnitude and diminished SR-Ca^{2+} uptake [157, 309], congruent with the consequence of heterogeneous SERCA2a expression in these models (Figure 4.5C, D).

Diastolic SR-Ca^{2+} content (Figure 4.5Di) remains more constant as the pacing rate increases from 60 to 120bpm for the homogeneous control and control group associated maps (λ = 1, 3 μm), SR-Ca^{2+} content increases from 120 to 150bpm. Longer correlation length scales associated with the HF group yield a reduction in SR-Ca^{2+} content between 60 and 80bpm, followed by an increase in Ca^{2+} load up to 120bpm, before it either falls sharply or remains constant (λ = 3, Map 1).

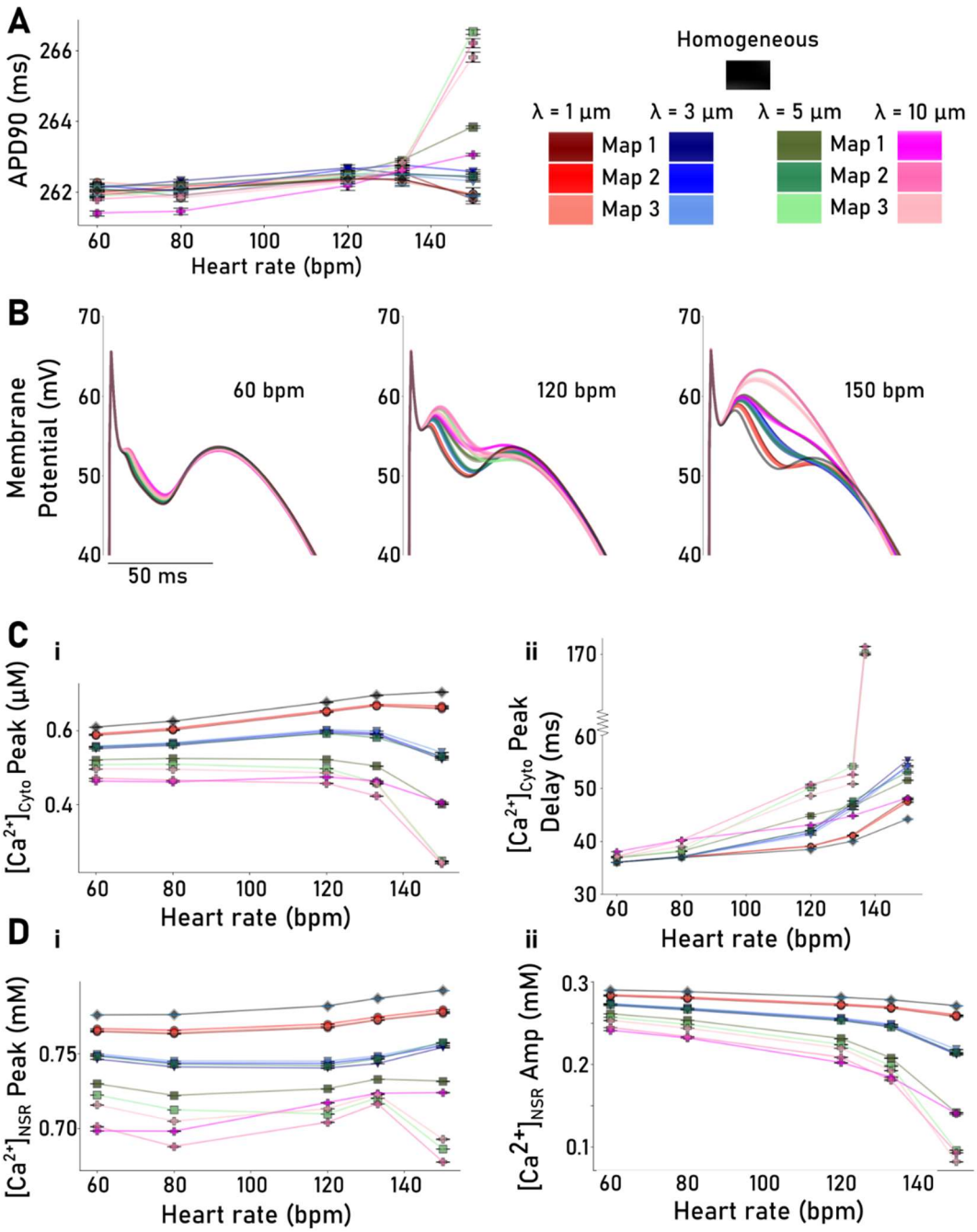

Figure 4.5 Rate-dependence of whole-cell AP and Ca^{2+} properties.

All plots display all homogeneous and heterogeneous conditions (legend top right). Panels A, C & D show average dynamics over 10 cardiac cycles at steady-state with standard error bars. A – APD90 (90% repolarisation) restitution curve (ms). B – Action Potential (AP) morphologies at 60, 120 and 150 bpm. C – (i) Ca^{2+} transient (CaT) peak magnitude (µM) and (ii) time delay from pacing stimulus to CaT peak (ms). D – (i) Peak Diastolic SR-Ca^{2+} (mM) and SR-Ca^{2+} amplitude (mM).

SR-Ca^{2+} release amplitude (Figure 4.5Dii) displays the same rate-dependence as CaT peak magnitude (Figure 4.5Ci), as expected.

The nature of the rate-dependence is also affected under heterogeneous conditions. In the homogeneous control, CaT peak magnitude increases at more rapid pacing rates. Conversely, in all heterogeneous conditions, pacing rates above 130 bpm yielded a reduction in the CaT peak. This reduction generally increased at larger correlation length scales.

4.3.4 Mechanisms Underlying Whole-Cell SR-Ca^{2+} Reduction and Heterogeneity

Despite the maintenance of whole-cell SERCA2a expression across the heterogeneous expression maps, reductions in whole-cell peak magnitude of cytosolic CaTs and diastolic SR-Ca^{2+} loads are present in all heterogeneous conditions studied compared to the homogeneous control (Figures 4.3, 4.5). This section aims to explain this non-trivial observation and necessitated additional simulations to unravel the mechanism underlying this observation.

4.3.4.1 Simulation Protocols

To study the relationship between CaT magnitude and SR-Ca^{2+} content, single CRU models at explicitly set SR Ca^{2+} loads between 550 and 1250 μM at 25 μM intervals were run 60 times at each SR-Ca^{2+} load to account for stochasticity (Figure 4.8B).

Homogeneous simulations on cell portions with modified whole-cell mean SERCA2a expression (scaled by x0.75, x1.25) were run at steady-state normal pacing to observe non-linearities in SERCA2a function in homogeneity (Figure 4.8Ci). To study the impact of inter-SR coupling on the observed reduction in SR-Ca^{2+}, a homogeneous and a heterogeneous simulation were run to steady-state at normal pacing with SR-Ca^{2+} diffusion removed from the model. (Figure 4.8Cii).

The relationship between SERCA2a expression and J_{up} was further explored using a set of SERCA2a expression maps constructed with one large central region of SERCA expression (Figure 4.9). This central region was varied in volume (up to ~ 17.2% of total cell volume) and expression (between a scale factor of x1.25 and x2 of the whole-cell mean SERCA2a expression) with the surrounding region adjusted to maintain the same whole-cell expression as the homogeneous control**.** Local SERCA fluxes, J_{up} in each voxel and whole-cell average J_{up} was recorded

throughout 10 cycles at steady-state at 120 bpm and compared to a homogeneous control. These are henceforth referred to as "central region simulations" for brevity and clarity.

4.3.4.2 Investigating Heterogeneous SR-Ca^{2+} Load

Heterogeneous SERCA2a expression resulted in heterogeneous local Ca^{2+} properties (Figure 4.6). During normal pacing (Figure 4.6A), the spatial distributions of cytosolic Ca^{2+} and SR-Ca^{2+} content followed a heterogeneous distribution correlating with the spatial organisation of SERCA2a expression; lower expression regions correlated with local regions of higher intracellular Ca^{2+} (Figure 4.6 Bi-ii), exhibiting greater diastolic Ca^{2+} and a greater local contribution to CICR than regions with higher SERCA2a expression. Regions of higher SERCA2a expression exhibited faster initial rates of SR-Ca^{2+} uptake (Figure 4.6Biii) than lower SERCA2a expression regions, with high values of SR-Ca^{2+} during the initial decay of the CaT. Regions with higher initial SR-Ca^{2+} content (correlating with higher SERCA2a expression) diffuse to the SR of neighbouring low SERCA2a expression regions with comparatively lower levels of SR-Ca^{2+}. Lower SERCA2a expression regions then exceed higher expression regions in SR-Ca^{2+} load towards the end of the systolic recovery phase as they continue to uptake local cytosolic Ca^{2+} long after it has been depleted in the higher SERCA2a expression regions. (Figure 4.6 Biv). This mechanism is illustrated in Figure 4.7.

4.3.4.3 Investigating Reduced SR-Ca^{2+} Load

Cell-average J_{up} decreased in all heterogeneous conditions compared to the homogeneous control in normal pacing (Figure 4.8A), corresponding with drops in CaT magnitude, diastolic [Ca^{2+}] and SR-Ca^{2+} load (Figure 4.3B). Whole-cell SERCA2a expression was kept constant across the homogeneous and heterogeneous conditions; thus, there must be some non-linearity in SR-Ca^{2+} uptake, inter-CRU spatial diffusion effects, or some combination of the two.

A non-linear relationship between peak cytosolic [Ca^{2+}] and diastolic SR-Ca^{2+} is observed (Figure 4.8Bi); higher SR-Ca^{2+} loads correlate with progressively greater increases in intracellular Ca^{2+}. Assuming SR-Ca^{2+} uptake correlates directly with SERCA2a expression, this suggests that CaT magnitude should increase under heterogeneous SERCA2a expression, contradictory to our observations (Figure 4.3)

and thus, a non-linearity must exist between cytosolic and SR Ca^{2+} concentrations and J_{up}. SR-Ca^{2+} uptake rate, J_{up}, is observed to have a non-linear relationship with intracellular Ca^{2+} (Figure 4.8Bii): decreasing cytosolic [Ca^{2+}] decreases J_{up} faster at lower levels. SR-Ca^{2+} itself is observed to have a lower but similarly non-linear impact on the SR-Ca^{2+} uptake rate (higher SR-Ca^{2+} loads result in lower J_{up} with increasing reductions); thus, J_{up} is much more sensitive to changes in cytosolic Ca^{2+} at lower levels (around the diastolic range).

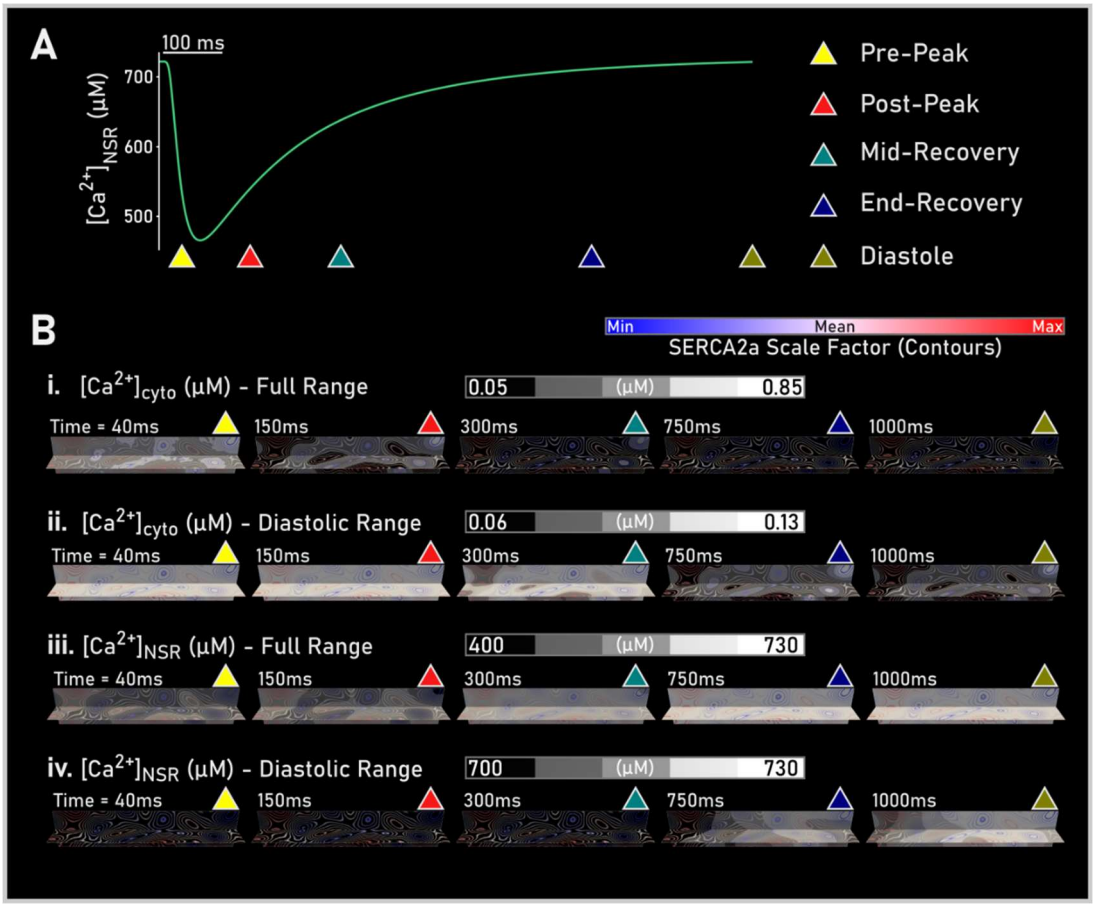

Figure 4.6 Spatial distributions of Ca^{2+} and SR-Ca^{2+} during normal pacing

Spatial Ca^{2+} and SR-Ca^{2+} analysis for one cycle at steady state at control pacing under a heterogeneous SERCA2a map of correlation length scale λ = 5 μm. Whole-cell average SR-Ca^{2+} load (A) is highlighted at different time-points (coloured triangles) for comparison with spatial snapshots in time of Ca^{2+} and SR-Ca^{2+} distributions (B) corresponding to A:
i) Cytosolic Ca^{2+} - Full Range, ii) Cytosolic Ca^{2+} - Diastolic, iii) SR-Ca^{2+} - Full Range, iv) SR-Ca^{2+} - Diastolic.

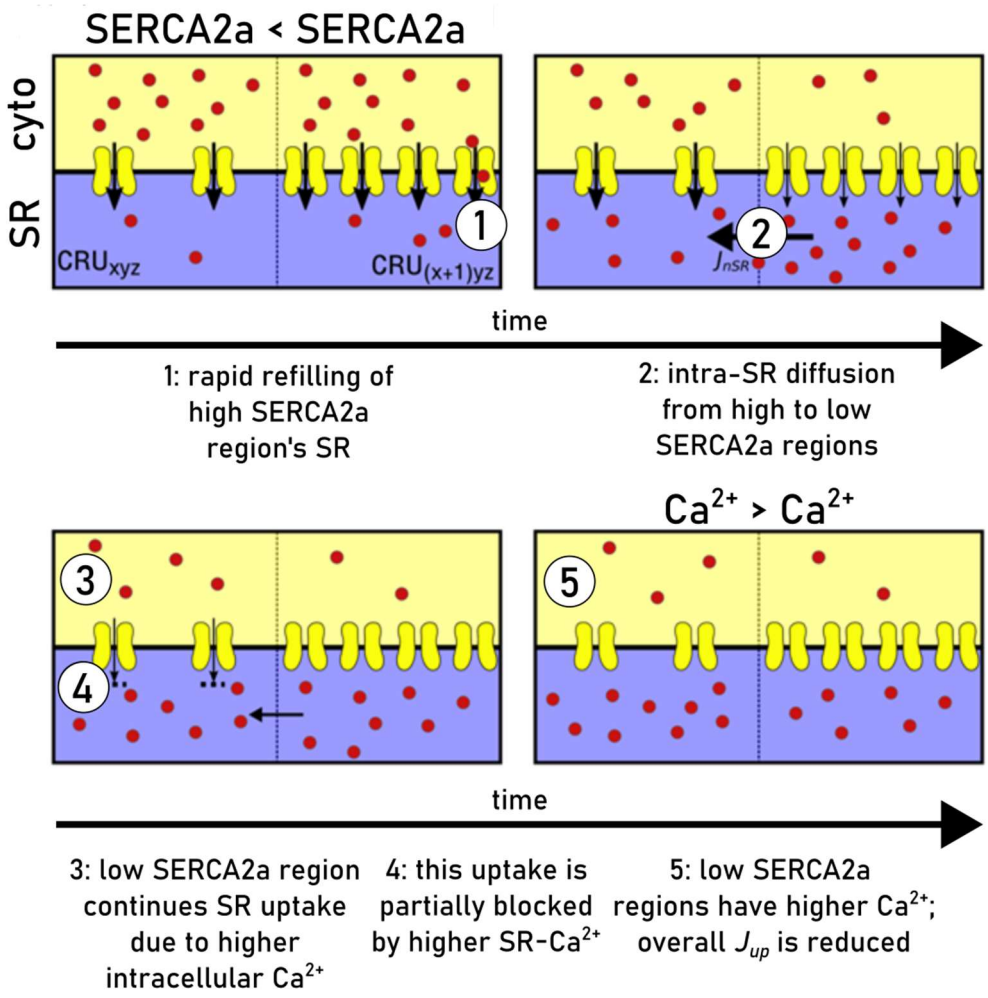

Figure 4.7 Cartoon mechanism of SR Ca^{2+} Heterogeneity

A cartoon illustration describing the mechanisms by which regions of lower SERCA2a concentration may exhibit higher local peak diastolic SR-Ca^{2+} during normal pacing. The upper panels precede the lower panels in time. Figure adapted from the Author's publication, Holmes et al. (2021) [2].

Adjusting whole-cell mean SERCA2a expression in homogeneous conditions also yields a non-linear change in J_{up}: at both normal pacing and 2Hz, reducing cell-average SERCA2a by 25% yielded a 50% larger change in cell-average J_{up} than increasing SERCA2a by 25% (Figure 4.8Ci). Thus, increases and decreases in the SR-Ca^{2+} uptake scale factor, G_{up} have a non-linear impact on J_{up} which indicates that higher SERCA2a expression regions do not compensate for lower SERCA2a expression regions. Therefore, heterogeneous SERCA2a expression will lower

whole-cell J_{up}, which has a non-linear relationship with both diastolic [Ca^{2+}] and SR-Ca^{2+} content.

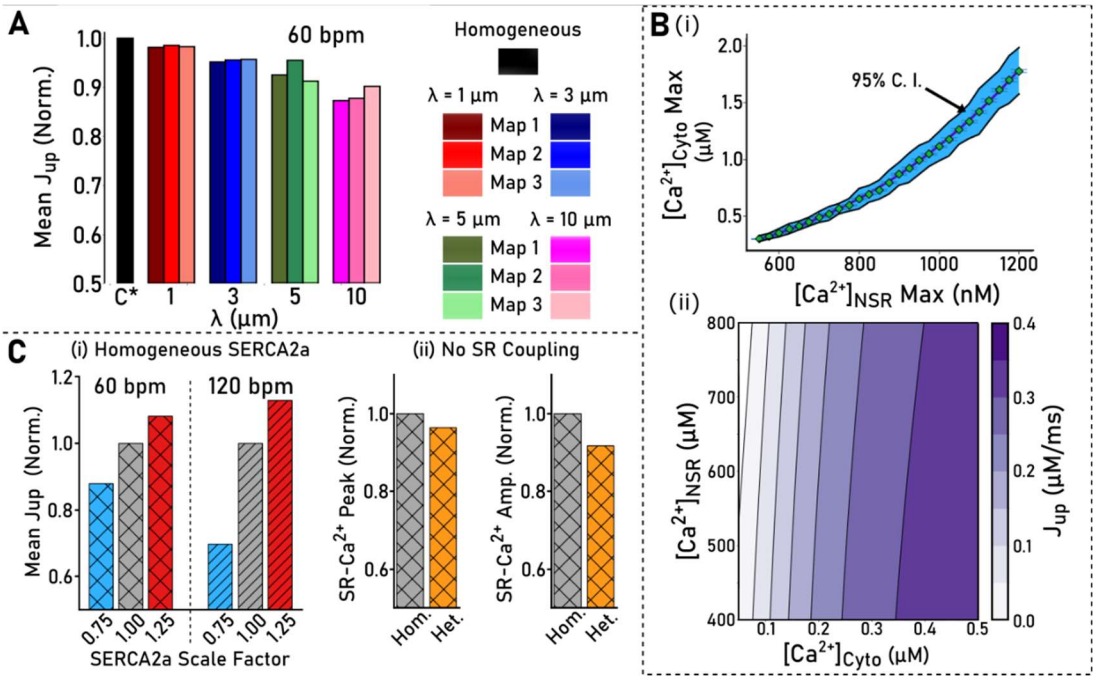

Figure 4.8 SERCA2a flux and non-linear relationships in Ca^{2+} handling.

A – Cell-average J_{up} in homogeneous and heterogeneous conditions; legend right. B – Non-linear relationships in peak $[Ca^{2+}]_{cyto}$ and peak $[Ca^{2+}]_{NSR}$ (upper) and in J_{up}, $[Ca^{2+}]_{cyto}$ and $[Ca^{2+}]_{NSR}$ (lower). C – (i) Normalised cell-average Jup vs scaled cell-average J_{up} in control at 1-2Hz, (ii) Normalised SR-Ca^{2+} peak and amplitude in a sample heterogeneous condition vs homogeneous control with no SR coupling.

Removing SR-coupling also yielded a reduction in cell-average peak SR-Ca^{2+} load (3.5%) and SR-Ca^{2+} amplitude (8.5%) in the heterogeneous condition (Figure 4.8Cii). This reduction is smaller than the reductions observed at normal pacing with normal SR coupling (Figure 4.3B); thus, inter-CRU SR diffusion contributes towards the reduction in whole-cell SR-Ca^{2+} but does not fully explain it.

Whole-cell mean J_{up} was measured in central region simulations relative to a homogeneous control (Figure 4.9A) and is observed to reduce in all heterogeneous conditions (Figure 4.9B). Larger reductions in cell-average J_{up} are associated with large central region volumes and larger central region SERCA2a expression (and thus, a lower outer region SERCA2a expression). This observation is congruent with the reduction in J_{up} observed in the normal pacing studies (Figure 4.8A) – larger

correlation length scales produce maps with larger spatial regions of high and low SERCA2a expression.

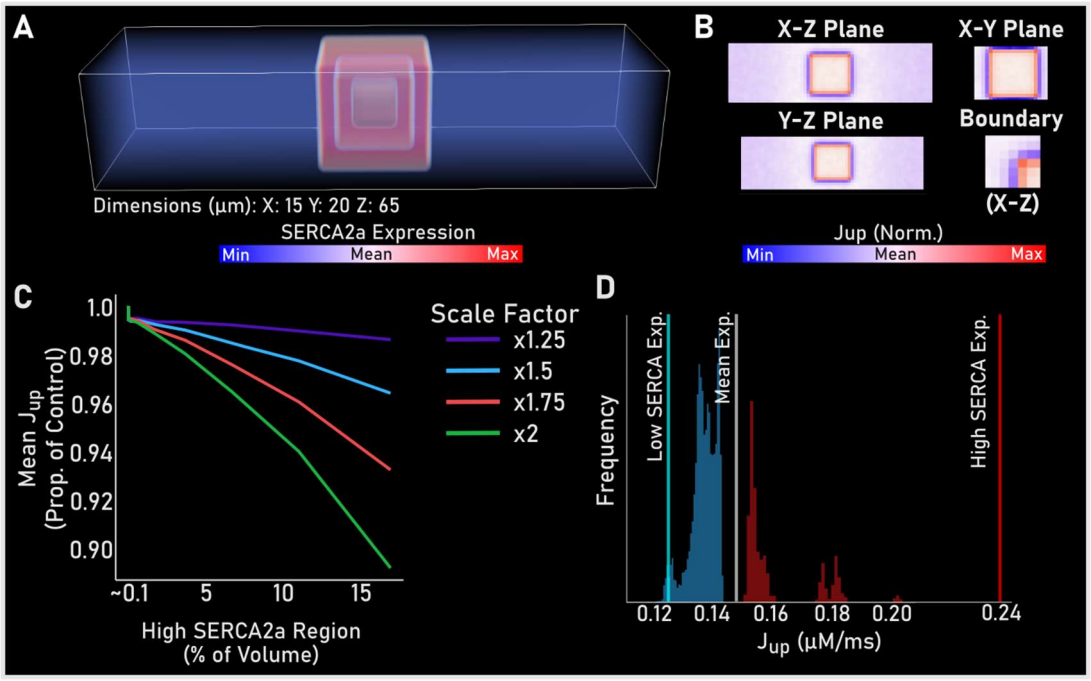

Figure 4.9 SERCA2a efficiency in Heterogeneous SERCA2a expression maps.

A - Schematic of the central region simulations. B – Example slices of spatial normalised mean J_{up} per voxel corresponding to A. C - Mean J_{up} per voxel as a proportion of the homogeneous condition by percentage cell volume and SERCA2a expression scale of the central region; legend right. D – Frequency histogram of J_{up} at x2 SERCA2a in the central region at 15% volume; low expression – blue, high expression – red. Vertical lines correspond to expected mean J_{up} of low and high regions and total mean J_{up}.

Local ${}^{x,y,z}J_{up}$ in individual CRUs were examined (Figure 4.9B, D) compared to expected local ${}^{x,y,z}_{Ex}J_{up}$ for the whole-cell and lower/high expectation values, given by the following equation:

$$ {}^{x,y,z}_{Ex}J_{up,} = \overline{{}^{Hom.}J_{up}} \times {}^{x,y,z}G_{up} $$

where (x, y, z) are the co-ordinates of the specific voxel, $\overline{{}^{Hom.}J_{up}}$ is the mean J_{up} in the homogeneous control model, and ${}^{x,y,z}G_{up}$ is the local. Therefore, the expected value of J_{up} in each voxel (CRU) is given by the mean whole-cell value in the

homogeneous model multiplied by the scale factor of the same voxel. Relative SR-Ca^{2+} uptake in regions of lower expression was generally higher than the expected value, while regions of higher expression were generally lower than the expected value. Therefore, the regions with high SERCA2a expression were not balancing the regions with lower SERCA2a expression. The large ranges and multiple peaks of local mean J_{up} suggest that this over/under-performance is dependent on spatial factors (Figure 4.9D).

The spatial distribution of J_{up} (Figure 4.9B) illustrates the localisation of the peaks in the J_{up} distribution. The boundaries between the high and low expression regions yield the highest and lowest flux values giving the peaks at the relative extremes of local J_{up} (Figure 4.9D). The large, low expression region is observed to have a shallow gradient of flux, which generally increases towards the central high expression region, which manifests as the tall, wide peak for lower SERCA2a expression regions. The lower J_{up} peak for the high SERCA2a expression region is given by the internal voxels within the central region. These spatial phenomena further support that SR coupling plays a role in determining SR-Ca^{2+} uptake as local Ca^{2+} parameters change with distance throughout the cell, as indicated by the previous analysis (Figure 4.8Ci).

To summarise these mechanisms: reduced local J_{up} in combination with maintained whole-cell NCX function leads to a loss of intracellular Ca^{2+} in heterogeneous conditions compared to the homogeneous control; thus, leading to a reduction in SR-Ca^{2+} load and a decrease in the magnitude of the CaT. Non-linearities in the dependence of SERCA2a function on both cytosolic and SR Ca^{2+} (Figure 4.8 B, C) result in a net reduction of J_{up} in the cell. The interplay between local J_{up} heterogeneity and SR coupling results in a loss of intracellular Ca^{2+} to NCX and results in the correlated spatial distribution of cytosolic and SR Ca^{2+} content observed in heterogeneous SERCA2a expression (Figure 4.6).

An additional, hypothetical mechanism is inferred by the non-linear relationship between J_{up} and SR-Ca^{2+} content, which demonstrates that increases in SR-Ca^{2+} content correlate with moderate reductions in SR-Ca^{2+} uptake. Thus, inter-CRU SR diffusion from higher SERCA2a regions into lower SERCA2a regions in the early

Ca^{2+} sequestration phase may further reduce local J_{up} compared to a lower SERCA2a region with no diffusion influx. However, proving this is complex and has not been done in this chapter.

4.3.5 Heterogeneous SERCA2a Expression Can Promote or Inhibit Ca^{2+} Transient Alternans

Introducing heterogeneous SERCA2a expression maps had complex effects on the generation of CaT alternans under conditions which promote alternans. The heterogeneous conditions were observed to induce one of three behaviours:

1. Alternans present under homogeneous conditions and shorter correlation length scales were inhibited at longer correlation length scales.
2. Alternans were induced under heterogeneous SERCA2a expression where they were not present in the homogeneous control.
3. Varying alternans magnitude or presence across maps under the same condition at the same correlation length scale.

A summary of these behaviours is given in Figure 4.10.

Excluding the control conditions (Figure 4.10; condition A), CaT alternans were present for a range of correlation length scales for all pro-arrhythmic conditions. Inter-map variation was present at all correlation length scales, but this was most prominent in the $\lambda = 3$ μm and $\lambda = 5$ μm maps; the $\lambda = 10$ μm maps produced the lowest incidence rate of CaT alternans. The highest correlation length scale, λ = 10 μm, produced the fewest and smallest alternans, only occurring in conditions with no down-regulation of SERCA2a. Generally, the difference between beat-to-beat CaT peak magnitude was larger in heterogeneous conditions. Examples demonstrating the three behaviours outlined above are given in Figure 4.11 and are discussed in turn.

In condition H (J_{up} reduced by 25%), the homogeneous control model produced stable beat-to-beat CaT alternans (Figure 4.11A). In the lowest correlation length scale of SERCA2a heterogeneity, $\lambda = 1$ μm, CaT alternans persist, but are less stable, have considerable inter-map variation and a reduced CaT peak magnitude in the larger beat. Longer correlation length scales ($\lambda \geq 3$ μm) show a very small CaT which indicates significant CICR disfunction. In a prior analysis, J_{up} was observed to be reduced in heterogeneous models; at 120bpm, this was measured to be a ~6-

7% reduction in cell-average J_{up} at $\lambda = 3$μm, up to a maximum of ~ 17% at the highest correlation length scale, $\lambda = 10$ μm. An additional reduction of 5% pushed these maps out of the alternan phase space and thus inhibited alternans.

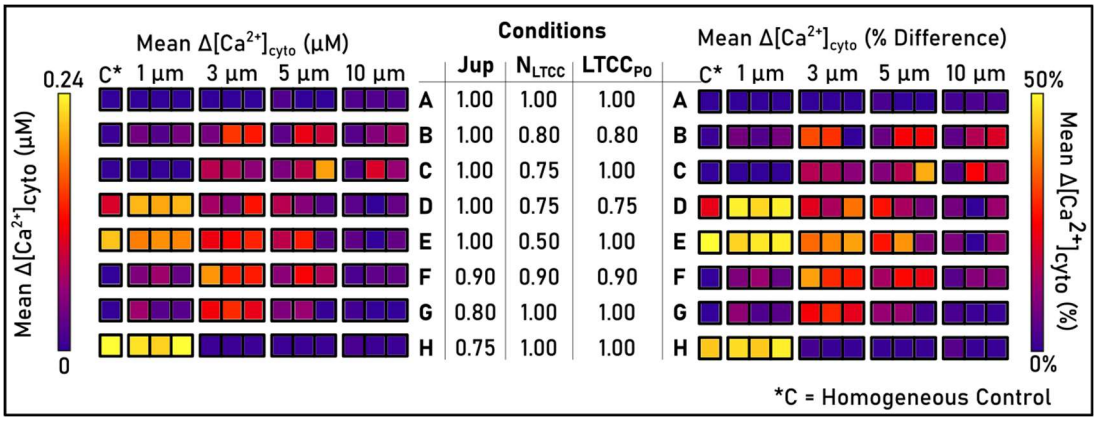

Figure 4.10 Summary of CaT alternan behaviour in control and pro-arrhythmic conditions

Colourmaps detailing the mean beat-to-beat difference in cytosolic Ca^{2+} (left) and percentage difference (right) in a range of conditions from control (A) to pro-arrhythmic (B-H) at 120 bpm. Conditions are described by scaling factors applied to each of J_{up}^{max} (whole-cell SERCA2a flux), N_{LTCC} (L-type Ca^{2+} Channel density) and $LTCC_{Po}$ (channel opening transition rate). Maps are organised from left to right.

In condition C, in which N_{LTCC} is reduced by 25%, the second and third behaviours are observed (Figure 4.11B). No CaT alternans are present under homogeneous or heterogeneous conditions where $\lambda = 1$ μm in any map (Figure 4.11Bi). At $\lambda = 3$ μm, small alternans were observed (Figure 4.10; condition C), with the largest alternans occurring on $\lambda = 5$ μm, map 3. In conditions E and H, it is observed that individual decreases in both N_{LTCC} and J_{up} produced alternans in the homogeneous control; condition F shows that a minor concomitant reduction of 10% in both variables is sufficient to promote alternans in maps with $\lambda = 3 – 5$ μm. Thus, this promotion can be explained by the reduction of whole-cell SERCA2a flux under heterogeneous conditions. The additional reduction of J_{up} pushes the model into the phase space required to generate CaT alternans as the correlation length scale increases.

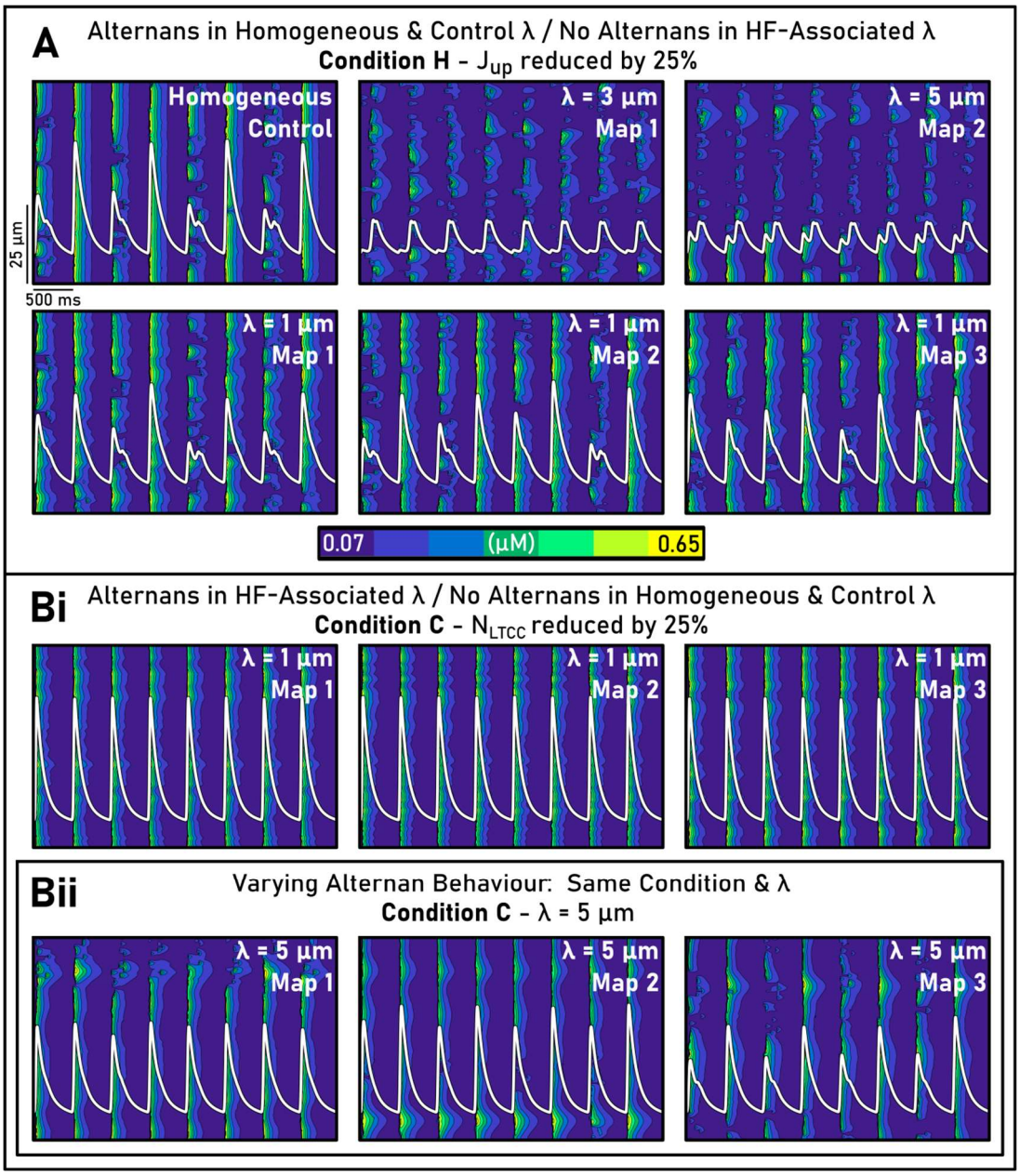

Figure 4.11 Inter-cellular variability in properties of CaT alternans

Alternans properties are visualised by superimposing cytosolic Ca^{2+} transients on intracellular Ca^{2+} z-axis linescans. A – Alternan behaviour in condition H (SR-Ca^{2+} uptake, J_{up}, reduced by 25%), for the homogeneous model, and select heterogeneous conditions. B – Alternan behaviour in condition C (L-Type Channel density, NLTCC, reduced by 25%) with correlation length scales of λ = 1 µm (i) and λ = 5 µm (ii).

The alternans produced in condition C, with a correlation length scale of $\lambda = 5$ µm, produce three distinct behaviours (Figure 4.11Bii). The reduction in whole-cell J_{up} for this set of three maps at 120 bpm was recorded as 11.6%, 8.6% and 13.8% for

maps 1, 2 and 3, respectively. In condition C, in heterogeneous expression maps ($\lambda = 5$ μm), only short, transient CaT alternans are observed in map 1; map 2 produces stable CaT alternans with a high CaT magnitude on both alternating beats; map 3 yields CaT alternans at a lower magnitude. Thus, despite map 1 yielding the median reduction in J_{up}, it produced no consistent CaT alternans. Observing the Ca^{2+} linescans reveals a much smoother CaT waveform in map 1, with a uniform rise and decay. This result indicates that both the correlation length scale of expression and the spatial organisation of expression play a role in promoting or inhibiting CaT alternans.

These shifts in behaviours (alternans to no alternans, and vice versa) generally occurred over the range of parameter combinations considered (Figure 4.10; conditions B-H). Small differences between these conditions can lead to large behavioural differences, demonstrated in conditions G and H. An additional 5% reduction in cell-average J_{up} pushes condition H into the threshold for producing CaT alternans in homogeneity, and $\lambda = 1$ μm maps whereas condition G produces alternans between $\lambda = 3 – 5$ μm, which no longer occur in condition H. These opposing behaviours over a small parameter range indicates the sensitivity of CaT alternans to model conditions. Heterogeneous SERCA2a expression and its spatial organisation can either push the cell into or out of the phase-space necessary for alternans, thus either inducing them where they were not present or inhibiting them where they were.

Figure 4.12 illustrates some mechanistic differences in CaT alternans in the homogeneous control model and under heterogeneous SERCA2a expression. Alternans under homogeneous conditions demonstrate effectively random spatial properties: the CRUs which contribute to the smaller CaT vary on a beat-to-beat basis (Figure 4.12A; left). Conversely, the introduction of SERCA2a heterogeneity reduced the random nature of CRU activation - the regions that activate or do not activate during the small beat were largely consistent (Figure 4.12A; right). The local CaTs in individual CRUs reveal that the more regularly structured CRU activation for the smaller beat is determined primarily by local diastolic $[Ca^{2+}]$ and secondarily by local SR-Ca^{2+} content (Figure 4.12B).

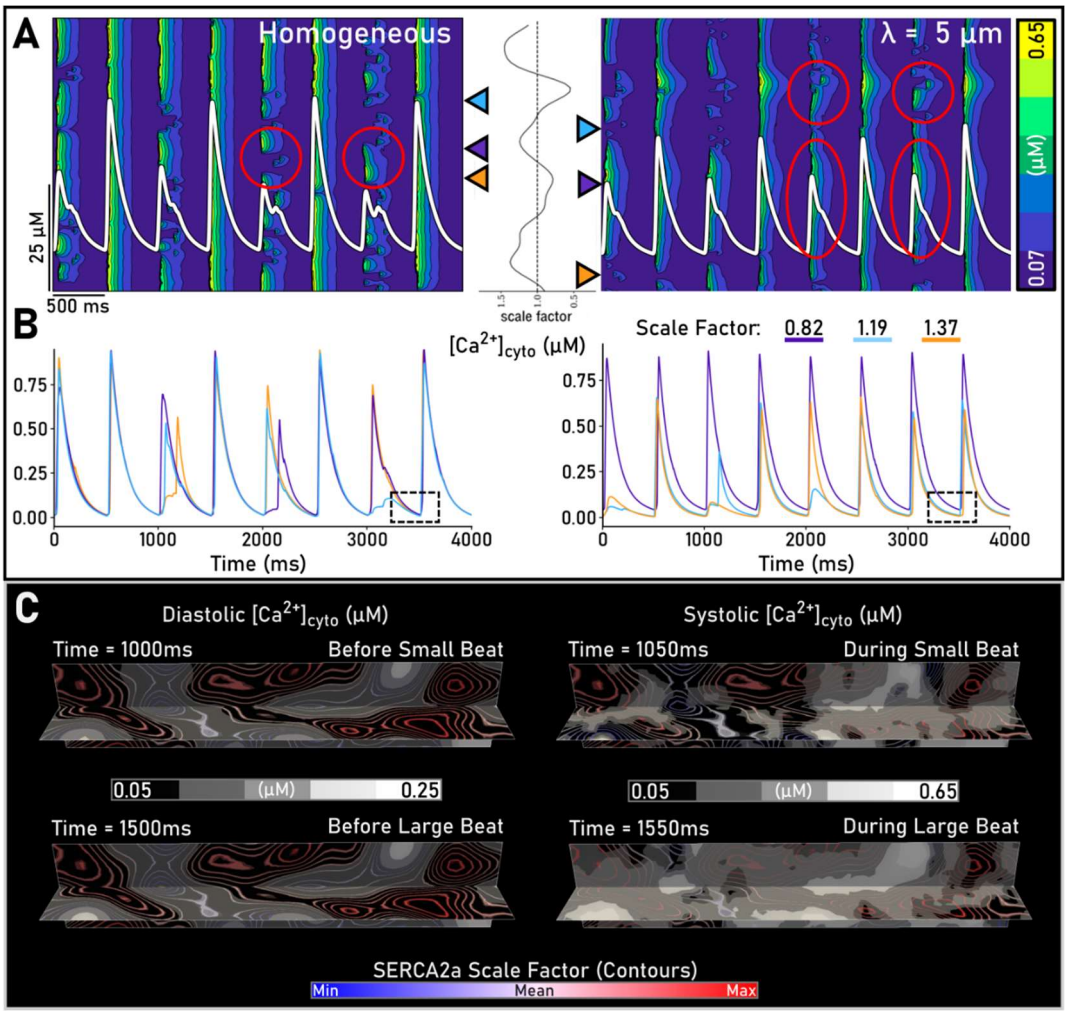

Figure 4.12 CaT alternans in heterogeneous SERCA2a expression and homogeneous control

A – Space-time plots show Ca^{2+} transient (CaT) alternans in two conditions: homogeneous (left) and heterogeneous (λ = 5 µm, right). The cell-average CaT is superimposed for context. Red-circled regions illustrate those which either show different behaviour on a beat-to-beat basis (left; homogeneous) or broadly similar behaviour (right; heterogeneous). B – Local CaT at three selected CRUs for the same two conditions; coloured triangle markers indicate the location of the CRU selected for each plot. In the heterogeneous condition, each CRU has its corresponding J_{up}^{max} scale factor, indicated by the colour key. The dotted square on each plot highlights the same inter-CRU diastolic Ca^{2+} levels in the homogeneous condition and different inter-CRU diastolic Ca^{2+} in the heterogeneous condition. C – 3D snapshots of diastolic and systolic Ca^{2+} levels mapped to an XZ- and XY-contour map of heterogeneous SERCA2a expression before and during a small and large alternan beat.

Lower SERCA2a regions have higher diastolic [Ca^{2+}] (Figure 4.12B, C), which increases the robustness of RyRs to reactivation and higher SR-Ca^{2+} content during the end phase of the CaT (Figure 4.7), yielding a greater local contribution to the CaT (Figure 4.12C). Conversely, the higher SERCA2a regions have a lower propensity of RyR reactivation due to lower diastolic and SR-$Ca^{2+,}$ which inhibits CICR. There is no significant variation in diastolic Ca^{2+} (Figure 4.12B) in the homogeneous model, nor in SR-Ca^{2+} content throughout the cell; thus, the alternan mechanism in homogeneity is not determined by local Ca^{2+}.

4.3.6 Heterogeneous SERCA2a Expression Has a Biphasic Impact on SCRE

4.3.6.1 Impact of SERCA2a heterogeneity on SCRE nucleation and propagation

Following the application of rapid pacing SR-Ca^{2+} loading protocols described in Section 4.2.5.3, SCRE activity was detected by measuring characteristics of any wave exceeding a suitable threshold in cytosolic Ca^{2+} (> 0.135 μM) over the quiescent period. Delayed after depolarisations (DADs) and triggered action potentials (TA, triggered activity) were recorded by measuring characteristics of any depolarisation in transmembrane potential, which exceeded suitable thresholds for each type of behaviour (> 1 mV deviation from resting potential for a DAD, V_m > -20 mV for TA).

In condition 1 (ISO + additional SERCA2a increase), the introduction of SERCA2a heterogeneity increased the count of DADs/TA; and hence the probability of TA occurring (Figure 4.13A). There was no observable trend between correlation length scale and the occurrence of TA, rather, the introduction of SERCA2a heterogeneity at any length scale increased the TA count relative to the homogeneous condition (Table 4.1). The mean magnitude of spontaneous CaT did not vary significantly between different length scales (Table 4.2); indicating fewer but larger SCRE in the heterogeneous models overall; however, mean CaT magnitude has significant inter-map variation both within and between length scales (Figure 4.13A)

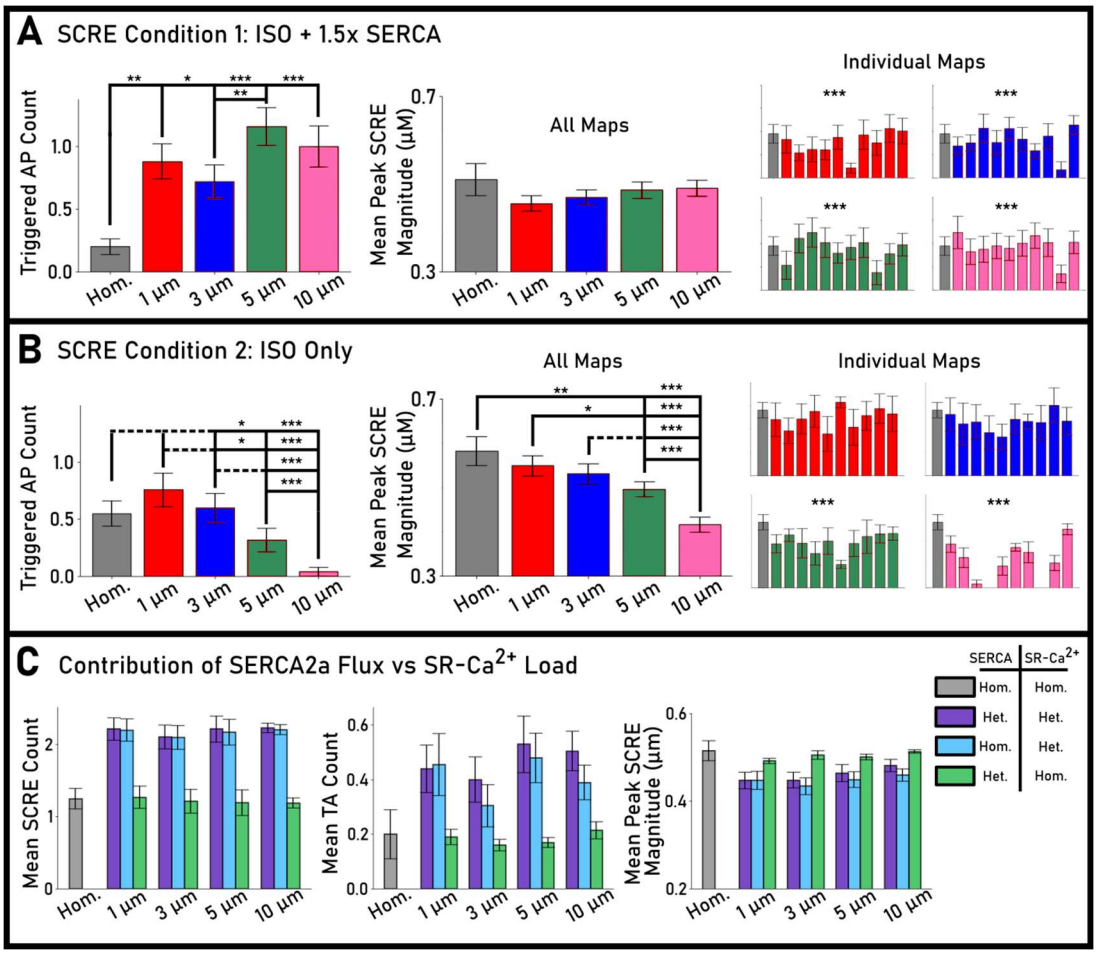

Figure 4.13 Impact of SERCA2a heterogeneity on spontaneous Ca^{2+} release events

Statistical summary of SCRE behaviour in all simulations for condition 1 (A) and condition 2 (B), showing triggered AP count (left) and mean peak SCRE CaT magnitude across all simulations (centre) and for each map (right). C – Comparison of mean SCRE count (left), TA count (centre) and SCRE magnitude (right) for different combinations of heterogeneous/homogeneous SERCA2a maps and SR-Ca^{2+} load in condition 1.

In contrast to Condition 1, in Condition 2 (ISO only; Figure 4.13B), heterogeneous SERCA2a expression significantly decreased mean peak CaT magnitude as length scale increases (Table 4.2). No significant differences were observed in the TA count for short length scales (corresponding to the control parameters, $\lambda = 1, 3$ μm), but at length scales correlating with RV-HF remodelled cells ($\lambda = 5, 10$ μm), a significant reduction in the TA count was observed.

Mean TA Count	Condition 1 (ISO + SERCA2a up)	Condition 2 (ISO Only)
Homogeneous	0.20 ± 0.06	0.55 ± 0.11
$\lambda = 1$ μm	0.44 ± 0.07 ($p < 0.05$)	0.75 ± 0.15
$\lambda = 3$ μm	0.36 ± 0.07 ($p < 0.05$)	0.59 ± 0.12
$\lambda = 5$ μm	0.58 ± 0.08 ($p < 0.01$)	0.32 ± 0.10
$\lambda = 10$ μm	0.50 ± 0.08 ($p < 0.01$)	0.05 ± 0.04

Table 4.1 Mean triggered activity (TA) count in condition 1 and condition 2.

A statistical summary of the mean numbers of spontaneously triggered action potentials recorded in the homogeneous and heterogeneous maps. Results are grouped by correlation length scale and enveloping condition. P values are in comparison with the homogeneous model in the respective condition.

Mean CaT Mag. (μM)	Condition 1 (ISO + SERCA2a up)	Condition 2 (ISO Only)
Homogeneous	0.508 ± 0.038	0.585 ± 0.033
$\lambda = 1$ μm	0.454 ± 0.019	0.550 ± 0.024
$\lambda = 3$ μm	0.465 ± 0.017	0.529 ± 0.028
$\lambda = 5$ μm	0.482 ± 0.019	0.493 ± 0.018 ($p < 0.05$)
$\lambda = 10$ μm	0.489 ± 0.018	0.413 ± 0.016 ($p < 0.01$)

Table 4.2 Mean SCRE CaT magnitude in condition 1 and condition 2

A statistical summary of the mean SCRE CaT magnitude of spontaneous Ca^{2+} release events in the homogeneous and heterogeneous maps. Results are grouped by correlation length scale and enveloping condition. P values are in comparison with the homogeneous model in the respective condition.

Heterogeneous SERCA2a expression clearly impacts the nucleation and propagation of spontaneous Ca^{2+} waves under both conditions; however, the primary mechanism underlying this behaviour is unclear. There are two likely candidate mechanisms dependent on SERCA2a heterogeneity. The first potential mechanism is through the

heterogeneous SR-Ca^{2+} uptake imposed by heterogeneous SERCA2a expression; this non-uniform efflux inherently impacts the magnitude of Ca^{2+} propagating into neighbouring CRUs. The second potential mechanism is through the heterogeneous SR-Ca^{2+} load described in Figure 4.7, as local regions of enhanced SR-Ca^{2+} load promote spontaneous Ca^{2+} sparks. These two candidate mechanisms were explored in further detail.

4.3.6.2 Relative Contributions of Heterogeneous Efflux and Heterogeneous SR-Ca^{2+} Load

To determine the primary mechanism underlying the increased incidence of TA, the relative contributions of heterogeneous efflux and SR-Ca^{2+} load must be determined. Additional simulations were performed, isolating the effects of heterogeneous efflux and SR-Ca^{2+} content in relative groups. Following rapid-pacing to steady-state to increase SR-Ca^{2+} load in the homogeneous control model and all heterogeneous SERCA2a expression maps, either: (1) heterogeneous J_{up} was imposed on a homogeneous SR-Ca^{2+} load to isolate the effects of heterogeneous Ca^{2+} efflux expression maps, or (2) homogeneous expression maps were imposed on the heterogeneous SR-Ca^{2+} loads produced through rapid-pacing of all heterogeneous conditions; thus, isolating the effects of heterogeneous SR-Ca^{2+} load. Each of these was performed in the same method as the original SCRE protocol (Section 4.2.5.3). The summary statistics of these simulations are presented in Figure 4.13C and Table 4.3.

In the isolated heterogeneous SR-Ca^{2+} load simulations (Figure 4.13C), all correlation length scales yielded a significant rise in the number of SCREs and the incidence of triggered activity compared to the isolated efflux condition; the values produced were congruent to the fully heterogeneous simulations. The mean CaT peak magnitude is significantly higher in homogeneous SR Ca^{2+} load conditions at all correlation length scales than in the heterogeneous SR Ca^{2+} load conditions, which was not observed in the previous set of maps.

	Mean SCRE Count	Mean TA Count	Mean CaT Mag. (μM)
Hom. SR Ca^{2+}, Hom. Flux (Control)	1.25 ± 0.14	0.20 ± 0.09	0.51 ± 0.02
Heterogeneous SR Ca^{2+}, Heterogeneous Flux (Heterogeneous)			
λ = 1 μm	2.22 ± 0.15	0.44 ± 0.09	0.44 ± 0.02
λ = 3 μm	2.11 ± 0.17	0.40 ± 0.08	0.44 ± 0.02
λ = 5 μm	2.22 ± 0.18	0.53 ± 0.10	0.46 ± 0.02
λ = 10 μm	2.23 ± 0.07	0.51 ± 0.07	0.48 ± 0.01
Heterogeneous SR Ca^{2+}, Homogeneous Flux (Isolated SR-Ca^{2+} Load)			
λ = 1 μm	2.20 ± 0.15	0.46 ± 0.11	0.44 ± 0.02
λ = 3 μm	2.10 ± 0.18	0.31 ± 0.07	0.43 ± 0.02
λ = 5 μm	2.17 ± 0.17	0.48 ± 0.09	0.45 ± 0.02
λ = 10 μm	2.20 ± 0.07	0.39 ± 0.06	0.46 ± 0.01
Homogeneous SR Ca^{2+}, Heterogeneous Flux (Isolated Efflux)			
λ = 1 μm	1.27 ± 0.15	0.19 ± 0.03	0.49 ± 0.01
λ = 3 μm	1.22 ± 0.17	0.16 ± 0.02	0.51 ± 0.01
λ = 5 μm	1.19 ± 0.17	0.17 ± 0.02	0.50 ± 0.01
λ = 10 μm	1.19 ± 0.07	0.22 ± 0.03	0.51 ± 0.01

Table 4.3 Summary statistics for heterogeneous efflux vs heterogeneous SR-Ca^{2+} content study

Statistical summary of mean SCRE count, TA count, and mean SCRE CaT magnitude of spontaneous Ca^{2+} release events in the homogeneous and heterogeneous conditions grouped by correlation length scale and isolated mechanism. All simulations performed under condition 1 (ISO + 1.5x SERCA2a) Values correspond to those in Fig 4.13C.

These data reveal that the heterogeneous SR-Ca^{2+} load is the primary mechanism driving the observed changes in SCRE activity, rather than the direct impact of

SERCA2a on Ca^{2+} wave propagation. This can explain the differences in the incidence of TA between conditions 1 and 2: in condition 1, increased global SERCA2a expression increases SR-Ca^{2+} uptake, loading the SR and inducing spontaneous Ca^{2+} waves which propagate throughout the cell. Without this global increase in condition 2, the net loss of SR-Ca^{2+} load under heterogeneous SERCA2a expression discussed prior inhibits the nucleation and propagation of Ca^{2+} waves and thus, reduces the magnitude and incidence of spontaneous activity.

4.3.6.3 Spatial Analysis of Ca^{2+} Spark Nucleation and Propagation

Spatial correlation between local SERCA2a expression and the dynamics of spontaneous Ca^{2+} waves were analysed using spatial intracellular Ca^{2+} and SR-Ca^{2+} concentrations at snapshots in time (Figure 4.14). The introduction of heterogeneous SERCA2a served to localise the nucleation of Ca^{2+} waves to regions of lower SERCA2a expression (Figure 4.14A). In the example illustrated, the three largest propagating Ca^{2+} waves originate from low SERCA2a regions situated between higher SERCA2a regions.

Whole-cell average (Figure 4.14B) and local (Figure 4.14C) intracellular [Ca^{2+}] and SR-Ca^{2+} content were compared for two depolarising SCRE occurring in the same simulation. At the first timestep shown (Figure 4.14C, 10 ms) during the initiation of the TA (Figure 4.14B), heterogeneous SR-Ca^{2+} load and diastolic [Ca^{2+}] levels were observed to anti-correlate with the SERCA2a expression map; i.e., the lower SERCA2a expression regions had the largest SR-Ca^{2+} load and largest diastolic [Ca^{2+}]. This observation is congruent with the previous analyses at normal pacing and alternan behaviour (Figures 4.6, 4.12). In the secondary depolarising SCRE, a similar anti-correlation between intracellular Ca^{2+} content and SERCA2a expression is observed (Figure 4.14D, 520ms). Following the propagation of the initial Ca^{2+} wave (t = 10 ms), secondary propagating Ca^{2+} sparks nucleate from both similar regions and in higher SERCA2a expression regions. Thus, the rapid SR-Ca^{2+} uptake in higher SERCA2a expression voxels is sufficient to generate spontaneous Ca^{2+} release shortly following an initial Ca^{2+} release. This phenomenon is not observed during the secondary, slower SCRE release, further supporting the conclusion that higher local SR-Ca^{2+} loads were the primary mechanism increasing the magnitude and incidence of SCRE in heterogeneity (Figure 4.13) as general whole-cell SR-Ca^{2+} content is reduced following the initial spontaneous event.

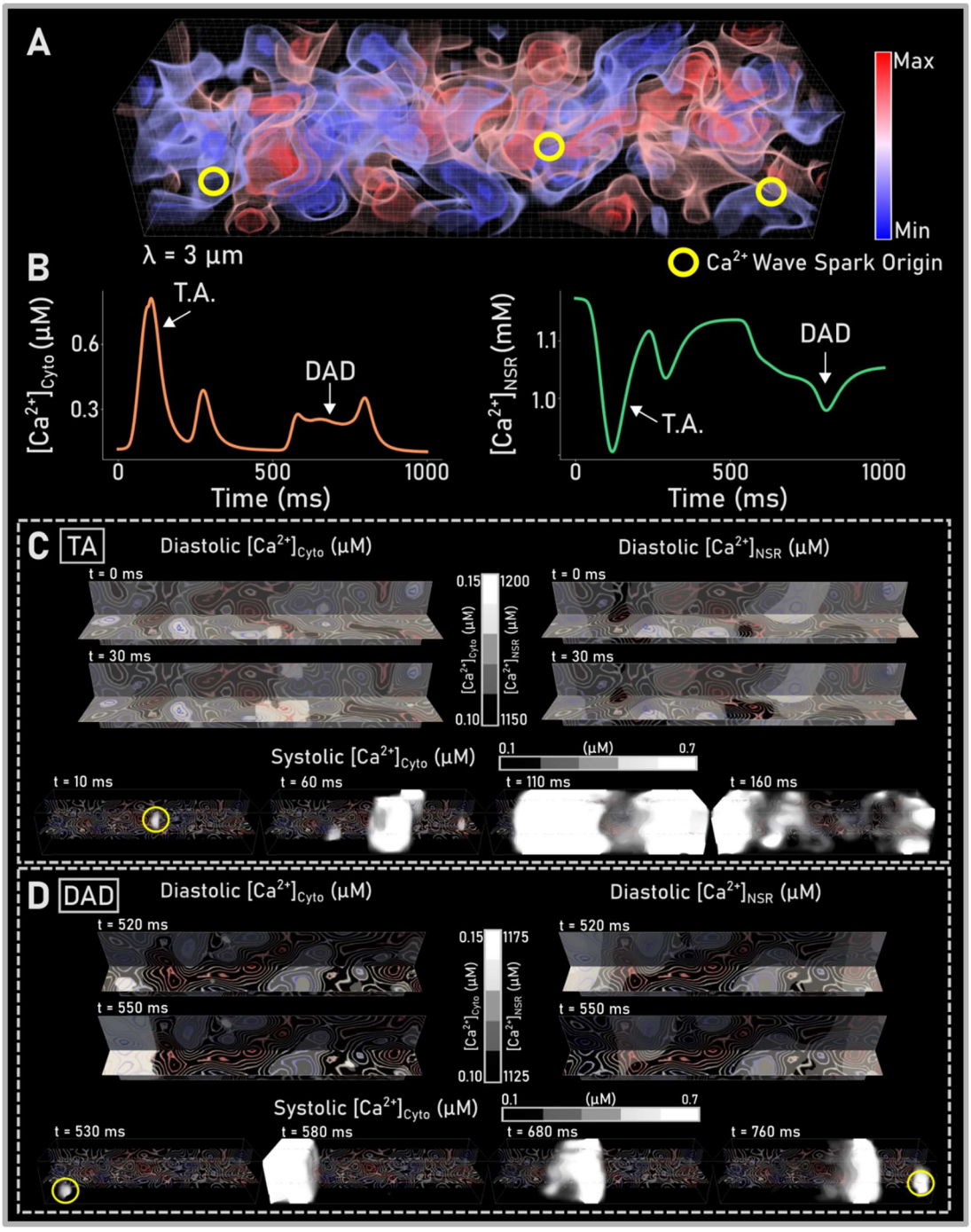

Figure 4.14 Spatial analysis of spontaneous Ca^{2+} wave nucleation

Spatial analysis of a triggered action potential (TA) and delayed after depolarisation (DAD). A – Heterogeneous SERCA2a expression map with correlation length scale, λ = 3 µm. Nucleation sites of spontaneous Ca^{2+} waves are highlighted in yellow circles. B – Whole-cell average cytosolic Ca^{2+} (left) and SR-Ca^{2+} (right). Snapshots in time of spatial intracellular Ca^{2+} and SR-Ca^{2+} scaled to diastolic (upper) and systolic (lower) ranges for TA (C) and DAD (B). Yellow circles correspond to nucleation sites highlighted in A.

4.4 Proof of Concept: Anisotropic Expression Maps

In Chapter 3, it was observed that the correlation length scale in rat ventricular cardiomyocytes is generally anisotropic (Figure 3.12). This study implemented isotropic maps only, motivated by a limited number of suitable image stacks within the dataset, and the motivation of simplicity – to study the functional implications of introducing heterogeneous SERCA2a expression without additional layers of complexity presented by anisotropy. However, this raises an important question: is the range of behaviour induced by heterogeneous SERCA2a expression sufficiently captured by isotropic length scales?

A short study into the importance and role of anisotropy in SERCA2a heterogeneity was performed to elucidate this question and identify further avenues of study.

4.4.1 Anisotropic Maps and Simulation Protocols

A series of anisotropic GRFs were generated using the toolkit developed in Chapter 3 (Figure 4.14). The introduction of anisotropy involved two new variables: anisotropic ratio (AR), the ratio of longitudinal and transversal length scales, AR = λ_1 / λ_2, and the orientation of these length scales. The orientation of length scales is denoted by type A and type B: type A ($\lambda_L < \lambda_T$) where the transversal correlation length scale is larger than the longitudinal correlation length scale ($\lambda_L < \lambda_T$) and type B ($\lambda_L > \lambda_T$) where the reverse is true. Anisotropic GRFs with mean correlation length scales of λ = 3, 5 and 10 μm and anisotropic ratios of 1.5, 2.0 and 2.5 were produced. These ARs were chosen as they encompassed the range of ARs observed in the SERCA2a-stained rat ventricular myocytes analysed in the proof-of-application study in Chapter 3 (see Section 3.5, Figure 3.12). Each AR was produced in type A and type B configurations at each length scale (Figure 4.15). Simulations were performed using the same approach as Sections 4.3 and Chapter 3 (Section 3.3, Figure 3.7). Expression maps were loaded into the MSCSF [49] and paced for 50 beats at a steady-state at normal pacing (60 bpm).

The specific longitudinal and transversal correlation length scales used to generate these maps are given in Table 4.4.

Anisotropy Ratio (AR)	1.5	2.0	2.5
Mean λ = 3 μm	λ = 2.4, 3.6	λ = 2, 4	λ = 1.725, 4.312
Mean λ = 5 μm	λ = 4, 8	λ = 3.33, 6.66	λ = 2.85, 7.15
Mean λ = 10 μm	λ = 8, 12	λ = 6.66, 13.33	λ = 5.71, 14.29

Table 4.4 Anisotropic map correlation length scales.

Pairs of correlation length scales, λ_1 and λ_2, were used to generate anisotropic GRF expression maps.

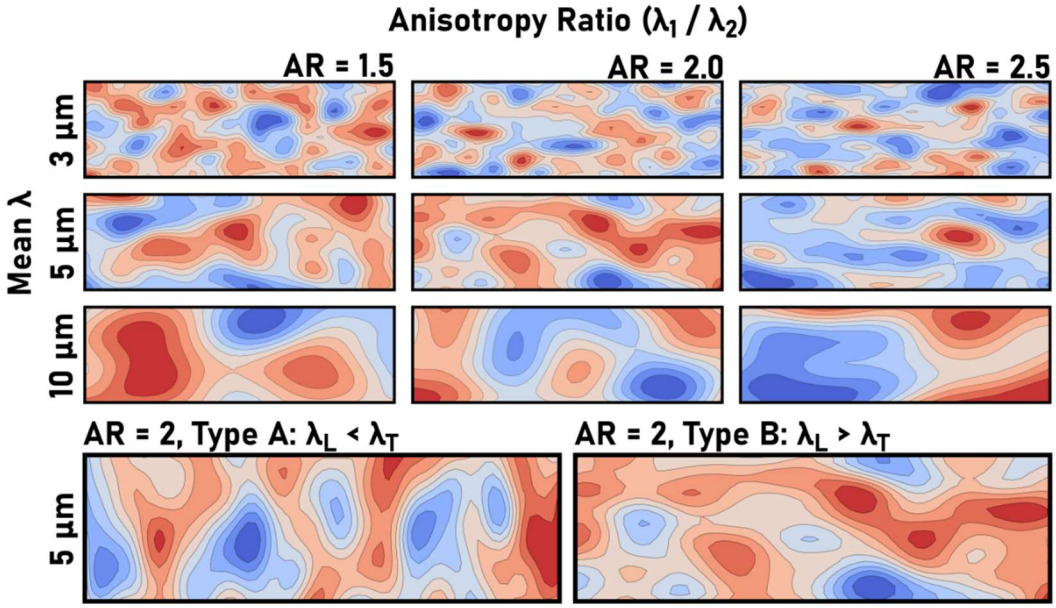

Figure 4.15 Anisotropic GRF SERCA2a expression maps

Anisotropic GRFs generated at correlation length scales of λ = 3, 5 and 10 μm at anisotropy ratios (AR) of 1.5, 2.0 and 2.5 in two configurations: type A (λL < λT) and type B (λL < λT).

4.4.2 Impact of Anisotropic SERCA2a Heterogeneity on Whole-Cell Dynamics

Under anisotropic SERCA2a heterogeneity, similar whole-cell dynamics patterns were observed under isotropic heterogeneity (Figure 4.16). At normal pacing, the transmembrane potential is largely unaffected other than minor variations in the notch potential and APD_{90} (Figure 4.16A), which can be explained by a reduction in the whole-cell CaT magnitude in heterogeneous conditions in comparison to the

homogeneous control (Figure 4.16B, D). This reduction of CaT magnitude correlates with a reduction in peak SR-Ca^{2+} load and amplitude (Figure 4.16C, F) in all heterogeneous conditions.

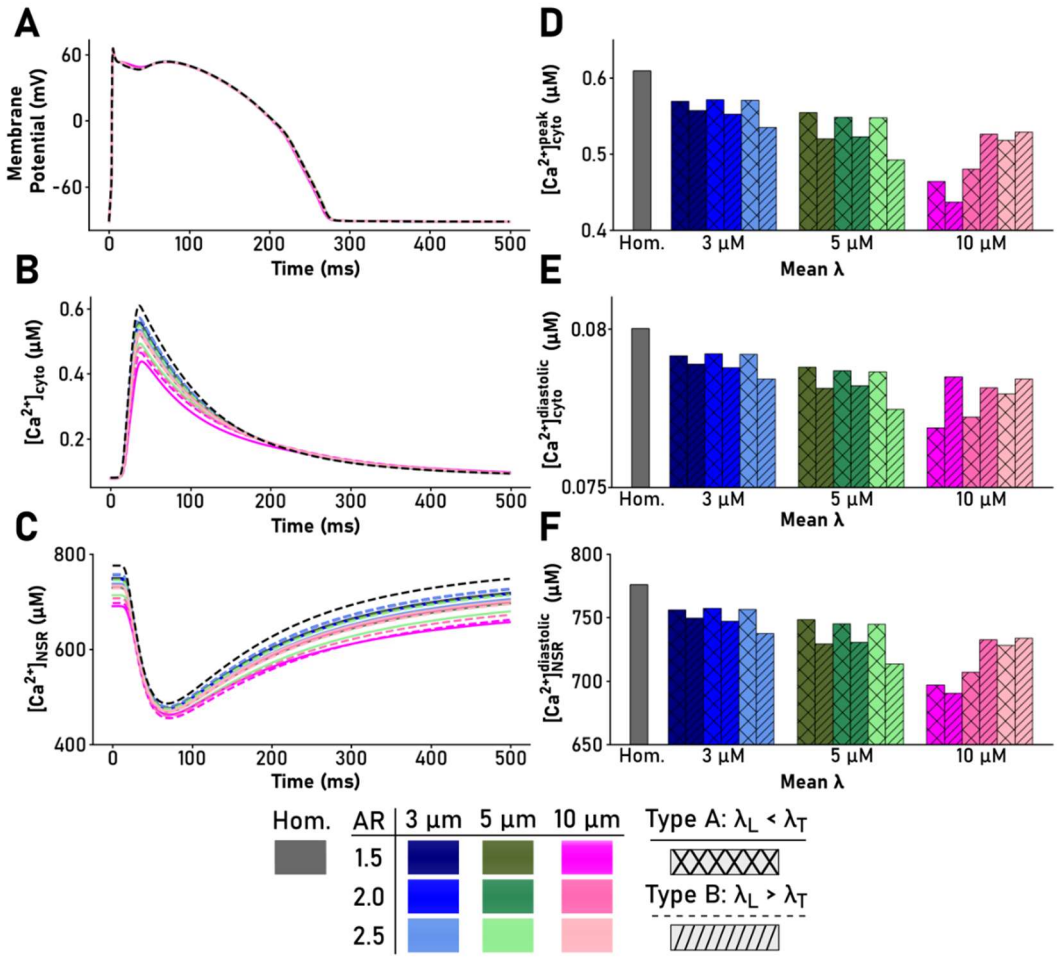

Figure 4.16 Whole-cell dynamics under anisotropic SERCA2a heterogeneity

Each panel represents cell-average values at steady state for all heterogeneous conditions and a homogeneous control (colour-coded); legend at the bottom. A – Transmembrane potential (mV), B – Cytosolic Ca^{2+} Transient (μM), C – SR-Ca^{2+} load (μM), D – Peak CaT magnitude (μM), E – Diastolic intracellular Ca^{2+} concentration (μM), F – peak diastolic SR-Ca^{2+} load (μM). Type A and type B configurations are distinguished by full or dashed lines in panels A-C and cross-hatch or diagonal-hatch patterns in panels D-F.

Congruent with expectations, differences in AR and orientation type yield differences in cell-average Ca^{2+} parameters, with differences between orientation types increasing with AR (Figure 4.16D-F). Large AR rations give a greater overlap of properties between mean correlation length scales than isotropic heterogeneity

maps at the same length scale (Figure 4.3B). In type A maps, where the longitudinal length-scale is smaller than the transversal, lower reductions in CaT magnitude, diastolic intracellular Ca^{2+} and peak SR-Ca^{2+} load are observed compared to type B maps. As AR increases, the directional correlation length scales increase and decrease, respectively, translating into whole-cell Ca^{2+} properties of shorter/longer isotropic correlation length scales. Thus, the correlation length scale along the cells longest axis is the primary determinant of whole-cell Ca^{2+} properties.

4.4.3 Impact of Anisotropic SERCA2a Heterogeneity on Ca^{2+} Transient Variability

Space-time snapshots of intracellular CaTs along the z-axis of the cell (the longitudinal axis) showcase the structure in CaT variability (Figure 4.17) correlating with SERCA2a expression along that axis. Higher and lower SERCA2a expression regions are correlated with more rapid / slower CaT decay, congruent with observations in isotropic heterogeneity (Figure 4.6). At low ARs, this CaT variability is visually similar to the variability in isotropic maps at the same mean correlation length scale and shows the most similar structure across type A and type B maps. As AR increases and the longitudinal length scale decreases/increases in type A and type B maps, respectively, the structure of CaT variability diverges from the mean correlation length scale and becomes more similar to lower / higher isotropic length scales. Thus, the relative directions of the correlation length scale become more important in determining variability in CaTs as the anisotropy ratio increases.

4.5 Discussion

4.5.1 Summary

In this chapter, the correlation length scales of SERCA2a expression heterogeneity in rat ventricular myocytes were quantified in healthy and MCT-treated RV-HF models for the first time (Figure 4.1, 4.2) using the variogram analysis protocol developed in Chapter 3. This analysis revealed that remodelling in RV-HF resulted in significantly longer correlation length scales and larger inter-cellular variability than in the control population. The image-based GRF computational modelling method developed in Chapter 3 was used to investigate the functional effects of

introducing SERCA2a expression heterogeneity at the observed correlation length scales associated with healthy and RV-HF myocytes in a human ventricular model.

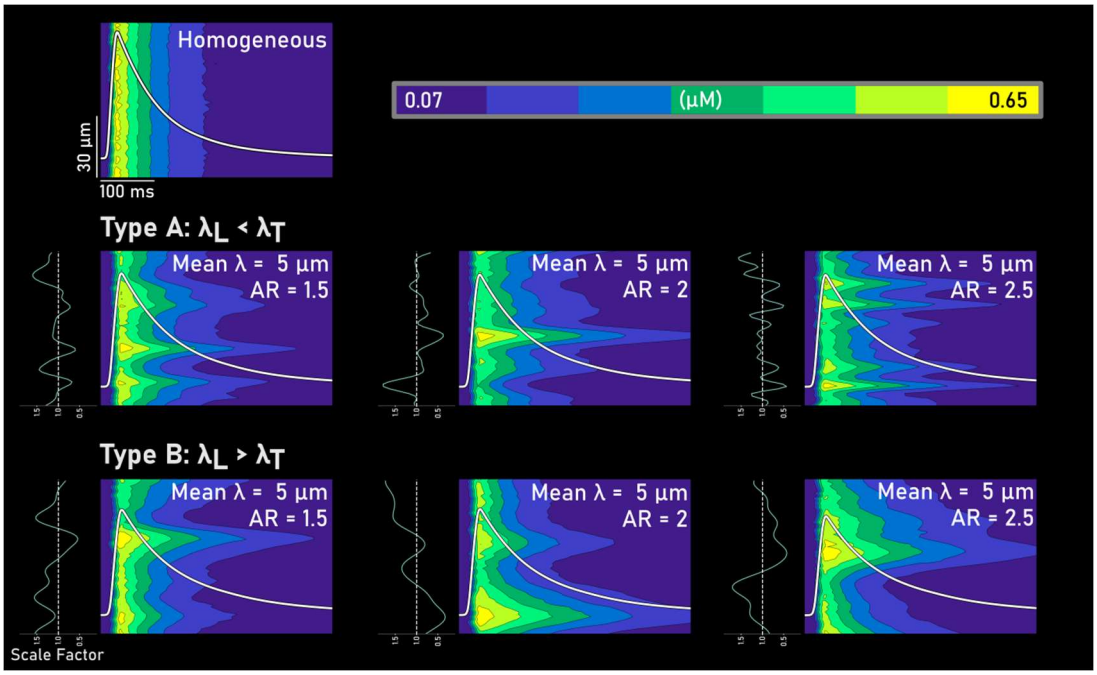

Figure 4.17 Ca^{2+} transient variability in anisotropic SERCA2a heterogeneity.

Space-time images of the Ca^{2+} transient (CaT) in the central longitudinal axis of the cell in the homogeneous, and mean λ = 5 µm conditions, corresponding to the conditions in Figure 4.15. Whole-cell average CaTs are overlayed in white. Each panel is accompanied by a plot showing the SERCA2a scale factor (left) along the same longitudinal axis.

Simulations revealed that under heterogeneous SERCA2a expression, the whole-cell CaT magnitude is reduced and more spatially disordered than in the homogeneous control model (Figures 4.3-4.5); these changes correlate with similar decreases in whole-cell SR-Ca^{2+} content. The magnitude of these changes was observed to increase as the correlation length scale increased; longer correlation length scales associated with HF-remodelling observed the largest changes and greatest inter-cellular Ca^{2+} variability. Additionally, heterogeneous diastolic [Ca^{2+}] and heterogeneous SR-Ca^{2+} load anti-correlating with SERCA2a expression were observed under the heterogeneous conditions (Figure 4.6). These cell-average changes were explained by a cell-average decrease in SERCA2a function (J_{up}), hypothesised to be due to non-linearities between maximal SR-Ca^{2+} uptake, and local Ca^{2+} parameters, and interplay with SR diffusion (Figures 4.6-4.9).

Additionally, pro-arrhythmic behaviour was analysed across a large range of heterogeneous maps against a homogeneous control in various conditions. Complex behaviours of alternans were observed: SERCA2a heterogeneity was shown to either promote or inhibit alternans depending on the environmental conditions (Figures 4.10-4.12). Rapid-pacing simulations illustrated an enhanced susceptibility for spontaneous Ca^{2+} release events and incidences of spontaneous transmembrane depolarisations in the heterogeneous models under a model of ISO and enhanced global J_{up} (Figures 4.13-4.14), demonstrated to be primarily due to heterogeneous SR-Ca^{2+} loading in rapid-pacing. A preliminary analysis of the functional effect of anisotropic heterogeneity at normal pacing revealed similar results to isotropic studies (Figures 4.15-4.17), with behaviour mostly determined by the correlation length scale along the primary axis of the cell.

This chapter discusses the contribution of observed inter-cellular variability in SERCA2a expression towards inter-cellular variability of Ca^{2+} dynamics, both during normal pacing and in pro-arrhythmic conditions.

4.5.1 Remodelling of SERCA2a in Heart Failure

Information regarding the sub-cellular distribution of SERCA2a is limited; however, existing microscopy immunofluorescence studies [303–305] are congruent that SERCA2a is most abundant around the z-lines of a cardiomyocyte and less abundant – but not absent – between these structures. Moreover, no study has previously quantified the spatial profile of SERCA2a heterogeneity in cardiomyocytes; this chapter presents the first characterisation of the correlation length scales and distribution of SERCA2a heterogeneity in rat ventricular cardiomyocytes.

A small range of correlation length scales was observed in the control group of rat ventricular cells (Figure 4.2A), implying inherent intercellular variation in the distributions of SERCA2a in healthy myocytes. Interestingly, a small significance was observed in correlation length scales between left and right control populations. Sabourin et al. (2018) [170] observed differences in the amplitudes and decay time of intracellular CaTs between rat LV and RV myocytes in control conditions; there may be a possibility that differences in SERCA2a expression may play some role in explaining those differences.

Analysis of RV-HF rat cells demonstrated a significant increase in correlation length scales and the inter-cellular variation of these length scales; thus, it can be concluded

that HF-induced remodelling in the MCT model induced significant structural changes to intracellular SERCA2a expression. Sabourin et al. (2018) [170] and Howe et al. (2021) [216] both observe remodelling of the SR in MCT models of RV-HF in rat ventricular myocytes, congruent to the observations made within this chapter.

Additionally, a significant increase in correlation length scale under RV-HF induced remodelling was observed in both LV and RV myocytes, with no significant difference between these populations. Howe et al. (2021) [216] presents a similar result in t-tubular remodelling in rat LV and RV myocytes, observing that the MCT pulmonary hypertension RV-HF model in rat significantly induces t-tubule remodelling in both the left and right ventricle. In the MCT-model of RV-HF, RV myocytes undergo hypertrophy, whereas LV myocytes experience mechanical loading and reduced filling, which leads to atrophic remodelling as a compensatory response [215, 216]. Similar impacts of RV hypertrophy and LV atrophy on the correlation length scale of SERCA2a expression were observed, despite the different remodelling mechanisms. Howe et al. (2021) [216] observed a similar loss in the regularity of junctophilin-2 in both the RV and LV under MCT-induced RV-HF, which could potentially play a role in determining the similar remodelling effects of SERCA2a expression. Additionally, Howe et al. (2021) [216] demonstrated a link between t-tubule remodelling and remodelling of the SR in both ventricles. These results reaffirm the suggestion that any research focused on developing mitigation strategies for RV-HF must consider both ventricles in these treatments; additionally, the work presented in this chapter supports evidence of SR remodelling in HF through quantification of SERCA2a heterogeneity in control and RV-HF.

4.5.3 Implications for Ca^{2+}-Induced-Ca^{2+}-Release and Contractile Performance

Heart failure is associated with a loss of CICR efficacy, underlain by reduced CICR and systolic activity [155]. The activity of SERCA2a is strongly observed to decrease in the failing human myocardium [3, 8, 15, 18, 60], correlated with reductions in SR-Ca^{2+} uptake [157, 167], higher diastolic Ca^{2+} [164, 165], and decreases in systolic function [14, 311] including contractility [296]. Decreased activity of SERCA2a is proposed to be a causal factor for reduced CICR. Studies have provided mixed conclusions regarding the expression of SERCA2a in heart

failure: some present evidence of down-regulation in SERCA2a expression [159–162, 310, 312], whereas others report no changes in HF [172, 288, 290] and some report reductions in certain cell types, but not others [313]. Even in studies using the MCT model of rat RV-HF, there are conflicting observations: Benoist et al. (2014) [130] observed a decrease in SERCA2a expression; Sabourin et al. (2018) [170] observed no change in SERCA2a expression.

This chapter puts forth that the structural remodelling of SERCA2a in HF (i.e., changes to its sub-cellular spatial profile) can, at least partially, explain the loss of CICR without any changes required to global SERCA2a expression. Correlation length scales of SERCA2a expression were significantly increased in RV-HF; longer correlation length scales yielded reductions in diastolic SR-Ca^{2+} load and the magnitude of the CaT (Figure 4.3), alongside increases in the spatial heterogeneity in the CaT (Figure 4.4). These combined effects of SERCA2a heterogeneity increased inter-cellular variability in CaT morphology, commonly associated with HF [314, 315]. The analysis in this chapter provides an alternative explanation for the loss in global SERCA2a function in RV-HF. The interplay of non-linear dampening of SR-Ca^{2+} uptake rate due to increased correlation length scales of SERCA2a expression associated with RV-HF induced remodelling and SR-coupling results in a cell-average reduction in SERCA2a activity, which reduces diastolic SR-Ca^{2+} load and CaT magnitude.

Other mechanisms have been proposed for a reduction in SR-Ca^{2+}: increased SR-Ca^{2+} leak through the RyRs [16]; increased Ca^{2+} leak through the inositol triphosphate receptors (IP3Rs) [316], observed to increase in HF and thought to contribute to cardiac remodelling [317, 318]; alterations in the expression or phosphorylation of SERCA2a regulating transmembrane micro-peptides such as phospholamban (PLB) [130, 170, 171]. Thus, it is likely that some combination of these remodelling effects, including the heterogeneous remodelling of SERCA2a and other Ca^{2+} flux channels, is responsible for the complex observations in RV-HF.

A more detailed understanding of the underlying mechanisms of this re-modelling is required to design effective treatment strategies for RV-HF patients. These pathological alterations in sub-cellular structure have clear impacts on intracellular Ca^{2+} variability (see the preliminary study in Chapter 3) and emphasise the need to develop methods of preserving or restoring the ultra-structure of the SR and t-

tubules in HF. Junctophilin-2 structurally connects the SR and t-tubules [175], playing a key role in the formation of dyadic structure, and is also down-regulated in heart failure and correlates with the loss of t-tubule structural integrity [176]. Restoration of junctophilin-2 has been observed to improve t-tubule morphology after remodelling through MCT-induced pulmonary arterial hypertension and thus may play an important role in determining future strategies in developing therapies for RV-HF [319].

4.5.4 Implications for Ca^{2+}-Transient Alternans

The importance of inter-CRU coupling and stochasticity in determining CaT alternan behaviour has been well-established in previous studies [197, 198, 200, 229, 320–322]. As introduced in Section 2.3.4, Rovetti et al. (2010) [198] proposed the '3R' theory of Ca^{2+} alternans, which formed the basis of a 'unified theory of Ca^{2+} alternans' by Qu et al. (2016) [197]. To briefly recap what has been stated previously, the 3 R's are randomness of Ca^{2+} spark activation, refractoriness of a CRU following a Ca^{2+} spark, recruitment, the process of CICR being elicited in neighbouring CRUs. The balance of these CRU properties determining the presence or absence of alternans can be described as an order-disorder phase transition [228], as local Ca^{2+} release is probabilistic, and the process of CICR is an all-or-nothing process in each CRU.

These properties underlying CaT alternans are directly and indirectly impacted by the activity of SERCA2a. Modified SERCA2a activity directly impacted inter-CRU coupling [323]: decreased SERCA2a activity gives a slower rate of SR-Ca^{2+} uptake, which leaves more Ca^{2+} available for inter-CRU diffusion in the cytosolic space and therefore increase the coupling between CRUs; thus, increasing Ca^{2+} spark recruitment. Additionally, the activity of SERCA2a influences SR-Ca^{2+} content, which influences the refractoriness of a CRU following a Ca^{2+} spark. Wan et al. (2005) observed experimentally that decreasing SERCA2a activity resulted in the promotion of CaT alternans; additionally, Benoist et al. (2012) [169] proposes that increased electrical and structural heterogeneity and dysfunctional SR-Ca^{2+} handling increases the probability of alternans. However, Nivala and Qu (2012) [324] show this relationship is more complex and increasing or decreasing SERCA may promote or inhibit alternans depending on the specific state of the whole system. The simulations analysed in this chapter support this complexity (Figure 4.10).

Complex behaviours of CaT alternans under SERCA2a heterogeneity were observed in this chapter (Figures 4.10-4.12). The simulation results demonstrate the sensitivity of alternan behaviours (emergence, inhibition, variability) to enveloping model conditions, revealing that introducing heterogeneity can critically shift the cell in and out of the parameter phase space in which alternans occur. Due to the critical dependence on over-arching model conditions, it is unclear whether heterogeneous SERCA2a expression generally acts to be arrhythmogenic by shifting HF cells into the pro-alternan phase space or protective by shifting HF cells out of the pro-alternan phase space (Figures 4.10, 4.11). SERCA2a expression heterogeneity may indeed be both arrhythmogenic and protective due to increased inter-cellular variability, and its relative impact on CaT alternan behaviour may shift throughout the progression of HF.

Introducing SERCA2a heterogeneity presents a clear deviation from the 3Rs theory of alternans. Heterogeneous SERCA2a expression in different cell regions was observed to constrain the random spatial nature of CaT alternans – the regions that activated or did not activate during the smaller beat were largely consistent throughout (Figure 4.12). This localisation leads to a largely similar spatial pattern of the CaT on subsequent beats, contrary to what is observed in homogeneous cells. The analysis revealed that this more regularly structured behaviour was determined by local intracellular Ca^{2+} and SR-$Ca^{2+,}$ which does not vary under homogeneous conditions; thus, this behaviour is specific to heterogeneous models. Colman et al. (2018) [49] observed a similar phenomenon using a super-resolution Ca^{2+} handling model with realistic sub-cellular structures. In that study, specific features of the cellular geometry, such as dyadic cleft cluster proximity and the relative presence of the SR or T-system, reduced the randomness in which regions of the cell activate on subsequent large or small beats; thus, reducing the spatial phase variation.

Song et al. (2018) [76] presents a similar computational investigation into the impact of heterogeneous t-tubule structure and t-tubule remodelling in HF using qualitative t-tubule structures. This study demonstrates that reduced t-tubule density may cause failing ventricular myocytes to become more susceptible to CaT alternans and Ca^{2+} waves; however, a heterogeneous t-tubular structure was observed to potentially reduce the likelihood of CaT alternans. Simultaneous investigation of SERCA2a and t-tubule distribution was outside of the scope of this chapter, but these results do support one of the major research themes in this thesis: how does heterogeneous

sub-cellular structure interact to influence Ca^{2+} variability? A comprehensive understanding of how sub-cellular heterogeneity is remodelled in heart failure and the co-localisation of these heterogeneities may be crucial in understanding CaT alternans in HF progression.

Upregulation of SERCA2a has been observed to ameliorate cellular alternans in HF [325, 326] and is a common therapeutic target for improving cardiac function in cell models of the failing human myocardium [301, 302]. This chapter elucidates the sensitivity of alternan phase-space to heterogeneous SERCA2a expression observed in healthy and HF-remodelled cardiomyocytes and may inform further studies into SERCA2a upregulation as a treatment for stabilising the heart in HF. It will be important to determine the sensitivity of the alternan phase-space to sub-cellular heterogeneity in the expression of other Ca^{2+} handling proteins and establish whether this remodelling of SERCA2a heterogeneity (and indeed, that of other proteins) precedes, follows or is concomitant with the remodelling of whole-cell channel expression in HF.

4.5.5 Implications for Spontaneous Arrhythmia Triggers

Heart failure is generally associated with an increased propensity for spontaneous triggers [327, 328]. SCREs large enough to produce a TA (see Section 2.3.4 for more information on this phenomenon, and re-entry) have been shown *in silico* to promote re-entry and focal excitations in tissue [50]. Liu et al. (2015) [329] and Campos et al. (2017) [330] have both demonstrated a mechanism by which SCRE-induced unidirectional excitation conduction block may possibly degrade into re-entry.

Venetucci et al. (2007) [331] discuss two mechanisms by which an increased SERCA2a expression may affect the incidence of SCRE; increased SR-Ca^{2+} content, which is associated with an increased incidence of SCRE directly [332]; more difficult Ca^{2+} propagation due to increased SR-Ca^{2+} uptake dampening the Ca^{2+} wavefront. Similarly, O'Neill et al. (2004) [333] observe a similar result experimentally with inhibited SERCA2a activity correlating with an increased incidence of spontaneous Ca^{2+} wave propagation. Sato et al. (2021) [334] also discusses the above pro- and anti-arrhythmic effects of SERCA2a expression on Ca^{2+} wave propagation; upregulation of SERCA2a was observed to enhance global SR-Ca^{2+} load, which increased the incidence and driving force of spontaneous Ca^{2+}

release but simultaneously accelerated local cytosolic [Ca^{2+}] decay which opposes Ca^{2+} wave propagation.

The results of this chapter demonstrate a whole-cell decrease in SR-Ca^{2+} content under heterogeneous but maintained cell-average SERCA2a expression, with local regions of enhanced SR-Ca^{2+} load corresponding with lower SERCA2a expression and vice versa. Whether SERCA2a heterogeneity itself may increase the probability of TA to manifest is unclear from this analysis (Figure 4.13), as the emergence of TA was critically dependent on the extent of SERCA2a up-regulation used to promote SR-Ca^{2+} loading: above a threshold, increased correlation length scale is associated with an increase in the appearance of SCRE and TA; below this threshold, an increase in length scale inhibited the emergence of TA. In either case, the inter-cellular variability in the emergence of TA was substantially increased in all heterogeneous conditions.

To the authors' knowledge, there are no studies focused on how heterogeneous SERCA2a distribution influences SCRE mechanisms; however, MacQuaide et al. (2015) [335] demonstrates a major impact of RyR distributions on the incidence and size of SCRE. Marchena and Echebarria (2018) [336] further demonstrate this *in silico*, observing a marked increase in Ca^{2+} spark frequency when RyR clusters are distributed in larger (more populous) clusters. Additionally, Galice et al. (2018) [337] observes that under heterogeneous RyR distributions, Ca^{2+} spark nucleation is localised to regions of higher RyR expression, which is congruent with the findings of MacQuaide et al. (2015) and Marchena and Echebarria (2018). In the present study, simulations demonstrated that Ca^{2+} nucleation was localised under SERCA2a heterogeneity to regions of lower SERCA2a expression (Figure 4.15) correlating with regions of enhanced SR-Ca^{2+} loading and diastolic [Ca^{2+}]. Sutanto et al. (2018) [258] also observed localisation of Ca^{2+} sparks to regions of higher RyR expression. In this study, Suntanto et al. (2018) observe that increases in RyR heterogeneity are correlated with an increased incidence of SCRE with a reduced total magnitude. There is no such clear observation within the present chapter; however, it is observed that under an ISO model with enhanced global SERCA2a, the introduction of SERCA2a heterogeneity correlates with an increase in the mean incidence of SCRE and an inconsistent reduction in mean peak magnitude (Figure 4.14C). Further investigation is required to correlate how respective heterogeneous expressions in RyR clusters and SERCA2a (and indeed, other Ca^{2+} channels)

interact to unravel the relative contributions of each heterogeneity in determining changes in whole-cell Ca^{2+} handling in both healthy and in pathology.

A reduction in I_{K1} is observed in HF and promotes the emergence of spontaneous action potentials from underlying SCRE [338] through increasing the diastolic membrane potential. However, no changes to ion-channel expression or activity, and instead isolated the impact of changes to sub-cellular heterogeneity in SERCA2a expression were implemented in this chapter. HF conditions, such as fibrosis and reduced I_{K1}, may significantly reduce the minimal substrate required for cellular TA to manifest in tissue, and thus the increased presence of individual cells, which are pro-TA, could underlie increased arrhythmia triggers in HF. Further investigation is required at the systems level to determine whether an increase in SERCA2a heterogeneity in HF contributes to increased arrhythmia triggers.

4.5.6 The Importance of Anisotropy

A short study into the functional effects of anisotropic heterogeneity on cell-average dynamics at normal pacing suggests that the longitudinal directional correlation length scale – i.e., the correlation length scale along the cell's longest axis, is the primary determinant for modifying Ca^{2+} handling properties. As the anisotropy ratio increases, the specific orientation of the cell's anisotropy becomes more important due to the cell's dimensions and correlation in those directions. Generally, whole-cell behaviour observed at normal pacing in anisotropic heterogeneity (cell-average properties and CaT variation) is observed in the range of isotropic length scales analysed in Section 4.3, which is congruent with the observation that longitudinal correlation length scale plays the largest role in determining whole-cell behaviour. However, this study was only performed in normal pacing, and anisotropy may play a larger role in determining intracellular Ca^{2+} dynamics under rapid pacing and pro-arrhythmogenic conditions. A comprehensive investigation of anisotropic SERCA2a expression or a more focused study using a selection of GRFs generated directly from experimentally quantified spatial variation parameters is a natural progression from the present chapter.

4.5.7 Limitations

4.5.7.1 Image Analysis Method

The limitations present within the variogram fitting method and toolkit used within this chapter are discussed in detail in Section 3.6.5; in this subsection, only the limitations of using this method pertaining to the current study are discussed.

Microscopy datasets carry inherent spatial variation due to experimental and environmental factors that may contribute to estimations of correlation length scales. Quality of staining, differences in imaging conditions and imaging modality may all result in additional sources of variation; thus, in order to control for the impact of some of these factors, only confocal microscopy images produced at the University of Leeds by the authors of the respective manuscript (Holmes et al. (2021) [2]) Additionally, the down-sampling process will partially mitigate this variation by averaging the dataset over a resolution 10-50 times larger than the original image. To ensure reliable comparisons between cells, all image data were down-sampled to the same spatial resolution (1 μm^2).

Fluorescence images for quantitative microscopy often include some offset, defined as some threshold of expression below which all values are equal to 0 – an inherent quality of the microscope itself [339]. This offset will not affect the heterogeneous expression of SERCA2a within the image but may present minor issues in correlation-type analyses, which were not corrected for in this analysis.

Due to differences in imaging quality, cell morphology and the depth of the datasets used in this analysis, many cells had insufficient z-axis information to provide a reliable variogram fitting procedure; thus, all available data was condensed into a 2D image (see Section 3.6.5). Longitudinal-transverse anisotropy is likely a feature in sub-cellular heterogeneous expression at the micron scale, and this may contribute to the large error sizes in the cells with a higher correlation length scale.

An insufficient number of rat ventricular myocytes were suitably large enough post-processing for a directional analysis. As a whole, the population of directional correlation length scales had too large an uncertainty and were excluded from the analysis; thus, this study only investigates the isotropic length scale. To ensure reliable values were obtained from this analysis, each cell was analysed three times using three different crops – each requiring 50 successful variogram fits using a

range of suitable binning parameters for each dataset (Fig 4.2B). The final values are a statistical mean and standard error for each cell.

The present study analysed myocytes only from healthy and RV-HF conditions, indicating that sub-cellular heterogeneity in SERCA2a is a remodelled feature in HF. These observations correlate with previous studies which discuss sub-cellular remodelling of t-tubules and the SR. Hence, it will be important to establish if this feature is present in other forms of HF (e.g., LV-HF or HF with preserved ejection fraction) and other pro-arrhythmogenic conditions, such as atrial fibrillation and ageing.

4.5.7.2 Computational Modelling

The limitations of the image-based GRF computational modelling method are discussed in detail in Chapter 3, Section 3.6.5. This subsection discusses the limitations of the modelling method and the assumptions and choices made concerning the present chapter only.

The model itself is an idealised representation of a ventricular myocyte with a persistent SR and sarcolemmal membrane, including the t-tubule, present within every voxel. This is not physiologically representative; thus, it may impact the results of some spatial dynamics within the model. This idealised model was selected to incorporate sufficient detail to meaningfully study the impact of SERCA2a heterogeneity while remaining computationally feasible to perform a comprehensive, large-scale study. Improvements could be made to this by mapping the presence of the sarcolemma and SR throughout a cardiomyocyte using imaging data; however, obtaining a congruent set of spatial information for a single myocyte is unfeasible, and there is significant inter-cellular variation in sub-cellular structure in control and HF-remodelling. Perhaps a qualitative approach could be taken by inferring these sub-structures using a limited dataset; however, this would introduce additional sources of uncertainty.

Four correlation length scales (λ = 1, 3, 5 and 10 μm) were decided upon for the computational study. This selection of correlation length scales represents the full range of heterogeneity observed in the image analysis study; expansive enough to investigate correlation length scales observed in both the control and MCT populations. Increasing the scale of this study to include the full range of integer

length scales may have provided a smoother gradient of behaviour in length-scale. However, due to this project's scope and computational tractability, it was determined that the range of length scales used were sufficient to reveal the full range of emergent behaviour.

SERCA2a heterogeneity of expression was measured in rat ventricular cardiomyocytes, and then the range of correlation length scales observed in these myocytes was implemented into a human ventricular cardiomyocyte model. Therefore, there is no certainty that similar correlation length scales would be present in humans due to inter-species differences, and this presents a limitation in translating the results of this study directly to human physiology. However, that is not to say that rat models are not useful for studying human electrophysiology; one advantage is that SR-dependent Ca^{2+} handling in rat ventricular myocytes makes it a sensitive model for studying the SR-dependent arrhythmia mechanisms discussed in this chapter [94]. The primary motivations for using a simplified version of the O'Hara-Rudy human ventricular model [46] were to (i) use a well-documented model such that any model-specific behaviours could be identified and (ii) the pre-existing implementation of this model in the MSCSF [50, 237].

The impact of SERCA2a heterogeneity was isolated in this study, which means that the full systems perspective is missed somewhat. It will be important that future studies look at combinations of SERCA2a heterogeneity with heterogeneous expression in other sub-cellular Ca^{2+} handling transporters such as NCX, LTCCs and RyRs. Combinations of these heterogeneities will undoubtedly influence local flux balances, SR-Ca^{2+} loading and Ca^{2+} variabilities (as observed in the preliminary study in Chapter 3). In addition to heterogeneity, incorporating observations of global remodelling of Ca^{2+}-handling and ion-current channel expression will provide a more physiologically complete model of cardiomyocytes in health and pathology. Furthermore, local SERCA2a activity is likely to be influenced by SERCA2a:PLB and the relative proportions of (non-)phosphorylated PLB [130, 170, 171], which was not investigated in this study as the motivation was to isolate the effects of SERCA2a heterogeneity.

Translating the impact of inter-cellular variability in SERCA2a expression into tissue models would provide more meaningful insights into the impact of SERCA2a

heterogeneity and increased inter-cellular Ca^{2+} variability on the emergence of cardiac arrhythmias.

4.6 Conclusions

This chapter quantifies the remodelling of SERCA2a sub-cellular heterogeneity in RV-HF in rat ventricular myocytes. This HF-associated remodelling is demonstrated to increase correlation length scale and inter-cellular variability compared to a control population. An image-based simulation approach demonstrated that heterogeneous SERCA2a expression contributes to reduced CICR under normal and rapid pacing. Heterogeneous SERCA2a was also observed to (potentially critically) modulate the emergence of pro-arrhythmic cellular phenomena. This chapter establishes that the spatial profile of SERCA2a in the sub-cellular volume, and potentially that of other Ca^{2+} handling proteins, may be remodelled in cardiovascular disease and contribute to the observed pathophysiological function.

5

A Novel, Congruent Single Cell Rabbit Atrial Electrophysiology Model to Study Ca^{2+} Variability

5.1 Introduction

AF is the most common, clinically relevant cardiac arrhythmia globally and is associated with a significant morbidity risk [7, 192]. Compounding this problem further is the relationship between AF and HF; patients with HF frequently develop AF, and AF is associated with a worsening or onset of HF (see Section 2.3 for further description of AF and HF). The rabbit atrial model is one of the most studied animal models for human heart physiology and pathophysiology [340], offering an attractive compromise between cost, similarity to human atrial electrophysiology, and the practicality of performing experiments quickly and efficiently (see Section 2.5.1 for more details). In addition to prominent similarities in electrophysiology to human models (presence of a strong I_{to} current [210], similar repolarisation dynamics [209, 341], similar SERCA2a and NCX function [26, 208]), the relative sizes of excitation wavelength and the size of the heart make rabbit hearts very suitable for studying human arrhythmias [212]. There exists a plethora of well-established models of generating HF [26] and inducing tachycardia and AF [342–346] in the rabbit atrium, providing a strong foundation for future experimental studies into rabbit atrial, and thus human atrial, pathophysiology.

The mechanisms underlying AF's rapid and irregular excitation inherently depend on the ion currents that form the AP and the non-linear interactions between these ion currents and their environment [43]. Thus, it is critical to fully characterise the dynamics of these ion currents to elucidate these mechanisms, and furthermore, how these ion current relationships influence the impact of pharmacological or surgical interventions. Despite the vast adoption of the rabbit atrial model in experimental and clinical fields and its role in studying AF, there are few sources of data parameterising these currents; moreover, contemporary computational models of rabbit atrial electrophysiology do not incorporate all these available data. As a result, the available contemporary computational models are limited in their translational capacity.

5.1.1 Existing Computational Models

The limited number of published computational rabbit atrial models can be traced through a single lineage throughout the last few decades, with subsequent models making slight variations.

In 1987 the first mathematical model of atrial-specific electrophysiology was developed by Hilgemann and Noble (1987) [249], derived from a general mammalian cardiomyocyte model developed by Di Francesco and Noble (1985) [347]. This model simulated Ca^{2+} flux through LTCCs, SR-Ca^{2+} release and Ca^{2+} dependent inactivation of I_{CaL} and activation of I_{NCX} to integrate experimental observations in rabbit atrial muscle [348]. The Hilgemann-Noble model used rabbit-specific data where possible [249], but due to experimental limitations at the time, these data were obtained from multi-cellular preparations and different tissues from different species such as guinea pigs [36]. The model was more general for small mammalian myocytes, producing a triangular AP similar to observations of rodent electrophysiology [349].

Lindblad et al. (1996) developed from the Hilgemann-Noble model to include rabbit atrial-specific electrophysiology data where possible, and in 1996 published a rabbit-atrial specific mathematical model [36], which incorporated rabbit atrial-specific experimental data for I_{Na}, I_{to}, I_{Kr}, I_{K1} and I_{NCX}, and dynamic Ca^{2+} buffering from the Giles laboratory group [350–355]. The sub-cellular structure introduced in this model, with uptake and release SR compartments, bulk cytosolic space, dynamic buffering and non-permeable regions analogous to mitochondria and nuclei, is present within most non-spatial Ca^{2+} handling models developed since. Despite these improvements, however, ionic current data still included elements from rabbit ventricular, SA and AV node studies – and in some instances where no other data was available, from other species (guinea pig, canine, calf and frog) [36]. Due to a lack of available Ca^{2+} handling data in rabbit atrial myocytes when the Lindblad model was developed, the model could only qualitatively simulate CaTs. The CaTs produced by the Lindblad model, and those models which inherited its Ca^{2+} handling system, have very rapid spike morphologies, with a very rapid decay similar to those seen in mice [356–358] which significantly differ from those recently measured in the Workman Lab [359]. These features pose a significant limitation in applying the Lindblad model to studying Ca^{2+} variability.

In 2009, Aslanidi et al. published an updated rabbit model, which significantly improved the Lindblad model [37, 242, 242], including a family of rabbit atrial electrophysiology models - incorporating electrical heterogeneity between atrial cell types. These updates aimed to modify the Lindblad model to closer match AP biomarkers quantified by Yamashita et al. (1995) [247] using new formulations of I_{K1} [247], I_{Na} [247, 248] and I_{CaL} [247, 360] derived from conductance and kinetics data from Yamashita et al. (1995) [247] and Ko et al. (2005) [360] Formulations for I_{to} were maintained from the Lindblad et al. (1996) model [36], which used rabbit atrial and ventricular myocyte data, with the maximal conductance decreased to more closely match experimental data from Yamashita et al. (1995) [247]. I_{sus} was modelled as a background current, and its conductance chosen empirically to adjust the APD in the model. Other currents present in the Aslanidi et al. (2009) model [242] were incorporated as presented in the Lindblad et al. (1996) model [36].

In 2020, Vagos et al. (2020) published a study integrating the Aslanidi AP model with a 2D spatio-temporal Ca^{2+} handling model developed by Jordi Heijman in Voigt et al. (2014) [361]. Vagos produced a new control model of the rabbit atrial AP using updated conductance parameters reverse-engineered from experimental AP and CaT data and then varied these conductances to produce a population of models which matched observed AP biomarkers in a wide range of published literature [36, 242, 247, 346, 359, 362–366]. This population approach provided a framework used to study tachycardia-induced remodelling in the rabbit atria [367].

5.1.2 Motivation for a Congruent Model

A significant portion of the ion current dynamics and conductance in the models described are derived from heterogeneous data sources or reverse-engineered from AP and CaT biomarkers observations. Consequently, these approaches have more potential sources of error and a greater reliance on unknown or reverse-engineered parameters, ultimately reducing their translational capacity to experiment and confidence in any emergent behaviours observed in these models. In addition, there exists a wide variability of data within published literature: range of variability in experimental conditions, specific reagents used or protocols employed to quantify ionic channel conductance, kinetics and their relative contributions to the AP or CaT. Differences in these experimental protocols may result in changes in observed

physiology, thus presenting uncertainty in combining mathematical descriptions of these ion channels from different laboratories.

The observed large variability in electrophysiological parameters and ion current kinetics may represent the variability inherent in normal physiology. However, this also provides a technical limitation in validating the models against experimental datasets from different sources – distinguishing the impacts of variability in experimental protocols and model-specific behaviours concomitantly is a major challenge. To avoid model-specific conclusions, research approaches often utilise multiple models. Ideally, mathematical models would be constructed and validated using experimental data from a single, congruent source to obtain a more concise understanding of where models and experiments differ, such as done in human atrial myocytes by Colman et al. (2018) [43]. Such models may be less powerful for general studies and insight but offer many advantages: greater confidence in explanations of emergent behaviours, greater confidence in validation and explanations of features observed under the same experimental conditions on which the model is based.

The factors underlying these differences are important to understand the relative roles and importance of ion currents, underlying kinetics, and variabilities in intracellular Ca^{2+} handling. Furthermore, validating a congruent model against experimental data from the same source provides valuable insight into rabbit atrial electrophysiology required to dissect the mechanistic impact of these interventions. Finally, a congruent validation protocol reveals what is missing within the model, which may motivate future elucidation through experiment.

5.1.3 Aims

This chapter aims to address the above through the development of a novel computational rabbit atrial myocyte model using recent rabbit left atrial data quantified by the Workman laboratory [33, 359, 368–371]. Thus, the objectives of this chapter are:

1. To produce a novel, lab-specific model of rabbit left atrial electrophysiology using experimental data from a single, congruent data source for development and validation.

2. To identify and discuss discrepancies between our model's predictions and experiment to reveal gaps in our understanding of rabbit atrial electrophysiology.
3. To conduct a preliminary study of Ca^{2+} variability as a result of modifying the conductance and kinetics of major ion currents and Ca^{2+} handling parameters.

5.2 Model Development

In this chapter, novel formulations were developed for primary ion currents underlying rabbit atrial AP (I_{to}, I_{CaL}, I_{K1} and I_{Na}) and characterised over many years by Workman Laboratory at the University of Glasgow [33, 359, 368–371]. These formulations were integrated with the Grandi-Bers human atrial Ca^{2+} handling model [44] (introduced in Section 2.8.4); the motivation underlying this choice is primarily due to the shortcomings of the Lindblad et al. (1996) [36] Ca^{2+} model in reproducing a physiological CaT, and the strength of the Grandi-Bers Ca^{2+} model in that regard. Where appropriate, rabbit-atrial specific formulations from the Aslanidi et al. (2009) rabbit atrial model [37, 242] (see Section 2.8.3) replaced the Grandi-Bers formulations. The Workman lab dataset provides conductance and kinetic information to produce updated formulations for the major ionic currents (I_{Na}, I_{CaL}, I_{K1}, I_{to}) from a congruent data source, ensuring these are proportionally correct. Additionally, Kettlewell et al. (2019) published the only absolute values of CaT magnitude under control and under pharmacological intervention [359], allowing for quantitative validation of intracellular Ca^{2+} handling.

5.2.1 Workman Laboratory Data

Experimental data and characterisation of ion channel conductance and kinetics were obtained from the Workman Laboratory and used with permission. A summary of the data obtained from each publication and unpublished works is detailed below. Information on experimental conditions, solutions, protocols and buffering can be found in the following publications:

Workman et al. (2012) [33]
Detailed voltage-dependence of steady-state I_{to} activation and inactivation, I_{to} kinetics of activation and deactivation, and I_{to} conductance; Ionic current

formulations from dynamic clamp data; APD, ERP and V_{max} data; Pharmacological I_{to} blocking intervention data (4-aminopyridine, 4-AP).

Kettlewell et al. (2019) [359]
Detailed voltage-dependence of steady-state I_{CaL} activation and inactivation, I_{CaL} kinetics of activation and inactivation and current-voltage dependence. Ionic current formulations from dynamic-clamp data; quantification of intracellular CaT.

Giommi, PhD Thesis (2021) [371]
Ba^{2+}-sensitive ramp currents for I_{K1} current-voltage relationships.

Priyanka Saxena, Workman Lab, Unpublished I_{Na} Data
An appropriate surrogate for I_{Na} data (as it cannot be measured under physiological conditions: Relationship between dV/dT_{max} and RMP, AP phase 0 traces.

In addition to the above, the Workman Laboratory has also provided the following data from other publications for validation:

Workman et al. (1999) [368]
Measurements of RMP; AP morphologies.

Workman et al. (2000) [369]
Pharmacological I_{CaL} blocking intervention data (nifedipine)

Kettlewell et al. (2013) [370]
Quantification of: CaT decay; Intracellular Ca^{2+} flux.

Only experimental steady-state activation and inactivate data and activation, and inactivation kinetics were used to fit these novel formulations, with only minor adjustments made for stabilisation purposes. Available data on AP morphology, AP biomarkers, quantification of intra-cellular CaTs and flux, or pharmacological intervention data were used only to validate the model. All formulations, unless stated otherwise, were fitted using a least-squares optimisation algorithm implemented in SciPy (Python ver. 3.6) [265] and then manually adjusted where appropriate.

5.2.2 Electrophysiology Model

The electrophysiological model developed (Figure 5.1) tracks 26 state variables and includes descriptions of 12 membrane currents: 9 passive ion channels, two ionic

pumps and one ionic exchanger. Thus, the total ionic current for this model, I_{tot}, is given by:

$$I_{tot} = I_{Na} + I_{CaL} + I_{to} + I_{K1} + I_{NCX} + I_{NaK} + I_{CaP} + I_{ClCa} + I_{Nab} + I_{Cab} + I_{Kb} + I_{Clb} \quad (5.1)$$

Where I_x is the current carried by the ion channel, pump or exchanger, x. The details and maximal conductance of these ionic currents are presented in Table 5.1. The above membrane currents are integrated with the Grandi-Bers human atrial Ca^{2+} handling model [44]. The cell is separated into four compartments, in order of size these are: the bulk cytosolic space (65% of cell volume); the SR (3.5%); the sarcolemmal space (2%); and the junctional cleft (0.077%); calculated using the proportion of junctional (11%) to non-junctional (89%) cell membrane. The remainder of the cell is considered as impermeable space occupied by the mitochondria and nucleus.

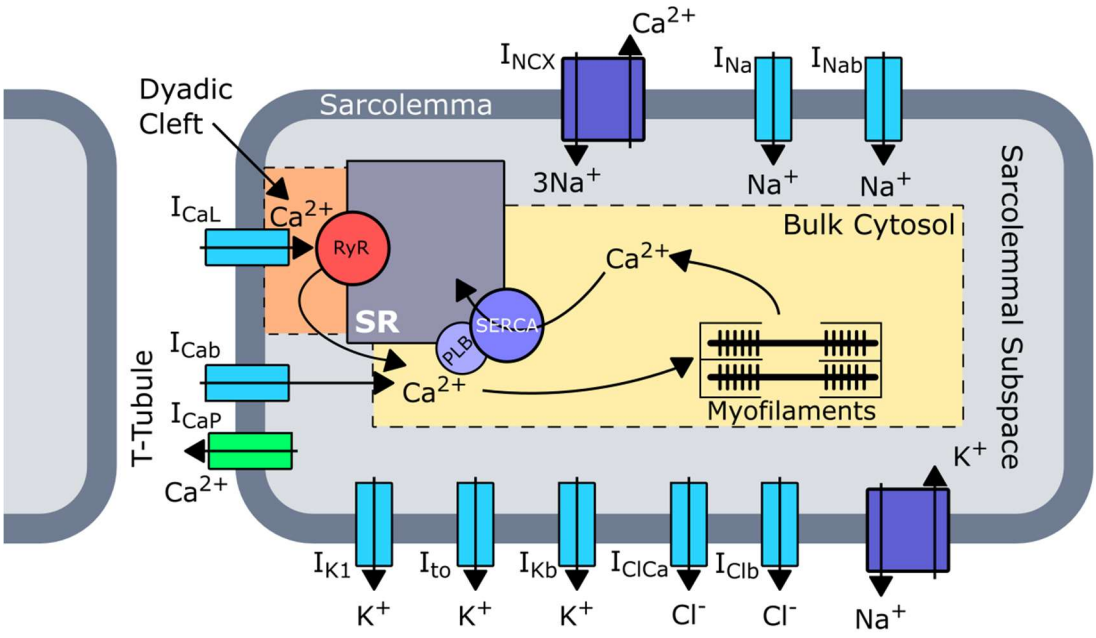

Figure 5.1 Rabbit Atrial Cell Model Schematic

A labelled model schematic illustrating the ionic currents and intracellular fluxes contained within the model. I_x refers to the current carried by the respective ionic channel, with directional arrows implying the net flow of current (note this may reverse with some ionic transporters). Compartments are labelled accordingly.

In addition to the membrane currents outlined in Table 5.1, descriptions of the inter-compartment Ca^{2+} fluxes include intracellular Ca^{2+} release, J_{rel}; SR-Ca^{2+} uptake (i.e., SERCA2a), J_{up}; and SR-Ca^{2+} leak, J_{leak}. The formulations for each flux were included in this model as given in [39, 44]. From this point, the model developed in this chapter is referred to as the "Holmes" or "novel" model.

Current	Description	$\bar{g}_x$ (Holmes)	$\bar{g}_x$ (Aslanidi) [242]
I_{Na}	Rapid inward Na^+ current	21.06 s/mF	15 s/mF
I_{to}	Transient outward K^+ current	0.303 s/mF	0.500 s/mF
I_{CaL}	L-Type Ca^{2+} current	0.448 s/mF	0.036 s/mF
I_{NaK}	Na^+-K^+ pump current	1.228 s/mF	1.288 s/mF
I_{Nab}	Background Na^+ current	4×10^{-4} s/mF	4×10^{-4} s/mF
I_{Kb}	Background K^+ current	0.002 s/mF	N/A

Table 5.1 Novel model membrane currents and their maximal conductance

Maximal conductance, $\bar{g}_x$, for ionic current, x, in the Holmes and Aslanidi models. Identical currents show in red. Note: the formulation for I_{Nab} is different due to the different model structures between the Holmes and Aslanidi models (compartmentalised vs non-compartmentalised I_{Nab}).

5.2.3 Simulation Protocols

Integral equations within the model are solved using the forward-Euler method (Section 2.7.1), and gating variables are updated using the Rush-Larsen method (Section 2.7.2), using a time step, dt, of 0.001 ms. As this model contains current formulations taken from the Aslanidi et al. (2009) rabbit atrial model [37, 242], where relevant, a simulation with identical conditions were run in the Aslanidi model for comparison. All simulations are paced to steady-state at 60 bpm by default, or 75 bpm to compare with Workman Lab conditions where appropriate; these are stated when required. The Aslanidi model is less stable and is paced for a shorter time due to the model breaking when run for long time periods; all measurements are taken from the stable period.

5.2.4 Characterisation of I_{K1} (Workman-Lab Data)

The inwardly rectifying K^+ current, I_{K1}, was directly fitted to a voltage pulse protocol performed by Giommi [371] on a population of 10 cells harvested from 6 rabbits. I_{K1} was recorded using a linear voltage pulse protocol (Figure 5.2A) increasing from -120 mV to +50 mV at a speed of 24 mV/s. In Figure 5.2, panel A shows voltage recordings from the same cell in control, with acute $BaCl_2$ superfusion (0.5 mM) and after washout of this intervention; the experimental data in panel B represents the average of 10 cells.

A polynomial formulation of I_{K1} was derived from the I-V relationship of Ba^{2+}-sensitive I_{K1} recordings, presented in equation 5.2 (Figure 5.2B).

$$I_{K1} = g_{K1} \cdot \begin{pmatrix} 11.959 + 8.63 \times 10^{-3} V_m + 2.68 \times 10^{-2} V_m^2 \\ -1.72 \times 10^{-5} V_m^3 - 4.10 \times 10^{-6} V_m^4 \end{pmatrix} \quad (5.2)$$

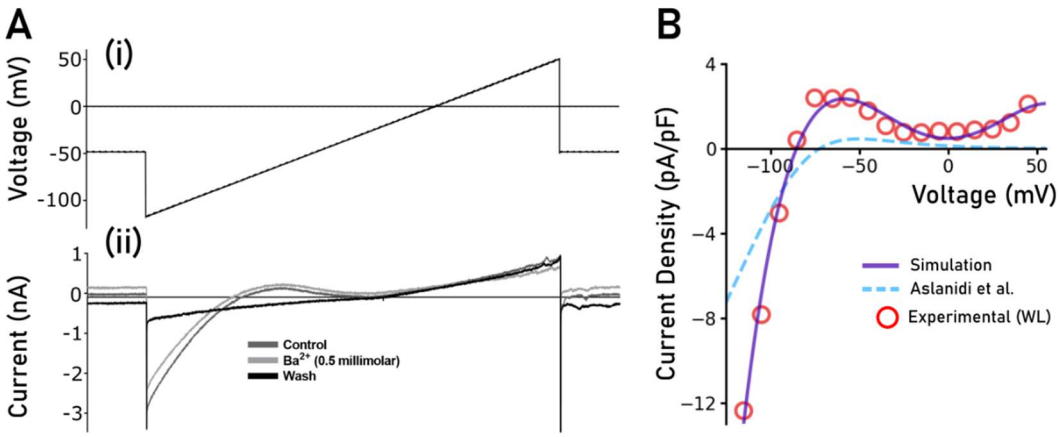

Figure 5.2 Fitting the I_{K1} current (Workman-Lab Data)

A – Linear voltage pulse protocol (i) and recorded I_{K1} current (ii) in one individual rabbit atrial myocyte performed by Giommi [371] and reproduced with permission. I_{K1} was measured in control, in the presence of $BaCl_2$ (0.5 mM) and after washout. B – Holmes and Aslanidi I_{K1} voltage-dependent current-density compared with experimental average Ba^{2+}-sensitive I_{K1} I-V relationship of 10 rabbit atrial cells.

5.2.5 Characterisation of I_{to} (Workman-Lab Data)

The formulation describing the transient outward K^+ current, I_{to}, was fit to voltage-clamp data (-90 mV to 50 mV, 10mV steps, rest potential of -50 mV with a 100ms pulse) obtained by Workman et al. (2012) [33] (Figure 5.3). Hodgkin-Huxley

formulations presented by the Workman Lab formed the basis of these formulations: steady-state formulations were implemented as stated in [33] (Figure 5.3A), formulations for time-constants were adjusted to more closely match observed activation and inactivation kinetics (Figure 5.3B). The maximal conductance of I_{to}, $\bar{g}_{to}$ was set to be 0.303 s/mF to match the Workman Lab current density after making these adjustments.

Thus, I_{to} is given by:

$$I_{to} = \bar{g}_{to} \cdot va_{Ito} \cdot vi_{Ito} \cdot (V_m - E_K) \tag{5.3}$$

where the dynamics of the gating variables, $x = va_{Ito}, vi_{Ito}$(activation and inactivation, respectively) are solved by the following equation (H-H formulism is described in Section 2.6.3):

$$x = x_{ss} - (x_{ss} - x_0) \cdot \exp\left(-\frac{dt}{x_\tau}\right) \tag{5.4}$$

with steady-states:

$$va_{Ito\_SS} = \frac{1}{1 + \exp\left(-\frac{V_m + 5.7}{11.1}\right)} \tag{5.5}$$

$$vi_{Ito\_SS} = \frac{1}{1 + \exp\left(\frac{V_m + 34.7}{7.4}\right)} \tag{5.6}$$

and time constants:

$$va_{Ito\_\tau} = 0.12 + 4.9 \cdot \exp\left(-\left(\frac{(V_m + 38.6)}{33.7}\right)^2\right) \tag{5.7}$$

$$va_{Ito\_\tau} = 11.77 + 69.67 \cdot \exp\left(-\left(\frac{(V_m + 81.59)}{-70.13}\right)^2\right) \tag{5.8}$$

Normalised voltage-dependence of the current in the novel model was compared to the Aslanidi model formulation and additional experimental works [372, 373]. The Aslanidi model contained three inactivation gates (Figure 5.3Aii, Bii), of which two share the same steady-state voltage dependence. The novel model developed in this chapter only required one inactivation gate to reproduce the Workman Lab's experimental data. The new formulation of I_{to} agrees more with the Workman Lab

dataset, and agrees well with I_{to} voltage-dependant current-density published in other works.

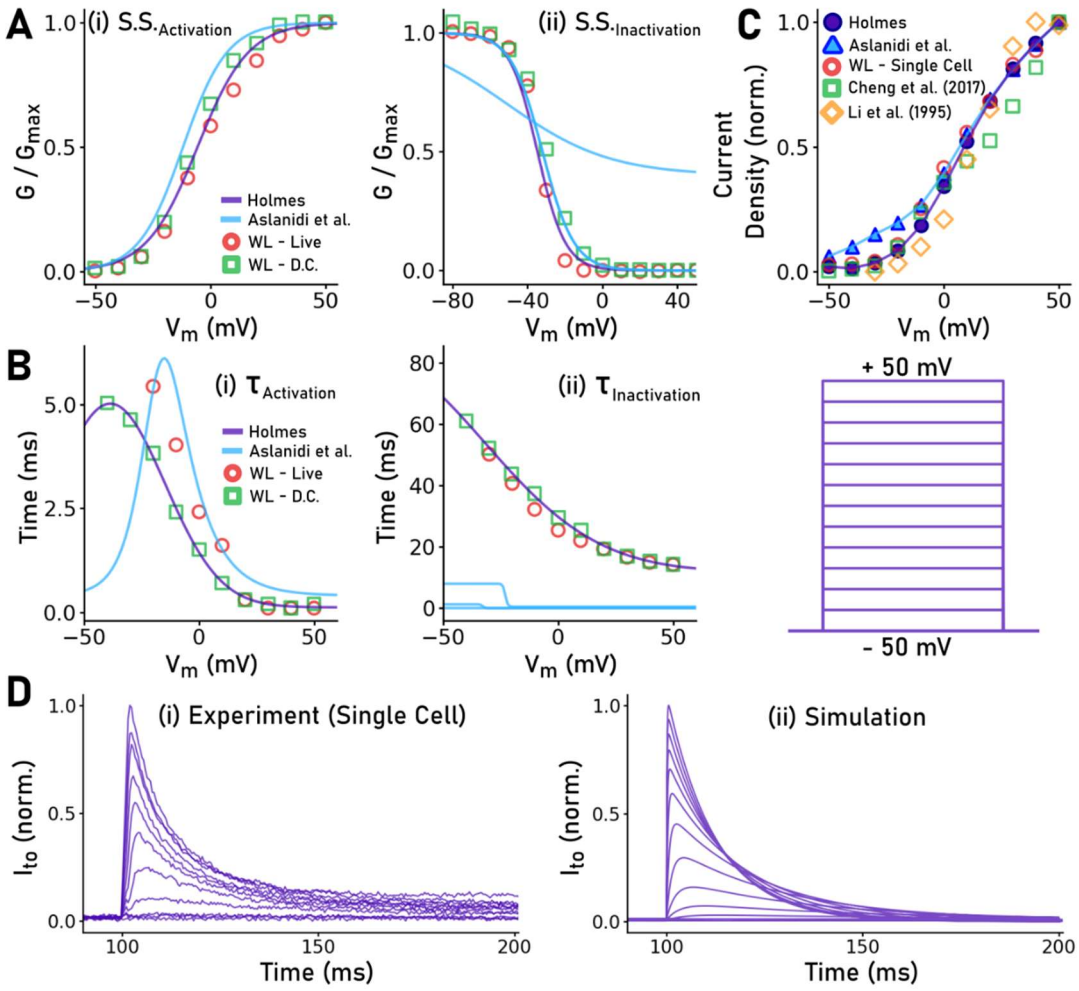

Figure 5.3 Fitting the I_{to} current (Workman-Lab Data)

Fitting the I_{to} activation and inactivation steady-states and kinetics to Workman Lab data published in [33]. Purple markers and lines represent the computational model. Red circles represent live recording data; green circles represent dynamic-clamp measurements. A – Fitting the (i) activation and (ii) inactivation steady states. B – Fitting the (i) activation and (ii) inactivation gating kinetics. C – Voltage-dependent current density in the Holmes and Aslanidi models normalised against the average data (Workman Lab) and other recent experimental data from Cheng et al. (2017) [372] and Li et al. (1995) [373]. D – Normalised (i) experimental I_{to} current traces from a single cell (Workman Lab) and (ii) the resulting simulated current traces for a simple voltage clamp protocol (-50 mV to +50 mV, 10 mV steps).

The existence of an associated sustained outwards current, I_{sus}, is debatable in the rabbit atrium [36, 353], and was considered negligible by Workman et al. (2012) [33], and thus has not been included within this model as the goal was to make a Workman Lab specific model, rather than a general rabbit atrial electrophysiology model.

5.2.6 Characterisation of I_{CaL} (Workman-Lab Data)

Due to its tight coupling with intracellular Ca^{2+} handling, I_{CaL} is a more challenging current to formulate than I_{K1} or I_{to}. In Kettlewell et al. (2019) [359], the dynamic clamp current formulation is a simplified version of the formulation developed by Nygren et al. (1998) [374]. The Nygren et al. (1998) formulation includes monophasic voltage-dependent activation, a bi-phasic inactivation, and is fitted with a static Ca^{2+} inactivation component as the dynamic-clamp method cannot simultaneously measure intracellular [Ca^{2+}] while clamping I_{CaL}. In the Workman Lab protocol, I_{CaL} must be pharmacologically inhibited in order to replace it with a dynamic-clamp current; thus, there is no CICR [359]. The Ca^{2+}-dependency of I_{CaL} inactivation was therefore simplified in the experiment by fixing the relative proportion of fast and slow decay, f_{Ca}, to 0.5. The Grandi-Bers Ca^{2+} handling model formulation has dynamic Ca^{2+}- dependent inactivation, and thus a different approach is required. Thus, I_{CaL} is formulated in a way that satisfies the requirement of fitting gating variables and the voltage-dependence of I_{CaL} while ensuring its compatibility with the Grandi-Bers Ca^{2+} handling model (Figure 5.4). The Grandi-Bers I_{CaL} formulation consists of Hodgkin-Huxley gating variables and kinetics. Modified formulations of steady-state activation and inactivation from the Workman Lab characterisations (Figure 5.4A) were combined with modified activation and inactivation kinetics from the Grandi-Bers model (Figure 5.4B). $\bar{g}_{CaL}$ was scaled accordingly to match observed voltage-dependence and current traces in the Workman Lab (Figure 5.4C-D).

Thus, the formulation for I_{CaL} is given as the following:

$$I_{CaL} = I_{CaL\_j} + I_{CaL\_sl} \tag{5.9}$$

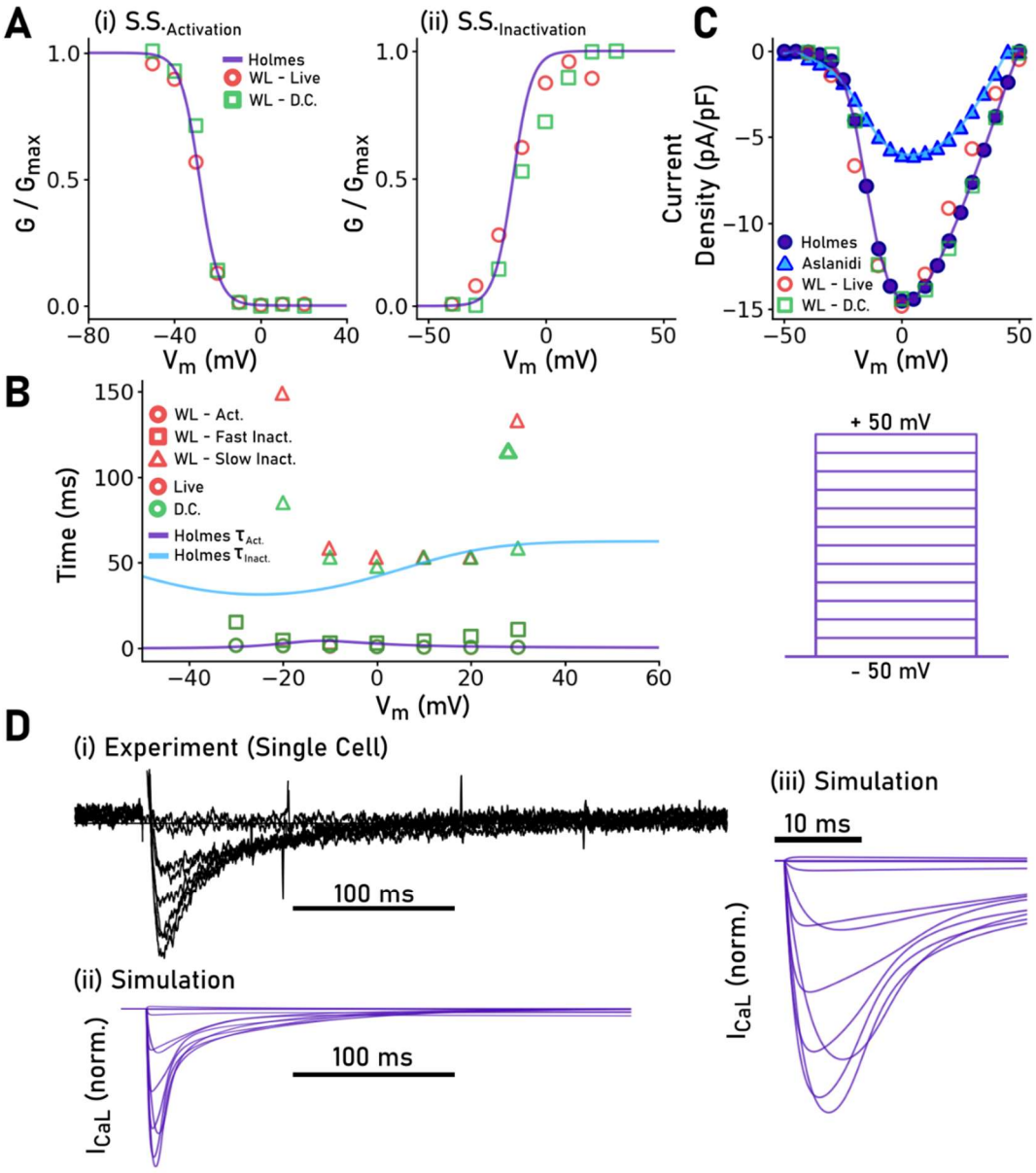

Figure 5.4 Fitting the I_{CaL} current (Workman Lab Data)

Novel I_{CaL} formulation compared to Workman Lab data. Panels A, B and C are mean data of cells obtained from 4 rabbits (n = 22-35 cells); Panel D experimental data from a single cell. A – Fitting the (i) activation and (ii) inactivation steady states. B – (i) activation and (ii) inactivation gating kinetics compared to Workman Lab data. C – Holmes and Aslanidi voltage-dependent I_{CaL} current density normalised against mean Workman Lab data. D – An experimental current trace (upper); Normalised (i) experimental I_{CaL} current traces from a single cell (Workman Lab) and (ii) the resulting simulated current traces for a simple voltage-clamp protocol (-50 mV to +50 mV, 10 mV steps) (lower).

where I_{CaL_j} and I_{CaL_sl} are computed for the junctional and non-junctional regions and are given as:

$$I_{CaL\_j} = F_{junc} \cdot \bar{g}_{CaL} \cdot va_{ICaL} \cdot vi_{ICaL} \cdot \left(1 - ci_{ICaL\_j}\right) \cdot (V_m - E_{Ca}) \quad (5.10)$$

$$I_{CaL\_sl} = \left(1 - F_{junc}\right) \cdot \bar{g}_{CaL} \cdot va_{ICaL} \cdot vi_{ICaL} \cdot \left(1 - ci_{ICaL\_sl}\right) \cdot (V_m - E_{Ca}) \quad (5.11)$$

The dynamics of the voltage-dependent activation and inactivation gating variable, $x = va_{ICaL}, vi_{ICaL}$, were solved using Eqn. 5.4. The activation steady-state was modified from the Workman Lab formulation, and the inactivation gate is as presented in [359]. These steady states are given by:

$$va_{ICaL\_SS} = \frac{1}{1 + \exp\left(\frac{(V_m + 14)}{-4}\right)} \quad (5.12)$$

$$vi_{ICaL\_SS} = \frac{1}{1 + \exp\left(\frac{(V_M + 28.3)}{4.4}\right)} \quad (5.13)$$

The time constants were scaled (va_{ICaL_τ} x 1.15, and vi_{ICaL_τ} x 1.25) from the formulations presented in the Grandi-Bers human Ca^{2+} handling model [44] to fit the voltage-dependent current density of the Workman Lab data, and thus are given by:

$$va_{ICaL\_\tau} = 1.15 \cdot va_{ICaL\_SS} \cdot \frac{\left(1 - \exp\left(-\left(\frac{V_m + 9.001}{6.0}\right)\right)\right)}{0.035 \cdot (V_m + 9.001)} \quad (5.15)$$

$$vi_{ICaL\_\tau} = \frac{1.25}{(0.0197 \cdot \exp\left(-\left(0.0337 \cdot (V_m + 25.0)\right)^2\right) + 0.02} \quad (5.16)$$

Moreover, Ca^{2+}-dependent inactivation is given as formulated in Grandi-Bers [44]:

$$\frac{dci_{ICaL\_sl}}{dt} = 1.7 \cdot [Ca^{2+}]_{sl} \cdot \left(1.0 - ci_{ICaL\_sl}\right) - 11.9 \times 10^{-3} * ci_{ICaL\_sl} \quad (5.17)$$

$$\frac{dci_{ICaL\_j}}{dt} = 1.7 \cdot [Ca^{2+}]_{j} \cdot \left(1.0 - ci_{ICaL\_j}\right) - 11.9 \times 10^{-3} * ci_{ICaL\_j} \quad (5.18)$$

5.2.7 Characterisation of I_{Na} (Workman-Lab Data)

The same approach to characterising I_{Na} was taken as presented by Colman et al. (2018) [43]: experimental data obtained from Priyanka Saxena in the Workman Laboratory relating RMP to dV/dT_{max} were used to modify the parameters of the I_{Na} formulation presented in Colman et al. (2018) [43], which itself is a

modification of the Luo-Rudy (1991) formulation [375]. The I_{Na} formulation used within the Aslanidi model is a modification of that which is presented within the Lindblad et al. (1996) model [36], and the voltage-dependence (RMP) of dV/dt_{max} for this model is shown along with the Luo-Rudy formulation (implemented in the novel model, replacing the new I_{Na} formulation) in Figure 5.5 for comparison. The voltage-dependence of dV/dT_{max} is shown for the Aslanidi model separately, as opposed to being implemented into the novel model, due to incompatibility issues.

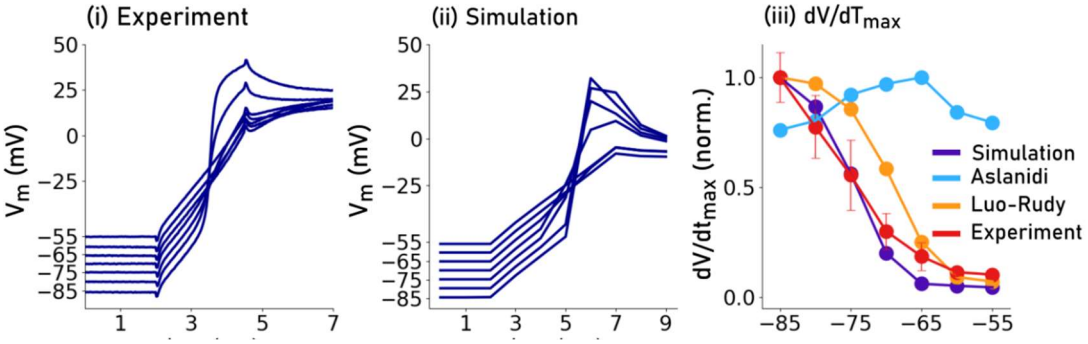

Figure 5.5 Parameterising the I_{Na} Current (Workman Lab Data)

Re-parameterising the I_{Na} formulation given by Colman et al. (2018) [43] using resting membrane potential (RMP). (i) Phase 0 AP upstroke with multiple RMP conditions in experiment. (ii) Phase 0 AP upstroke with multiple RMP conditions, performed by shifting I_{K1} E_{rev}. (iii) Relationship between dV/dT_{max} and RMP for experiment (red), the novel model (purple), the Aslanidi model (blue) and Lou-Rudy I_{Na} formulation (orange).

The new formulations resulted in good agreement between the simulated and experimental phase 0 traces (Figure 5.5i-ii); the simulation reproduced the rapid upstroke reaching the peak voltage in 4 ms after the stimulus. The voltage-dependence (RMP) of dV/dT_{max} much more closely matched experimental values (Figure 5.5iii), within the standard error presented by the Workman Lab from -85 to -65 mV, significantly more similar than the Luo-Rudy formulation. The Aslanidi model produced a biphasic voltage-dependence of dV/dT_{max} which did not match the experiment or the other formulations. It must be noted again for clarity that this is presented for the Aslanidi model and not for the I_{Na} formulation from the Aslanidi model implemented into the novel model.

The maximal upstroke velocity for rabbit atria was measured to be upwards of 500 mV/s [33] at 75bpm in the Workman Lab dataset. This magnitude is significantly

higher than observed in other published characterisations of dV/dT_{max} [376–378], and proved to cause instabilities in the model when dV/dT_{max} approached this value. Instead, $\bar{g}_{Na}$ was scaled as high as possible ($\bar{g}_{Na} = 21.06$ s/mF) without causing instabilities within the model to achieve a maximum dV/dT_{max} of 237 mV/s.

The formulation for I_{Na} is given as:

$$I_{Na} = I_{Na\_j} + I_{Na\_sl} \tag{5.19}$$

where I_{Na_j} and I_{Na_sl} are computed for the junctional and non-junctional regions and are given as:

$$I_{Na\_j} = F_{junc} \cdot \bar{g}_{Na} \cdot va_{INa}^3 \cdot vi_{INa\_1} \cdot vi_{INa\_2} \cdot (V_m - E_{Na}) \tag{5.20}$$

$$I_{Na\_sl} = (1 - F_{junc}) \cdot \bar{g}_{Na} \cdot va_{INa}^3 \cdot vi_{INa\_1} \cdot vi_{INa\_2} \cdot (V_m - E_{Na}) \tag{5.21}$$

The dynamics of the voltage-dependent activation and inactivation gating variables, $x = va_{INa}, vi_{INa\_1}, vi_{INa\_2}$ were again calculated using Eqn. 5.4 with activation and inactivation steady-states, $x_{ss} = va_{INa\_SS}, vi_{INa\_1\_ss}, vi_{INa\_2\_ss}$ and activation and inactivation kinetics, $x_\tau = va_{INa\_\tau}\, vi_{INa\_1\_\tau}, vi_{INa\_2\_\tau}$, given as combinations of α and β:

$$x_{ss} = \frac{x_\alpha}{x_\alpha + x_\beta} \tag{5.23}$$

$$x_\tau = \frac{1}{x_\alpha + x_\beta} \tag{5.24}$$

α and β are voltage-dependent, and are given as the following:

$$va_{INa\_\alpha} = \frac{0.32 \cdot (V_m + 39.13)}{1 + \exp\big(-0.09(V_m + 39.13)\big)} \tag{5.24}$$

$$va_{INa\_\beta} = 0.08 \cdot \exp\left(-\frac{V_m - 8}{11.0}\right) \tag{5.25}$$

If $V_m < -40\ mV$:

$$vi_{INa\_1\_\alpha} = 0.135 \cdot \exp\left(-\frac{V_m + 85}{6.8}\right) \tag{5.26}$$

$$vi_{INa\_1\_\beta} = 3.285 \cdot \exp\big(0.079 \cdot (V_m + 5)\big) + 31000 \cdot \exp\big(0.35 \cdot (V_m + 5)\big) \tag{5.27}$$

$$vi_{INa\_2\_\alpha} = \big(-127140 \cdot \exp(0.2444 \cdot V_m) - 3.474 \times 10^{-5} \cdot \exp\big(-0.04391 \cdot (V_m + 5)\big)\big) \cdot \left(\frac{V_m + 42.78}{1 + \exp(0.3111 \cdot (V_m + 84.23)}\right) \quad (5.28)$$

$$vi_{INa\_2\_\beta} = \frac{0.10908 \cdot \exp\big(-0.01052 \cdot (V_m + 5)\big)}{1 + \exp\big(-0.1378 \cdot (V_m + 45.14)\big)} \quad (5.29)$$

Else:

$$vi_{INa\_1\_\alpha} = 0 \quad (5.30)$$

$$vi_{INa\_1\_\beta} = \frac{1}{(0.13 \cdot \left(1 + \exp\left(-\frac{V_m + 15.86}{11.1}\right)\right)} \quad (5.31)$$

$$vi_{INa\_2\_\alpha} = 0 \quad (5.32)$$

$$vi_{INa\_2\_\beta} = \frac{\big(0.3 \cdot \exp\big(-2.535 \times 10^{-7} \cdot (V_m + 5)\big)\big)}{1 + \exp(-0.1 \cdot (V_m + 37)\ )} \quad (5.33)$$

5.2.8 Grandi-Bers Ca^{2+} Handling Model and Aslanidi Model Currents

The above formulations were integrated with the Grandi-Bers human atrial Ca^{2+} handling model (introduced in Section 2.8.4), using the formulations and parameters as described in Shannon et al. (2004) [39], and updated in Grandi et al. (2011) [44]. The Grandi-Bers Ca^{2+} model contains descriptions of four subcellular compartments, Ca^{2+} fluxes and buffering as described in Section 5.2.2 and illustrated in Figure 5.1. These will be briefly described here.

The Grandi-Bers model contains a Markovian formulation of RyR function and SR-Ca^{2+} release (J_{rel}), and descriptions of active SR-Ca^{2+} uptake (SERCA2a, J_{up}), and passive SR-Ca^{2+} leak (J_{leak}). These were integrated into the model as described in Grandi et al. (2011) [44]. Additionally, formulations for the sarcolemma Ca^{2+} pump, I_{CaP}, the Na^+-Ca^{2+} exchanger, the Ca^{2+}-dependent chloride current, $I_{Cl(Ca)}$, chloride (Cl^-) background current, I_{Clb}, and K^+ background current, I_{Kb} were included in the model as described.

Formulations for the sarcolemma Na^+-K^+ pump, I_{NaK}, and N^+ and Ca^{2+} background currents (I_{Nab}, I_{Cab}) included within the Grandi-Bers model were replaced with rabbit-atrial specific formulations from the Aslanidi et al. (2009) rabbit atrial model as described in publication [242].

In addition to the above, the Grandi-Bers Ca^{2+} model included descriptions of N^{+} buffering in the cytosol and sarcolemma subspaces, along with compartmental Ca^{2+} buffering. These included troponin-C, calmodulin and myosin buffers in the cytosol and calsequestrin in the SR, which were incorporated into the model. All buffers were included as described in publication [39, 44]

5.2.9 Exclusion of K^{+} Repolarising Currents: I_{Kr} and I_{Ks}

Formulations for the rapid- and slow-delayed rectifying K^{+} currents, I_{Kr} and I_{Ks} are included in the existing pool of rabbit atrial models [36, 37, 242, 249, 367] as minor currents. There is discussion within the literature about the importance of these ionic currents on rate-dependence and repolarisation reserve [341, 379, 380]. However, to the authors' knowledge, these currents' voltage-dependence and kinetics have not been characterised together in the rabbit atria within recent literature. The Lindblad model uses I_{Kr} data from rabbit atrial cells measured by Muraki et al. (1995) [362], however, Muraki et al. (1995) state that I_{Ks} was observed to be less than ~10% of the magnitude of I_{Kr} and thus could not be quantitatively studied. The I_{Ks} data used within the model is instead obtained from rabbit sinoatrial or atrial-ventricular node pacemaking cells.

Thus, in order to determine the necessity of including these currents, formulations for I_{Kr} and I_{Ks} from Aslanidi et al. (2009) [242], using 50% and 100% of the conductance as given by Aslanidi, and the updated conductances given by Vagos et al. (2020) [367] were applied to the model to determine the effect these currents have on the action potential, the intracellular CaT and SR-Ca^{2+} (see Table 5.2). The relative changes to APD_{50}, APD_{90}, CaT amplitude and SR-Ca^{2+} load amplitude can be observed in Figure 5.6. The inclusion of I_{Kr} and I_{Ks} made no major differences to APD (APD_{50} < 2%; APD_{90} < 2%), CaT amplitude (< 1%) or SR-Ca^{2+} amplitude (< 1%). Thus, these currents were not included in the control model to avoid including additional sources of variability.

Model	$\bar{g}_{Kr}$ (s/mF)	$\bar{g}_{Ks}$ (s/mF)
Control	0	0
50% Aslanidi I_{Kr} and I_{Ks}	0.0025	0.025
100% Aslanidi I_{Kr} and I_{Ks}	0.005	0.05
Vagos I_{Kr} and I_{Ks}	0.07	0.05

Table 5.2 I_{Kr} and I_{Ks} maximal conductance tested for the control model

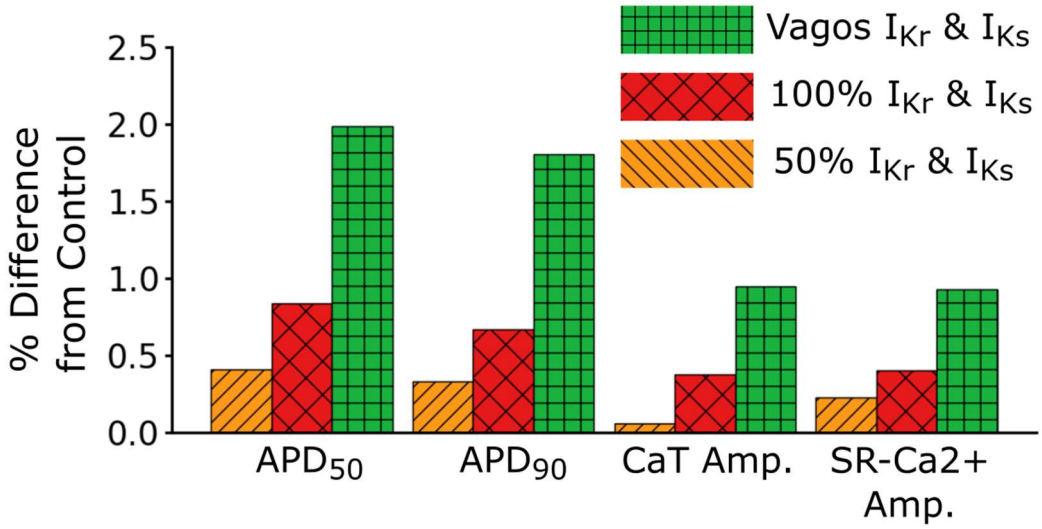

Figure 5.6 APD and Ca^{2+} handling differences with the inclusion of I_{Kr} and I_{Ks}

Percentage difference in APD_{50}, APD_{90}, CaT amplitude and SR-Ca^{2+} amplitude with the inclusion of I_{Kr} and I_{Ks} in the Holmes model with three sets of maximal conductance, $\bar{g}_{Kr}$ and $\bar{g}_{Ks}$. Simulations ran for 10 minutes to reach steady-state at 60 bpm. Differences are given as absolute differences from the control model.

5.3 Results

5.3.1 Model Stability

Every simulation in the Holmes model was run for 10 minutes to reach a steady-state and confirm stability (Figure 5.7). The Holmes model reached stability at around 7 minutes of pacing (Figure 5.7A) and was capable of stable pacing at pacing

rates up to 600 bpm (10 Hz) (Figure 5.7B). The rabbit heart has been observed to pace between approximately 110 – 340 bpm (120.75 ± 6.93 bpm, Lang et al. (2011) [381]; 130-330 bpm, Joukar (2021) [80]; 198-330 bpm, Lord et al. (2010) [382]); thus the model is able to reproduce the range of physiologically observed pacing rates.

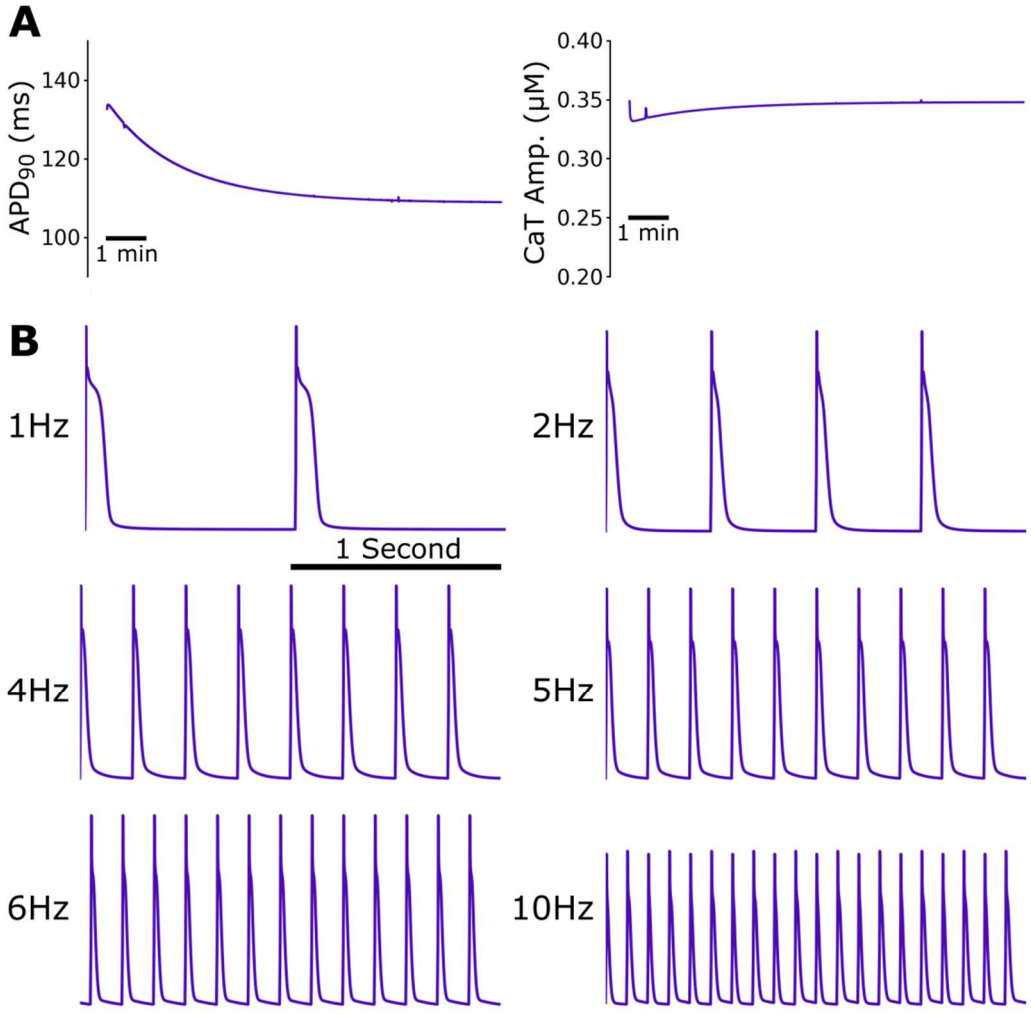

Figure 5.7 Holmes model stability and pacing characteristics

A – Action Potential Duration (APD_{90}) drift and Ca^{2+} transient (CaT) amplitude drift over a 10 minute period at 60 bpm, stabilising after around 7 minutes of pacing. B – 2 seconds of steady-state pacing at (1-10Hz).

5.3.1 Action Potential Morphology and Characteristics

The resultant action potential of the novel model described is presented in Figure 5.8, alongside an Aslanidi model AP, APs provided by the Workman Laboratory (75

bpm, Figure 5.8A), and then against a range of experimental rabbit atrial APs from other groups (60 bpm, Figure 5.8B).

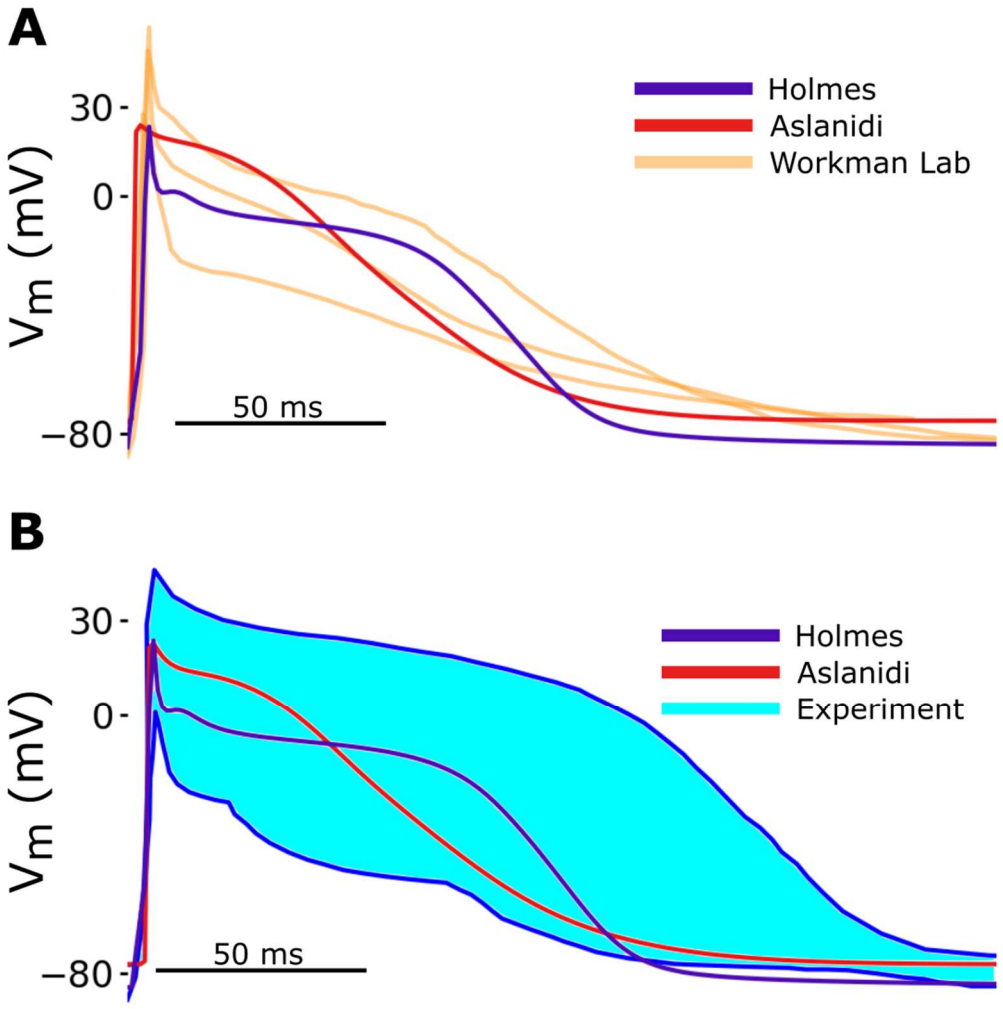

Figure 5.8 Simulated AP morphology validation and experimental comparison

Steady-state action potential (AP) produced using the Holmes model, compared to the Aslanidi model, and experimental data. A – APs at 75bpm produced by the Holmes model (purple), the Aslanidi model (red) and recorded in the Workman Lab (orange) [33, 359]. B – APs at 60 bpm for the Holmes and Aslanidi models against a range of experimental AP morphologies (blue) taken from [33, 343, 359, 366, 377, 378, 383–385].

The simulated AP morphology is within reasonable agreement with those recorded in the Workman Lab (Figure 5.8A). The model reproduces Phase 0, Phase 1 and

Phase 2 AP morphology observed by the Workman Lab, including a Phase 0-1 spike and a long phase 2 plateau phase. The Aslanidi model produces an AP without the Phase 0-1 spike and demonstrates a more rapid repolarisation than the Workman Laboratory APs. Thus, the novel model produces a more similar AP morphology to Workman Lab data than the Aslanidi model.

Figure 5.8B shows the two computational models compared to a wide range of experimentally recorded APs published by various groups [33, 343, 359, 366, 377, 378, 383–385]. The novel model's AP morphology at 60 bpm also demonstrates good agreement with APs recorded from wider groups and closely matched recorded APs from Jiang et al. (2017) [377] and Zeng et al. (2017) [385] with long, shallow plateau phases, a rapid phase 3 repolarisation and a rectangular morphology. The Aslanidi model at 60bpm produces a small Phase 0-1 spike, which agrees with the wider experimental data.

In order to draw quantitative comparisons between APs, commonly used biomarkers must be compared (see Section 2.2.5 for a detailed discussion of AP characterisation). Figure 5.9 shows APDs for the novel model, Aslanidi model, Workman Lab datasets, and experimental data from other groups.

The novel model shows good agreement with published APD_{90} values from Workman et al. (2012) [33] (98.7 ms, Holmes; 103 $\pm$ 6 ms, Workman Lab [33]) (Figure 5.9Ai). The Aslanidi model produces a shorter APD_{90} (97.3 ms, Aslanidi) which falls short of this range. APD_{90} of the novel model (109.9 ms) is directly in agreement with published APD_{90} values from Fu et al. (2016; 105.7 $\pm$ 29.7 ms) [386], Grieser et al. (2014; 120 $\pm$ 20 ms) [346] and Al Abed et al. (2016; 116 $\pm$ 34 ms) [376] (Figure 5.9Aii). Both the Holmes and Aslanidi models produce an APD_{90} at 60 bpm~~,~~ well within the total observed experimental range.

APD_{50} in the Holmes model at 75 bpm (67.5 ms) is significantly higher than values published by Workman et al. (2012) (25 $\pm$ 4 ms) [33] (Figure 5.9Bi), and outside of the standard deviation of the pool of recorded Workman Lab APs (41.5 $\pm$ 24.1 ms), but exists within the total observed range. The Aslanidi model produces a shorter APD_{50} (56.4 ms) which falls within the standard deviation of Workman Lab APs. The Holmes model APD_{50} does not directly agree with any specific published observations but exists well within the bounds of total experimental observations (Figure 5.9Bii).

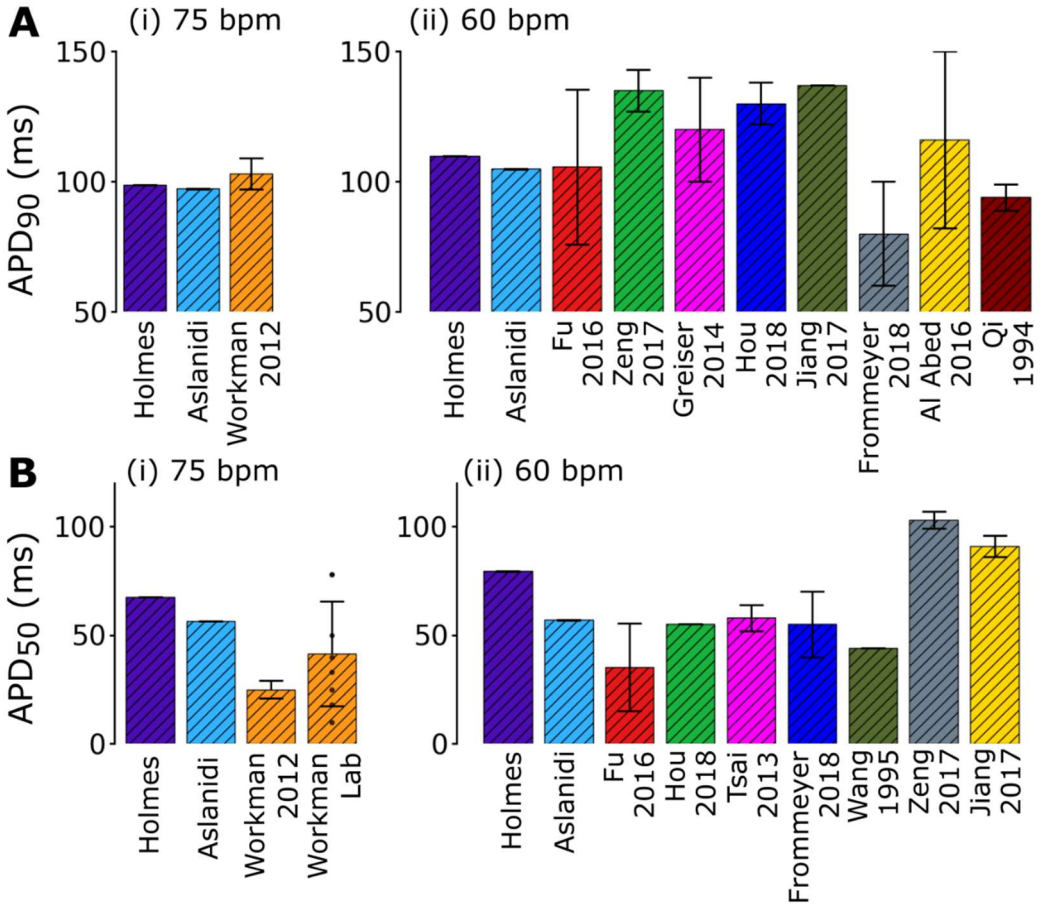

Figure 5.9 Simulated APD validation and comparison with experimental data

Action potential duration (APD) biomarkers produced by the novel and Aslanidi rabbit atrial models, compared with experimental data from the Workman Lab [33], and wider experimental groups (labelled underneath each bar [346, 363, 364, 366, 376, 377, 384–387]. Dots on Workman Lab data represent individual cell measurements, error bars on "Workman Lab" data represent standard deviation, all other error bars are taken as published. A – APD_{90}, B – APD_{50}. (i) 75 bpm, (ii) 60 bpm.

The novel model produces an APA (115.2 mV) which exists within the standard deviation of data from the Workman Lab (121.7 ± 9.85 mV, Figure 5.10A), whereas the Aslanidi model produced a significantly lower APA (100.3 mV), lower than all Workman Lab values. APA in the novel model is within direct agreement with published values from Jiang et al. (2017) [377] and Verkerk et al. (2012) [378]. Both

the Holmes and Aslanidi models produce an APA within the total observed experimental range.

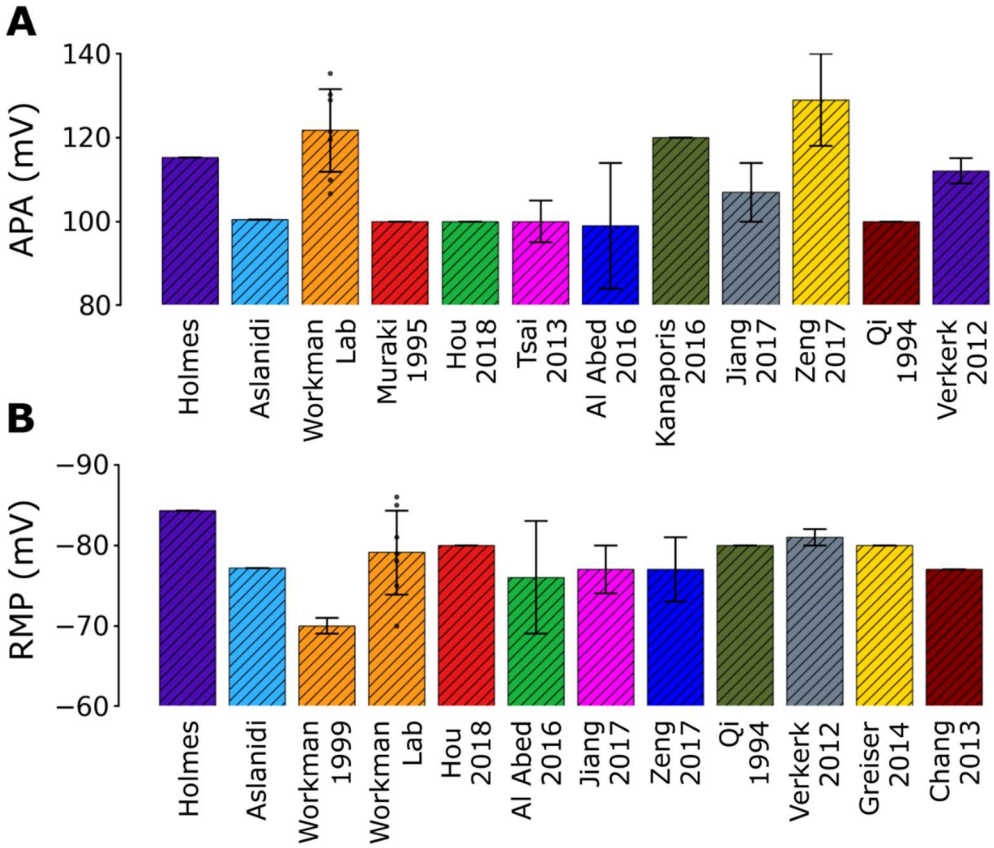

Figure 5.10 Simulated APA and RMP validation and comparison with experimental data

Action potential amplitude (APA) and resting membrane potential (RMP) produced by the novel and Aslanidi rabbit atrial models, compared with experimental data from the Workman Lab [368], and wider experimental groups (labelled underneath each bar) [346, 362, 364, 365, 365, 366, 377, 378, 384, 385, 388]. Dots on Workman Lab data represent individual cell measurements, error bars on "Workman Lab" data represent standard deviation, all other error bars are taken as published. A – APA B – RMP.

RMP in the novel model (−84.3 mV) is significantly lower than published in Workman et al. (1999) (−70 ± 1 mV) [368], and lower than observed within a standard deviation of Workman Lab data, but within the total range of observations (Figure 5.10B). The Aslanidi model also produces a higher RMP (−77.2 mV) than published in Workman et al. (1999) [368] but is in agreement with the full Workman Lab dataset. The Holmes model produces an RMP lower than any other published

experimental data, whereas the Aslanidi model is congruent with many published studies [376, 377, 385, 388].

As previously mentioned in Section 5.2.7, it proved difficult to reproduce dV/dT_{max} in agreement with measurements published in Workman et al. (2012) [33]. The dV/dT_{max} produced in the novel model (236.7 V/s) is smaller than the Workman Lab values (520 ± 20 V/s), but is within agreement of values published by Jiang et al. (2017; 231 ± 10 V/s) [377]. Other published values of dV/dT_{max} from Al Abed et al. (2016) [376] and Verkerk et al. (2012) [378] are 100 V/s (no error provided) and 342 ± 40 V/s respectively, thus the dV/dT_{max} produced by the novel model falls within observed experimental values. The Aslanidi et al. (2009) model [242] produces a dV/dT_{max} of 165 V/s (no error provided), which is within the range observed experimentally, but much lower than observed in the Workman Lab.

5.3.2 Ca^{2+} Transient Morphology and Characteristics

Kettlewell et al. (2019) [359] provide the only quantification of intracellular [Ca^{2+}] in rabbit atrial myocytes to the authors' knowledge. Thus, this provides a novel opportunity to validate the CaT produced by the novel rabbit atrial model CaT against congruent experimental data. Figure 5.11 shows the normalised simulated CaTs from the Holmes and Aslanidi models compared against Workman Lab data and quantification of diastolic and systolic [Ca^{2+}].

The CaT produced by the novel model is observed to have a much more similar CaT peak delay (41 ms) to the Workman Lab data (single cell, ~55 ms, from the rolling average) than the Aslanidi model (5 ms) (Figure 5.11A). The FWHM of the CaT is longer in the Workman Lab data (single cell, ~240 ms, from the rolling average) than in either the Holmes model (~ 150 ms) or the Aslanidi model (~ 20 ms). Overall, the Holmes model CaT matches the experimental CaT morphology much more similar than the Aslanidi model CaT but is still shorter than observed. Additionally, this reaffirms the choice of Ca^{2+} handling model used (Section 5.2)

Comparison of diastolic and systolic intracellular [Ca^{2+}] between the models (Figure 5.11B) shows varied agreement across the Holmes and Aslanidi models and the Workman Lab data. Diastolic [Ca^{2+}] in the Holmes model (0.163 μM) is significantly higher than the mean Workman Lab values (0.066 ± 0.032 μM, Kettlewell et al. (2019) [359]), but within the full range of experimental values.

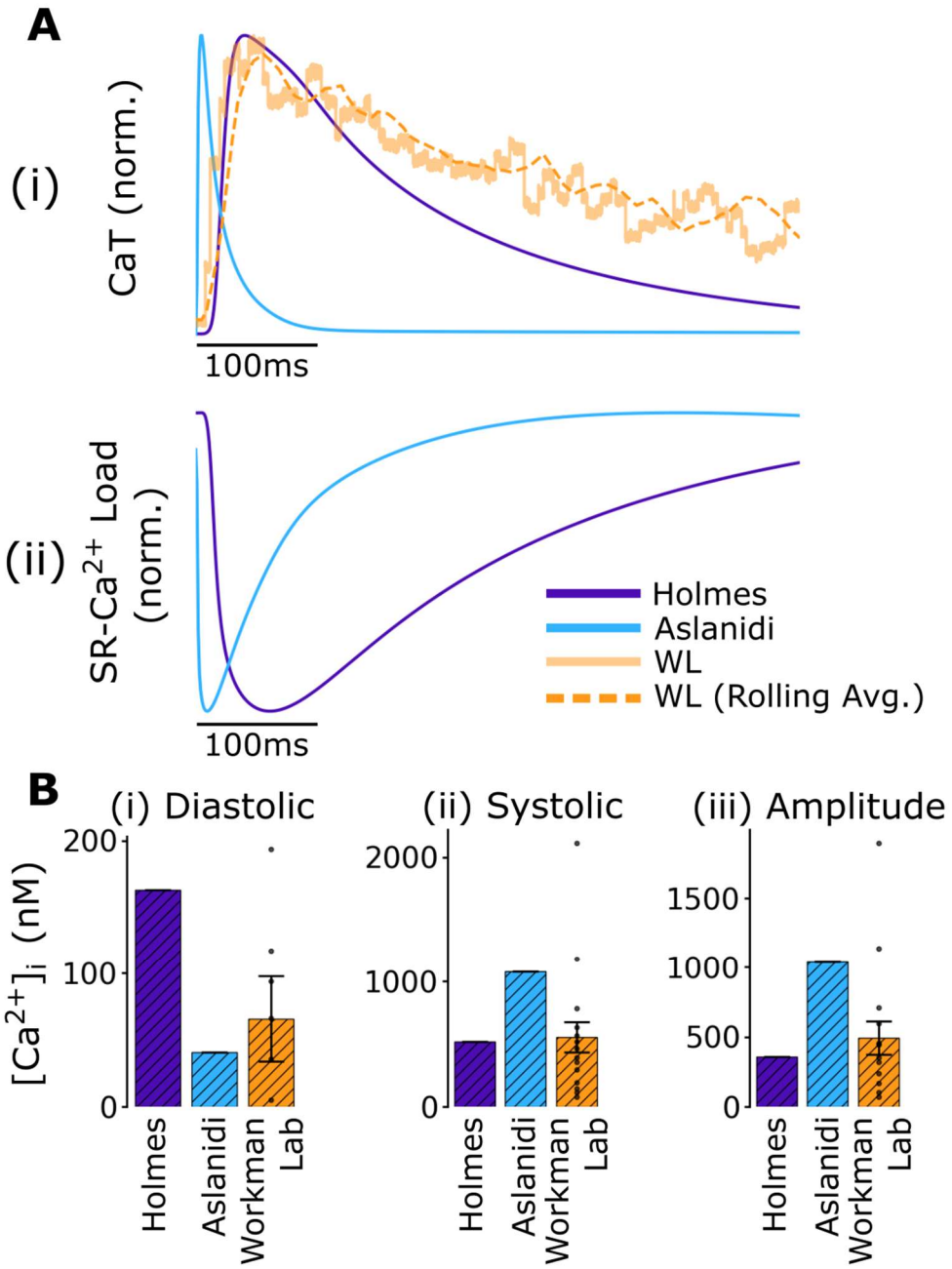

Figure 5.11 Simulated CaT validation with experimental data

Steady-state CaT produced using the Holmes model, compared with the Aslanidi model and published Workman Lab data (Kettlewell et al. 2019 [36]. A – Normalised (i) CaT from Holmes (purple) and Aslanidi (blue) models compared to a experimentally recorded CaT (orange) with rolling average (dashed line) from a single cell, and (ii) SR Ca^{2+} load. B – Quantification of (i) diastolic and (ii) systolic $[Ca^{2+}]$, and (iii) CaT amplitude. Error bars are taken from publication, dots represent individual cell measurements.

The Aslanidi model produces a lower diastolic [Ca^{2+}] (0.041 μM), which more closely agrees with the Workman Lab data. Systolic [Ca^{2+}] in the Holmes model (0.520 μM) is congruent with Workman Lab observations (0.555 ± 0.120 μM), whereas the Aslanidi model produces a significantly higher peak (1.084 μM), but this still lies in the upper bounds of the Workman Lab data. CaT amplitude in the Holmes model (0.367 μM) is significantly lower than the mean Workman Lab values (0.494 ± 0.120 μM); it should be noted that this is a direct consequence of the lower diastolic, and similar systolic [Ca^{2+}] measurements, and still agrees well within the observed range of Workman Lab experimental data. The Aslanidi model produces a significantly larger CaT amplitude due to the notably large systolic [Ca^{2+}] peak. This value further deviates from the mean values presented by the Workman Lab but is still within the total observed range published in Kettlewell et al. (2019) [359].

5.3.3 Rate-Dependence and Restitution

There is a lack of published experimental data describing the rate-dependence of APD, and APDR in rabbit atrial myocytes, two exceptions being Fu et al. (2016) [386] and Verkerk et al. (2012) [378]. A comparison of simulated steady-state APD rate-dependence and these experimental data is shown in Figure 5.12A.

Both the Fu et al. (2016) [386] and Verkerk et al. (2012) [378] data show no significant changes in APD_{90} as pacing rate increases, whereas APD_{90} decreases as pacing rate increases in both simulated models (Figure 5.12Ai). APD_{90} decreases more sharply in the Holmes model than the Aslanidi model from 60 bpm to 200 bpm when the Aslanidi model APD_{90} drops significantly from 60.2 ms at 200 bpm to 26.1 ms at 240 bpm. The Holmes model APD_{90} continues decreasing at a shallower rate as the pacing rate increases to 340bpm. The rapid shift in APD in the Aslanidi model between 200 and 240bpm has potentially large implications for arrhythmias in that pacing region, whereas the smoother rate-dependence curve in the novel model may act to inhibit potential excitation wave break in tissue models [389–391]; however, this is outside of the scope of this study.

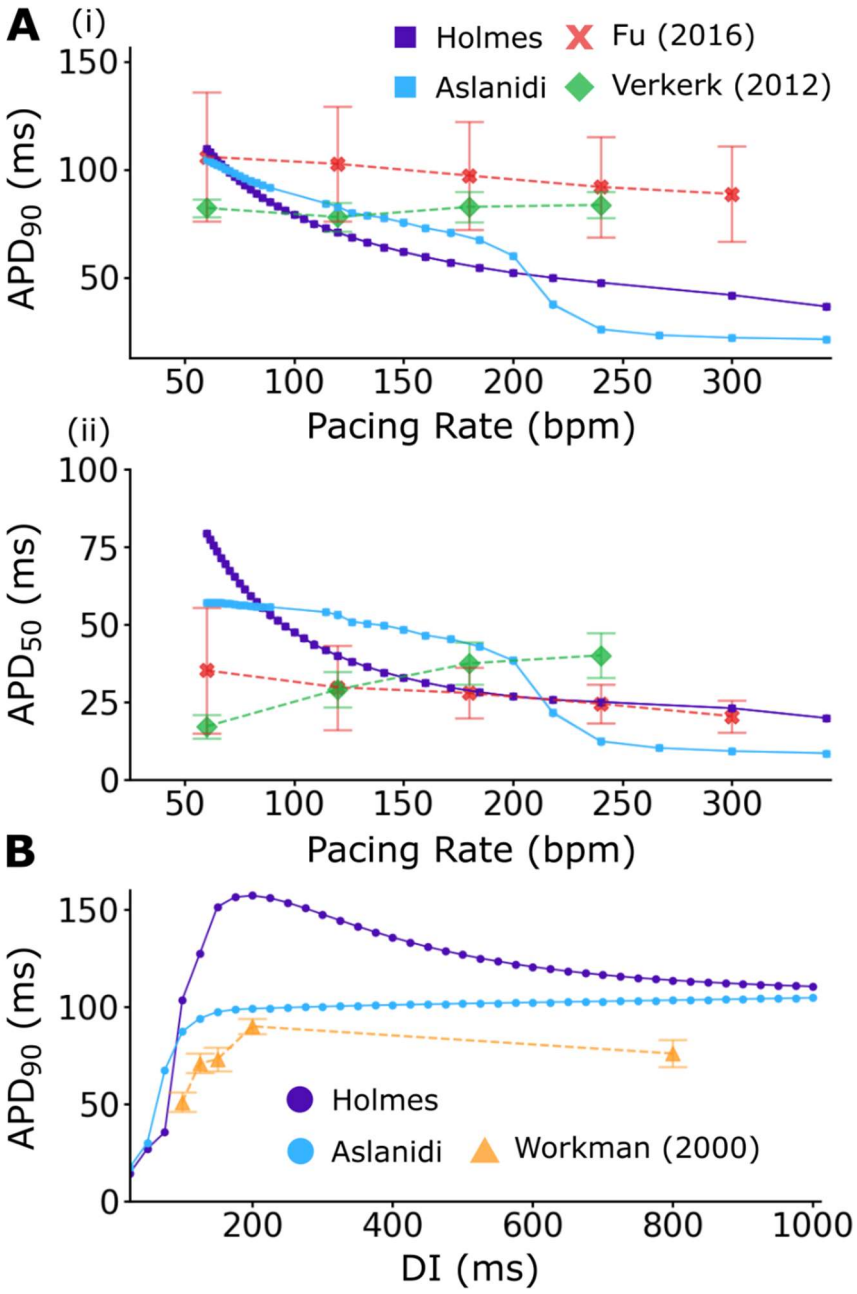

Figure 5.12 APD rate-dependence and S1-S2 restitution

Comparison of Holmes and Aslanidi APD rate-dependence and APD restitution (APDR) curves. A – Steady-state APD at pacing rates between 60 – 340 bpm for the simulated Holmes and Aslanidi models and experimental data (see legend) [378, 386]. B – APDR curve for Holmes and Aslanidi models produced using an S1-S2 protocol, S1 (75 bpm) to steady-state followed by S2 (diastolic interval, DI) and published Workman Lab [369] rate-change APD_{90} data.

APD_{50} is observed to significantly increase at higher pacing rates in data published by Verkerk et al. (2012) [378] and not change significantly with increased pacing in the data published by Fu et al. (2016) [386] (Figure 5.12Aii). Similar to the trends in APD_{90}, APD_{50} decreases more sharply in the Holmes model than the Aslanidi model up until 200 bpm, where the Aslanidi model decreases significantly. APD_{50} in the novel model continues decreasing at a shallower rate as the pacing rate increases to 340bpm. Both models yielded significantly lower APD_{90} at higher pacing rates than experiment; thus, this may indicate a limitation in using these models in studies at higher pacing rates. However, the novel model produced an APD_{50} steady-state rate-dependence, which agrees with experimental data from Fu et al. (2016) [382] in rabbits' physiological pacing range, which suggests an improvement over the Aslanidi model.

In Figure 5.12B, APDR curves for the novel and Aslanidi models were created using an S1-S2 protocol. Models were paced to a steady-state by the S1 stimulus (75 bpm), followed by perturbation by an extra S2 stimulus at progressively decreasing intervals (DI = 1000 to 25 ms). The Holmes model APD_{90} increases as the DI shortens, progressively becoming steeper towards 200 ms, whereas APD_{90} sharply falls as the DI shortens to 25 ms. Conversely, the Aslanidi model shallowly decreases as DI shortens from 1000ms to 200ms, where it sharply drops further. The Workman Lab rate-change data shows the effects of a progressively increasing S2 stimulation rate APD_{90} in the Workman lab dataset increases from an S2 stimulus of 800ms to 200ms, where it then declines sharply as DI increases to 100ms. The Workman APDR curve is significantly lower than the Holmes or Aslanidi APDR curves at all DI but holds the same morphology as the Holmes model. Other than the data presented by the Workman Lab, there is no other published rabbit atrial APDR data to the authors' knowledge. Additionally, the author of this thesis did not find any quantification of the rate-dependence of intracellular $[Ca^{2+}]$ in rabbit atrial myocytes; thus, in Figure 5.13, the two simulated models are compared.

Individual values for $[Ca^{2+}]$ at various pacing rates shown in Figure 5.13 are presented in Table 5.3. Diastolic $[Ca^{2+}]$ in the Holmes model (Figure 5.13A) is observed to increase non-linearly as the pacing rate increases from 60 bpm to 300bpm, where the diastolic $[Ca^{2+}]$ plateaus towards 340 bpm. Systolic $[Ca^{2+}]$ increases similarly from 60 bpm to 300 bpm, before decreasing towards 340bpm (Figure 5.13B). This results in a CaT magnitude which slowly increases from 60bpm

to 240bpm, then decreases towards 340 bpm (5.13C). Both systolic [Ca^{2+}] and CaT amplitude at all pacing rates are within the full range of values observed at 60 bpm by the Workman Lab (Figure 5.11, Kettlewell et al. (2019) [359]), and thus, it can be inferred that this is within the physiological range of rabbit atrial cells.

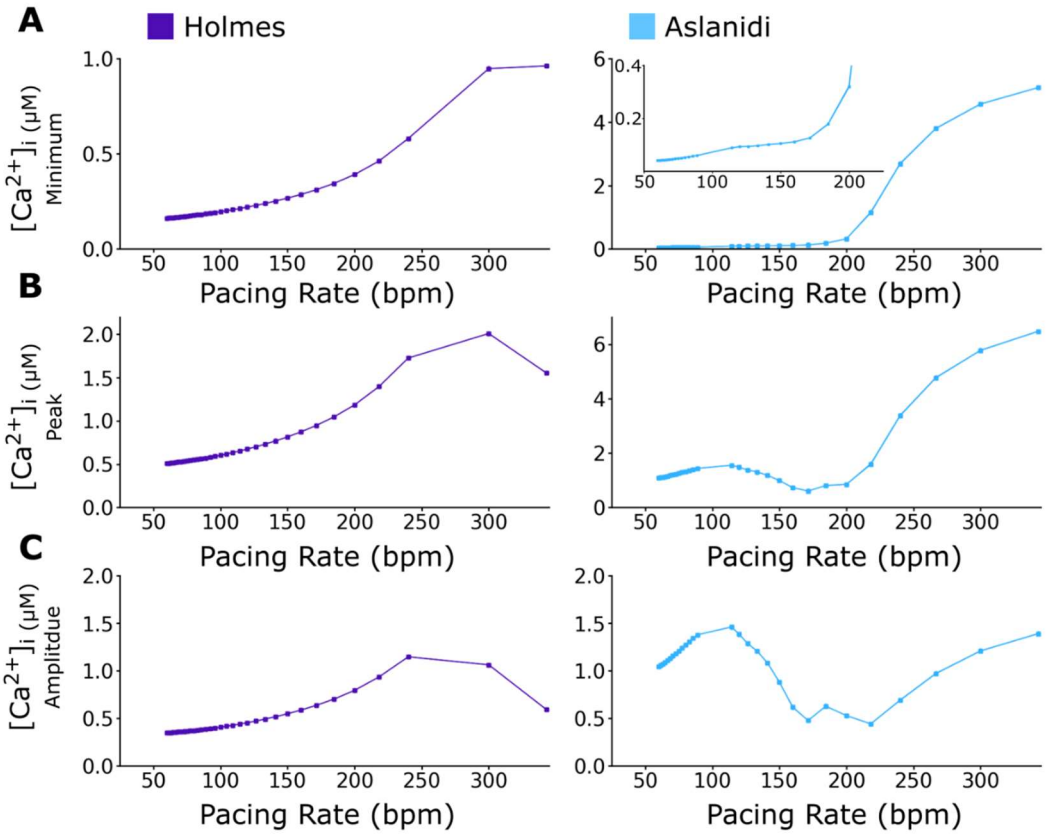

Figure 5.13 Simulated rate-dependence of [Ca^{2+}] in Holmes and Aslanidi models

Comparison of Holmes (left) and Aslanidi (right) [Ca^{2+}] steady-state rate-dependence at pacing rates between 60 – 340 bpm for the simulated Holmes and Aslanidi models. A – Diastolic (minimum) [Ca^{2+}]; B – Systolic (peak) [Ca^{2+}]; C – CaT amplitude. Inlay in Panel A (right) shows steady-state diastolic [Ca^{2+}] in 60 – 200pm range for the Aslanidi model.

Pacing Rate (bpm)	60	75	120	240	300	600
Diastolic (Minimum) [Ca^{2+}] (μM)						
Holmes	0.162	0.172	0.220	0.580	0.947	1.144
Aslanidi	0.041	0.049	0.094	2.696	4.57	6.678
Systolic (Peak) [Ca^{2+}] (μM)						
Holmes	0.509	0.538	0.675	1.727	2.010	1.574
Aslanidi	1.084	1.258	1.480	3.389	5.782	8.660
CaT Amplitude [Ca^{2+}] (μM)						
Holmes	0.347	0.366	0.455	1.147	1.063	0.43
Aslanidi	1.043	1.209	1.386	0.693	1.212	1.982

Table 5.3 Rate-dependence of intracellular [Ca^{2+}] in simulated models

Diastolic intracellular [Ca^{2+}] in the Aslanidi model increases more slowly than the Holmes model from 60bpm to 200bpm (60bpm, 0.041 μM; 200bpm, 0.318 μM), where the levels of diastolic [Ca^{2+}] increase dramatically over a short-range (240bpm, 2.296 μM) and continue to increase at a rapid rate up to 340bpm (Figure 5.13A). Systolic [Ca^{2+}] increases between 60bpm and 120 bpm, then decreases in a dip between 120 bpm and 200 bpm, where it sharply rises similarly to the diastolic [Ca^{2+}] (Figure 5.13B). This produces a more variable CaT amplitude as the pacing rate increases with a complex triphasic morphology (Figure 5.13C).

The large diastolic and systolic [Ca^{2+}] values in the Aslanidi model at pacing rates above 240 bpm are a model-breaking limitation. These values exceed 2 – 5 times the maximal observed value for systolic [Ca^{2+}] and well exceed physiological ranges. These values would result in Ca^{2+} overload in a cardiomyocyte, promoting arrhythmogenic cellular phenomena such as SCRE and alternans [15, 392]. Ca^{2+} overload is associated with AF pathology due to the characteristic rapid pacing rates [393], and at these levels, cell death [394]. Thus, due to these exceedingly unphysiological values, any results produced by the Aslanidi model at these pacing rates could not be interpreted with any physiological meaning. Overall, the novel model produces more stable and more physiological systolic and CaT amplitude measurements across the range of rabbit heart pacing rates, indicating better

suitability for studying Ca^{2+} handling rate-dependence. Moreover, this novel model addresses the issue of Ca^{2+} overload at rapid pacing rates observed in the Aslanidi model.

5.3.4 Alternans

AP and CaT alternans spontaneously emerge in the novel model at pacing rates exceeding 400 bpm (above the normal physiological ranges for rabbit heart rate. An example of this behaviour is shown in Figure 5.14. Alternans are described in Section 2.3.4.

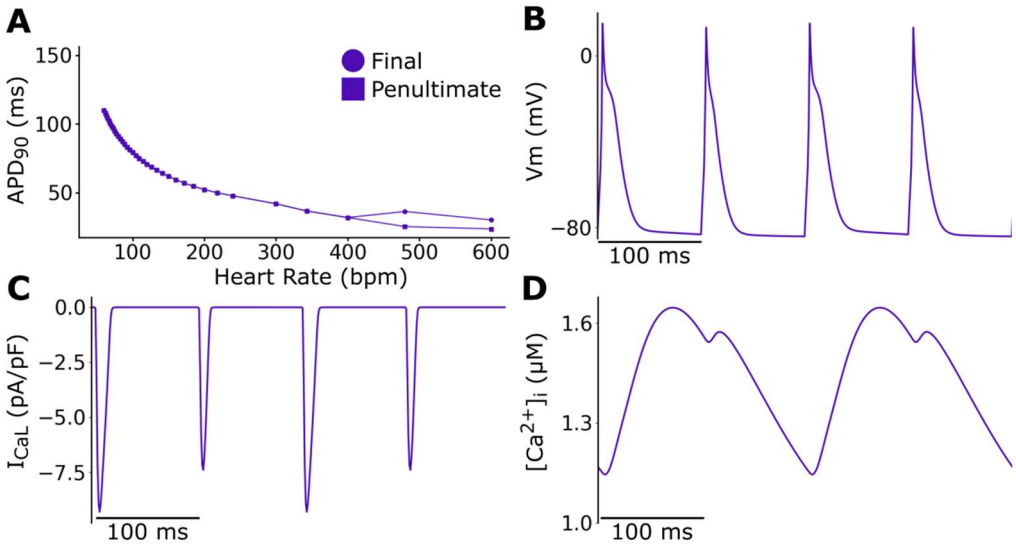

Figure 5.14 Alternans at rapid pacing rates in the novel model

Alternans occur spontaneously at supraphysiological pacing rates in the novel model. A – Steady-state APDR curve for APD_{90} of the final and penultimate beat with a bifurcation above 400 bpm. Example of alternans shown at 600 bpm (10 Hz) in B – AP, C - I_{CaL} and D – CaT.

At pacing rates of 480 bpm and above, the steady-state APDR curve bifurcates from a constant APD response to increased pacing to an alternating long-short APD pattern (Figure 5.14A). This long-short alternation in APD (Figure 5.14B) shows the largest difference in the phase 2 plateau phase, which is significantly shortened, corresponding to a decreased I_{CaL} for the shorter beat (Figure 5.14C). CaT decay is longer than the cycle length of the simulation, and thus a secondary peak occurs through the action of voltage-gated LTCCs before the prior CaT has fully decayed. Larger intracellular $[Ca^{2+}]$ during the voltage window in which I_{CaL} is most active

affected I_{CaL} Ca^{2+}-dependent inactivation; thus, I_{CaL} is smaller on the "short" beat, which contributes towards the plateau shortening observed in the AP.

5.3.5 I_{to} Dynamic Clamp

The novel model and the Aslanidi model were compared against experimental data from the Workman Lab under the application of dynamic-clamp intervention, which assessed the role of I_{to} by adding or subtracting I_{to} by adjusting dynamic clamp current (Workman et al. (2012) [33]). In the simulated models, the magnitude of I_{to} was scaled by a factor between 0 and 2 at intervals which matched the experimental data (~ 20% current addition or reduction per step).

Partial inhibition of I_{to} (~20-40% inhibition, 5-10 nS) in the experimental study (Figure 5.15A) resulted in a slowed phase 1 repolarisation (evident through small increases in early-stage repolarisation, APD_{30}), and the phase 2 plateau occurring at elevated membrane potentials. APD is moderately prolongated with partial I_{to} inhibition. In the Holmes model (Figure 5.15B), partial inhibition of I_{to} of the same magnitude (20-40%) produced a slowing of phase 1 repolarisation. However, this manifests significantly larger in APD_{30} than in the experimental data due to the presence of a notch in AP following the phase 0-1 spike increasing in duration, which is not present in the Workman Lab data. The phase 2 plateau is elevated, similar to the experiment, and APD is prolonged significantly at all stages of repolarisation, whereas APD prolongation in the experimental dataset is primarily in the early-mid repolarisation phases (APD_{30} – APD_{50}), with a smaller effect. The Aslanidi model (Figure 5.15C), similarly to the Holmes model and experiment, experiences a slower phase 1 repolarisation and an elevated plateau. APD prolongation occurs equally across all phases of repolarisation, similar to the Holmes model and unlike experiment.

Major inhibition of I_{to} in the experimental data (~80% I_{to} block, 20 nS)~~,~~ slows phase 1 repolarisation further, and elevates the plateau phase higher than partial inhibition (Figure 5.15A). Despite no presence of I_{to} past 100 ms [33], late-stage APD prolongation occurs. In the Holmes model, major I_{to} inhibition (60-80%) produces a "spike and dome" morphology (Figure 5.15B), in which during the domes increase, I_{CaL} current is larger than I_{to}.

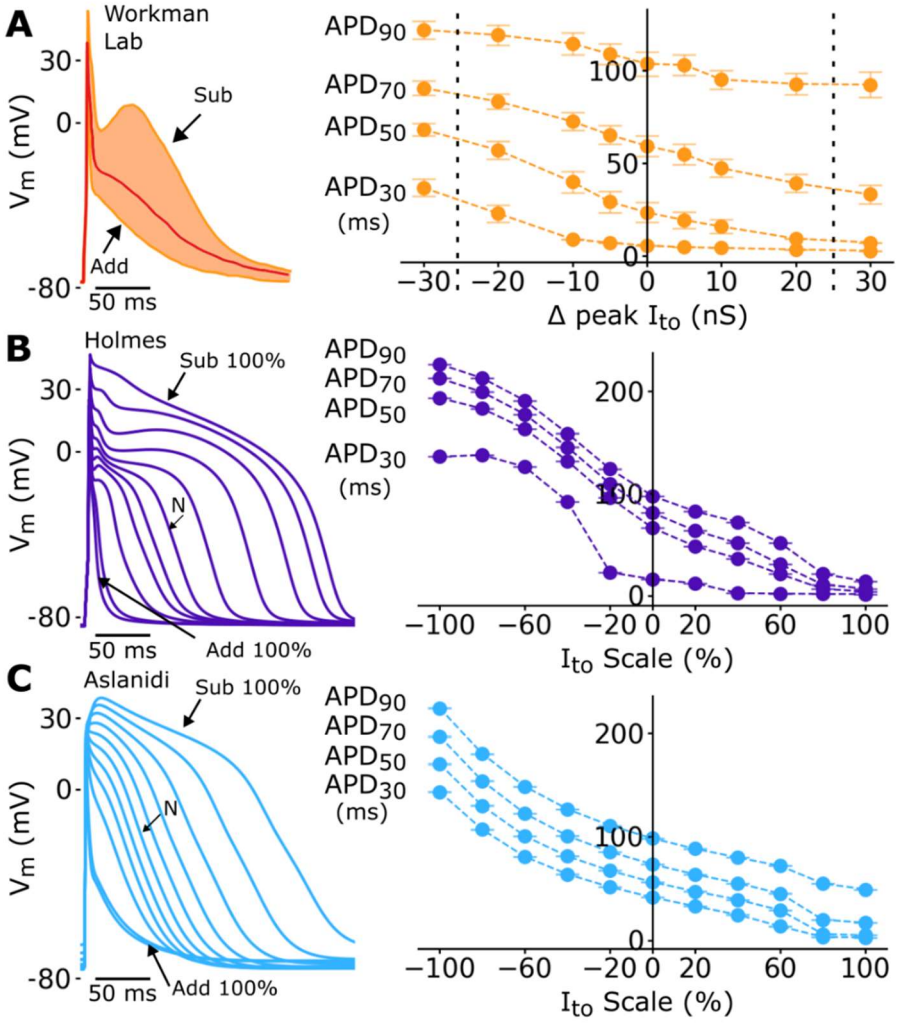

Figure 5.15 Comparison of effects of increasing or decreasing I_{to} conductance on simulated and experimental APs

Comparison of simulated and experimental intervention of an I_{to} dynamic-clamp protocol. A – Workman Lab range of AP morphology and APD changes as a result of adding or subtracting I_{to} via dynamic-clamp. Dotted lines on the APD plot represent 0 and 200% scaling. B – Holmes model simulated I_{to} magnitude scaling from 0 – 200%. C – Aslanidi model simulated I_{to} scaling from 0 – 200%. Workman Lab data was published in Workman et al. (2012) [33].

This "spike and dome" morphology is also seen in the experimental data at full I_{to} block (25-30 nS). Phase 1 repolarisation is markedly slower than in partial inhibition, lowering the magnitude of the phase 0-1 spike. APD prolongation increases significantly again at all stages of repolarisation, with APD_{90} increasing by more than 100% at 60%, 80% and 100% inhibition (control = 97.6 ms; -60% =

190.9 ms; -80% = 212.9 ms; -100% = 226.4 ms), compared to a modest ~ 20 ms (~ 20% increase in APD_{90}) increase from control to full I_{to} block in the Workman Lab data. Thus, the Holmes model significantly overestimates the impact of I_{to} inhibition at higher levels of I_{to} block.

Similarly, the Aslanidi model shows similar behaviour at higher I_{to} inhibition (Figure 5.15C), with APD_{90} increasing exponentially as I_{to} reduction increases (control = 97.2 ms; -80% = 180.1 ms; -100% = 225.5 ms). In the Aslanidi model, the AP peak is delayed and increased with 40% I_{to} suppression and above, with an increased APD at all stages of repolarisation significantly larger than observed within the Workman Lab data. Thus, the Aslanidi model also significantly overestimates the impact of I_{to} inhibition.

Increasing I_{to} via injecting a larger dynamic clamp current in the experimental data (Figure 5.15A) enhanced phase 1 repolarisation, depressing the phase 2 plateau. APD is moderately shortened at all levels of inhibition, most prominently in mid-repolarisation (APD_{50}, APD_{70}). In the Holmes model (Figure 5.15B), moderate upscaling of I_{to} (+20 - 60%) results in larger phase 1 repolarisation, a depressed plateau phase and a significantly shorted APD at mid and late repolarisation stages (APD_{50}, APD_{70} and APD_{90}). Due to the Holmes AP morphology (and Workman Lab AP morphology), APD_{30} remains similar as the phase 0-1 spike is sufficient to reach the 30% repolarisation threshold. Larger I_{to} scaling (+80% - 100%) shortens APD_{90} to very short timescales (< 25 ms) due to rapid membrane repolarisation through the respective activation windows of I_{to} and I_{CaL}. Similar to I_{to} inhibition, the Holmes model overestimates the impact of enhanced I_{to} at larger scales.

Enhancing I_{to} in the Aslanidi model (Figure 5.15C) more accurately reproduced observed changes to AP morphology observed in the Workman Lab data. APD moderately decreases across all repolarisation phases at all levels of enhanced I_{to}, producing a triangular morphology at 180% and 200% I_{to} scaling similar to that of the Workman lab data, but with a significantly lower APD_{70} and APD_{90}. In comparison with the Holmes model, the Aslanidi model better estimates the impact of enhanced I_{to}. In order to understand this, the repolarising currents I_{Kr}, I_{Ks} and I_{sus} which are in the Aslanidi model but not in the novel model were investigated (Figure 5.16; see Section 2.2.1, Table 2.1 for a description of these currents).

As the magnitude of I_{to} was decreased, the rapid and slow delayed rectifier K^+ current peak values were shifted later in the AP, increasing in duration and magnitude under depressed I_{to} current (Figure 5.16 B, C); thus, in addition to depressed I_{to}, I_{Kr} and I_{Ks} contribute relatively more to repolarisation.

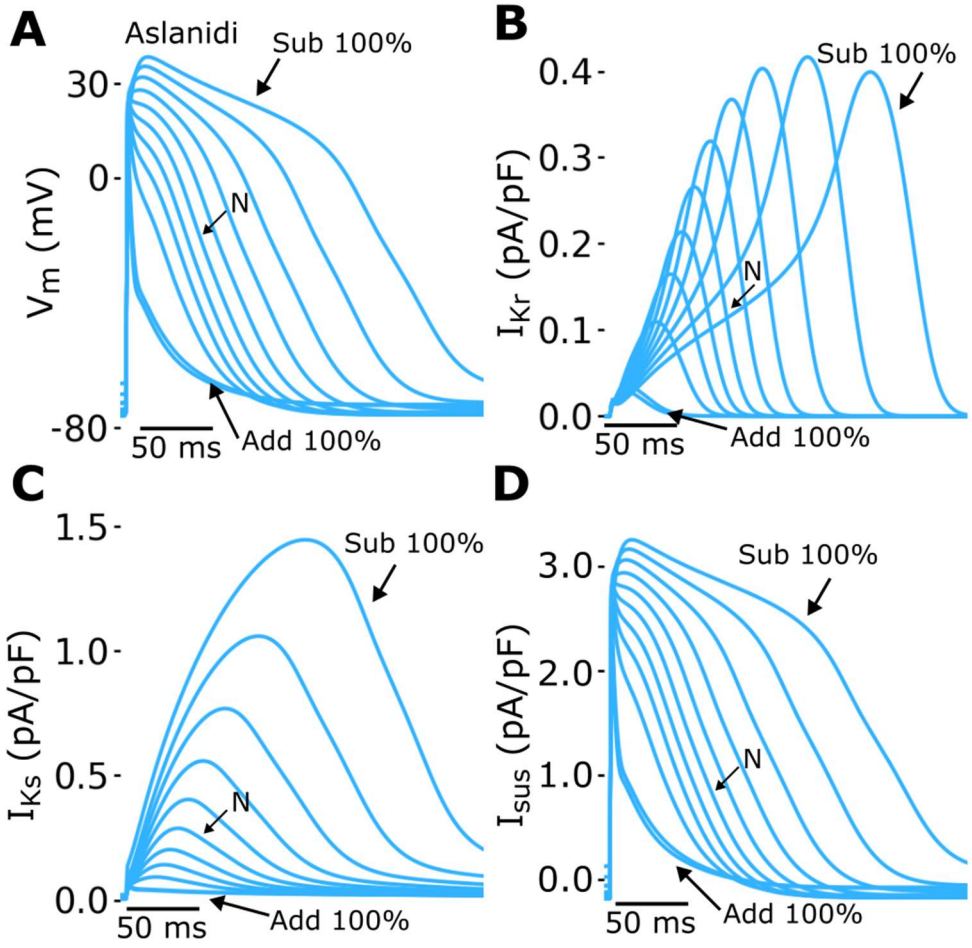

Figure 5.16 Repolarising currents in the Aslanidi model under I_{to} dynamic clamp

Repolarising currents in the Aslanidi model under the same I_{to} dynamic clamp conditions (0 - 200% I_{to} current) as in Figure 5.15. A – AP (as shown in Figure 5.15); B – Rapid delayed rectifier K^+ current, I_{Kr}; C – Slow delayed rectifier K^+ current, I_{Ks}; D – Sustained outward current, I_{sus}.

The sustained outward current, I_{sus}, in the Aslanidi et al. (2009) model [242] is modelled as a voltage-dependent background current with no gating mechanisms; hence, it followed the same morphology as the AP (Figure 5.16D) and contributed relatively more under reduced I_{to}. I_{sus} has the largest magnitude of these

repolarising currents, and therefore contributes the most to repolarisation in the reduction (or absence) of I_{to}.

As the magnitude of I_{to} was increased, both the rapid and delayed rectifier currents reduced significantly and had a shorter duration of activity (Figure 5.16B, C); thus, these currents contribute relatively less. I_{sus} follows the same morphology as the AP and is smaller in magnitude under enhanced I_{to} magnitude. Therefore, under enhanced I_{to}, the other repolarisation currents in the Aslanidi model decrease in magnitude and duration. As I_{to} increases, the other repolarising currents decrease, compensating for the enhanced I_{to} and hence play a role in preventing rapid repolarisation after the upstroke phase; as I_{to} decreases, these repolarising currents increase, partially compensating for reduced repolarisation. These small currents may therefore explain, at least partially, the discrepancies observed between the novel model and the experimental I_{to} dynamic-clamp results.

5.3.6 I_{CaL} Window-Widening Dynamic Clamp

The novel model was compared against experimental data from the Workman Lab under the application of dynamic-clamp intervention of I_{CaL} dynamic-clamp window widening (Figure 5.17) [359].

The activation and inactivation curves of I_{CaL} were progressively widened by simultaneously negatively shifting the $V_{0.5}$ of the activation curve, and positively shifting the $V_{0.5}$ of the inactivation curve in 0.5 mV steps from 2.5 mV to 4.5 mV (Figure 5.17A). The overlapping region underneath the curves indicates the voltage region in which I_{CaL} channels that have not inactivated may potentially re-activate, producing one or more additional I_{CaL} peaks. The Aslanidi model produced minor changes in AP morphology when I_{CaL} window-widening was applied (not pictured) and thus is not discussed.

In the Workman Lab data, increasing the width of this window resulted in prolonged APD through increasing the duration of the phase 2 plateau inside the window regions (highlighted in grey, Figure 5.17B, C). Increasing the window in which I_{CaL} can reactivate prolongs I_{CaL} decay time (Figure 5.15D), and as symmetrical widening increased further (7mV and above), EADs are observed (Figure 5.17B) until 9mV, where a non-repolarising AP is produced with multiple, continuous

EADs. These EADs are shown to be a result of the re-activation of LTCCs during this window phase.

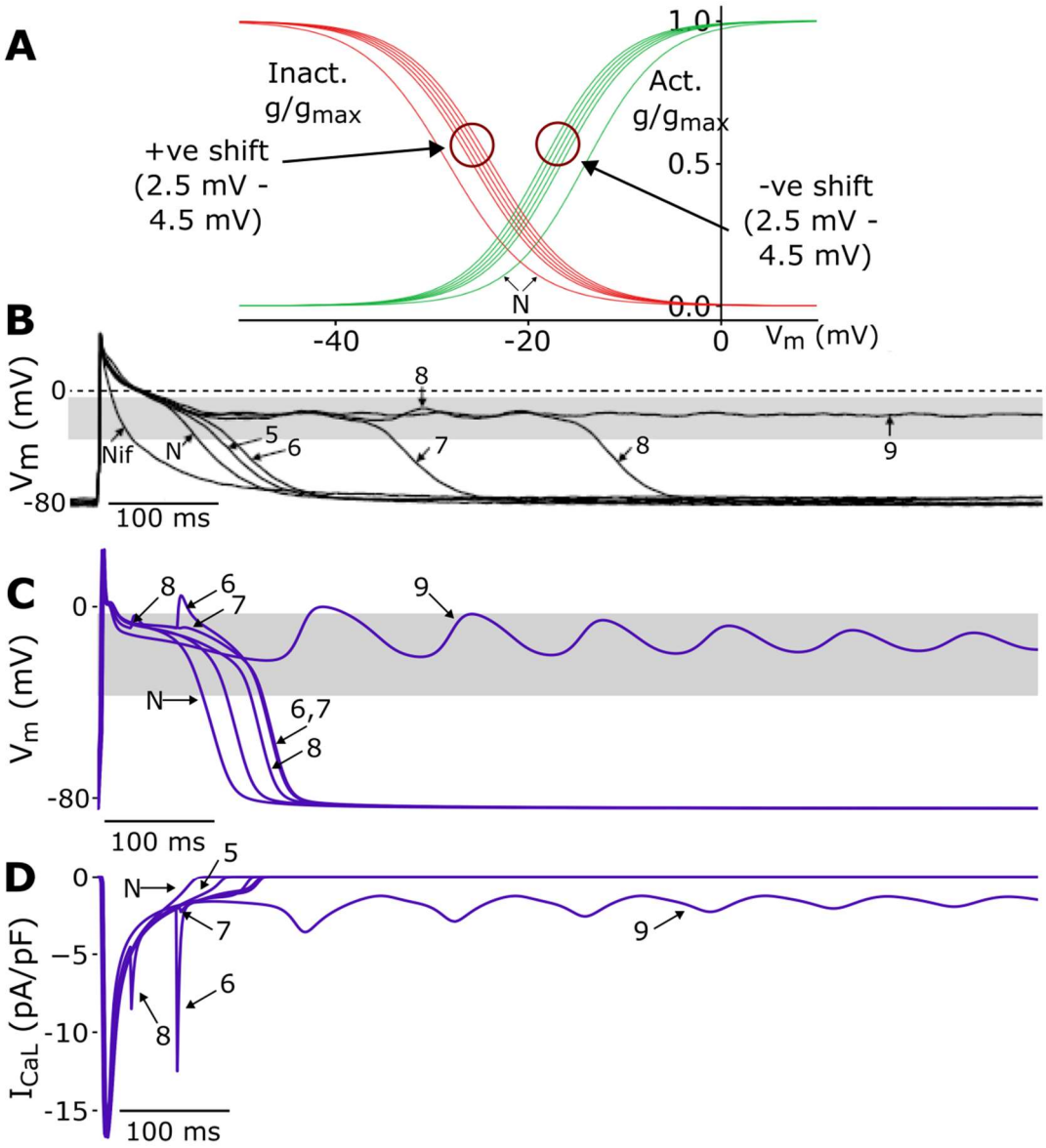

Figure 5.17 Comparison of effects of symmetrical I_{CaL} window-widening on simulated and experimental APs

Comparison of simulated and experimental effects of symmetrical I_{CaL} window-widening. A – I_{CaL} activation and inactivation $V_{0.5}$ shifting from normal (N) by 2.5 mV to 4.5 mV (5 – 9 mV total). B – Workman Lab experimental APs from dynamic clamp widening in A. C – Novel model simulated APs with window-widening in A. D – Simulated I_{CaL} current traces for the novel model. Panel B modified from Kettlewell et al. (2019) [359]

The Holmes model was used to reproduce this experiment in Figure 5.17C: all simulations with window widening (labelled numerically by the total symmetrical mV shift) produced a prolonged APD compared to the control (or normal, N) simulation. Unlike the Workman Lab data, the Holmes model produces EADs at smaller window shifts (6mV onwards), and the scale APD prolongation is not as dependent on window-widening as in the experimental data, where each widening step increases APD progressively. In the Holmes model, the APD prolongation appears to be dependent on the timing an EAD occurs – the 8 mV shift produces an earlier EAD than the 6 and 7 mV shifts. The 7 mV shift produces a smaller EAD than the 6 mV shift but has a similar repolarisation phase and APD. Similar to the Workman Lab data, a symmetrical window-widening of 9mV produces a non-repolarising AP with multiple, continuous EADs.

APD prolongation in the simulation is markedly shorter in the Holmes model than observed in the experimental data, which may be a result of the sharp phase 3 repolarisation phase in comparison to the Workman Lab AP, or may indicate missing ionic flux within in the model, which plays an important role in prolonging the AP when the I_{CaL} reactivation window shifts. Additionally, symmetrical window-widening above 8mV resulted in a transient period of EADs before the novel model reached a stable state. Above a window-widening of 12 mV, the model never repolarises during the 10 minutes of simulation time. The novel model's ability to reproduce EADs with I_{CaL} window shifting makes it suitable for an investigation into how variability in I_{CaL} gating effects rabbit atrial electrophysiology.

5.3.7 Pharmacological Interventions: 4-AP and Nifedipine

The Workman Lab dataset provided data on two pharmacological interventions studied: 4-aminopyridine (4-AP), an I_{to} current blocker (Workman et al. (2000) [369]); and Nifedipine (Nif), an I_{CaL} current blocker (Kettlewell et al. (2019) [359]) at 75bpm and 60 bpm respectively. These studies used concentrations of 1 mM 4-AP, which results in a 90% I_{to} current block, and 3 μM Nif, which results in a 68% I_{CaL} current block. The two simulated models are used to reproduce these interventions and compared to Workman Lab data in Figures 5.18 and 5.19. As the role of I_{to} was investigated in Section 5.3.5, only the specific condition of 4-AP (1 mM) was applied, whereas for the Nif study, I_{CaL} block between 30% and 90% was

applied, including the specific Nif (3 μM) condition, highlighted for direct comparison.

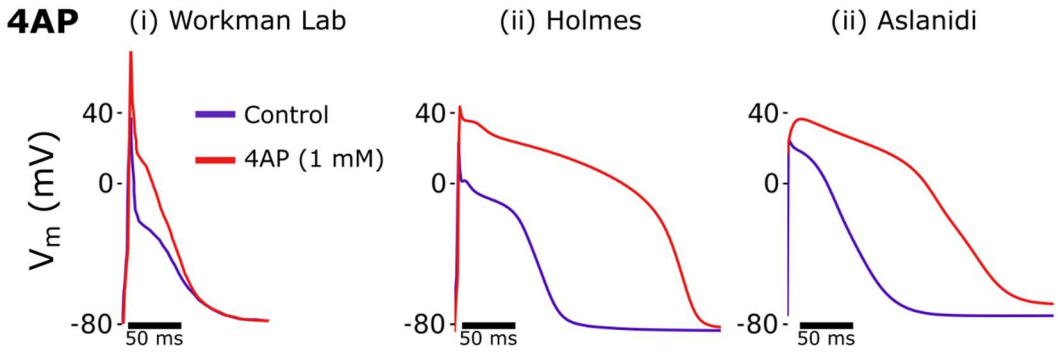

Figure 5.18 Comparison of effects of 4-AP on simulated and experimental APs

Comparison of pharmacological intervention of 4-aminopyridine (4-AP, 1 mM; ~ 90% I_{to} block). 4-AP intervention and control APs for (i) Workman Lab data, (ii) Holmes model and (iii) Aslanidi model.

As stated in Section 5.3.5, major reduction of I_{to} experimentally results in a lesser phase 1 AP repolarisation and elevated phase 2 plateau phase (Figure 5.18i); conversely to the I_{to} reduction study published in Workman et al. (2012) [33], APD is not prolonged with reduced I_{to} in this study (Figure 5.14A). This particular AP morphology has a much lower plateau, which is elevated from significantly below 0 mV, to passing through 0 mV, which will inherently result in a lower I_{to} current in both control and 4-AP intervention comparison to the data presented in Workman et al. (2012) [33] and thus a smaller relative change. The Holmes simulated 4-AP intervention (Figure 5.18ii) also produced a lesser phase 1 repolarisation, resulting in a much smaller spike and a similarly elevated AP plateau phase. APD_{90} increased by ~125% with the 4-AP intervention (control, APD_{90} = 98.7 ms; 4-AP (1 mM), APD_{90} = 220.1 ms), which is substantially larger than Workman Lab data in either Workman et al. (2000) [369] or Workman et al. (2012) [33]. Thus, the Holmes model significantly overestimates the impact of the 4-AP intervention.

Similarly, the Aslanidi model (Figure 5.18iii) displays a lesser phase 1 repolarisation, which instead leads to an increase in membrane potential in phase 1 with major I_{to} inhibition (as observed in Figure 5.14). This again results in an elevated plateau phase and a significantly prolonged APD in the intervention

compared to control, similar to that observed in the Holmes model (control, APD_{90} = 97.1 ms; 4-AP (1 mM), APD_{90} = 220.0 ms). Thus, the Aslanidi model also significantly overestimates the impact of the 4-AP intervention.

The role of I_{CaL} was assessed via the application of Nif (3 μM) in the Workman Lab data (Figure 5.19). This intervention results in a depressed, shorter phase 2 plateau, resulting in a more triangular morphology but a similar APD compared to the control AP (Figure 5.19Ai). The novel model reproduces this shorter, depressed plateau phase but overestimates the impact of Nif intervention on the AP at the concentration introduced in the Workman Lab data (~68% I_{CaL} block) (Figure 5.19Aii). A 40% block of I_{CaL} produces a similar result to the application of Nif in the Workman Lab data, but all scales of I_{CaL} block of 40% and above results in rapidly repolarising triangular morphologies. The Aslanidi model better estimates the impact of Nif on the AP (Figure 5.19Aiii); all scales of I_{CaL} block 40% and above produced similar morphologies as the Workman Lab data, with similar APDs to control.

Kettlewell et al. (2019) [359] present CaT morphology and quantification in the presence of Nif (3 μM); thus, the estimated impact of Nif intervention on simulated Ca^{2+} handling can be assessed in the novel and Aslanidi models. The normalised CaT (Figure 5.19B) for the Aslanidi model produces the same ultra-rapid peak (~ 5 ms) and decay (FWHM ~ 20 ms) as the control model (Figure 5.11A, 5.20B). The Holmes model CaT morphology shows strong agreement to the Workman Lab CaT under the intervention of Nif, with similar CaT peak delay times (Holmes, ~ 100 ms; Workman Lab, ~ 80 ms) and CaT decay (FWHM: Holmes, ~ 370 ms; Workman Lab, ~ 360 ms). However, it must be noted that this agreement is only morphological, as the novel model yielded severe impairment of CICR under the intervention of Nif (Figure 5.19C).

Intracellular diastolic and systolic [Ca^{2+}] biomarkers under the intervention of Nif (Figure 5.19C) in the novel model is observed to be within reasonable agreement with Workman Lab data, falling outside of the standard deviation of the dataset but well within observed values. However, the CaT amplitude was very small (~10 nM), and while this tiny magnitude was similar to the smallest CaT amplitude observations of the Workman Lab dataset, it is clear that CICR was impaired (Figure 5.20).

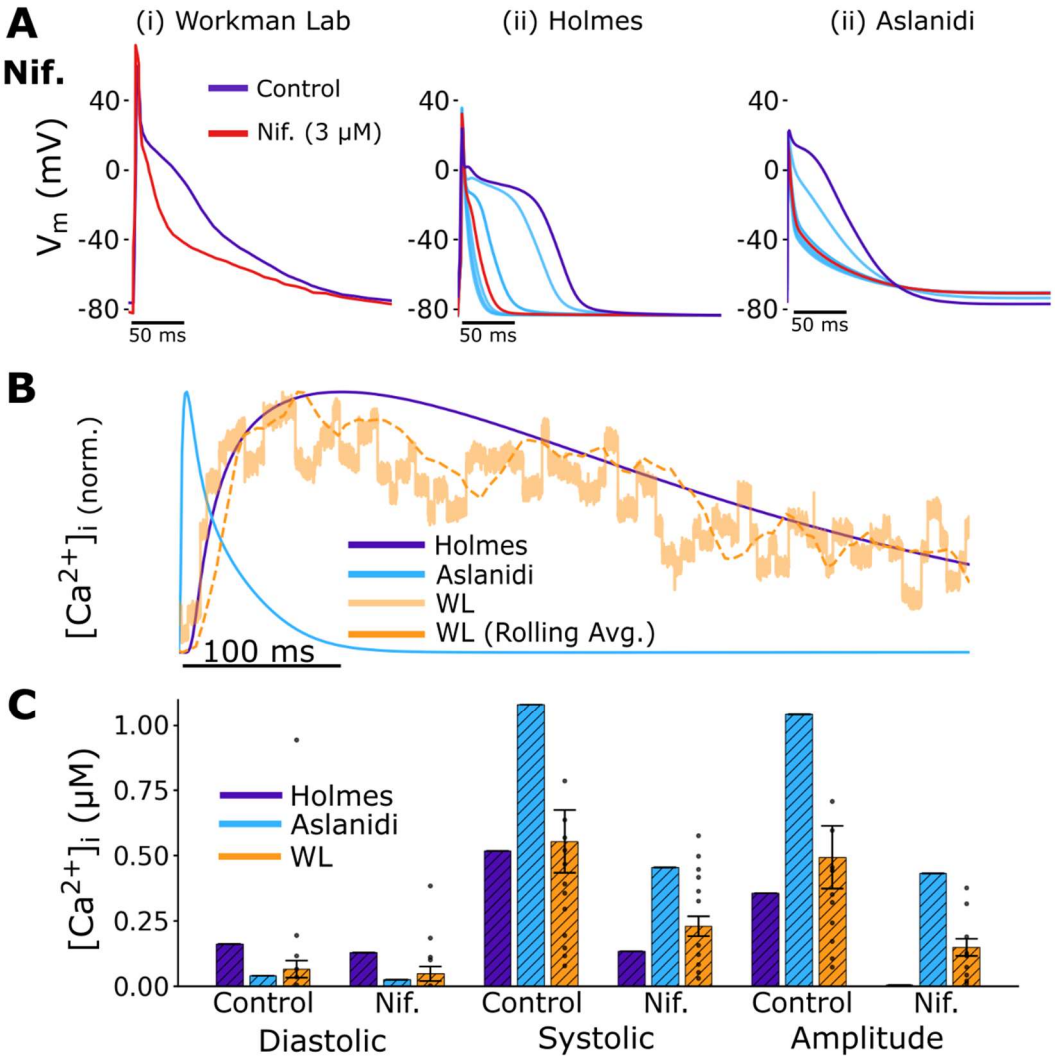

Figure 5.19 Comparison of effects of nifedipine on simulated and experimental APs and CaT.

Comparison of pharmacological intervention of nifedipine (Nif, 3 μM; ~68% I_{CaL} block). A – Nif intervention and control APs for (i) Workman Lab data, (ii) Holmes model and (iii) Aslanidi model. B - Normalised CaTs for each dataset are shown along with an experimental rolling average. C- Quantification of diastolic and systolic $[Ca^{2+}]$, and CaT amplitude in control and under the effect of Nif.

Under the intervention of Nif, the AP produced by the novel model had a negligible plateau phase and rapidly repolarised within 50 ms (Figure 5.20A); the Aslanidi model maintained a similar APD to control under this intervention and produces a similar morphology to the Workman Lab (Figure 5.20B; Figure 5.19A). However, the Aslanidi model displayed large disagreement with Workman Lab CaT

morphology (Figure 5.19B). The Aslanidi model produced a similar CaT morphology with a rapid peak and rapid decay in both control and Nif intervention, with a significantly reduced CaT peak magnitude with Nif (Figure 5.20B), rather than the delayed peak and prolonged decay observed in the Workman Lab. Thus, the Aslanidi model underestimated the impact of Nif on the CaT. Conversely, the novel model overestimated this impact, and the very small CaT (Figure 5.20B, inlay) is indicative of CICR impairment.

The novel models' overestimation of the impact of I_{CaL} block on the action potential, in combination with the direct reduction of I_{CaL} reduced the duration of I_{CaL} considerably (Figure 5.20C), which in turn reduced the flow of Ca^{2+} ions into the cell during the I_{CaL} activation window. The minor fluctuation in intracellular Ca^{2+} was not enough to meet the threshold to activate RyRs and elicit CICR; Kettlewell et al. (2019) [359] also recorded minor CaT amplitudes between ~10 – 20 nM, which may also have been due to impaired CICR. I_{CaL} in the Aslanidi model is affected in a similar way; however, this did not result in similarly drastic changes to the CaT. Additionally, the short, rapid spike morphology of the CaT implies a smaller impact on AP morphology, whereas, in the novel model, CaT has a marked impact. The Na^{+}-Ca^{2+} exchanger also yielded little change from control in the Aslanidi model under Nif intervention (Figure 5.20D), compared to very large changes in the novel model. This, along with the similar CaT morphology under the changes observed in I_{CaL}, implies that that the Aslanidi model underestimates changes in CaT morphology under the intervention of Nif.

Thus, it may be inferred that differences in AP morphology between the novel model and Workman Lab data under the intervention of Nif may be due to some combination of factors. The coupling of intracellular Ca^{2+} and Ca^{2+} currents in the novel model resulted in an overestimation of the impact of reduced I_{CaL}. Alternatively, or additionally, the relative presence (or lack thereof) of minor ionic currents in the novel model which act to depolarise the membrane at lower potentials, which in physiology act to protect against rapid repolarisation when I_{CaL} Is reduced. The Aslanidi model produced a more similar AP to experiment with I_{CaL} block; however, the major differences in CaT morphology, and relatively small impact of I_{CaL} block on the CaT and I_{NCX} suggests this AP agreement may only be

superficial, and it is not mechanistically a better reproduction of the experimental results.

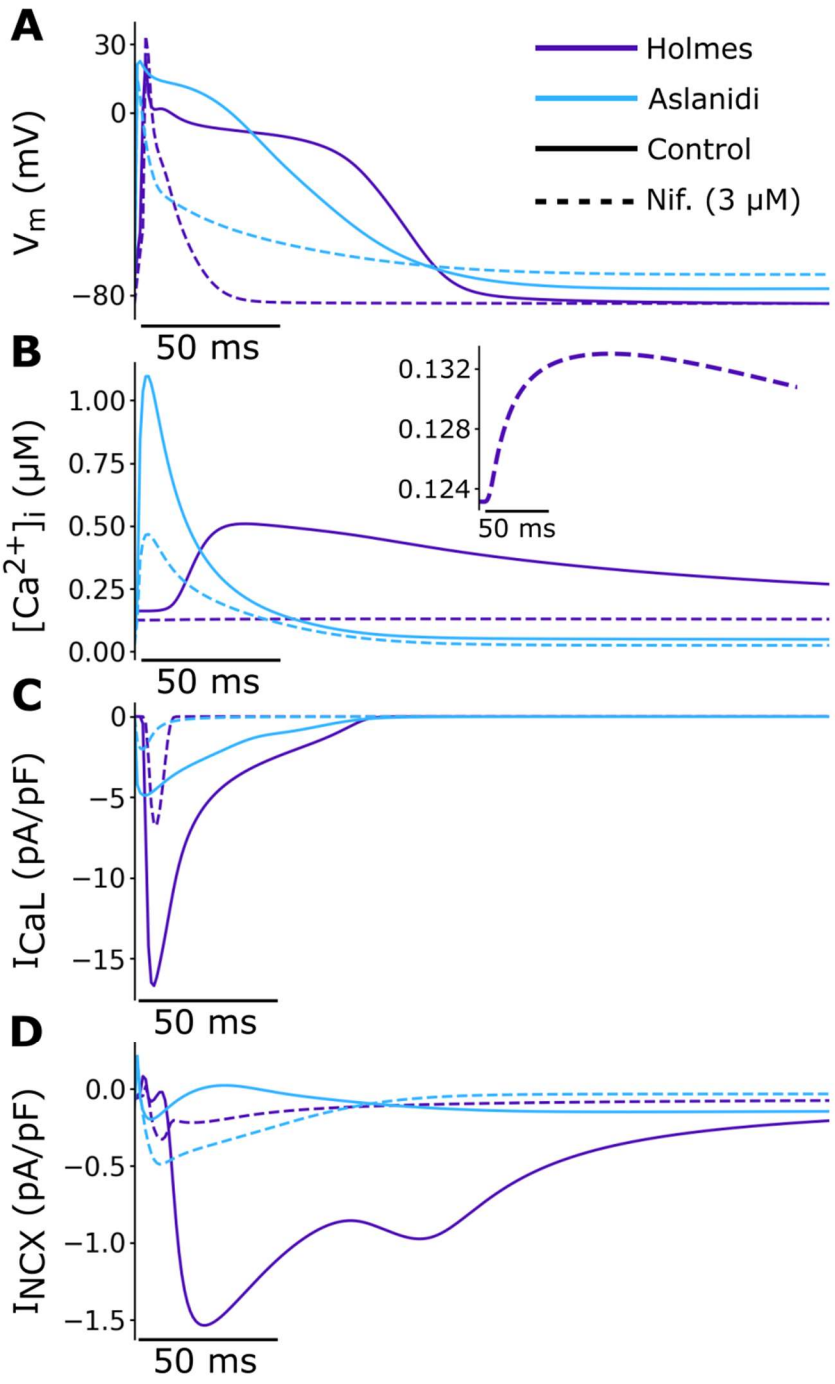

Figure 5.20 Comparison of effects of nifedipine between simulated models

Comparison of effects of nifedipine (Nif, 3 µM; ~68% I_{CaL} block) between the novel and Aslanidi model on A – AP; B – CaT, inlay displays novel model under Nif intervention for the same time scale; C - I_{NCX}. Full lines represent control; dashed lines represent intervention.

5.4 Preliminary Study: Ionic Flux Scaling and Ca^{2+} Handling Variability

The novel model developed in this chapter was used in a preliminary study to investigate the effects of scaling ionic currents and Ca^{2+} handling parameters on the CaT. Major repolarising (I_{to} and I_{K1}) and depolarising (I_{CaL} and I_{NCX}) ionic currents, and Ca^{2+} handling variables which modulate the maximal flux rates of SR-Ca^{2+} uptake (SERCA2a, J_{up}) and SR-Ca^{2+} release (J_{rel}) were scaled in magnitude between x0 and x2 (0 – 200%) at control pacing. All simulations ran for 10 minutes to ensure a steady-state, where the final cycles were analysed.

5.4.1 Modulation of repolarising K^+ Currents: I_{to} and I_{K1}

Repolarising currents underlying the AP are associated with modulating APD, which may impact intracellular Ca^{2+} handling by prolonging or shortening the time period in which membrane potential exists in the range Ca^{2+} currents are most active. The two K^+ currents formulated from Workman Lab data, I_{to} and I_{K1}, were scaled – higher confidence in these currents compared to congruent data, in theory, provides a higher level of confidence in these analyses.

The impact of I_{to} scaling is presented in Figure 5.21; however, the reader may recall that the novel model overestimates the impact of major inhibition or enhancement of I_{to} (Figure 5.14, Figure 5.18). Thus this analysis will focus on the mid-range of I_{to} scaling (scale factor 0.5 – 1.5), as disentangling the impact of I_{to} scaling, and model-specific limitations on the intracellular CaT is a difficult challenge. Despite this, APs and CaTs at these scale factors are presented in Figure 5.21 for completeness. Additionally, impacts of I_{to} modulation on AP morphology is described in Section 5.3.4.

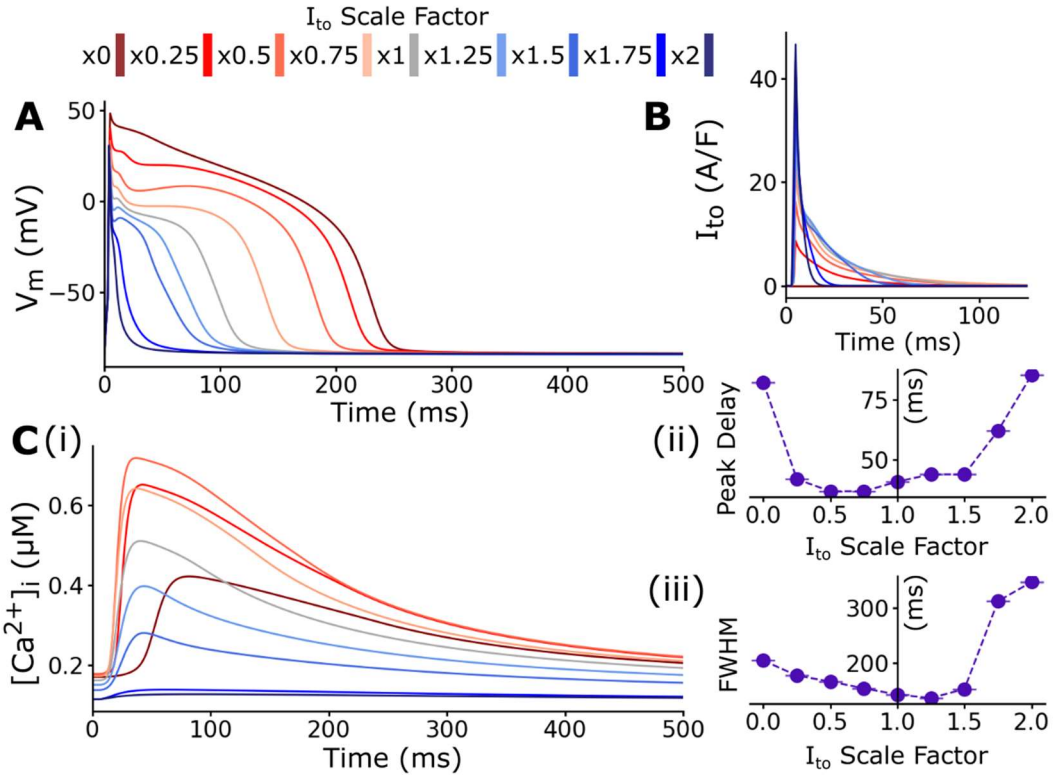

Figure 5.21 I_{to} scaling: effects on AP and CaT at control pacing.

I_{to} magnitude in the Holmes model is scaled by a factor of 0 to 2 in 0.25 intervals at control pacing. A – Steady-state AP at each I_{to} scaling. B - I_{to} current for the same AP. C – (i) Steady-state CaT at each I_{to} scaling; (ii) CaT peak delay (ms) and (iii) CaT duration quantified using FWHM at each I_{to} scaling averaged over the last 10 beats; error bars signify standard deviation. Figure legend at the top relates the colour to scale factor across all panels.

Decreasing the magnitude of I_{to} leads to a smaller peak, and shorter presence of the I_{to} current during the AP, which underlies APD prolongation and elevated plateau potential described in Section 5.3.4 (Figure. 5.21A, B). This APD prolongation is accompanied by higher diastolic [Ca^{2+}] (x0.5 I_{to}: 0.138 μM; x1 I_{to}: 0.162 μM; x1.5 I_{to}: 0.178 μM), and a larger CaT peak magnitude as I_{to} scaling is decreased (x0.5 I_{to}: 0.717 μM; x1 I_{to}: 0.510 μM; x1.5 I_{to}: 0.280 μM). (Figure 5.21Ci). These changes cause a mild increase in the CaT peak delay (Figure 5.21Cii) and a moderate increase in the width of the CaT.

Overall, moderate I_{to} scaling has a marked impact on diastolic [Ca^{2+}] and CaT morphology. Prolongation of the APD, particularly of the phase 2 plateau,

modulates the time period in which membrane potential lies in the region I_{CaL} is most active (see Section 5.3.5), which promotes or inhibits Ca^{2+} efflux through these channels. Thus, CICR is impacted as this is dependent on LTCC activity, which is visible in changes in the CaT.

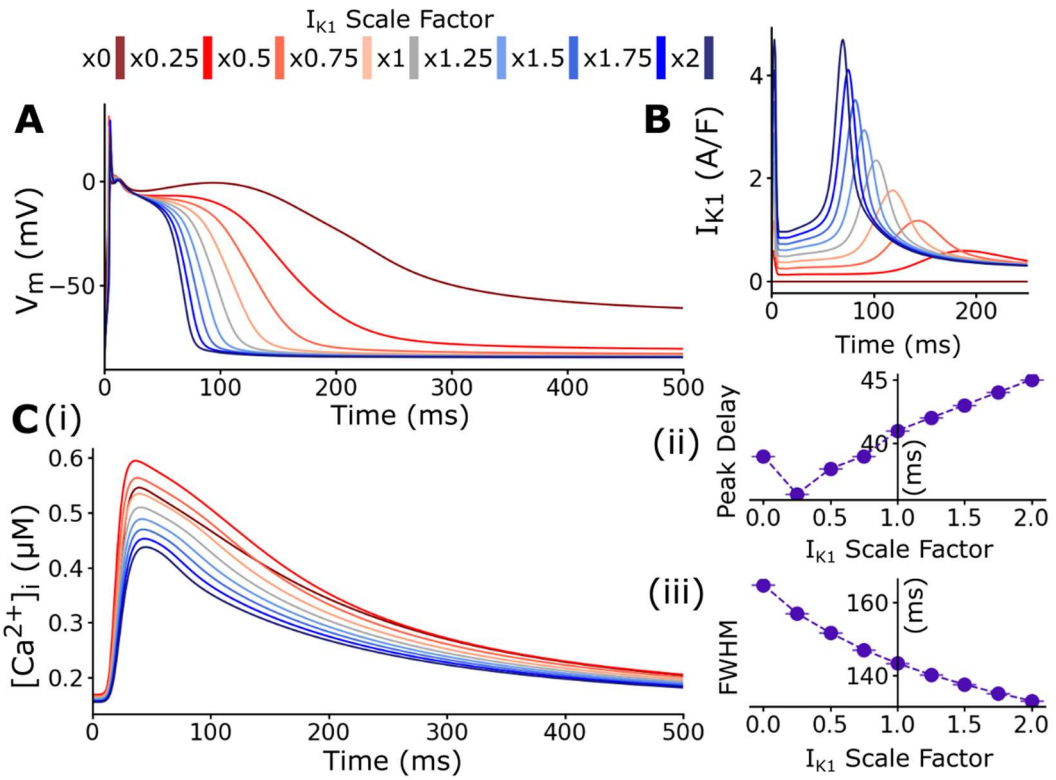

Figure 5.22 I_{K1} scaling: effects on AP and CaT at control pacing.

I_{K1} in the Holmes model is scaled by a factor of 0 to 2 in 0.25 intervals at control pacing. A – Steady-state AP at each I_{K1} scaling. B - I_{K1} current for the same AP. C – (i) Steady-state CaT at each I_{K1} scaling; (ii) CaT peak delay (ms) and (iii) CaT duration quantified using FWHM at each I_{K1} scaling averaged over the last 10 beats; error bars signify standard deviation. Figure legend at the top relates the colour to scale factor across all panels.

I_{K1} scaling also has a significant effect on AP morphology (Figure 5.22A), primarily through modulation of late-stage repolarisation at x0.5 – x2 scaling and then through a rise in RMP at x0 – x0.25 scaling. The late plateau phase is less affected by I_{K1} scaling and is not elevated or depressed unless I_{K1} is blocked completely. Scaling I_{K1} primarily increases the magnitude of the current during the AP (Figure 5.22B)

but has a secondary effect of linearly delaying the second peak of I_{to} current from ~75ms after stimulation at 200% scaling to ~175ms at 25% scaling.

CaT morphology is less affected by I_{K1} than I_{to} (Figure 5.22C). Diastolic [Ca^{2+}] remains similar for all values of I_{K1} scaling, and CaT peak magnitude increases as I_{K1} is reduced between x0.25 and x2. Full block of I_{K1} causes a significant rise in RMP, as expected, and this deviates from this trend, with a smaller increase in CaT peak magnitude than x0.5 or x0.75 scaling. For all I_{K1} scale factors, there is a small increase in CaT width as I_{K1} is decreased, and little change in the CaT peak delay at all scales.

Both I_{to} and I_{K1} impact AP morphology through prolongation or shortening of phase 2 and phase 3 repolarisation, respectively. I_{to} has the larger effect on intracellular Ca^{2+}, the impact of I_{to} between 0.5x and x1.5 scaling was greater than the full range of I_{K1} modulation investigated.

5.4.2 Modulation of depolarising Ca^{2+} Currents: I_{CaL} and I_{NCX}

Two depolarising Ca^{2+} currents were investigated, I_{CaL} and I_{NCX}, which both exhibit Ca^{2+}-dependence: Ca^{2+}-dependent inactivation in the I_{CaL} formulation, whereas I_{NCX} accounts for intra- and extra-cellular concentrations of Ca^{2+} and Na^{+} ions. The reader may recall that this model overestimated the impact of applying Nifedipine, a pharmacological I_{CaL} inhibitor, in Section 5.3.6, thus the impact of I_{CaL} is primarily investigated in the range of x0.5 – x2 scaling.

Increasing I_{CaL} prolongs APD (Figure 5.23A), primarily through the extension of the phase 2 plateau (x0.75 – x2 scaling), through the model shows a depressed plateau phase for x0.5 scaling. This prolongation is associated with an increase in I_{CaL} magnitude, and prolongation of I_{CaL} activation in the AP (Figure 5.23B). Due to its critical role in initiating CICR, enhanced or inhibited I_{CaL} has a major impact on CaT peak magnitude (Figure 5.23C) (x0.5 I_{CaL}: 0.149 μM; x1 I_{CaL}: 0.510 μM; x1.5 I_{CaL}: 0.924 μM; x2 I_{CaL}: 1.67 μM). A biphasic relationship between I_{CaL} scale and CaT peak delay is observed (Figure 5.23Ci). From x0 to x1 I_{CaL}, the time-to-peak decreases due to a larger efflux of Ca^{2+} ions through LTCCs, which promotes faster CICR; from x1 to x2 I_{CaL}, CaT peak delay increases due to a prominent, later peak in the CaT. This delayed increase may be due to increased and prolongated I_{CaL} activation (Figure 5.23B), due to APD prolongation in the voltage window I_{CaL} is

largest, which produces further Ca^{2+} influx after the initial CICR mechanism. There is no change in the width of the CaT above x0.75 scaling. The increases present below this scaling are likely due to the overestimation of the impact of I_{CaL} inhibition on the AP (Figure 5.19, Figure 5.23A). Overall, it is clear that the modulation of I_{CaL} produces significant variation in the CaT.

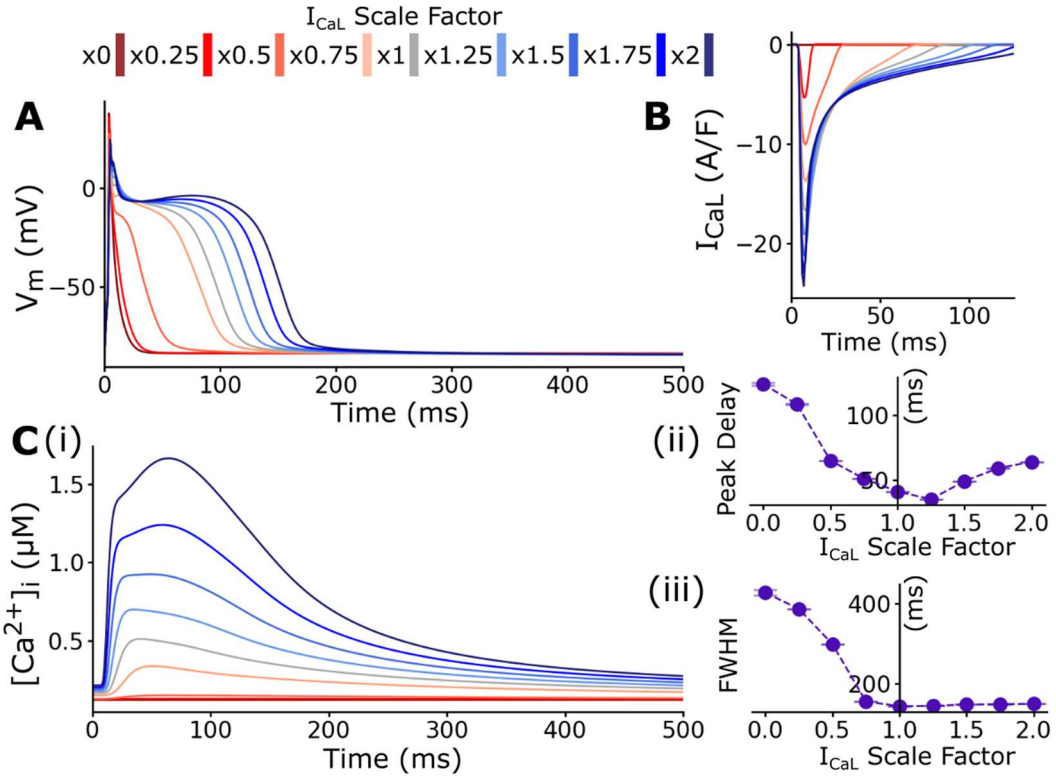

Figure 5.23 I_{CaL} scaling: effects on AP and CaT at normal pacing.

I_{CaL} in the Holmes model is scaled by a factor of 0 to 2 in 0.25 intervals at control pacing. A – Steady-state AP at each I_{CaL} scaling. B - I_{CaL} current for the same AP. C – (i) Steady-state CaT at each I_{CaL} scaling; (ii) CaT peak delay (ms) and (iii) CaT duration quantified using FWHM at each I_{CaL} scaling averaged over the last 10 beats; error bars signify standard deviation. Figure legend at the top relates the colour to scale factor across all panels.

I_{NCX} was selected to be modulated as it plays an important role in the extrusion of intracellular Ca^{2+} after cellular contraction (see Section 2.2.3 for more detail). Within the novel model, its presence is a source of uncertainty, as it was taken from the Grandi-Bers human Ca^{2+} handling model without modification [44]. Scaling

I_{NCX} may provide insight into its role in the rabbit atrial AP and CaT, shown in Figure 5.24.

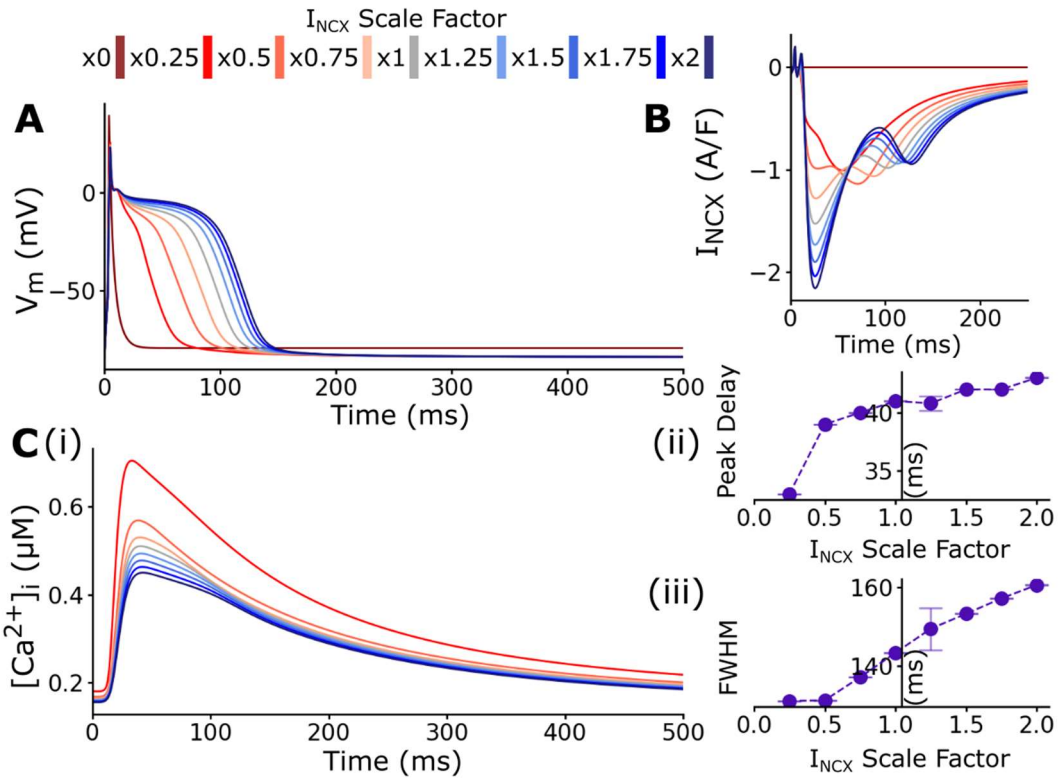

Figure 5.24 I_{NCX} scaling: effects on AP and CaT at normal pacing.

I_{NCX} in the Holmes model is scaled by a factor of 0 to 2 in 0.25 intervals at control pacing. A – Steady-state AP at each I_{NCX} scaling. B - I_{NCX} current for the same AP. C – (i) Steady-state CaT at each I_{NCX} scaling; (ii) CaT peak delay (ms) and (iii) CaT duration quantified using FWHM at each I_{NCX} scaling averaged over the last 10 beats; error bars signify standard deviation. Figure legend at the top relates the colour to scale factor across all panels.

Scaling I_{NCX} produces a significant impact on APD (Figure 5.24A): enhanced I_{NCX} prolongs the phase 2 plateau while inhibited I_{NCX} shortens it compared to the control scale. In the absence of I_{NCX}, no plateau phase is observed, and the AP rapidly repolarises. The effect of scaling I_{NCX} has a complex effect on the morphology of the I_{NCX} current during the AP (Figure 5.24B). The initial peak and secondary negative peak remains similar, increasing in magnitude as I_{NCX} scale increases, however, the upwards inflection following this is shifted, and relative changes to current magnitude are enhanced (x0.5 to x2 scaling), or this upwards inflection does

not exist (x0 to x0.25 scaling). As scaling increases at all levels, I_{NCX} activity is slightly prolonged.

At full I_{NCX} block, diastolic and systolic [Ca^{2+}] rise with each subsequent beat and does not stabilise; explained by due to the role of I_{NCX} in extruding intracellular Ca^{2+} following ECC, and the long pacing times required to reach steady-state in the model. From x0.25 to x2 scaling, peak CaT magnitude decreases as I_{NCX} increases and produces a flatter, broader peak (Figure 5.24Ci). This is due to I_{NCX} extruding Ca^{2+} in greater quantities before 100ms (Figure 5.24B, first negative peak), thus acting against the CICR mechanism. This broader peak does not impact the peak delay time (Figure 5.24Cii) but does increase the CaT width (Figure 5.20Ciii) considerably.

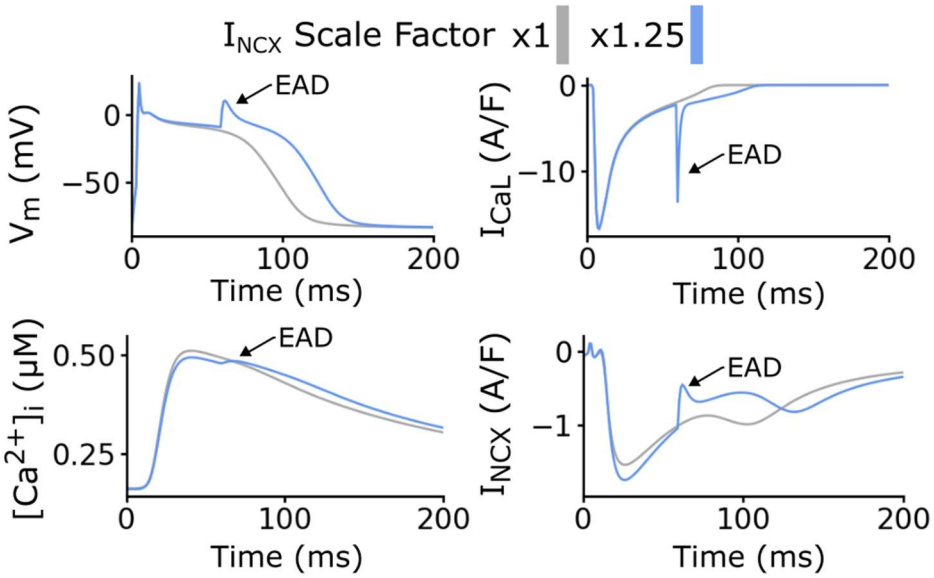

Figure 5.25 EAD produced through enhanced I_{NCX} scaling

An example of a simulated EAD in the Holmes model with enhanced I_{NCX} (x1.25) at normal pacing. The timing of the EAD coincides with the re-activation of I_{CaL} and a sharp increase in I_{NCX}. Control (x1 scale factor) is shown for comparison.

At x1.25 I_{NCX}, a large standard deviation is observed in the FWHM (Figure 5.20Ciii), caused by an EAD (Figure 5.25). As a predominately inward (depolarising) current, increasing in I_{NCX} promotes EADs through APD prolongation [395, 396]. Additional EADs were produced during pacing to steady-

state at higher I_{NCX} scaling (not shown). Overall, scaling both Ca^{2+} dependent currents exhibited major influence on Ca^{2+} variability and AP morphology.

5.4.3 Modulation of Ca^{2+} Fluxes: J_{up} and J_{rel}

In addition to modulation of ionic currents, the rates of SR-Ca^{2+} uptake and release, J_{up} and J_{rel} were scaled from 0 to 200% to investigate how they affected the AP and CaT in the novel model and assess the role these fluxes have on the Ca^{2+} dependent currents, I_{CaL} and I_{NCX}.

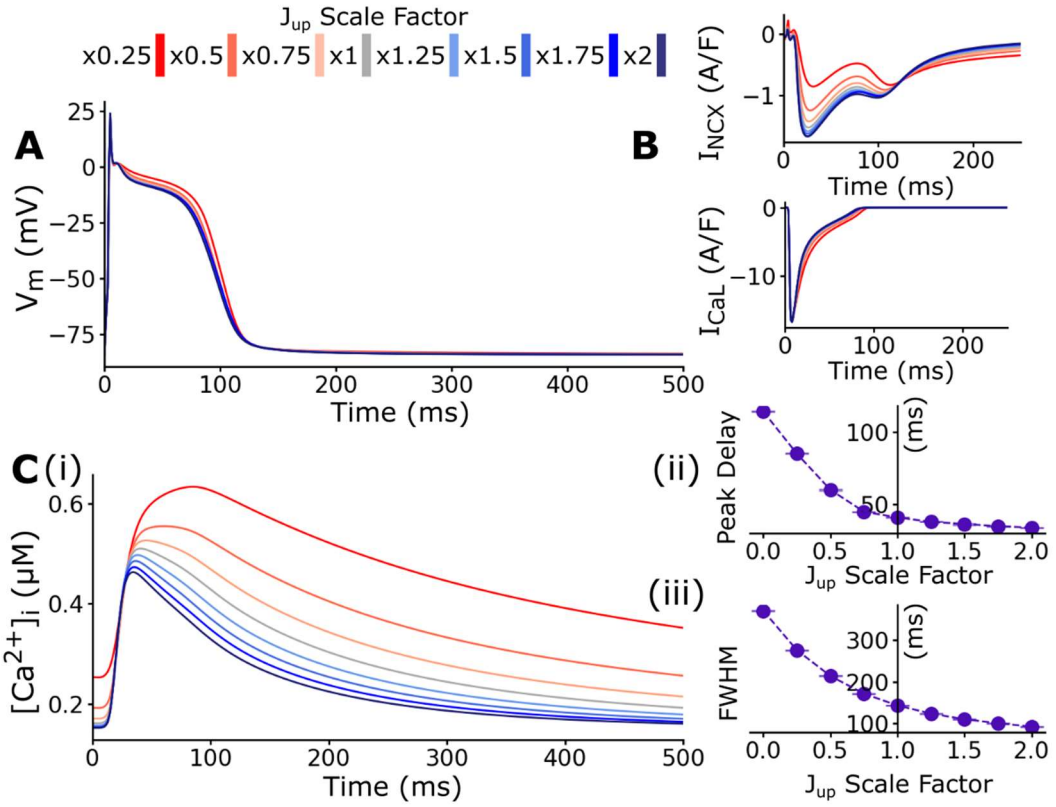

Figure 5.26 J_{up} scaling: effects on AP and CaT at normal pacing

J_{up} in the Holmes model is scaled by a factor of 0 to 2 in 0.25 intervals at control pacing. A – Steady-state AP. B – Ca^{2+}-dependent currents, I_{NCX} and I_{CaL}, for the same AP. C – (i) Steady-state CaT; (ii) CaT peak delay (ms) and (iii) CaT duration quantified using FWHM at each J_{up} scaling averaged over the last 10 beats; error bars signify standard deviation. Figure legend at the top relates the colour to scale factor across all panels. x0 scaling is excluded from panels A, B and Ci for clarity but included in Cii-iii.

J_{up} scaling produced little effect on AP morphology (Figure 5.26A): reducing J_{up} resulted in a minor elevation of the phase 2 plateau but did not affect APD. Similarly, scaling J_{up} has little impact on I_{CaL} (Figure 5.26B), but does significantly modulate the magnitude of I_{NCX} without complex morphological changes observed when scaling I_{NCX} directly (Figure 5.24B), which supports the hypothesis that APD prolongation was the cause of those complexities.

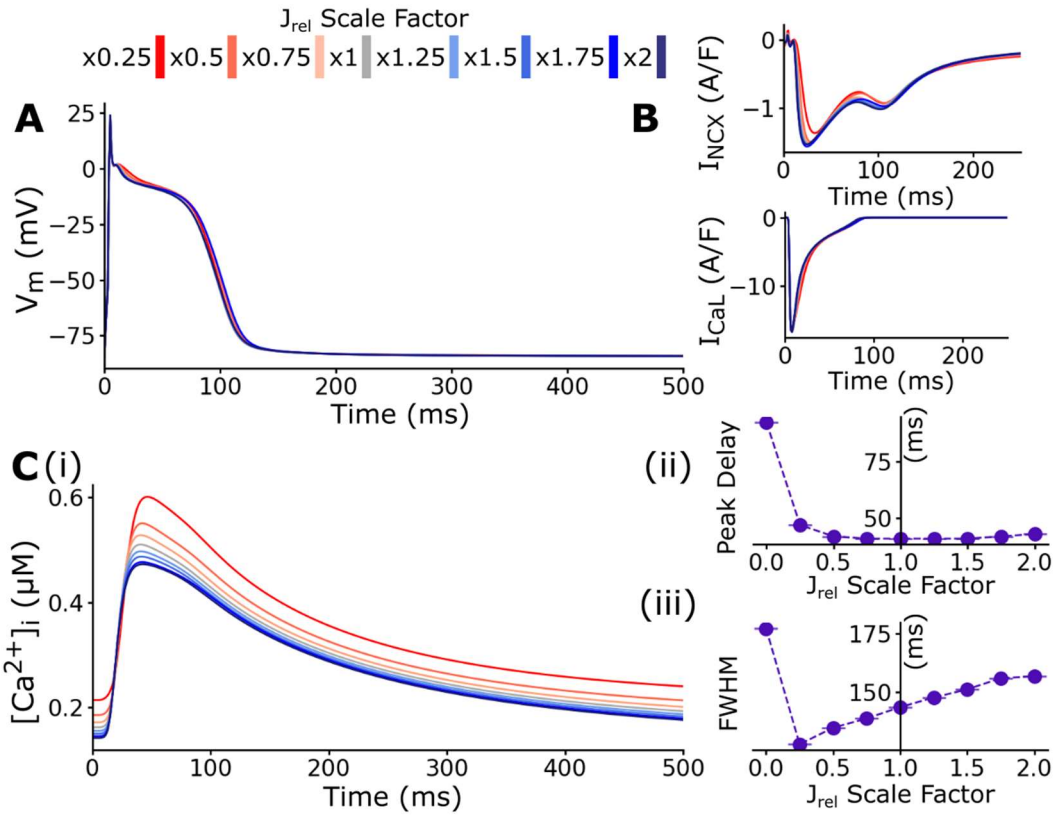

Figure 5.27 J_{rel} scaling: effects on AP and CaT at normal pacing.

J_{rel} in the Holmes model is scaled by a factor of 0 to 2 in 0.25 intervals at control pacing. A – Steady-state AP. B – Ca^{2+}-dependent currents, I_{NCX} and I_{CaL}, for the same AP. C – (i) Steady-state CaT; (ii) CaT peak delay (ms) and (iii) CaT duration quantified using FWHM at each J_{rel} scaling averaged over the last 10 beats; error bars signify standard deviation. Figure legend at the top relates the colour to scale factor across all panels. x0 scaling is excluded from panels A, B and Ci for clarity but included in Cii-iii.

Reduced SR-Ca^{2+} uptake results in a prolonged CaT (Figure 5.26C), as expected due to the role of SERCA2a in ECC (refer to Section 2.2.3 for a detailed discussion). Additionally, reduced SR-Ca^{2+} uptake correlated with an increase in diastolic [Ca^{2+}]

and CaT magnitude, which is congruent with the experimental literature [14, 164, 165] and the results of reduced global SERCA2a activity discussed in Chapter 4. CaT peak delay time and CaT width both increased exponentially with a reduction in J_{up}, as a consequence of slower Ca^{2+} sequestration. As expected, a complete block of J_{up} caused intracellular Ca^{2+} loading and the model did not reach steady state (not shown).

Similarly, to changes in the rate of SR-Ca^{2+} uptake, modulation of SR-Ca^{2+} release rate also produced a minor impact on AP morphology (Figure 5.27A) and also made minor changes to I_{CaL} or I_{NCX} currents throughout the AP (Figure 5.27B). Decreasing J_{rel} from x1 to x0 produced larger changes in the CaT than increasing J_{rel} from x1 to x2 (Figure 5.27Ci). A reduction in the rate of SR-Ca^{2+} release resulted in an increase in diastolic [Ca^{2+}] and CaT magnitude, similar to reducing J_{up} but at a much lower magnitude. This behaviour is observed at steady-state, following a period of pacing in which the higher levels of SR-Ca^{2+} reduced SR-Ca^{2+} load over time, as J_{up} no longer balanced this by increasing SR-Ca^{2+} uptake this led to a smaller CaT magnitude at steady-state – this effect correlated well with increases in J_{rel}. These changes did not result in changes to CaT peak delay (except for total J_{rel} block, Figure 5.27Cii), and produced a minor increase in the FWHM of the CaT as J_{rel} increased (Figure 5.27Cii).

Overall, modulation of J_{up} produced much more prominent impacts on intracellular Ca^{2+} handling than J_{rel}, with neither SR-Ca^{2+} flux playing a significant role in determining AP morphology, or I_{CaL} current during the AP. However, scaling of J_{up} produced a significant change in magnitude of I_{NCX} current during the action potential, with the forward-mode of I_{NCX} increasing as J_{up} increased.

5.5 Discussion

In this chapter, a novel model of rabbit atrial electrophysiology has been developed specifically for the Workman Lab dataset [33, 359, 368–371] (rather than a general model), utilising mathematical descriptions of the primary ion currents underlying rabbit atrial electrophysiology based on rabbit atrial myocyte data from a single, congruent source (Figures 5.1 - 5.6). These formulations were integrated with the Grandi-Bers human atrial Ca^{2+} handling model [44], with rabbit-atrial specific

formulations from the Aslanidi et al. (2009) rabbit atrial model [37, 242] replacing human-specific formulations where possible. This novel model was tested for stability (Figure 5.7) then validated against a collection of data obtained by Workman Lab: comparing AP morphology (Figure 5.8); AP biomarkers (APD, APA, RMP; Figures 5.9, 5.10); CaT and intracellular [Ca^{2+}] (Figure 5.11); rate-dependence of APD; CaTs and alternans (Figures 5.11 - 5.14), as well as pharmacological and dynamic clamp interventions (Figures 5.15 – 5.20). Additionally, the novel model was compared with a range of experimental data from the wider literature throughout this chapter, alongside the Aslanidi rabbit atrial model to provide insight into what is missing from the model, which aims to explain the discrepancies between simulation and experiment. This model was then used for a preliminary study into the effects of modulating the conductance of several ionic currents and Ca^{2+} flux parameters on intra-cellular Ca^{2+} variability (Figures 5.20 - 5.27).

5.5.1 Model Validation and Comparison

The novel rabbit atrial model can be paced to a steady-state up to 600 bpm (10 Hz) (Figure 5.7). Stable pacing at 10 Hz (600 bpm) has not been published in other studies so far: Aslanidi et al. (2009) showed unstable pacing at 600 bpm with a rising RMP and CaT loading [242], and the author of this thesis published a short study integrating the Aslanidi model with the Colman et al. (2017) integrated spatio-temporal Ca^{2+} handling model [3, 49] which reached a pacing rate of 6-8 Hz. This offers an advantage over existing general models and may provide the basis of a platform to study atrial tachycardia or fibrillation which requires pacing rates exceeding 350-400 bpm [344, 397].

The novel model produces APs within agreement with Workman Lab recorded AP morphologies (Figure 5.8). This prolonged plateau phase is not present within the Aslanidi model, potentially due to the inclusion of a greater repolarisation reserve – the existence of a redundancy of repolarising currents, which provide a safety mechanism to prevent excessive APD prolongation and EADs [341, 398].

AP biomarkers generally match well with Workman Lab quantified biomarkers, including APD_{50}, APD_{90}, APA and RMP at a control pacing rate of 75 bpm (Figures 5.9, 5.10). There exists a discrepancy between recorded dV/dT_{max} values by the Workman Lab and the model's produced values, due to inducing model instabilities

by increasing dV/dT_{max} through scaling I_{Na} conductance any higher. However, the value produced by the model is in direct agreement with Jiang et al. (2017) [377] and well within the range published in the wider experimental literature.

Normalised CaT morphology shows an improved agreement with individual cell CaTs recorded by the Workman Lab over the Aslanidi model (Figure 5.11), with similar time-to-peak values, with the caveat of a shorter CaT decay timescale (measured as FWHM) than the Workman Lab CaT but within reasonable agreement. For the first time, a model of rabbit atrial electrophysiology was able to validate the produced CaT with quantified intracellular [Ca^{2+}] measurements from a congruent data source [359].

The novel model showed good agreement with systolic [Ca^{2+}] and CaT amplitude measurements and produced a diastolic [Ca^{2+}] within the full range of observed values with better agreement than the Aslanidi model. It should be noted that the Aslanidi rabbit atrial model used contains a qualitative rather than quantitative description of intracellular Ca^{2+} and does not include a Ca^{2+}-dependent component of I_{CaL}; thus, it is not well suited for Ca^{2+}-handling studies [242]. Other studies using this model often integrate the Aslanidi electrophysiological AP model with more physiological, non-rabbit specific Ca^{2+} handling models [3, 242, 367]. This novel model takes a similar approach using the Grandi-Bers human atrial Ca^{2+} handling model. This represents an improvement over the Aslanidi model in two ways: firstly, by the integration of a novel formulation of I_{CaL} validated against congruent experimental data with agreement; secondly, the resulting CaT was validated against quantitative experimental data with agreement. The Vagos et al. (2020) [48] population model (see 5.1.1 for details), which used the Heijman human atrial Ca^{2+} handling model [361], also validates CaT morphology against Kettlewell et al. (2019) [359] with good agreement, but without any further validation against pharmacological interventions.

There is a lack of published data of rabbit atrial APD-rate dependence, and as such, the model was validated against two non-congruent examples from Verkerk et al. (2012) [378] and Fu et al. (2016) [386], with which neither the novel nor Aslanidi simulated models reproduce consistent agreement (Figure 5.12). The Holmes model produced an APD_{50} rate dependence curve which agrees with Fu et al. (2016) for rabbit-associated pacing rates (120 bpm – 300bpm) but not at lower pacing rates.

Both simulated models showed significantly different APD_{90} rate dependences. The novel model produced an APDR curve (S1-S2 protocol) which follows a similar trajectory to the Workman et al. (2000) [369] dataset but at significantly higher values of APD_{90}. The decrease of APD_{50} as the pacing rate increased is in opposition with Hou et al. (2017) [366], who discussed early-stage prolongation of APD_{20} and APD_{50} as a result of the relative rate-dependent reductions of I_{to} and I_{CaL} due to their slow reactivation kinetics.

The author of this thesis published a short conference proceeding where the Aslanidi AP model was integrated with the Colman et al. (2017; 2020) spatio-temporal Ca^{2+} handling model [3, 49], which provided better agreement with the data published by Verkerk et al. (2012) [378]. This suggests that differences in the relative simulated intracellular Ca^{2+} handling may play a role in determining APD rate-dependence. To the author's knowledge, there is no published data on CaT rate-dependence in rabbit atrial myocytes. However, the novel model CaT rate-dependence data (Figure 5.13) shows that CaT amplitude increases non-linearly as the pacing rate increases from 60 bpm to 300 bpm. A larger CaT magnitude is associated with a prolonged APD [193, 308]; thus, differences in simulated intracellular Ca^{2+} handling and reality may explain the differences in APD rate-dependence.

The novel model produced spontaneous AP and CaT alternans at pacing rates, including and exceeding 480 bpm (Figure 5.14); to the author's knowledge, this feature has not been published in other contemporary rabbit atrial models, but this phenomenon has been demonstrated experimentally. Kulkarni et al. (2015) [399] observed that a significant portion of isolated whole rabbit hearts underwent pacing-induced alternans at pacing rates exceeding 375 bpm. Martišienė et al. (2015) [400] also discuss observations of pacing-rate induced alternans in isolated rabbit hearts with acute regional ischemia. Thus, future work in developing this novel model to a tissue-scale model may present interesting opportunities to research alternans at larger scales in health and pathology.

5.5.2 Reproducing Pharmacological and Dynamic Clamp Interventions

The novel model developed in this chapter significantly overestimates the impact of large inhibition of enhancement of I_{to} on the AP compared to experimental dynamic-clamp injection of I_{to} performed by the Workman Lab (Figure 5.15) [33], and under the intervention of an I_{to} channel blocker, 4-AP (Figure 5.18). Moderate

alterations to I_{to} scaling were qualitatively reproduced, however all scaling resulted in overestimations in morphological and quantitative impacts on APD. The emergence of this behaviour in a model containing primary ion currents well characterised to reproduce action, kinetics and relative magnitudes from a congruent source suggests that there must be a discrepancy between simulation and reality.

Overestimation of the effects of increasing the magnitude of I_{to} on AP morphology in the novel model suggests a gap in knowledge of quantified inward currents active at more negative voltage ranges, such as I_{NCX} or background currents (I_{Nab}, I_{Cab}, I_{Clb}). Overestimation of APD shortening was also observed in a congruent human atrial electrophysiology model by Colman et al. (2018) [43], which did not contain updated formulations of these currents. The Aslanidi model more accurately estimates the impact of I_{to} enhancement on the AP; this model contains a different description of I_{NCX}, which may support this conclusion, however differences in intracellular Ca^{2+} handling may also play a role. Additionally, the Aslanidi model contains formulations for repolarisation reserve currents, I_{Kr}, I_{Ks} and I_{sus}. As I_{to} was increased, the magnitudes of these currents decreased (Figure 5.16); conversely, when I_{to} was decreased, these currents increased in magnitude and produced greater contributions towards repolarisation. The magnitude of these currents were substantially lower than I_{to} under control conditions, however under modulated I_{to}, the presence of a greater repolarisation reserve may play an important role. Of these currents, only I_{Kr} was fitted to rabbit atrial cell data. There is no quantification of I_{Ks} to the authors knowledge, despite some acknowledgement as a minor current in rabbit atria [362] and there is disagreement on the presence, or role, of I_{sus} in rabbit atria [33, 242].

The effects of symmetrical I_{CaL} window-widening observed by the Workman Lab were well reproduced in the Holmes model (Figure 5.17). Increasing the window size resulted in APD prolongation, which qualitatively agreed with the experiment, although with significantly shorter prolongation than observed by the Workman Lab [359]. Larger window shifts produced EADs in both model and experiment, with both producing non-repolarising EADs with multiple activations at a 9 mV window shift. This agreement indicates this model's suitability to be used in studying I_{CaL} variability and kinetics.

Pharmacological intervention of Nif, an I_{CaL} blocker was compared in the simulated models and experiment, revealing an overestimation of the effect of I_{CaL} block on APD shortening in the novel model (Figure 5.19). The Aslanidi model, similar to as observed in the I_{to} dynamic-clamp and 4-AP intervention studies did not suffer from this and produced an estimation in agreement with experimental data. Quantified CaT measurements were taken under the intervention of Nif by the Workman Lab [359] and compared with simulated CaTs. The novel model produced a good agreement with CaT morphologies measured by the Workman Lab [359]; however, the model may have overestimated the impact of Nif on Ca^{2+} handling, resulting in a small LTCC influx which was not sufficient to induce CICR (Figure 5.20). The Workman Lab dataset contains some cells measured to have a similarly minor CaT amplitude, suggesting evidence of CICR impairment. The Aslanidi model produced better AP morphology agreement under the influence of Nif (Figure 5.19) but large disagreements in CaT morphology. Analysis of Ca^{2+} currents and the CaT (Figure 5.20) suggests that the Aslanidi model reproduces a similar AP morphology through an unphysiological mechanism.

5.5.3 Insights into Rabbit Atrial Electrophysiology: Discrepancies Between Simulation and Experiment

In theory, the single-source approach to model development inherently provides a higher level of confidence than more generalised models due to the exclusion of reverse-engineered parameter fitting or ambiguity in the combinations of ionic currents underlying the AP. Thus, discrepancies between simulation and experiment provide insight into ionic currents' role in Ca^{2+} handling parameters, which are not formulated from these congruent data. This chapter provides several such insights through analysing these differences.

One such example is the role of minor ionic currents associated with repolarisation reserve, which may play a role in the discrepancies observed in I_{to} modulation and 4-AP intervention (Figures 5.15, 5.16, 5.18). These currents include the rapid and slow delayed rectifier currents, I_{Kr} and I_{Ks}, which were purposefully excluded from the novel model, and the sodium-potassium pump I_{NaK}. The model purposefully excluded formulations for I_{Kr} and I_{Ks}, as no congruent data was present within the Workman Lab dataset, existing formulations in the Aslanidi model for I_{Ks} are developed from sinoatrial and atrioventricular nodal myocyte data [242], and upon

testing, it made minor changes to AP biomarkers using previously published conductance values from Aslanidi et al. (2009) [242] and Vagos et al. (2020) [367]. Including these currents with updated formulations may contribute towards resolving this; however, there is a lack of recently available data on these currents in the rabbit atria. The only available data is Muraki et al. (1995) [362], who published measurements of I_{Kr} in rabbit atrial cells. This highlights a gap in our collective understanding of repolarising currents in the rabbit atrial myocyte.

The novel model also displayed overestimation of the impact of the APD-shortening phenomenon (I_{to} enhancement, Figure 5.15; I_{CaL} block, Figure 5.19). Furthermore, this discrepancy was also present when factoring in good agreement between simulation and experimental CaTs. The Aslanidi model, which had major differences in CaT compared with the experiment, produced a more agreeable AP morphology under these changes and contained a different description of I_{NCX}. The Aslanidi model, however, shows relatively small changes to I_{NCX} with I_{CaL} block (Figure 2.20B), and only CaT magnitude (and not peak delay, or CaT width) was modified under I_{CaL} block (Figure 2.20C). This result implies that the Aslandi model better represents the Workman Lab Nif intervention AP data due to a shortcoming of its Ca^{2+} handling system underestimating the impact of Nif. The role of I_{NCX} and other outward background currents is unclear, and some combination of these may play a significant role in rabbit atrial depolarisation at lower membrane potentials. Recent data describing the current-voltage relationship of nickel-sensitive I_{NCX} current is published by Tsai et al. [384]; however, gating kinetics have only been published by Earm et al. (1990) [401] and Ho and Earm (1991) [402], which were used to characterise I_{NCX} in the Lindblad et al. (1996) model [36] and subsequently the Aslanidi et al. (2009) model [242].

5.5.4 Ca^{2+} Handling Variability

A preliminary study was performed, investigating the effects of modulating four primary ionic currents (I_{to}, I_{K1}, I_{CaL} and I_{NCX}) and rates of SR-Ca^{2+} uptake and release (J_{up} and J_{rel}) on the CaT. Theoretically, a single-source cell model provides an excellent tool to assess the role of ion channel and Ca^{2+} handling variability [43]. This is due to a reduction in uncertainty from integrating data from multiple experimental sources or inherently present with formulations and model parameters reverse-engineered from APs or CaT data.

Despite the shortcomings of the model in reproducing experimental results with large I_{to} inhibition or enhancement, even moderate scaling of I_{to} (50% to 150%; Figure 5.21) produced significant changes in CaT morphology compared to I_{K1}. Reduction of I_{to} prolongs and elevates the phase 2 plateau in membrane potential in rabbit atrial myocytes [33, 366, 403], extending the time period in the re-activation window of LTCC channels. Modulations to this time period, or indeed the window itself (Figure 5.15), will alter LTCC flux and thus the CaT. Scaling the I_{K1} current (Figure 5.22) primarily modulates late-stage phase 3 repolarisation, which has a lesser impact on this I_{CaL} window timing, which may determine its less critical role in determining Ca^{2+} variability.

Scaling the maximal conductance of Ca^{2+} dependent channels had a large impact on intracellular Ca^{2+} handling. Modulation of I_{CaL} (Figure 2.23) resulted in large changes to diastolic [Ca^{2+}] and CaT peak magnitude by increasing or decreasing the influx of Ca^{2+} and prolongation or shortening of I_{CaL} activation duration in the AP. The role of I_{NCX} in determining intracellular Ca^{2+} behaviour carried some uncertainty due to being human atrial-specific (Figure 5.24); however, increased I_{NCX} was shown to promote the genesis of EADs, which is congruent with observations by Zhong et al. (2018) [395] in rabbit ventricular myocytes and described in a review of EAD mechanisms by Qu et al. (2013) [396]. Further elucidation of the role if I_{NCX} in rabbit atrial myocytes (or better yet, within a larger congruent collection of rabbit atrial electrophysiology data) would be of great benefit to understanding the underlying mechanisms behind these arrhythmogenic cellular phenomena. Modulation of SR-Ca^{2+} fluxes resulted in minor to negligible changes in AP morphology, but largely influenced intracellular Ca^{2+} handling congruent to our understanding of the roles of SERCA2a and RyR (Figure 5.26, 5.28; see Section 2.2.3). There is notable differences between human atrial and rabbit atrial Ca^{2+} handling which may result in significant morphological differences: the relative increase in the role of the smaller Ca^{2+} flux parameters such as the sarcolemmal Ca^{2+}-ATPase channel, I_{CaP} [26, 208], or background Ca^{2+} currents; in rabbit atrial cells, SR-Ca^{2+} uptake is approximately 50% faster than in human [211].

To summarise, modulation of the primary currents underlying the AP (I_{to}, I_{CaL}) had largest impacts on Ca^{2+} handling variability either through impacting the duration of

the voltage-ranges I_{CaL} is most active; or through directly modulating Ca^{2+} influx into the cell. Modulation of I_{NCX} was observed to result in moderate variation of the CaT and increasing I_{NCX} resulted in the genesis of EADs, which highlights the importance of elucidating this current further. Furthermore, modulation of Ca^{2+} parameters produced large changes in Ca^{2+} morphology; developing a rabbit atrial-specific Ca^{2+} model would provide more confidence in analysing the impacts of these parameters.

5.5.5 Limitations

The various limitations of computational electrophysiological modelling are well described throughout the literature [1, 36, 62, 77, 404]; these are briefly discussed in Section 1.1 and Chapter 6. This section will discuss the limitations of the novel model itself and the wider study.

While the primary ion currents which underlie the AP were well fitted to experimental data from a single, congruent source of rabbit atrial measurements provided by the Workman Lab [33, 359, 368–370], this model included the Grandi-Bers human atrial Ca^{2+} handling model [44], with the inclusion of some rabbit atrial-specific ionic currents from the Aslanidi model [37, 242]. The inclusion of these non-congruent sources introduced a degree of uncertainty in the results produced from the novel model and is combative with the ideal of using single-source data. Limitations on the available data from the Workman Lab meant only some AP biomarkers and the CaT could be sufficiently validated and were not sufficient to inform the development of a novel rabbit-atrial specific Ca^{2+} handling system. Developing a rabbit-atrial specific Ca^{2+} handling model, which could be based upon several contemporary models from several groups [39, 44, 49, 361], is a natural improvement to developing a congruent single-source model of rabbit atrial electrophysiology. Additionally, developing a rabbit-specific isoprenaline (ISO) model would have enabled further congruent validation against experimental data provided by the Workman Lab; however, this was not performed in this study.

Across the range of dynamic-clamp and pharmacological interventions, the novel model consistently over-estimated the impact of significant APD prolongation or shortening effects from scaling the magnitude of I_{to} and I_{CaL}, when compared to Workman Lab data. As discussed in Section 5.5.4, this highlights experimental gaps in quantified data of the magnitude and kinetics of minor ionic currents. This insight

supports an aim of this chapter, however, to use this model to identify discrepancies between the novel model's predictions and experiment.

There are a wide variety of factors that are not included in this model or discussed within this chapter which may have an impact on ionic currents and Ca^{2+} handling, such as a detailed description of Ca^{2+}-dependent kinase II (CaMKII) or the late sodium current, I_{NaL} [384] (although, this was found to be negligible in rabbit atrial myocytes by Hou et al. (2017) [366]). Several repolarising currents thought to exist in rabbit atria have been excluded from this model due to a lack of available data, such as the acetylcholine-activated inward-rectifying potassium current, I_{KACh}, which is observed to exist in the rabbit atrium [405]. The model also did not contain a description of a sustained outward current, often denoted as I_{sus} and suspected to be a non-inactivating component of I_{to}, which is present in other rabbit atrial models [242, 367]. However, the exclusion of this current supported the approach to produce a novel rabbit atrial model specific to Workman Lab data.

The model described in this chapter is a single cell model with no spatio-temporal description of Ca^{2+} handling, which is required to investigate further the pro-arrhythmogenic cellular phenomenon underlying AF. As previously mentioned, developing a rabbit atrial-specific spatio-temporal Ca^{2+} handling model would produce a platform well-suited for these analyses.

Finally, despite a single-source cell model being a very suitable tool for investigating and interpreting data from a population variability approach, or a sensitivity analysis [43], only a preliminary study into ionic channel and Ca^{2+} variability was produced in this chapter. Scaling this up to a full population model approach would be a natural next step in using this model to investigate intracellular Ca^{2+} variability further.

5.6 Conclusions

A novel lab-specific model of rabbit atrial electrophysiology was developed in this chapter, incorporating novel formulations for the primary ionic currents which determine the AP from a single, congruent source provided by the Workman Lab. Validation of this novel lab-specific model against congruent experimental data revealed discrepancies between simulation and experiment; our knowledge of quantified magnitudes and gating kinetics of minor repolarising currents (I_{Kr}, I_{Ks}

and I_{sus}) is lacking for rabbit atrial electrophysiology, as well as our understanding of the role of I_{NCX} in determining Ca^{2+} variability and its role in promoting pro-arrhythmic phenomena. Despite these discrepancies, the novel model offers many advantages over contemporary, general models for future study: reproduction of EADs under symmetrical I_{CaL} window-widening; stable pacing up to 10 Hz; production of pacing-dependent alternans; and a validated set of balanced primary ionic currents. A preliminary study into Ca^{2+} variability reaffirmed the need for further elucidation of the role of I_{NCX} and minor repolarising currents in the rabbit atria, and for developing a rabbit atrial-specific Ca^{2+} handling model. The novel, lab-specific model produced in this chapter may form the basis of further development using modern rabbit atrial electrophysiology data and complements the existing pool of contemporary computational rabbit atrial models.

6
General Discussion

6.1 Reviewing Aims

To achieve the aims outlined at the beginning of this thesis (Section 1.3), novel methods, tools, and models were developed to investigate Ca^{2+} handling variability. Models are ultimately simplifications of reality and do not capture the full range of physiological complexity in biological systems; however, incorporating simulations into physiological studies can provide quantitative and mechanistic insights that are extremely difficult to determine experimentally. The accuracy and realism achieved in computational models inherently depend on our understanding of reality as determined through experiments. Moreover, the development of these models is often motivated by a desire to explain experimentally observed phenomena. Therefore, experimental work drives forward the development of computational models. Updated computational models provide further insights not possible experimentally, which then drives forward experimental research. The continued development and advancement of computational models and tools to supplement experimental work has led to the development and application of joint experiment-simulation approaches such as those used and developed within this thesis.

Before discussing the major results and developments presented within this thesis, it is necessary to restate the aims of this thesis and recapitulate the original work presented which achieve these objectives. Each chapter within this thesis discusses the development and application of novel approaches to studying Ca^{2+} variability per the three aims of this thesis:

1. To develop a novel method to quantify the spatial profile of sub-cellular heterogeneity in channel protein expression within a cardiomyocyte.
2. To assess the importance and role of sub-cellular heterogeneity in the sarco/endoplasmic reticulum Ca^{2+}-ATPase (SERCA2a) pump in determining whole-cell electrophysiological behaviour in control and pathology.

3. To develop a novel, congruent electrophysiological model of the rabbit atrial myocyte suitable to study the relationship between intracellular Ca^{2+} variability and ionic channel variability.

In Chapter 3, this thesis introduces a new method and marker to quantify the spatial profile of heterogeneity in the expression of stained proteins in subcellular microscopy datasets, the correlation length scale. By leveraging the strengths of computational modelling and data analysis, the work in this chapter further bridges the gap between experiment and simulation by presenting, for the first time, a quantification of the correlation length scale and anisotropy of Ca^{2+} channel variability. Furthermore, a novel image-based computational modelling approach to quantify the functional impact of that variability in simulation. The author packaged this novel method into an open-source toolkit, opening further avenues of research incorporating this new marker. The development of these methods achieves the first objective of this thesis and provides a method to achieve the second.

Chapter 4 presents the first study characterising the spatial profile of SERCA2a in health and HF-induced remodelling by utilising the approach developed in Chapter 3. Furthermore, this chapter presents the first comprehensive investigation into the role of SERCA2a heterogeneity in Ca^{2+} handling variability and the modulation of two pro-arrhythmic cellular phenomena: alternans and SCRE. The isolation of expression heterogeneity of any singular protein species is experimentally impossible; thus, this study provides new insights into the contributions of SERCA2a heterogeneity to Ca^{2+} handling variability and pro-arrhythmic cellular phenomenon in health and disease. The work presented within this chapter demonstrates the value of the correlation length scale as a quantifiable marker of heterogeneous expression and how variation in this parameter impacts Ca^{2+} handling variability in normal and pathological conditions, thus achieving this thesis's second aim.

Finally, Chapter 5 describes developing and validating a novel, congruent, lab-specific single-cell model of the rabbit atrial cardiomyocyte. The novel model contains balanced novel formulations of the primary ionic currents underlying the action potential from a single source. This gives greater confidence in its behaviours and, perhaps more importantly, differences from experimental observations than more generalised, contemporary models. Investigating the discrepancies between

simulated and experimental dynamic clamp and pharmacological interventions revealed gaps in the quantification of I_{NCX} and the minor currents associated with repolarisation reserve in rabbit atrial myocytes. A preliminary application study into the impacts of ionic and Ca^{2+} channel modulation further demonstrated the importance of minor currents in rabbit atrial electrophysiology. The model developed is suitable for studying Ca^{2+} handling variabilities and will become a complementary tool alongside other contemporary electrophysiology models; thus, the final objective of this thesis is satisfied.

6.2 Analysing Sub-Cellular Heterogeneity

In Section 2.3.3, the cardiac remodelling associated with various pathologies was introduced. To briefly recap this: the physiological remodelling of cardiomyocytes due to disease, injury or maladaptation has been extensively linked to changes in the expression of ionic currents and Ca^{2+} handling proteins. The elucidation of subcellular structure and its remodelling in pathology is a highly active research area. Advancements in cellular microscopy imaging in confocal high-resolution fluorescent imaging [13, 216, 277, 406] and super-resolution techniques such as dSTORM, DNA-PAINT and expansion microscopy [12] have enabled the visualisation of the underlying structure and localisation of these key targets. Sheard et al. (2019) [12] demonstrated these techniques to resolve individual RyRs, providing insight into heterogeneous RyR cluster sizes throughout the cell, describing RyR and phosphorylation site distribution throughout healthy and failing rat ventricular myocytes. Pinali et al. (2013) [182] used electron microscopy to reconstruct sub-cellular t-system and SR membrane structures. Jayasinghe et al. (2009) [13] used confocal and total internal reflection fluorescence imaging to demonstrate a moderate co-localisation of NCX and dyads.

A desire to understand the properties of Ca^{2+} signalling in cardiomyocytes has led to the development of many techniques and tools. Picht et al. (2007) developed SparkMaster, an image-analysis plugin to analyse Ca^{2+} sparks in x-y linescans automatically; Shkryl et al. (2012) [206] utilise four-dimensional confocal imaging (x, y, z and t) to detect and measure the amplitude, width and kinetics of Ca^{2+} sparks; Steele and Steele (2014) [407] developed an open-source toolkit to automate Ca^{2+} spark detection and analysis in 3D image stacks.

These developments in both imaging and data analysis led to the creation of advanced, combined methods to correlate the nucleation and properties of Ca^{2+} sparks with underlying sub-cellular structures. Tian et al. (2019) [408] present a method of unbiased, automatic analysis of large 2D datasets correlating local Ca^{2+} signalling in various degrees of hypertrophy and observing highly organised Ca^{2+} sparks in healthy cells, and the degradation of this organisation concomitant with degradation of the t-tubule network in hypertrophy. Hurley et al. (2021) [205] utilising combined imaging techniques to correlate Ca^{2+} spark origin with participating RyRs.

The novel method of quantifying heterogeneity developed in this thesis – the "Sub-cellular Heterogeneity Analysis Toolkit" – represents another new development in this field. The correlation length scale of expression, λ, is a novel marker to measure and compare the underlying sub-cellular organisation of ionic transporters, flux channels and other proteins in cardiomyocytes. Furthermore, the previous studies focus on the t-system and the dyads and co-localisation of different proteins at sub-micron scales; this technique allows for the spatially non-uniform distribution of these channels at the whole-cell scale to be quantified. The open-source toolkit was developed to utilise existing high-resolution fluorescent imaging data; thus, previously obtained experimental data may be reanalysed using this approach to quantify spatial correlation in protein expression without additional experimental cost. Moreover, the recycling of experimental data for new purposes actively reduces the use of animals in research, making this approach both economically and ethically desirable.

This novel toolkit was detailed and used in a published preliminary study [1] which quantified the spatial characteristics of SERCA2a and RyR in healthy rat ventricular myocytes, measuring isotropic and anisotropic variation through correlation across x-y datasets. This study revealed that SERCA2a and RyR distributions in rat ventricular myocytes are generally anisotropic and show greater variation in correlation length scale than in relative whole-cell expression. The extent of variation in RyR distribution in cardiomyocytes has been recently described [10, 12]. However, the distribution of SERCA2a had not been quantified, and no previous study has studied the correlation of expression of either protein.

Furthermore, the spatial profile of SERCA2a expression heterogeneity in rat ventricular myocytes was quantified and compared in control and RV-HF for the first time. Correlation length scales were observed to increase in RV-HF compared to control in both RV and LV myocytes, suggesting that hypertrophy and atrophy remodelling significantly impact the spatial organisation of SERCA2a to a similar magnitude. These findings reaffirm and support recent observations of LV remodelling in RV-HF [215, 216] and demonstrate the value of correlation length scales as a biomarker to quantify the extent of this remodelling and compare spatial heterogeneity in control and pathology.

The correlation between all channels as a single system, both in regards to localisation and relative expression, is largely unknown. This new method presents exciting opportunities to compare sub-cellular expression heterogeneity across different cell types, different species, or in different stages of pathology. A full characterisation of the heterogeneity and correlation length scales in primary channels would provide substantial insight into the cellular structures underlying ECC. Furthermore, comprehensive studies of correlation length scales of primary Ca^{2+} flux channels, regulatory proteins and ionic channels may provide significant insight into the mechanisms underlying observed electrophysiological differences at different stages of conditions such as AF, with well-defined stages of progression and severity [121, 122]. Elucidating the relative changes in sub-cellular structures through the progression from paroxysmal to severe, permanent AF may provide novel insights into the mechanisms of progression at a cellular level.

6.3 Modelling Sub-Cellular Heterogeneity

Correlating sub-cellular structure to function presents a significant research challenge. The simultaneous imaging of multiple proteins becomes incrementally more difficult with each additional target, and due to diffusive coupling between sub-cellular regions, Ca^{2+} heterogeneity is non-trivial. It does not follow linearly from any individual channel expression – thus, Ca^{2+} must also be imaged in the same cells. Image-based computational modelling is an ideal method for exploring the structure-function dynamics of sub-cellular structures; however, the incorporation of imaging data in whole-cell computational models has been significantly limited, either in scope, scalability or through theoretical analysis in the absence of appropriate data. Improvements in image-based modelling techniques

have been detailed in recent studies: Soeller et al. (2009) [277] produced a quantitative RyR distribution model by examining a section of a single rat ventricular myocyte and reproducing experimentally measured RyR localisation in a network of CRUs, similar to that of the idealised MSCSF approach [1] used in this thesis. Sutanto et al. (2018) [258] discretises confocal microscopy images of RyR expression in segments and stretches this distribution to a 2D expression map. Song et al. (2018) [76] produces qualitative t-tubule network maps based on network structures observed in healthy and failing rat ventricular myocytes. Our lab describes a method of direct image-based modelling based on reconstructions of high-resolution sub-cellular structures (Colman et al. (2017; 2020) [1, 50]).

The novel image-based computational modelling method, which complements the variogram analysis approach, presents a novel development that addresses some of the limitations of the above approaches. Spatial correlation and variability parameters quantified by the toolkit are used to produce GRFs, which are used as expression maps in a 3D computational model. This approach is advantageous over previously published approaches in larger, systematic studies due to its scalability through non-unique map generation while still using analysed, quantitative experimental data directly through converting image parameters into GRFs or generating GRFs congruent to the range of experimental data. Additionally, the GRF method allows for the variation of the novel correlation length scale, whole-cell expression, cellular organisation (through unique map generation) and anisotropy. This method provides an image-based modelling technique capable of large-scale comprehensive studies relating the heterogeneity of channel expression to its role in the underlying function and variability observed in cellular Ca^{2+} dynamics.

Another advantage of this approach, demonstrated in the proof-of-concept application in Chapter 3, is the ability to simultaneously model the heterogeneous expression of multiple targets. Existing image-based modelling studies, including the SERCA2a study in this thesis, frequently discuss the limitation of only considering the distribution of one target or one sub-cellular structure [76, 258]; this method need not suffer this limitation. For example, a limitation of the comprehensive SERCA2a study in this thesis is that the role of PLB has not been explored, as local SERCA2a activity is likely to be determined by exact local combinations of SERCA2a:PLB. Provided adequate immunofluorescence data of PLB and SERCA2a, these methods could be used to address this limitation by

modelling the heterogeneous expressions of PLB and SERCA2a concomitantly. Additionally, this approach could be used to develop qualitative spatial Ca^{2+} models of HF (or other conditions) through simultaneous modulation of those primary channels observed to remodel in HF. However, such a model would be more generalised given the tractability of large-scale simulations studies with such a large parameter space.

6.4 Ca^{2+} Variability Under Heterogeneous SERCA2a Expression

Simulation studies have been performed with implementations of heterogeneous RyR, t-tubule and SR structures; however, no study until now examines the structure-function relationship of SERCA2a. Additionally, this is the first comprehensive study investigating the impact of correlation length scale on Ca^{2+} variability, demonstrating the application of the methods developed in Chapter 3 and providing novel insights into the role of SERCA2a expression in determining Ca^{2+} variability.

The introduction of SERCA2a heterogeneity at all correlation length scales was observed to increase spatial heterogeneity in intracellular [Ca^{2+}], whereas the homogeneous model produced a CaT more spatially homogeneous than observed experimentally [257]. Longer correlation length scales associated with RV-HF remodelling produced further increasing spatial heterogeneity in the CaT; this matches experimental observations of increasing intra-cellular spatial variation of the CaT in failing cardiomyocytes [314, 315]. Therefore, heterogeneous SERCA2a expression (and possibly the heterogeneous expression of other Ca^{2+} channels) is partially responsible for the observed variability in CaT properties even among adjacent cardiomyocytes [409].

As discussed in Section 4.1.1, there is are conflicting observations in the impact of HF-induced remodelling on SERCA2a expression and SR-Ca^{2+}. Interestingly, two studies using the same model of MCT-induced RV-HF in rat ventricular myocytes as this study reported increased SR-Ca^{2+} content. Sabourin et al. (2018) [170] report an increase in SR-Ca^{2+} content under maintained whole-cell expression of SERCA2a; Benoist et al. (2014) report an increase in SR-Ca^{2+} in failing myocytes, with downregulation of SERCA2a expression.

In a previous study, Benoist et al. (2012) [169] acknowledge that an increase in SR-Ca^{2+} is not compatible with the observed decrease in SERCA2a activity, which is consistent in HF remodelling across the literature [130, 159–162, 169, 170, 310, 312], and therefore must also depend on other factors. Sabourin et al. (2018) [170] propose that Store-Operated Ca^{2+} entry (SOCE) may explain the increase in SR-Ca^{2+} content specifically in hypertrophied RV cells; however that they do not contribute to this in control. The role of SOCE in cardiomyocytes is very unclear and certainly warrants further study to understand if it plays a role in maintaining Ca^{2+} homeostasis. Other studies propose that alterations in the expression or phosphorylation of PLB may play a role in determining the homeostatic response to HF-remodelling [130, 170, 171].

The simulations performed in Chapter 4 demonstrated that heterogeneous SERCA2a expression correlated with a decrease in global SERCA2a function through an alternative mechanism without changes to whole-cell SERCA2a expression or the expression or function of any other protein. This isolated mechanism may play a significant role in determining whole-cell ECC, particularly following HF associated remodelling in which this reduction is generally predicted to increase. It is hypothesised that the combination of sub-cellular and global inter-cellular heterogeneities interact to underly observed inter-cellular variability. This observed decrease in SERCA2a function through the heterogeneous dampening mechanism proposed in Section 4.3.4 may, for example, compound with observations of reduced SERCA2a expression.

This thesis also provides novel insights into the correlation between regions of SERCA2a distribution and altered diastolic [Ca^{2+}] and SR-Ca^{2+} load. Simulations demonstrate that this heterogeneous pattern of local Ca^{2+} correlates against SERCA2a expression – lower SERCA2a expression correlates with higher diastolic [Ca^{2+}] and SR Ca^{2+} load. This heterogeneous distribution of local Ca^{2+} ultimately plays a role in determining spatio-temporal pro-arrhythmic behaviours.

Complex behaviours in alternans are observed under heterogeneous SERCA2a expression. If only considering the whole-cell average modulation of Ca^{2+} dynamics, such as a decrease in SR-Ca^{2+} uptake, and in SR-Ca^{2+} content, then the results of these simulations are congruent with Qu et al. (2016)'s 'unified theory of CaT alternans' [197]; however, a spatial dependence on the heterogeneous distribution of

local Ca^{2+} properties present a change in mechanism from this theory. The spatial profile of CRU activation in each subsequent small beat is localised to regions of lower SERCA2a expression, correlating with enhanced diastolic [Ca^{2+}] and SR Ca^{2+} load, a mechanism which is not present in homogeneous studies. A similar constriction on the phase variation of alternans was observed by Colman et al. (2017) [49], further strengthening the case for a fundamental difference in mechanism for CaT alternans in heterogeneous structures. This difference in mechanism of CaT alternans may have critical implications for the most effective and safe method of managing these phenomena.

The role of SERCA2a heterogeneity in determining SCRE behaviour was unclear and highly spatially dependent. This is not a surprising result, given the complex role of SERCA2a in determining SCRE in homogeneous conditions [334, 410, 411]. Inter-cellular variability in the genesis of triggered activity and the mean magnitude of SCREs was observed; however, dissecting the role of SERCA2a heterogeneity in the promotion or inhibition of spontaneous activity will require further investigation at the systems level. However, some interesting points arise regarding the localisation of Ca^{2+} wave nucleation and sub-cellular heterogeneity. In the present study, Ca^{2+} waves primarily originated from regions of lower SERCA2a expression (and, therefore, higher diastolic [Ca^{2+}] and SR-Ca^{2+} load). Galice et al. (2018) [337] observe a similar localisation phenomenon experimentally in heterogeneous RyR distributions: the vast majority of Ca^{2+} sparks are generated in larger RyR clusters; Sutanto et al. (2018) [258] observed congruent localisation in an image-based simulation study of heterogeneous RyR expression. Modelling concomitant heterogeneous expressions in the primary Ca^{2+} channels and regulatory proteins which determine CICR may provide novel insights into how the various heterogeneities impact the localisation of spontaneous Ca^{2+} activity.

6.5 Novel, Congruent Rabbit Atrial Model

Since the development of the first computational model of cardiac electrophysiology by Denis Noble (1961) [32], a wide variety of generalised and species-specific models have been developed with the motivation of dissecting the multi-scale mechanisms underlying the complex, dynamic behaviours of normal and pathological physiology [412]. The implementation of computational methods is most effective when used alongside experimental and clinical research to encompass

all aspects of cardiovascular study. The “virtual heart” project embodies this idea; to produce a complete, functional virtual heart model which can be applied to all areas of medical cardiology to aid cardiologists in the prevention, diagnosis and treatment of CVDs [413]. The most desired computational models are, of course, human-specific models, but due to the ethical and logistical issues leading to a scarcity of human cardiomyocyte data, suitable animal models are used as a substitute.

Sections 2.5 and 5.1 discussed the rabbit model of heart failure; to re-iterate: rabbit models are one of the most popular models for studying human physiology and pathophysiology [340, 414], particularly in the study of AF [342–346]. Despite this, the development of contemporary rabbit atrial electrophysiology models is limited; most currently used models are derivations of the Aslanidi et al. (2009) rabbit atrial model [242].

The novel, congruent lab-specific model in this study addresses some of the limitations of the Aslanidi model (as discussed in Section 5.5). Additionally, it provides an additional contemporary model that can be used for comparison that is not heavily derived from it. A model's functionality must be well understood for it to have meaningful applications for informing experimental or clinical research [415]; comparing results across multiple models describing similar electrophysiology is one way of ensuring that the conclusions drawn from a study are not model-specific. Rabbit atrial modelling studies suffered from this limitation previously due to the heavy similarities in ionic current formulations and Ca^{2+} handling models. The inclusion of novel formulations of primary ion channel currents from a congruent source, a different Ca^{2+} handling model and minimal common currents between the model developed in this thesis and the Aslandi model provides a sufficiently large difference to enable comparisons with the Aslanidi model or the derivated models.

When developing lab-specific models, it is important to observe and discuss where the model agrees with simulation, and perhaps more important to discuss where it does not. The inclusion of primary ion channel currents from a single source provides great confidence in the relative roles and balance of those currents in the model, thus enabling greater confidence in discussing what is missing in the model or what is misinformed when these differences arise. One such example is in the development of this novel model, and its validation against dynamic clamp and pharmacological interventions revealed potentially important roles for I_{Kr} and I_{Ks} in

repolarisation reserve; currents that I originally considered non-essential due to their minor influence on the AP and CaT under normal pacing. If reformulated with novel data, these may have reduced the overestimation of APD prolongation as a result of increasing the magnitude of I_{CaL} or decreasing I_{to}.

A natural progression from the rabbit model developed in this thesis would be to develop upon the Ca^{2+} handling system to produce the first rabbit-atrial specific Ca^{2+} handling model. Developing a fully species-specific model using the lab-specific, congruent primary ion channel currents would provide a currently unmatched platform to study the rabbit models of arrhythmia *in silico*. However, there is a need for further quantification of rabbit atrial Ca^{2+} handling, and idealistically, the minor currents underlying repolarisation reserve, before such a model can be developed. For the time being, this novel rabbit atrial model provides a useful tool for studying Ca^{2+} variability and as part of multi-model studies using the rabbit atrial model.

6.6 Closing Words

This thesis details the development and application of novel methods, computational models and analysis tools to study Ca^{2+} variability. Applying these joint experimental-simulation techniques provides novel insights into the structure-function relationship of sub-cellular heterogeneity, gaps in quantification of ionic transporters, and the impact of Ca^{2+} variability on whole-cell electrophysiology. Ultimately, the relationship between simulation and experiment is symbiotic: Experiments explain the physiology from which models are developed and improved, and simulation informs future work through studies that can not be performed experimentally. It is the author's belief that further development of sophisticated computational models incorporating experimental image-data and quantified electrophysiology datasets will continue to advance our global understanding of the underlying mechanisms of cardiac function in health and disease. These contained works represent a step forward in this regard.

Bibliography

[1] Colman MA, Holmes M, Whittaker DG, et al. Multi-scale approaches for the simulation of cardiac electrophysiology: I – Sub-cellular and stochastic calcium dynamics from cell to organ. *Methods*. Epub ahead of print 29 February 2020. DOI: 10.1016/j.ymeth.2020.02.011.

[2] Holmes M, Hurley M, Sheard T, et al. Increased SERCA2a sub-cellular heterogeneity in right-ventricular heart failure inhibits excitation-contraction coupling and modulates arrhythmogenic dynamics. 2021; 23.

[3] Holmes M, P Benson A, Aslanidi O, et al. A Novel Model of the Rabbit Atrial Myocyte for the Study of Ca2+ Mediated Arrhythmia. Epub ahead of print 30 December 2018. DOI: 10.22489/CinC.2018.188.

[4] Martini FH, Bartholomew EF, Nath JL. *Fundamentals of Anatomy and Physiology, Global Edition*. 11th ed. Pearson Education Canada, 2018.

[5] Katz AM. *Physiology of the Heart*. 5th ed. Wolters Kluwer Health: Lippincott, Williams & Wilkins, 2011.

[6] McLeod K. *An Essential Introduction to Cardiac Electrophysiology*. Imperial College Press, Imperial College London, 2014.

[7] Zoni-Berisso M, Lercari F, Carazza T, et al. Epidemiology of atrial fibrillation: European perspective. *Clin Epidemiol* 2014; 213.

[8] Timmis A, Townsend N, Gale CP, et al. European Society of Cardiology: Cardiovascular Disease Statistics 2019. *Eur Heart J* 2020; 41: 12–85.

[9] British Heart Foundation: Heart & Circulatory Disease Statistics 2021, https://www.bhf.org.uk/what-we-do/our-research/heart-statistics/heart-statistics-publications/cardiovascular-disease-statistics-2021 (accessed 30 September 2021).

[10] Jayasinghe I, Clowsley AH, Lin R, et al. True Molecular Scale Visualization of Variable Clustering Properties of Ryanodine Receptors. *Cell Rep* 2018; 22: 557–567.

[11] Rudy Y, Silva JR. Computational biology in the study of cardiac ion channels and cell electrophysiology. *Q Rev Biophys* 2006; 39: 57–116.

[12] Sheard TMD, Hurley ME, Colyer J, et al. Three-Dimensional and Chemical Mapping of Intracellular Signaling Nanodomains in Health and Disease with Enhanced Expansion Microscopy. *ACS Nano* 2019; 13: 2143–2157.

[13] Jayasinghe ID, Cannell MB, Soeller C. Organization of Ryanodine Receptors, Transverse Tubules, and Sodium-Calcium Exchanger in Rat Myocytes. *Biophys J* 2009; 97: 2664–2673.

[14] Bers DM. Cardiac excitation–contraction coupling. 2002; 415: 8.

[15] Eisner D, Bode E, Venetucci L, et al. Calcium flux balance in the heart. *J Mol Cell Cardiol* 2013; 58: 110–117.

[16] Eisner DA, Caldwell JL, Kistamás K, et al. Calcium and Excitation-Contraction Coupling in the Heart. *Circ Res* 2017; 121: 181–195.

[17] Nattel S, Dobrev D. The multidimensional role of calcium in atrial fibrillation pathophysiology: mechanistic insights and therapeutic opportunities. *Eur Heart J* 2012; 33: 1870–1877.

[18] Feng J, Yue L, Wang Z, et al. Ionic mechanisms of regional action potential heterogeneity in the canine right atrium. *Circ Res* 1998; 83: 541–551.

[19] Gemmell P, Burrage K, Rodriguez B, et al. Population of Computational Rabbit-Specific Ventricular Action Potential Models for Investigating Sources of Variability in Cellular Repolarisation. *PLOS ONE* 2014; 9: e90112.

[20] Muszkiewicz A, Britton OJ, Gemmell P, et al. Variability in cardiac electrophysiology: Using experimentally-calibrated populations of models to move beyond the single virtual physiological human paradigm. *Prog Biophys Mol Biol* 2016; 120: 115–127.

[21] Tixier E, Lombardi D, Rodriguez B, et al. Modelling variability in cardiac electrophysiology: a moment-matching approach. *J R Soc Interface* 2017; 14: 20170238.

[22] Hearse DJ, Sutherland FJ. EXPERIMENTAL MODELS FOR THE STUDY OF CARDIOVASCULAR FUNCTION AND DISEASE. *Pharmacol Res* 2000; 41: 597–603.

[23] Zaragoza C, Gomez-Guerrero C, Martin-Ventura JL, et al. Animal models of cardiovascular diseases. *J Biomed Biotechnol* 2011; 2011: 497841.

[24] Cesarovic N, Lipiski M, Falk V, et al. Animals in cardiovascular research: Clinical relevance and translational limitations of animal models in cardiovascular medicine. *Eur Heart J* 2020; 41: 200–203.

[25] Odening KE, Baczko I, Brunner M. Animals in cardiovascular research: important role of rabbit models in cardiac electrophysiology. *Eur Heart J* 2020; 41: 2036.

[26] Milani-Nejad N, Janssen PML. Small and Large Animal Models in Cardiac Contraction Research: Advantages and Disadvantages. *Pharmacol Ther* 2014; 141: 235–249.

[27] Arevalo HJ, Boyle PM, Trayanova NA. Computational Rabbit Models to Investigate the Initiation, Perpetuation, and Termination of Ventricular Arrhythmia. *Prog Biophys Mol Biol* 2016; 121: 185–194.

[28] Hasenfuss G. Animal models of human cardiovascular disease, heart failure and hypertrophy. *Cardiovasc Res* 1998; 39: 60–76.

[29] Qu Z, Hu G, Garfinkel A, et al. Nonlinear and Stochastic Dynamics in the Heart. *Phys Rep* 2014; 543: 61–162.

[30] Vagos M, van Herck IGM, Sundnes J, et al. Computational Modeling of Electrophysiology and Pharmacotherapy of Atrial Fibrillation: Recent Advances and Future Challenges. *Front Physiol* 2018; 9: 1221.

[31] Trayanova NA, Chang KC. How computer simulations of the human heart can improve anti-arrhythmia therapy. *J Physiol* 2016; 594: 2483–2502.

[32] Noble D. A modification of the Hodgkin--Huxley equations applicable to Purkinje fibre action and pace-maker potentials. *J Physiol* 1962; 160: 317–352.

[33] Workman AJ, Marshall GE, Rankin AC, et al. Transient outward K+ current reduction prolongs action potentials and promotes afterdepolarisations: a dynamic-clamp study in human and rabbit cardiac atrial myocytes. *J Physiol* 2012; 590: 4289–4305.

[34] Gattoni S, Røe ÅT, Frisk M, et al. The calcium–frequency response in the rat ventricular myocyte: an experimental and modelling study. *J Physiol* 2016; 594: 4193–4224.

[35] Niederer SA, Smith NP. A Mathematical Model of the Slow Force Response to Stretch in Rat Ventricular Myocytes. *Biophys J* 2007; 92: 4030–4044.

[36] Lindblad DS, Murphey CR, Clark JW, et al. A model of the action potential and underlying membrane currents in a rabbit atrial cell. *Am J Physiol* 1996; 271: H1666-1696.

[37] Aslanidi OV, Dewey RS, Morgan AR, et al. Electrophysiologically detailed models of the right and left rabbit atria: Pharmacological impacts on propagation and arrhythmogenesis. IEEE, pp. 69–72.

[38] Aslanidi OV, Dewey RS, Morgan AR, et al. Regional differences in rabbit atrial action potential properties: Mechanisms, consequences and pharmacological implications. IEEE, pp. 141–144.

[39] Shannon TR, Wang F, Puglisi J, et al. A mathematical treatment of integrated Ca dynamics within the ventricular myocyte. *Biophys J* 2004; 87: 3351–3371.

[40] Hund TJ, Rudy Y. Rate Dependence and Regulation of Action Potential and Calcium Transient in a Canine Cardiac Ventricular Cell Model. *Circulation* 2004; 110: 3168–3174.

[41] Varela M, Colman MA, Hancox JC, et al. Atrial Heterogeneity Generates Re-entrant Substrate during Atrial Fibrillation and Anti-arrhythmic Drug Action: Mechanistic Insights from Canine Atrial Models. *PLOS Comput Biol* 2016; 12: e1005245.

[42] Ramirez RJ, Nattel S, Courtemanche M. Mathematical analysis of canine atrial action potentials: rate, regional factors, and electrical remodeling. *Am J Physiol Heart Circ Physiol* 2000; 279: H1767-1785.

[43] Colman MA, Saxena P, Kettlewell S, et al. Description of the Human Atrial Action Potential Derived From a Single, Congruent Data Source: Novel Computational Models for Integrated Experimental-Numerical Study of Atrial Arrhythmia Mechanisms. *Front Physiol* 2018; 9: 1211.

[44] Grandi E, Pandit SV, Voigt N, et al. Human Atrial Action Potential and Ca2+ Model: Sinus Rhythm and Chronic Atrial Fibrillation. *Circ Res* 2011; 109: 1055–1066.

[45] Courtemanche M, Ramirez RJ, Nattel S. Ionic mechanisms underlying human atrial action potential properties: insights from a mathematical model. *Am J Physiol* 1998; 275: H301-321.

[46] O'Hara T, Virág L, Varró A, et al. Simulation of the undiseased human cardiac ventricular action potential: model formulation and experimental validation. *PLoS Comput Biol* 2011; 7: e1002061.

[47] Hinch R, Greenstein JL, Tanskanen AJ, et al. A simplified local control model of calcium-induced calcium release in cardiac ventricular myocytes. *Biophys J* 2004; 87: 3723–3736.

[48] Vagos MR, Arevalo H, Heijman J, et al. A Novel Computational Model of the Rabbit Atrial Cardiomyocyte With Spatial Calcium Dynamics. *Front Physiol* 2020; 11: 556156.

[49] Colman MA, Pinali C, Trafford AW, et al. A computational model of spatio-temporal cardiac intracellular calcium handling with realistic structure and spatial flux distribution from sarcoplasmic reticulum and t-tubule reconstructions. *PLOS Comput Biol* 2017; 13: e1005714.

[50] Colman MA. Arrhythmia mechanisms and spontaneous calcium release: Bi-directional coupling between re-entrant and focal excitation. *PLOS Comput Biol* 2019; 15: e1007260.

[51] Restrepo JG, Weiss JN, Karma A. Calsequestrin-mediated mechanism for cellular calcium transient alternans. *Biophys J* 2008; 95: 3767–3789.

[52] Nivala M, de Lange E, Rovetti R, et al. Computational Modeling and Numerical Methods for Spatiotemporal Calcium Cycling in Ventricular

Myocytes. *Front Physiol*; 3. Epub ahead of print 8 May 2012. DOI: 10.3389/fphys.2012.00114.

[53] Walker MA, Gurev V, Rice JJ, et al. Estimating the probabilities of rare arrhythmic events in multiscale computational models of cardiac cells and tissue. *PLoS Comput Biol* 2017; 13: e1005783.

[54] Grandi E, Pasqualini FS, Bers DM. A novel computational model of the human ventricular action potential and Ca transient. *J Mol Cell Cardiol* 2010; 48: 112–121.

[55] Colman MA, Aslanidi OV, Kharche S, et al. Pro-arrhythmogenic effects of atrial fibrillation-induced electrical remodelling: insights from the three-dimensional virtual human atria. *J Physiol* 2013; 591: 4249–4272.

[56] Luo CH, Rudy Y. A dynamic model of the cardiac ventricular action potential. I. Simulations of ionic currents and concentration changes. *Circ Res* 1994; 74: 1071–1096.

[57] Land S, Park-Holohan S-J, Smith NP, et al. A model of cardiac contraction based on novel measurements of tension development in human cardiomyocytes. *J Mol Cell Cardiol* 2017; 106: 68–83.

[58] Benson AP, Aslanidi OV, Zhang H, et al. The canine virtual ventricular wall: a platform for dissecting pharmacological effects on propagation and arrhythmogenesis. *Prog Biophys Mol Biol* 2008; 96: 187–208.

[59] Prakosa A, Arevalo HJ, Deng D, et al. Personalized virtual-heart technology for guiding the ablation of infarct-related ventricular tachycardia. *Nat Biomed Eng* 2018; 2: 732–740.

[60] Davies MR, Wang K, Mirams GR, et al. Recent developments in using mechanistic cardiac modelling for drug safety evaluation. *Drug Discov Today* 2016; 21: 924–938.

[61] Iaizzo PA. *Handbook of Cardiac Anatomy, Physiology and Devices*. 3rd ed. Springer International Publishing, 2015.

[62] Colman MA. *Mechanisms of Atrial Arrhythmias*. Springer International Publishing Switzerland, 2014.

[63] Armentano RL, Fischer EIC, Cymberknop L. *Biomechanical Modelling of the Cardiovascular System*. IOP Publishing, 2019.

[64] Friedberg MK, Redington AN. Right Versus Left Ventricular Failure. *Circulation* 2014; 129: 1033–1044.

[65] Monteiro LM, Vasques-Nóvoa F, Ferreira L, et al. Restoring heart function and electrical integrity: closing the circuit. *Npj Regen Med* 2017; 2: 1–13.

[66] Monfredi O, Dobrzynski H, Mondal T, et al. The anatomy and physiology of the sinoatrial node--a contemporary review. *Pacing Clin Electrophysiol PACE* 2010; 33: 1392–1406.

[67] Boyett MR, Honjo H, Kodama I. The sinoatrial node, a heterogeneous pacemaker structure. *Cardiovasc Res* 2000; 47: 658–687.

[68] Woodcock EA, Matkovich SJ. Cardiomyocytes structure, function and associated pathologies. *Int J Biochem Cell Biol* 2005; 37: 1746–1751.

[69] Theakston E, Walker C, O'Sullivan M, et al. Stochastic Modelling of Cardiac Cell Structure. *Conf Proc Annu Int Conf IEEE Eng Med Biol Soc IEEE Eng Med Biol Soc Conf* 2010; 2010: 3257–60.

[70] de Tombe PP, ter Keurs HEDJ. Cardiac muscle mechanics: Sarcomere length matters. *J Mol Cell Cardiol* 2016; 91: 148–150.

[71] Cooke R. The Sliding Filament Model : 1972–2004. *J Gen Physiol* 2004; 123: 643–656.

[72] Luby-Phelps K. The physical chemistry of cytoplasm and its influence on cell function: an update. *Mol Biol Cell* 2013; 24: 2593–2596.

[73] Edwards JN, Blatter LA. Cardiac alternans and intracellular calcium cycling. *Clin Exp Pharmacol Physiol* 2014; 41: 524–532.

[74] Satoh H, Delbridge LM, Blatter LA, et al. Surface:volume relationship in cardiac myocytes studied with confocal microscopy and membrane capacitance measurements: species-dependence and developmental effects. *Biophys J* 1996; 70: 1494–1504.

[75] Richards MA, Clarke JD, Saravanan P, et al. Transverse tubules are a common feature in large mammalian atrial myocytes including human. *Am J Physiol Heart Circ Physiol* 2011; 301: H1996-2005.

[76] Song Z, Liu MB, Qu Z. Transverse tubular network structures in the genesis of intracellular calcium alternans and triggered activity in cardiac cells. *J Mol Cell Cardiol* 2018; 114: 288–299.

[77] Benson AP, Stevenson-Cocks HJ, Whittaker DG, et al. Multi-scale approaches for the simulation of cardiac electrophysiology: II – Tissue-level structure and function. *Methods* 2021; 185: 60–81.

[78] Nattel S, Frelin Y, Gaborit N, et al. Ion-channel mRNA-expression profiling: Insights into cardiac remodeling and arrhythmic substrates. *J Mol Cell Cardiol* 2010; 48: 96–105.

[79] Gaborit N, Le Bouter S, Szuts V, et al. Regional and tissue specific transcript signatures of ion channel genes in the non-diseased human heart. *J Physiol* 2007; 582: 675–693.

[80] Joukar S. A comparative review on heart ion channels, action potentials and electrocardiogram in rodents and human: extrapolation of experimental insights to clinic. *Lab Anim Res* 2021; 37: 25.

[81] Santana LF, Cheng EP, Lederer WJ. How does the shape of the cardiac action potential control calcium signaling and contraction in the heart? *J Mol Cell Cardiol* 2010; 49: 901–903.

[82] Grant AO. Cardiac ion channels. *Circ Arrhythm Electrophysiol* 2009; 2: 185–194.

[83] Scriven DRL, Dan P, Moore EDW. Distribution of Proteins Implicated in Excitation-Contraction Coupling in Rat Ventricular Myocytes. *Biophys J* 2000; 79: 2682–2691.

[84] Junker J, Sommer JR, Sar M, et al. Extended junctional sarcoplasmic reticulum of avian cardiac muscle contains functional ryanodine receptors. *J Biol Chem* 1994; 269: 1627–1634.

[85] Bootman MD, Smyrnias I, Thul R, et al. Atrial cardiomyocyte calcium signalling. *Biochim Biophys Acta* 2011; 1813: 922–934.

[86] Hesketh GG, Van Eyk JE, Tomaselli GF. Mechanisms of Gap Junction Traffic in Health and Disease. *J Cardiovasc Pharmacol* 2009; 54: 263–272.

[87] Carmeliet E. Conduction in cardiac tissue. Historical reflections. *Physiol Rep* 2019; 7: e13860.

[88] Goodenough DA. Bulk isolation of mouse hepatocyte gap junctions. Characterization of the principal protein, connexin. *J Cell Biol* 1974; 61: 557–563.

[89] Workman AJ, Kane KA, Rankin AC. The contribution of ionic currents to changes in refractoriness of human atrial myocytes associated with chronic atrial fibrillation. *Cardiovasc Res* 2001; 52: 226–235.

[90] Winslow RL, Rice J, Jafri S, et al. Mechanisms of Altered Excitation-Contraction Coupling in Canine Tachycardia-Induced Heart Failure, II. *Circ Res* 1999; 84: 571–586.

[91] Hardy MEL, Pervolaraki E, Bernus O, et al. Dynamic Action Potential Restitution Contributes to Mechanical Restitution in Right Ventricular Myocytes From Pulmonary Hypertensive Rats. *Front Physiol* 2018; 9: 205.

[92] Qu Z, Xie Y, Garfinkel A, et al. T-Wave Alternans and Arrhythmogenesis in Cardiac Diseases. *Front Physiol* 2010; 1: 154.

[93] Comtois P, Kneller J, Nattel S. Of circles and spirals: bridging the gap between the leading circle and spiral wave concepts of cardiac reentry. *Eur Eur Pacing Arrhythm Card Electrophysiol J Work Groups Card*

Pacing Arrhythm Card Cell Electrophysiol Eur Soc Cardiol 2005; 7 Suppl 2: 10–20.

[94] Edwards AG, Louch WE. Species-Dependent Mechanisms of Cardiac Arrhythmia: A Cellular Focus. *Clin Med Insights Cardiol* 2017; 11: 1179546816686061.

[95] Nerbonne JM, Kass RS. Molecular physiology of cardiac repolarization. *Physiol Rev* 2005; 85: 1205–1253.

[96] Vigmond EJ, Tsoi V, Yin Y, et al. Estimating Atrial Action Potential Duration from Electrograms. *IEEE Trans Biomed Eng* 2009; 56: 1546–1555.

[97] Schram G. Differential Distribution of Cardiac Ion Channel Expression as a Basis for Regional Specialization in Electrical Function. *Circ Res* 2002; 90: 939–950.

[98] Ravens U, Wettwer E. Ultra-rapid delayed rectifier channels: molecular basis and therapeutic implications. *Cardiovasc Res* 2011; 89: 776–785.

[99] Zhang H, Holden AV, Noble D, et al. Analysis of the Chronotropic Effect of Acetylcholine on Sinoatrial Node Cells. *J Cardiovasc Electrophysiol* 2003; 13: 465–474.

[100] Hashimoto N. Acetylcholine-Activated Potassium Channel as a Novel Target for AF Treatment. *Atr Fibrillation*; 19.

[101] Ravens U, Cerbai E. Role of potassium currents in cardiac arrhythmias. *Eur Eur Pacing Arrhythm Card Electrophysiol J Work Groups Card Pacing Arrhythm Card Cell Electrophysiol Eur Soc Cardiol* 2008; 10: 1133–1137.

[102] Walden AP, Dibb KM, Trafford AW. Differences in intracellular calcium homeostasis between atrial and ventricular myocytes. *J Mol Cell Cardiol* 2009; 46: 463–473.

[103] Brette F, Komukai K, Orchard CH. Validation of formamide as a detubulation agent in isolated rat cardiac cells. *Am J Physiol-Heart Circ Physiol* 2002; 283: H1720–H1728.

[104] Smyrnias I, Mair W, Harzheim D, et al. Comparison of the T-tubule system in adult rat ventricular and atrial myocytes, and its role in excitation–contraction coupling and inotropic stimulation. *Cell Calcium* 2010; 47: 210–223.

[105] Zheng J, Zhang J, Danioko S, et al. A 12-lead electrocardiogram database for arrhythmia research covering more than 10,000 patients. *Sci Data* 2020; 7: 48.

[106] Alday EAP, Colman MA, Langley P, et al. Novel non-invasive algorithm to identify the origins of re-entry and ectopic foci in the atria from 64-

lead ECGs: A computational study. *PLoS Comput Biol* 2017; 13: e1005270.

[107] Cheng S, Keyes MJ, Larson MG, et al. Long-term Outcomes in Individuals with a Prolonged PR Interval or First-Degree Atrioventricular Block. *JAMA J Am Med Assoc* 2009; 301: 2571–2577.

[108] Kashani A, Barold SS. Significance of QRS complex duration in patients with heart failure. *J Am Coll Cardiol* 2005; 46: 2183–2192.

[109] Couderc J-P, Lopes CM. Short and Long QT Syndromes: does QT length really matter? *J Electrocardiol* 2010; 43: 396–399.

[110] Jones SW. Whole-Cell and Microelectrode Voltage Clamp. In: *Neurophysiological Techniques, I*. New Jersey: Humana Press, pp. 143–192.

[111] Antzelevitch C, Burashnikov A. Overview of Basic Mechanisms of Cardiac Arrhythmia. *Card Electrophysiol Clin* 2011; 3: 23–45.

[112] Electrocardiography | BioNinja, https://ib.bioninja.com.au/standard-level/topic-6-human-physiology/62-the-blood-system/electrocardiography.html (accessed 5 October 2021).

[113] Zellerhoff S, Pistulli R, Mönnig G, et al. Atrial Arrhythmias in Long-QT Syndrome under Daily Life Conditions: A Nested Case Control Study. *J Cardiovasc Electrophysiol* 2008; 20: 401–7.

[114] Alboni P, Gianfranchi L, Brignole M. Treatment of persistent sinus bradycardia with intermittent symptoms: are guidelines clear? *EP Eur* 2009; 11: 562–564.

[115] Awtry E, Jeon C, Ware MG. *Blueprints Cardiology*. Lippincott Williams & Wilkins, 2006.

[116] Koplan BA, Stevenson WG. Ventricular Tachycardia and Sudden Cardiac Death. *Mayo Clin Proc* 2009; 84: 289–297.

[117] Nattel S, Shiroshita-Takeshita A, Brundel BJJM, et al. Mechanisms of atrial fibrillation: lessons from animal models. *Prog Cardiovasc Dis* 2005; 48: 9–28.

[118] Chen P-S, Wu T-J, Ting C-T, et al. A Tale of Two Fibrillations. *Circulation* 2003; 108: 2298–2303.

[119] Benjamin EJ, Wolf PA, D'Agostino RB, et al. Impact of atrial fibrillation on the risk of death: the Framingham Heart Study. *Circulation* 1998; 98: 946–952.

[120] Anter E, Jessup M, Callans DJ. Atrial fibrillation and heart failure: treatment considerations for a dual epidemic. *Circulation* 2009; 119: 2516–2525.

[121] Chiang C-E, Naditch-Brûlé L, Murin J, et al. Distribution and risk profile of paroxysmal, persistent, and permanent atrial fibrillation in routine clinical practice: insight from the real-life global survey evaluating patients with atrial fibrillation international registry. *Circ Arrhythm Electrophysiol* 2012; 5: 632–639.

[122] Nattel S, Dobrev D. Electrophysiological and molecular mechanisms of paroxysmal atrial fibrillation. *Nat Rev Cardiol* 2016; 13: 575–590.

[123] Calkins H, Kuck KH, Cappato R, et al. 2012 HRS/EHRA/ECAS Expert Consensus Statement on Catheter and Surgical Ablation of Atrial Fibrillation: recommendations for patient selection, procedural techniques, patient management and follow-up, definitions, endpoints, and research trial design. *Eur Eur Pacing Arrhythm Card Electrophysiol J Work Groups Card Pacing Arrhythm Card Cell Electrophysiol Eur Soc Cardiol* 2012; 14: 528–606.

[124] Criteria I of M (US) C on SSCD. *Ischemic Heart Disease*. National Academies Press (US), https://www.ncbi.nlm.nih.gov/books/NBK209964/ (2010, accessed 4 October 2021).

[125] Richardson W, Clarke S, Quinn T, et al. Physiological Implications of Myocardial Scar Structure. *Compr Physiol* 2015; 5: 1877–1909.

[126] Vigmond E, Vadakkumpadan F, Gurev V, et al. Towards predictive modelling of the electrophysiology of the heart. *Exp Physiol* 2009; 94: 563–577.

[127] Inamdar AA, Inamdar AC. Heart Failure: Diagnosis, Management and Utilization. *J Clin Med* 2016; 5: 62.

[128] Murphy SP, Ibrahim NE, Januzzi JL Jr. Heart Failure With Reduced Ejection Fraction: A Review. *JAMA* 2020; 324: 488–504.

[129] Dassanayaka S, Jones SP. Recent Developments in Heart Failure. *Circ Res* 2015; 117: e58–e63.

[130] Benoist D, Stones R, Benson AP, et al. Systems approach to the study of stretch and arrhythmias in right ventricular failure induced in rats by monocrotaline. *Prog Biophys Mol Biol* 2014; 115: 162–172.

[131] Sabbah HN. Silent disease progression in clinically stable heart failure. *Eur J Heart Fail* 2017; 19: 469–478.

[132] Cohn JN, Ferrari R, Sharpe N. Cardiac remodeling—concepts and clinical implications: a consensus paper from an international forum on cardiac remodeling. *J Am Coll Cardiol* 2000; 35: 569–582.

[133] Luo Min, Anderson Mark E. Mechanisms of Altered Ca2+ Handling in Heart Failure. *Circ Res* 2013; 113: 690–708.

[134] Roger VL. Epidemiology of Heart Failure. *Circ Res* 2013; 113: 646–659.

[135] Henkel DM, Redfield MM, Weston SA, et al. Death in Heart Failure. *Circ Heart Fail* 2008; 1: 91–97.

[136] Tomaselli GF, Zipes DP. What Causes Sudden Death in Heart Failure? *Circ Res* 2004; 95: 754–763.

[137] Jones NR, Hobbs FR, Taylor CJ. Prognosis following a diagnosis of heart failure and the role of primary care: a review of the literature. *BJGP Open*; 1: bjgpopen17X101013.

[138] Azevedo PS, Polegato BF, Minicucci MF, et al. Cardiac Remodeling: Concepts, Clinical Impact, Pathophysiological Mechanisms and Pharmacologic Treatment. *Arq Bras Cardiol* 2016; 106: 62–69.

[139] Ellison GM, Waring CD, Vicinanza C, et al. Physiological cardiac remodelling in response to endurance exercise training: cellular and molecular mechanisms. *Heart Br Card Soc* 2012; 98: 5–10.

[140] Dobrev D, Ravens U. Remodeling of cardiomyocyte ion channels in human atrial fibrillation. *Basic Res Cardiol* 2003; 98: 137–148.

[141] Severs NJ, Bruce AF, Dupont E, et al. Remodelling of gap junctions and connexin expression in diseased myocardium. *Cardiovasc Res* 2008; 80: 9–19.

[142] Holzem KM, Efimov IR. Arrhythmogenic remodelling of activation and repolarization in the failing human heart. *Europace* 2012; 14: v50–v57.

[143] Janse MJ. Electrophysiological changes in heart failure and their relationship to arrhythmogenesis. *Cardiovasc Res* 2004; 61: 208–217.

[144] Pitt GS, Dun W, Boyden PA. Remodeled cardiac calcium channels. *J Mol Cell Cardiol* 2006; 41: 373–388.

[145] Horiuchi-Hirose M, Kashihara T, Nakada T, et al. Decrease in the density of t-tubular L-type Ca2+ channel currents in failing ventricular myocytes. *Am J Physiol Heart Circ Physiol* 2011; 300: H978-988.

[146] Vassort G, Talavera K, Alvarez JL. Role of T-type Ca2+ channels in the heart. *Cell Calcium* 2006; 40: 205–220.

[147] Tsuji Y, Zicha S, Qi X-Y, et al. Potassium channel subunit remodeling in rabbits exposed to long-term bradycardia or tachycardia: discrete arrhythmogenic consequences related to differential delayed-rectifier changes. *Circulation* 2006; 113: 345–355.

[148] Li G-R, Lau C-P, Ducharme A, et al. Transmural action potential and ionic current remodeling in ventricles of failing canine hearts. *Am J Physiol Heart Circ Physiol* 2002; 283: H1031-1041.

[149] Beuckelmann DJ, Näbauer M, Erdmann E. Alterations of K+ currents in isolated human ventricular myocytes from patients with terminal heart failure. *Circ Res* 1993; 73: 379–385.

[150] Zicha S, Xiao L, Stafford S, et al. Transmural expression of transient outward potassium current subunits in normal and failing canine and human hearts. *J Physiol* 2004; 561: 735–748.

[151] Rose J, Armoundas AA, Tian Y, et al. Molecular correlates of altered expression of potassium currents in failing rabbit myocardium. *Am J Physiol Heart Circ Physiol* 2005; 288: H2077-2087.

[152] Pogwizd SM, Schlotthauer K, Li L, et al. Arrhythmogenesis and contractile dysfunction in heart failure: Roles of sodium-calcium exchange, inward rectifier potassium current, and residual beta-adrenergic responsiveness. *Circ Res* 2001; 88: 1159–1167.

[153] Nattel S, Burstein B, Dobrev D. Atrial Remodeling and Atrial Fibrillation: Mechanisms and Implications. *Circ Arrhythm Electrophysiol* 2008; 1: 62–73.

[154] Benoist D, Stones R, Drinkhill M, et al. Arrhythmogenic substrate in hearts of rats with monocrotaline-induced pulmonary hypertension and right ventricular hypertrophy. *Am J Physiol - Heart Circ Physiol* 2011; 300: H2230–H2237.

[155] del Monte F, Hajjar RJ. Intracellular devastation in heart failure. *Heart Fail Rev* 2008; 13: 151–162.

[156] Xu M, Zhou P, Xu S-M, et al. Intermolecular Failure of L-type Ca2+ Channel and Ryanodine Receptor Signaling in Hypertrophy. *PLOS Biol* 2007; 5: e21.

[157] Piacentino V, Weber CR, Chen X, et al. Cellular Basis of Abnormal Calcium Transients of Failing Human Ventricular Myocytes. *Circ Res* 2003; 92: 651–658.

[158] Beuckelmann DJ, Näbauer M, Erdmann E. Intracellular calcium handling in isolated ventricular myocytes from patients with terminal heart failure. *Circulation* 1992; 85: 1046–1055.

[159] Kawase Y, Hajjar RJ. The cardiac sarcoplasmic/endoplasmic reticulum calcium ATPase: a potent target for cardiovascular diseases. *Nat Clin Pract Cardiovasc Med* 2008; 5: 554–565.

[160] Hasenfuss G, Reinecke H, Studer R, et al. Relation between myocardial function and expression of sarcoplasmic reticulum Ca(2+)-ATPase in failing and nonfailing human myocardium. *Circ Res* 1994; 75: 434–442.

[161] Dash R, Frank KF, Carr AN, et al. Gender Influences on Sarcoplasmic Reticulum Ca2+-handling in Failing Human Myocardium. *J Mol Cell Cardiol* 2001; 33: 1345–1353.

[162] Pieske B, Maier LS, Bers DM, et al. Ca2+ Handling and Sarcoplasmic Reticulum Ca2+ Content in Isolated Failing and Nonfailing Human Myocardium. *Circ Res* 1999; 85: 38–46.

[163] Lou Q, Janardhan A, Efimov IR. Remodeling of Calcium Handling in Human Heart Failure. *Adv Exp Med Biol* 2012; 740: 1145–1174.

[164] Frank KF, B�lck B, Brixius K, et al. Modulation of SERCA: implications for the failing human heart. *Basic Res Cardiol* 2002; 97: 1–1.

[165] Schillinger W, Lehnart SE, Prestle J, et al. Influence of SR Ca(2+)-ATPase and Na(+)-Ca(2+)-exchanger on the force-frequency relation. *Basic Res Cardiol* 1998; 93 Suppl 1: 38–45.

[166] Weber CR, Piacentino V, Houser SR, et al. Dynamic regulation of sodium/calcium exchange function in human heart failure. *Circulation* 2003; 108: 2224–2229.

[167] Lipskaia L, Chemaly ER, Hadri L, et al. Sarcoplasmic reticulum Ca2+ ATPase as a therapeutic target for heart failure. *Expert Opin Biol Ther* 2010; 10: 29–41.

[168] Pieske B, Maier LS, Schmidt-Schweda S. Sarcoplasmic reticulum Ca2+ load in human heart failure. *Basic Res Cardiol* 2002; 97 Suppl 1: I63-71.

[169] Benoist D, Stones R, Drinkhill MJ, et al. Cardiac arrhythmia mechanisms in rats with heart failure induced by pulmonary hypertension. *Am J Physiol - Heart Circ Physiol* 2012; 302: H2381–H2395.

[170] Sabourin J, Boet A, Rucker-Martin C, et al. Ca2+ handling remodeling and STIM1L/Orai1/TRPC1/TRPC4 upregulation in monocrotaline-induced right ventricular hypertrophy. *J Mol Cell Cardiol* 2018; 118: 208–224.

[171] Chu G, Kranias EG. Phospholamban as a therapeutic modality in heart failure. *Novartis Found Symp* 2006; 274: 156–171; discussion 172-175, 272–276.

[172] Schwinger Robert H.G., Böhm Michael, Schmidt Ulrich, et al. Unchanged Protein Levels of SERCA II and Phospholamban but Reduced Ca2+ Uptake and Ca2+-ATPase Activity of Cardiac Sarcoplasmic Reticulum From Dilated Cardiomyopathy Patients Compared With Patients With Nonfailing Hearts. *Circulation* 1995; 92: 3220–3228.

[173] Voigt N, Heijman J, Wang Q, et al. Cellular and Molecular Mechanisms of Atrial Arrhythmogenesis in Patients With Paroxysmal Atrial Fibrillation. *Circulation* 2014; 129: 145–156.

[174] Belevych AE, Terentyev D, Terentyeva R, et al. The relationship between arrhythmogenesis and impaired contractility in heart failure: role of altered ryanodine receptor function. *Cardiovasc Res* 2011; 90: 493–502.

[175] Guo A, Zhang C, Wei S, et al. Emerging mechanisms of T-tubule remodelling in heart failure. *Cardiovasc Res* 2013; 98: 204–215.

[176] Wei S, Guo A, Chen B, et al. T-tubule remodeling during transition from hypertrophy to heart failure. *Circ Res* 2010; 107: 520–531.

[177] Dibb KM, Clarke JD, Horn MA, et al. Characterization of an Extensive Transverse Tubular Network in Sheep Atrial Myocytes and its Depletion in Heart Failure. *Circ Heart Fail* 2009; 2: 482–489.

[178] Louch WE, Sejersted OM, Swift F. There Goes the Neighborhood: Pathological Alterations in T-Tubule Morphology and Consequences for Cardiomyocyte Ca2+ Handling. *J Biomed Biotechnol* 2010; 2010: 503906.

[179] Louch WE, Mørk HK, Sexton J, et al. T-tubule disorganization and reduced synchrony of Ca2+ release in murine cardiomyocytes following myocardial infarction. *J Physiol* 2006; 574: 519–533.

[180] Song L-S, Sobie EA, McCulle S, et al. Orphaned ryanodine receptors in the failing heart. *Proc Natl Acad Sci U S A* 2006; 103: 4305–4310.

[181] Setterberg IE, Le C, Frisk M, et al. The Physiology and Pathophysiology of T-Tubules in the Heart. *Front Physiol* 2021; 12: 1193.

[182] Pinali C, Bennett H, Davenport JB, et al. Three-dimensional reconstruction of cardiac sarcoplasmic reticulum reveals a continuous network linking transverse-tubules: this organization is perturbed in heart failure. *Circ Res* 2013; 113: 1219–1230.

[183] Anger M, Lompré A-M, Vallot O, et al. Cellular Distribution of Ca^{2+} Pumps and Ca^{2+} Release Channels in Rat Cardiac Hypertrophy Induced by Aortic Stenosis. *Circulation* 1998; 98: 2477–2486.

[184] Cheng H, Lederer MR, Lederer WJ, et al. Calcium sparks and [Ca2+]i waves in cardiac myocytes. *Am J Physiol* 1996; 270: C148-159.

[185] Cheng H, Lederer WJ. Calcium Sparks. *Physiol Rev* 2008; 88: 1491–1545.

[186] Bányász T, Chen-Izu Y, Balke CW, et al. A New Approach to the Detection and Statistical Classification of Ca2+ Sparks. *Biophys J* 2007; 92: 4458–4465.

[187] Hüser J, Lipsius SL, Blatter LA. Calcium gradients during excitation-contraction coupling in cat atrial myocytes. *J Physiol* 1996; 494 (Pt 3): 641–651.

[188] MacQuaide N, Dempster J, Smith GL. Measurement and Modeling of Ca2+ Waves in Isolated Rabbit Ventricular Cardiomyocytes. *Biophys J* 2007; 93: 2581–2595.

[189] Kushnir A, Marks AR. The Ryanodine Receptor in Cardiac Physiology and Disease. *Adv Pharmacol San Diego Calif* 2010; 59: 1–30.

[190] Weiss JN, Garfinkel A, Karagueuzian HS, et al. Early Afterdepolarizations and Cardiac Arrhythmias. *Heart Rhythm Off J Heart Rhythm Soc* 2010; 7: 1891–1899.

[191] Wit AL, Boyden PA. Triggered activity and atrial fibrillation. *Heart Rhythm* 2007; 4: S17-23.

[192] Heijman J, Voigt N, Nattel S, et al. Cellular and Molecular Electrophysiology of Atrial Fibrillation Initiation, Maintenance, and Progression. *Circ Res* 2014; 114: 1483–1499.

[193] Zhao Z, Wen H, Fefelova N, et al. Revisiting the ionic mechanisms of early afterdepolarizations in cardiomyocytes: predominant by Ca waves or Ca currents? *Am J Physiol Heart Circ Physiol* 2012; 302: H1636-1644.

[194] Zang Y, Xia L. Cellular mechanism of cardiac alternans: an unresolved chicken or egg problem. *J Zhejiang Univ Sci B* 2014; 15: 201–211.

[195] You T, Luo C, Zhang K, et al. Electrophysiological Mechanisms Underlying T-Wave Alternans and Their Role in Arrhythmogenesis. *Front Physiol* 2021; 12: 614946.

[196] Walker ML, Rosenbaum DS. Repolarization alternans: implications for the mechanism and prevention of sudden cardiac death. *Cardiovasc Res* 2003; 57: 599–614.

[197] Qu Z, Liu MB, Nivala M. A unified theory of calcium alternans in ventricular myocytes. *Sci Rep* 2016; 6: 35625.

[198] Rovetti R, Cui X, Garfinkel A, et al. Spark-induced sparks as a mechanism of intracellular calcium alternans in cardiac myocytes. *Circ Res* 2010; 106: 1582–1591.

[199] Weiss JN, Karma A, Shiferaw Y, et al. From pulsus to pulseless: the saga of cardiac alternans. *Circ Res* 2006; 98: 1244–1253.

[200] Restrepo JG, Karma A. Spatiotemporal intracellular calcium dynamics during cardiac alternans. *Chaos* 2009; 19: 037115.

[201] Thorn K. A quick guide to light microscopy in cell biology. *Mol Biol Cell* 2016; 27: 219–222.

[202] Holgate JH, Webb J. MICROSCOPY | Light Microscopy and Histochemical Methods. In: Caballero B (ed) *Encyclopedia of Food*

Sciences and Nutrition (Second Edition). Oxford: Academic Press, pp. 3917–3922.

[203] Kleppner D. Photon. *Access Sci*. Epub ahead of print 2019. DOI: 10.1036/1097-8542.511100.

[204] Tipler PA, Mosca G. *Physics for Scientists and Engineers*. 6th Edition. New York, NY: W. H. Freeman and Company, 2008.

[205] Hurley ME, Sheard TMD, Norman R, et al. A correlative super-resolution protocol to visualise structural underpinnings of fast second-messenger signalling in primary cell types. *Methods* 2021; 193: 27–37.

[206] Shkryl VM, Blatter LA, Ríos E. Properties of Ca2+ sparks revealed by four-dimensional confocal imaging of cardiac muscle. *J Gen Physiol* 2012; 139: 189–207.

[207] Crossman DJ, Jayasinghe ID, Soeller C. Transverse tubule remodelling: a cellular pathology driven by both sides of the plasmalemma? *Biophys Rev* 2017; 9: 919–929.

[208] Camacho P, Fan H, Liu Z, et al. Small mammalian animal models of heart disease. *Am J Cardiovasc Dis* 2016; 6: 70–80.

[209] Zicha S, Moss I, Allen B, et al. Molecular basis of species-specific expression of repolarizing K+ currents in the heart. *Am J Physiol Heart Circ Physiol* 2003; 285: H1641-1649.

[210] Varró A, Lathrop DA, Hester SB, et al. Ionic currents and action potentials in rabbit, rat, and guinea pig ventricular myocytes. *Basic Res Cardiol* 1993; 88: 93–102.

[211] Su Z, Li F, Spitzer KW, et al. Comparison of sarcoplasmic reticulum Ca2+-ATPase function in human, dog, rabbit, and mouse ventricular myocytes. *J Mol Cell Cardiol* 2003; 35: 761–767.

[212] Panfilov AV. Is heart size a factor in ventricular fibrillation? Or how close are rabbit and human hearts? *Heart Rhythm* 2006; 3: 862–864.

[213] Fowler ED, Benoist D, Drinkhill MJ, et al. Decreased creatine kinase is linked to diastolic dysfunction in rats with right heart failure induced by pulmonary artery hypertension. *J Mol Cell Cardiol* 2015; 86: 1–8.

[214] Bueno-Beti C, Sassi Y, Hajjar RJ, et al. Pulmonary Artery Hypertension Model in Rats by Monocrotaline Administration. In: Ishikawa K (ed) *Experimental Models of Cardiovascular Diseases: Methods and Protocols*. New York, NY: Springer, pp. 233–241.

[215] Han J-C, Guild S-J, Pham T, et al. Left-Ventricular Energetics in Pulmonary Arterial Hypertension-Induced Right-Ventricular Hypertrophic Failure. *Front Physiol*; 8. Epub ahead of print 9 January 2018. DOI: 10.3389/fphys.2017.01115.

[216] Howe K, Ross JM, Loiselle DS, et al. Transverse tubule remodelling in the atrophied left ventricle in right-sided heart failure. *Am J Physiol-Heart Circ Physiol*. Epub ahead of print 24 September 2021. DOI: 10.1152/ajpheart.00298.2021.

[217] The Principles of Humane Experimental Technique. *Med J Aust* 1960; 1: 500–500.

[218] Hubrecht RC, Carter E. The 3Rs and Humane Experimental Technique: Implementing Change. *Animals* 2019; 9: 754.

[219] Franco NH, Sandøe P, Olsson IAS. Researchers' attitudes to the 3Rs—An upturned hierarchy? *PLOS ONE* 2018; 13: e0200895.

[220] Animals (Scientific Procedures) Act 1986. *Wikipedia*, https://en.wikipedia.org/w/index.php?title=Animals_(Scientific_Procedures)_Act_1986&oldid=1020148225 (2021, accessed 18 October 2021).

[221] Legislation for the protection of animals used for scientific purposes - Environment - European Commission, https://ec.europa.eu/environment/chemicals/lab_animals/legislation_en.htm (accessed 18 October 2021).

[222] NC3Rs, https://www.nc3rs.org.uk/ (accessed 18 October 2021).

[223] Hodgkin AL, Huxley AF. The components of membrane conductance in the giant axon of Loligo. *J Physiol* 1952; 116: 473–496.

[224] Hodgkin AL, Huxley AF. A quantitative description of membrane current and its application to conduction and excitation in nerve. *J Physiol* 1952; 117: 500–544.

[225] Hodgkin AL, Huxley AF. Currents carried by sodium and potassium ions through the membrane of the giant axon of Loligo. *J Physiol* 1952; 116: 449–472.

[226] Hodgkin AL, Huxley AF, Katz B. Measurement of current-voltage relations in the membrane of the giant axon of Loligo. *J Physiol* 1952; 116: 424–448.

[227] Hodgkin AL, Huxley AF. The dual effect of membrane potential on sodium conductance in the giant axon of Loligo. *J Physiol* 1952; 116: 497–506.

[228] Alvarez-Lacalle E, Echebarria B, Spalding J, et al. Calcium Alternans is Due to an Order-Disorder Phase Transition in Cardiac Cells. *Phys Rev Lett* 2015; 114: 108101.

[229] Alvarez-Lacalle E, Peñaranda A, Cantalapiedra IR, et al. Calcium alternans is a global order-disorder phase transition. Robustness on Ryanodine Receptor release dynamics. In: *2015 Computing in Cardiology Conference (CinC)*. 2015, pp. 329–332.

[230] Song Z, Xie L-H, Weiss JN, et al. A Spatiotemporal Ventricular Myocyte Model Incorporating Mitochondrial Calcium Cycling. *Biophys J* 2019; 117: 2349–2360.

[231] Walker MA, Williams GSB, Kohl T, et al. Superresolution modeling of calcium release in the heart. *Biophys J* 2014; 107: 3018–3029.

[232] Song Z, Ko CY, Nivala M, et al. Calcium-voltage coupling in the genesis of early and delayed afterdepolarizations in cardiac myocytes. *Biophys J* 2015; 108: 1908–1921.

[233] Nivala M, Song Z, Weiss JN, et al. T-tubule disruption promotes calcium alternans in failing ventricular myocytes: Mechanistic insights from computational modeling. *J Mol Cell Cardiol* 2015; 79: 32–41.

[234] Stern MD, Capogrossi MC, Lakatta EG. Spontaneous calcium release from the sarcoplasmic reticulum in myocardial cells: mechanisms and consequences. *Cell Calcium* 1988; 9: 247–256.

[235] Katra RP, Laurita KR. Cellular mechanism of calcium-mediated triggered activity in the heart. *Circ Res* 2005; 96: 535–542.

[236] Blatter LA, Kockskämper J, Sheehan KA, et al. Local calcium gradients during excitation-contraction coupling and alternans in atrial myocytes. *J Physiol* 2003; 546: 19–31.

[237] Colman MA, Perez Alday EA, Holden AV, et al. Trigger vs. Substrate: Multi-Dimensional Modulation of QT-Prolongation Associated Arrhythmic Dynamics by a hERG Channel Activator. *Front Physiol*; 8. Epub ahead of print 4 October 2017. DOI: 10.3389/fphys.2017.00757.

[238] Butcher JC. *Numerical Methods for Ordinary Differential Equations*. 3rd Edition. Wiley, 2016.

[239] Rush S, Larsen H. A practical algorithm for solving dynamic membrane equations. *IEEE Trans Biomed Eng* 1978; 25: 389–392.

[240] Coudière Y, Lontsi CD, Pierre C, et al. Rush-Larsen time-stepping methods of high order for stiff problems in cardiac electrophysiology. *ArXiv171202260 Math*, http://arxiv.org/abs/1712.02260 (2017, accessed 28 June 2018).

[241] Marsh ME, Ziaratgahi ST, Spiteri RJ. The Secrets to the Success of the Rush–Larsen Method and its Generalizations. *IEEE Trans Biomed Eng* 2012; 59: 2506–2515.

[242] Aslanidi OV, Boyett MR, Dobrzynski H, et al. Mechanisms of Transition from Normal to Reentrant Electrical Activity in a Model of Rabbit Atrial Tissue: Interaction of Tissue Heterogeneity and Anisotropy. *Biophys J* 2009; 96: 798–817.

[243] Aslanidi OV, Robinson R, Cheverton D, et al. Electrophysiological substrate for a dominant reentrant source during atrial fibrillation. *Conf*

Proc Annu Int Conf IEEE Eng Med Biol Soc IEEE Eng Med Biol Soc Annu Conf 2009; 2009: 2819–2822.

[244] Bartolucci C, Passini E, Hyttinen J, et al. Simulation of the Effects of Extracellular Calcium Changes Leads to a Novel Computational Model of Human Ventricular Action Potential With a Revised Calcium Handling. *Front Physiol* 2020; 11: 314.

[245] Dutta S, Mincholé A, Quinn TA, et al. Electrophysiological properties of computational human ventricular cell action potential models under acute ischemic conditions. *Prog Biophys Mol Biol* 2017; 129: 40–52.

[246] Dutta S, Chang KC, Beattie KA, et al. Optimization of an In silico Cardiac Cell Model for Proarrhythmia Risk Assessment. *Front Physiol* 2017; 8: 616.

[247] Yamashita T, Nakajima T, Hazama H, et al. Regional Differences in Transient Outward Current Density and Inhomogeneities of Repolarization in Rabbit Right Atrium. *Circulation* 1995; 92: 3061–3069.

[248] Ko JH, Park WS, Kim SJ, et al. Slowing of the inactivation of voltage-dependent sodium channels by staurosporine, the protein kinase C inhibitor, in rabbit atrial myocytes. *Eur J Pharmacol* 2006; 534: 48–54.

[249] Hilgemann DW, Noble D. Excitation-Contraction Coupling and Extracellular Calcium Transients in Rabbit Atrium: Reconstruction of Basic Cellular Mechanisms. *Proc R Soc Lond B Biol Sci* 1987; 230: 163–205.

[250] Endoh M. Muscarinic regulation of Ca2+ signaling in mammalian atrial and ventricular myocardium. *Eur J Pharmacol* 1999; 375: 177–196.

[251] Hatem SN, Coulombe A, Balse E. Specificities of atrial electrophysiology: Clues to a better understanding of cardiac function and the mechanisms of arrhythmias. *J Mol Cell Cardiol* 2010; 48: 90–95.

[252] Yang P-C, Giles WR, Belardinelli L, et al. Mechanisms of flecainide induced negative inotropy: An in silico study. *J Mol Cell Cardiol* 2021; 158: 26–37.

[253] Wilhelms M, Hettmann H, Maleckar M, et al. Benchmarking electrophysiological models of human atrial myocytes. *Front Physiol* 2013; 3: 487.

[254] Eisner DA, Kashimura T, Venetucci LA, et al. From the ryanodine receptor to cardiac arrhythmias. *Circ J Off J Jpn Circ Soc* 2009; 73: 1561–1567.

[255] Levy D, Kenchaiah S, Larson MG, et al. Long-Term Trends in the Incidence of and Survival with Heart Failure.

http://dx.doi.org/10.1056/NEJMoa020265. Epub ahead of print 7 October 2009. DOI: 10.1056/NEJMoa020265.

[256] Ceornodolea AD, Bal R, Severens JL. Epidemiology and Management of Atrial Fibrillation and Stroke: Review of Data from Four European Countries. *Stroke Res Treat* 2017; 2017: 8593207.

[257] Biesmans L, Macquaide N, Heinzel FR, et al. Subcellular heterogeneity of ryanodine receptor properties in ventricular myocytes with low T-tubule density. *PloS One* 2011; 6: e25100.

[258] Sutanto H, van Sloun B, Schönleitner P, et al. The Subcellular Distribution of Ryanodine Receptors and L-Type Ca2+ Channels Modulates Ca2+-Transient Properties and Spontaneous Ca2+-Release Events in Atrial Cardiomyocytes. *Front Physiol* 2018; 9: 1108.

[259] Holmes M, Hurley ME, Sheard TMD, et al. Sub-cellular Heterogeneity in SERCA Determines Spatial Calcium Dynamics in Cardiomyocytes. *Biophys J* 2020; 118: 172a–173a.

[260] Müller S, Schüler L. *GeoStat-Framework/GSTools: v1.3.3 'Pure Pink'*. Zenodo. Epub ahead of print 8 August 2021. DOI: 10.5281/zenodo.5169658.

[261] Müller S, Schüler L. *GeoStat-Framework/GSTools: Bouncy Blue*. Zenodo. Epub ahead of print 18 January 2019. DOI: 10.5281/zenodo.2543658.

[262] HUANG C, HSING T, CRESSIE N. Nonparametric estimation of the variogram and its spectrum. *Biometrika* 2011; 98: 775–789.

[263] Arregui-Mena JD, Margetts L, Mummery PM. Practical Application of the Stochastic Finite Element Method. *Arch Comput Methods Eng* 2016; 23: 171–190.

[264] Sudret B. Stochastic Finite Element Methods and Reliability A State-of-the-Art Report. 189.

[265] Jones E, Oliphant E, Peterson P, et al. SciPy: Open Source Scientific Tools for Python. *SciPy.org*, http://www.scipy.org/ (2001).

[266] Clayton RH. Dispersion of Recovery and Vulnerability to Re-entry in a Model of Human Atrial Tissue With Simulated Diffuse and Focal Patterns of Fibrosis. *Front Physiol*; 9. Epub ahead of print 2018. DOI: 10.3389/fphys.2018.01052.

[267] Rodríguez-Cantano R, Sundnes J, Rognes ME. Uncertainty in cardiac myofiber orientation and stiffnesses dominate the variability of left ventricle deformation response. *ArXiv180102989 Phys*, http://arxiv.org/abs/1801.02989 (2018, accessed 30 September 2020).

[268] Medina R, Garreau M, Toro J, et al. Markov random field modeling for three-dimensional reconstruction of the left ventricle in cardiac angiography. *Ieee Trans Med Imaging* 2006; 25: 1087–1100.

[269] González-Gaitán S, de Souza RS, Krone-Martins A, et al. Spatial field reconstruction with INLA: application to IFU galaxy data. *Mon Not R Astron Soc* 2019; 482: 3880–3891.

[270] Themelis KE, Lanusse F, Jeffrey N, et al. Modelling Data with both Sparsity and a Gaussian Random Field: Application to Dark Matter Mass Mapping in Cosmology. In: *2018 26th European Signal Processing Conference (EUSIPCO)*. 2018, pp. 376–379.

[271] Passini E, Pellegrini A, Caiani E, et al. Computational analysis of Head-Down Bed Rest effects on cardiac action potential duration. In: *Computing in Cardiology 2013*. 2013, pp. 357–360.

[272] Qt | Cross-platform software development for embedded & desktop, https://www.qt.io (accessed 4 November 2021).

[273] PyQt5 Reference Guide — PyQt 5.7 Reference Guide, https://doc.bccnsoft.com/docs/PyQt5/index.html (accessed 4 November 2021).

[274] Van Rossum G, Fred L. D. *Python 3 Reference Manual*. CreateSpace, https://www.python.org/ (2009).

[275] Clark A. *Pillow (PIL Fork) Documentation*. readthedocs, https://pillow.readthedocs.io/en/stable/index.html (2015, accessed 5 November 2021).

[276] Hunter JD. Matplotlib: A 2D Graphics Environment. *IEEE Comput Sci Eng* 2007; 9: 90–95.

[277] Soeller C, Jayasinghe ID, Li P, et al. Three-dimensional high-resolution imaging of cardiac proteins to construct models of intracellular Ca^{2+} signalling in rat ventricular myocytes: Ca^{2+} release unit distribution and Ca^{2+} waves. *Exp Physiol* 2009; 94: 496–508.

[278] Li P, Wei W, Cai X, et al. Computational modelling of the initiation and development of spontaneous intracellular Ca2+ waves in ventricular myocytes. *Philos Trans R Soc Math Phys Eng Sci* 2010; 368: 3953–3965.

[279] Zhihao L, Jingyu N, Lan L, et al. SERCA2a: a key protein in the Ca2+ cycle of the heart failure. *Heart Fail Rev* 2020; 25: 523–535.

[280] Periasamy M, Bhupathy P, Babu GJ. Regulation of sarcoplasmic reticulum Ca2+ ATPase pump expression and its relevance to cardiac muscle physiology and pathology. *Cardiovasc Res* 2008; 77: 265–273.

[281] Louch WE, Stokke MK, Sjaastad I, et al. No Rest for the Weary: Diastolic Calcium Homeostasis in the Normal and Failing Myocardium. *Physiology* 2012; 27: 308–323.

[282] Limas CJ, Olivari MT, Goldenberg IF, et al. Calcium uptake by cardiac sarcoplasmic reticulum in human dilated cardiomyopathy. *Cardiovasc Res* 1987; 21: 601–605.

[283] Meyer Markus, Schillinger Wolfgang, Pieske Burkert, et al. Alterations of Sarcoplasmic Reticulum Proteins in Failing Human Dilated Cardiomyopathy. *Circulation* 1995; 92: 778–784.

[284] Hasenfuss G, Reinecke H, Studer R, et al. Calcium cycling proteins and force-frequency relationship in heart failure. *Basic Res Cardiol* 1996; 91 Suppl 2: 17–22.

[285] Brixius K, Savvidou-Zaroti P, Mehlhorn U, et al. Increased Ca2+-sensitivity of myofibrillar tension in heart failure and its functional implication. *Basic Res Cardiol* 2002; 97 Suppl 1: I111-117.

[286] Arai M, Matsui H, Periasamy M. Sarcoplasmic reticulum gene expression in cardiac hypertrophy and heart failure. *Circ Res* 1994; 74: 555–564.

[287] Mercadier JJ, Lompré AM, Duc P, et al. Altered sarcoplasmic reticulum Ca2(+)-ATPase gene expression in the human ventricle during end-stage heart failure. *J Clin Invest* 1990; 85: 305–309.

[288] Schwinger RHG, Münch G, Bölck B, et al. Reduced Ca2+-Sensitivity of SERCA 2a in Failing Human Myocardium due to Reduced Serin-16 Phospholamban Phoshorylation. *J Mol Cell Cardiol* 1999; 31: 479–491.

[289] Movsesian MA, Colyer J, Wang JH, et al. Phospholamban-mediated stimulation of Ca2+ uptake in sarcoplasmic reticulum from normal and failing hearts. *J Clin Invest* 1990; 85: 1698–1702.

[290] Frank K, Bölck B, Bavendiek U, et al. Frequency dependent force generation correlates with sarcoplasmic calcium ATPase activity in human myocardium. *Basic Res Cardiol* 1998; 93: 405–411.

[291] MacLennan DH, Kranias EG. Phospholamban: a crucial regulator of cardiac contractility. *Nat Rev Mol Cell Biol* 2003; 4: 566–577.

[292] Sikkel MB, Hayward C, MacLeod KT, et al. SERCA2a gene therapy in heart failure: an anti-arrhythmic positive inotrope. *Br J Pharmacol* 2014; 171: 38–54.

[293] Lompré AM, Lambert F, Lakatta EG, et al. Expression of sarcoplasmic reticulum Ca(2+)-ATPase and calsequestrin genes in rat heart during ontogenic development and aging. *Circ Res* 1991; 69: 1380–1388.

[294] Lakatta EG. Myocardial adaptations in advanced age. *Basic Res Cardiol* 1993; 88 Suppl 2: 125–133.

[295] Cain BS, Meldrum DR, Joo KS, et al. Human SERCA2a levels correlate inversely with age in senescent human myocardium. *J Am Coll Cardiol* 1998; 32: 458–467.

[296] Fragoso-Medina J, Zarain-Herzberg A. SERCA2a: its role in the development of heart failure and as a potential therapeutic target. *Res Rep Clin Cardiol* 2014; 5: 43–55.

[297] Bassani JWM, Bassani RA. SERCA upregulation: Breaking the positive feedback in heart failure? *Cardiovasc Res* 2005; 67: 581–582.

[298] del Monte F, Hajjar RJ, Harding SE. Overwhelming Evidence of the Beneficial Effects of SERCA Gene Transfer in Heart Failure. *Circ Res* 2001; 88: e66–e67.

[299] Lyon AR, Sato M, Hajjar RJ, et al. Gene therapy: targeting the myocardium. *Heart* 2008; 94: 89–99.

[300] Kawase Y, Ly HQ, Prunier F, et al. Reversal of Cardiac Dysfunction After Long-Term Expression of SERCA2a by Gene Transfer in a Pre-Clinical Model of Heart Failure. *J Am Coll Cardiol* 2008; 51: 1112–1119.

[301] Federica del Monte null, Harding SE, Schmidt U, et al. Restoration of Contractile Function in Isolated Cardiomyocytes From Failing Human Hearts by Gene Transfer of SERCA2a. *Circulation* 1999; 100: 2308–2311.

[302] Jaski BE, Jessup ML, Mancini DM, et al. Calcium upregulation by percutaneous administration of gene therapy in cardiac disease (CUPID Trial), a first-in-human phase 1/2 clinical trial. *J Card Fail* 2009; 15: 171–181.

[303] He W, Huang D, Guo S, et al. Association with SERCA2a directs phospholamban trafficking to sarcoplasmic reticulum from a nuclear envelope pool. *J Mol Cell Cardiol* 2020; 143: 107–119.

[304] Jorgensen AO, Shen AC, Daly P, et al. Localization of Ca2+ + Mg2+-ATPase of the sarcoplasmic reticulum in adult rat papillary muscle. *J Cell Biol* 1982; 93: 883–892.

[305] Drago GA, Colyer J, Lederer WJ. Immunofluorescence Localization of SERCA2a and the Phosphorylated Forms of Phospholamban in Intact Rat Cardiac Ventricular Myocytes a. *Ann N Y Acad Sci* 1998; 853: 273–279.

[306] Bondarenko VE, Bett GCL, Rasmusson RL. A model of graded calcium release and L-type Ca2+ channel inactivation in cardiac muscle. *Am J Physiol-Heart Circ Physiol* 2004; 286: H1154–H1169.

[307] Tomek J, Tomková M, Zhou X, et al. Modulation of Cardiac Alternans by Altered Sarcoplasmic Reticulum Calcium Release: A Simulation Study. *Front Physiol* 2018; 9: 1306.

[308] Zhao N, Li Q, Zhang K, et al. Heart failure-induced atrial remodelling promotes electrical and conduction alternans. *PLoS Comput Biol* 2020; 16: e1008048.

[309] Hobai IA, O'Rourke B. Decreased sarcoplasmic reticulum calcium content is responsible for defective excitation-contraction coupling in canine heart failure. *Circulation* 2001; 103: 1577–1584.

[310] Hasenfuss G, Reinecke H, Studer R, et al. Relation between myocardial function and expression of sarcoplasmic reticulum Ca(2+)-ATPase in failing and nonfailing human myocardium. *Circ Res* 1994; 75: 434–442.

[311] Bers DM. SARCOPLASMIC RETICULUM CA RELEASE IN INTACT VENTRICULAR MYOCYTES. 15.

[312] Aguero J, Ishikawa K, Hadri L, et al. Characterization of right ventricular remodeling and failure in a chronic pulmonary hypertension model. *Am J Physiol Heart Circ Physiol* 2014; 307: H1204-1215.

[313] Lou Q, Fedorov VV, Glukhov AV, et al. Transmural Heterogeneity and Remodeling of Ventricular Excitation-Contraction Coupling in Human Heart Failure. *Circulation* 2011; 123: 1881–1890.

[314] Wasserstrom JA, Sharma R, Kapur S, et al. Multiple Defects in Intracellular Calcium Cycling in Whole Failing Rat Heart. *Circ Heart Fail* 2009; 2: 223–232.

[315] Díaz M e., Eisner D a., O'Neill S c. Depressed Ryanodine Receptor Activity Increases Variability and Duration of the Systolic Ca2+ Transient in Rat Ventricular Myocytes. *Circ Res* 2002; 91: 585–593.

[316] Harzheim D, Movassagh M, Foo RS-Y, et al. Increased InsP3Rs in the junctional sarcoplasmic reticulum augment Ca2+ transients and arrhythmias associated with cardiac hypertrophy. *Proc Natl Acad Sci U S A* 2009; 106: 11406–11411.

[317] Harzheim D, Talasila A, Movassagh M, et al. Elevated InsP3R expression underlies enhanced calcium fluxes and spontaneous extra-systolic calcium release events in hypertrophic cardiac myocytes. *Channels Austin Tex* 2010; 4: 67–71.

[318] Go LO, Moschella MC, Watras J, et al. Differential regulation of two types of intracellular calcium release channels during end-stage heart failure. *J Clin Invest* 1995; 95: 888–894.

[319] Prins KW, Tian L, Wu D, et al. Colchicine Depolymerizes Microtubules, Increases Junctophilin-2, and Improves Right Ventricular Function in

Experimental Pulmonary Arterial Hypertension. *J Am Heart Assoc*; 6: e006195.

[320] Cantalapiedra IR, Alvarez-Lacalle E, Peñaranda A, et al. Minimal model for calcium alternans due to SR release refractoriness. *Chaos Woodbury N* 2017; 27: 093928.

[321] Wilson LD, Rosenbaum DS. Mechanisms of arrythmogenic cardiac alternans. *EP Eur* 2007; 9: vi77–vi82.

[322] Wilson LD, Jeyaraj D, Wan X, et al. Heart Failure Enhances Susceptibility to Arrhythmogenic Cardiac Alternans. *Heart Rhythm Off J Heart Rhythm Soc* 2009; 6: 251–259.

[323] Qu Z, Nivala M, Weiss JN. Calcium Alternans in Cardiac Myocytes: Order From Disorder. *J Mol Cell Cardiol* 2013; 58: 100–109.

[324] Nivala M, Qu Z. Calcium alternans in a couplon network model of ventricular myocytes: role of sarcoplasmic reticulum load. *Am J Physiol - Heart Circ Physiol* 2012; 303: H341–H352.

[325] Stary V, Puppala D, Scherrer-Crosbie M, et al. SERCA2a upregulation ameliorates cellular alternans induced by metabolic inhibition. *J Appl Physiol* 2016; 120: 865–875.

[326] Cutler MJ, Wan X, Plummer BN, et al. Targeted Sarcoplasmic Reticulum Ca2+ ATPase 2a Gene Delivery to Restore Electrical Stability in the Failing Heart. *Circulation* 2012; 126: 2095–2104.

[327] Qu Z, Weiss JN. Mechanisms of Ventricular Arrhythmias: From Molecular Fluctuations to Electrical Turbulence. *Annu Rev Physiol* 2015; 77: 29–55.

[328] Curran J, Brown KH, Santiago DJ, et al. Spontaneous Ca Waves in Ventricular Myocytes from Failing Hearts Depend on Ca2+-calmodulin-dependent Protein Kinase II. *J Mol Cell Cardiol* 2010; 49: 25–32.

[329] Liu MB, de Lange E, Garfinkel A, et al. Delayed afterdepolarizations generate both triggers and a vulnerable substrate promoting reentry in cardiac tissue. *Heart Rhythm* 2015; 12: 2115–2124.

[330] Campos FO, Shiferaw Y, Vigmond EJ, et al. Stochastic spontaneous calcium release events and sodium channelopathies promote ventricular arrhythmias. *Chaos Interdiscip J Nonlinear Sci* 2017; 27: 093910.

[331] Venetucci LA, Trafford AW, O'Neill SC, et al. The sarcoplasmic reticulum and arrhythmogenic calcium release. *Cardiovasc Res* 2008; 77: 285–292.

[332] MacLennan DH, Chen SRW. Store overload-induced Ca2+ release as a triggering mechanism for CPVT and MH episodes caused by mutations in RYR and CASQ genes. *J Physiol* 2009; 587: 3113–3115.

[333] O'Neill SC, Miller L, Hinch R, et al. Interplay between SERCA and sarcolemmal Ca2+ efflux pathways controls spontaneous release of Ca2+ from the sarcoplasmic reticulum in rat ventricular myocytes. *J Physiol* 2004; 559: 121–128.

[334] Sato D, Uchinoumi H, Bers DM. Increasing SERCA function promotes initiation of calcium sparks and breakup of calcium waves. *J Physiol* 2021; 599: 3267–3278.

[335] Macquaide N, Tuan H-TM, Hotta J, et al. Ryanodine receptor cluster fragmentation and redistribution in persistent atrial fibrillation enhance calcium release. *Cardiovasc Res* 2015; 108: 387–398.

[336] Marchena M, Echebarria B. Computational Model of Calcium Signaling in Cardiac Atrial Cells at the Submicron Scale. *Front Physiol* 2018; 9: 1760.

[337] Galice S, Xie Y, Yang Y, et al. Size Matters: Ryanodine Receptor Cluster Size Affects Arrhythmogenic Sarcoplasmic Reticulum Calcium Release. *J Am Heart Assoc* 2018; 7: e008724.

[338] Klein MG, Shou M, Stohlman J, et al. Role of suppression of the inward rectifier current in terminal action potential repolarization in the failing heart. *Heart Rhythm* 2017; 14: 1217–1223.

[339] North AJ. Seeing is believing? A beginners' guide to practical pitfalls in image acquisition. *J Cell Biol* 2006; 172: 9–18.

[340] Kang C, Brennan JA, Kuzmiak-Glancy S, et al. Technical advances in studying cardiac electrophysiology – Role of rabbit models. *Prog Biophys Mol Biol* 2016; 121: 97–109.

[341] Husti Z, Tábori K, Juhász V, et al. Combined inhibition of key potassium currents has different effects on cardiac repolarization reserve and arrhythmia susceptibility in dogs and rabbits. *Can J Physiol Pharmacol* 2015; 93: 535–544.

[342] Brunner M, Peng X, Liu GX, et al. Mechanisms of cardiac arrhythmias and sudden death in transgenic rabbits with long QT syndrome. *J Clin Invest* 2008; 118: 2246–2259.

[343] Chen Y-J, Chen S-A, Chen Y-C, et al. Electrophysiology of single cardiomyocytes isolated from rabbit pulmonary veins: implication in initiation of focal atrial fibrillation. *Basic Res Cardiol* 2002; 97: 26–34.

[344] Li H, Scherlag BJ, Kem DC, et al. The Propensity for Inducing Atrial Fibrillation: A Comparative Study on Old versus Young Rabbits. *J Aging Res* 2014; 2014: e684918.

[345] Zhou Z-W, Zheng H-C, Zhao L-F, et al. Effect of berberine on acetylcholine-induced atrial fibrillation in rabbit. *Am J Transl Res* 2015; 7: 1450–1457.

[346] Greiser M, Kerfant B-G, Williams GSB, et al. Tachycardia-induced silencing of subcellular Ca2+ signaling in atrial myocytes. *J Clin Invest* 2014; 124: 4759–4772.

[347] Di Francesco D, Noble D. A model of cardiac electrical activity incorporating ionic pumps and concentration changes. *Philos Trans R Soc Lond B Biol Sci* 1985; 307: 353–398.

[348] Heijman J, Erfanian Abdoust P, Voigt N, et al. Computational models of atrial cellular electrophysiology and calcium handling, and their role in atrial fibrillation. *J Physiol* 2016; 594: 537–553.

[349] Baczkó I, Jost N, Virág L, et al. Rabbit models as tools for preclinical cardiac electrophysiological safety testing: Importance of repolarization reserve. *Prog Biophys Mol Biol* 2016; 121: 157–168.

[350] Shimoni Y, Banno H, Clark RB. Hyperthyroidism selectively modified a transient potassium current in rabbit ventricular and atrial myocytes. *J Physiol* 1992; 457: 369–389.

[351] Fedida D, Giles WR. Regional variations in action potentials and transient outward current in myocytes isolated from rabbit left ventricle. *J Physiol* 1991; 442: 191–209.

[352] Fedida D, Shimoni Y, Giles WR. Alpha-adrenergic modulation of the transient outward current in rabbit atrial myocytes. *J Physiol* 1990; 423: 257–277.

[353] Giles WR, Imaizumi Y. Comparison of potassium currents in rabbit atrial and ventricular cells. *J Physiol* 1988; 405: 123–145.

[354] Giles WR, van Ginneken AC. A transient outward current in isolated cells from the crista terminalis of rabbit heart. *J Physiol* 1985; 368: 243–264.

[355] Clark RB, Giles WR, Imaizumi Y. Properties of the transient outward current in rabbit atrial cells. *J Physiol* 1988; 405: 147–168.

[356] Mancarella S, Yue Y, Karnabi E, et al. Impaired Ca2+ homeostasis is associated with atrial fibrillation in the alpha1D L-type Ca2+ channel KO mouse. *Am J Physiol Heart Circ Physiol* 2008; 295: H2017-2024.

[357] Li X, Zima AV, Sheikh F, et al. Endothelin-1–Induced Arrhythmogenic Ca2+ Signaling Is Abolished in Atrial Myocytes of Inositol-1,4,5-Trisphosphate(IP3)–Receptor Type 2–Deficient Mice. *Circ Res* 2005; 96: 1274–1281.

[358] Shanmugam M, Gao S, Hong C, et al. Ablation of phospholamban and sarcolipin results in cardiac hypertrophy and decreased cardiac contractility. *Cardiovasc Res* 2011; 89: 353–361.

[359] Kettlewell S, Saxena P, Dempster J, et al. Dynamic clamping human and rabbit atrial calcium current: narrowing I CaL window abolishes early afterdepolarizations. *J Physiol* 2019; 597: 3619–3638.

[360] Ko JH, Park WS, Earm YE. The protein kinase inhibitor, staurosporine, inhibits L-type Ca2+ current in rabbit atrial myocytes. *Biochem Biophys Res Commun* 2005; 329: 531–537.

[361] Voigt Niels, Heijman Jordi, Wang Qiongling, et al. Cellular and Molecular Mechanisms of Atrial Arrhythmogenesis in Patients With Paroxysmal Atrial Fibrillation. *Circulation* 2014; 129: 145–156.

[362] Muraki K, Imaizumi Y, Watanabe M, et al. Delayed rectifier K+ current in rabbit atrial myocytes. *Am J Physiol* 1995; 269: H524-532.

[363] Wang Z, Fermini B, Feng J, et al. Role of chloride currents in repolarizing rabbit atrial myocytes. *Am J Physiol* 1995; 268: H1992-2002.

[364] Qi A, Yeung-Lai-Wah JA, Xiao J, et al. Regional differences in rabbit atrial repolarization: importance of transient outward current. *Am J Physiol-Heart Circ Physiol* 1994; 266: H643–H649.

[365] Kanaporis G, Blatter LA. Calcium-activated chloride current determines action potential morphology during calcium alternans in atrial myocytes. *J Physiol* 2016; 594: 699–714.

[366] Hou J, Li W, Fei Y, et al. ICaL and Ito mediate rate-dependent repolarization in rabbit atrial myocytes. *J Physiol Biochem*; 74. Epub ahead of print 14 December 2017. DOI: 10.1007/s13105-017-0603-z.

[367] Vagos MR, Arevalo H, Heijman J, et al. A Computational Study of the Effects of Tachycardia-Induced Remodeling on Calcium Wave Propagation in Rabbit Atrial Myocytes. *Front Physiol* 2021; 12: 399.

[368] Workman AJ, Kane KA, Rankin AC. Ionic basis of a differential effect of adenosine on refractoriness in rabbit AV nodal and atrial isolated myocytes. *Cardiovasc Res* 1999; 43: 974–984.

[369] Workman AJ, Kane KA, Rankin AC. Rate-dependency of action potential duration and refractoriness in isolated myocytes from the rabbit AV node and atrium. *J Mol Cell Cardiol* 2000; 32: 1525–1537.

[370] Kettlewell S, Burton FL, Smith GL, et al. Chronic myocardial infarction promotes atrial action potential alternans, afterdepolarizations, and fibrillation. *Cardiovasc Res* 2013; 99: 215–224.

[371] Giommi A. *Does the small conductance Ca2+-activated K+ current (ISK) flow under physiological conditions in rabbit and human atrial isolated cardiomyocytes?* PhD, University of Glasgow, https://theses.gla.ac.uk/81927/ (2021, accessed 9 October 2021).

[372] Cheng H, Cannell MB, Hancox JC. Differential responses of rabbit ventricular and atrial transient outward current (Ito) to the Ito modulator NS5806. *Physiol Rep* 2017; 5: e13172.

[373] Li GR, Feng J, Wang Z, et al. Comparative mechanisms of 4-aminopyridine-resistant Ito in human and rabbit atrial myocytes. *Am J Physiol-Heart Circ Physiol* 1995; 269: H463–H472.

[374] Nygren A, Fiset C, Firek L, et al. Mathematical Model of an Adult Human Atrial Cell: The Role of K+ Currents in Repolarization. *Circ Res* 1998; 82: 63–81.

[375] Luo CH, Rudy Y. A model of the ventricular cardiac action potential. Depolarization, repolarization, and their interaction. *Circ Res* 1991; 68: 1501–1526.

[376] Al Abed A, Lovell NH, Dokos S. Local Heterogeneous Electrical Restitution Properties of Rabbit Atria. *J Cardiovasc Electrophysiol* 2016; 27: 743–753.

[377] Jiang W, Zeng M, Cao Z, et al. Icariin, a Novel Blocker of Sodium and Calcium Channels, Eliminates Early and Delayed Afterdepolarizations, As Well As Triggered Activity, in Rabbit Cardiomyocytes. *Front Physiol*; 8. Epub ahead of print 29 May 2017. DOI: 10.3389/fphys.2017.00342.

[378] Verkerk A, Geuzebroek G, Veldkamp M, et al. Effects of Acetylcholine and Noradrenalin on Action Potentials of Isolated Rabbit Sinoatrial and Atrial Myocytes. *Front Physiol* 2012; 3: 174.

[379] Viswanathan PC, Shaw RM, Rudy Y. Effects of IKr and IKs heterogeneity on action potential duration and its rate dependence: a simulation study. *Circulation* 1999; 99: 2466–2474.

[380] Jia X, Zheng S, Xie X, et al. MicroRNA-1 Accelerates the Shortening of Atrial Effective Refractory Period by Regulating KCNE1 and KCNB2 Expression: An Atrial Tachypacing Rabbit Model. *PLOS ONE* 2013; 8: e85639.

[381] Lang D, Petrov V, Lou Q, et al. Spatio-temporal control of the heart rate in the rabbit heart. *J Electrocardiol* 2011; 44: 626–634.

[382] Lord B, Boswood A, Petrie A. Electrocardiography of the normal domestic pet rabbit. *Vet Rec* 2010; 167: 961–965.

[383] Guo D, Young L, Wu Y, et al. Increased late sodium current in left atrial myocytes of rabbits with left ventricular hypertrophy: its role in the genesis of atrial arrhythmias. *Am J Physiol-Heart Circ Physiol* 2010; 298: H1375–H1381.

[384] Tsai W-C, Chen Y-C, Kao Y-H, et al. Distinctive sodium and calcium regulation associated with sex differences in atrial electrophysiology of rabbits. *Int J Cardiol* 2013; 168: 4658–4666.

[385] Zeng M, Jiang W, Tian Y, et al. Andrographolide inhibits arrhythmias and is cardioprotective in rabbits. *Oncotarget* 2017; 8: 61226–61238.

[386] Fu H, Li G, Liu C, et al. Probucol prevents atrial ion channel remodeling in an alloxan-induced diabetes rabbit model. *Oncotarget* 2016; 7: 83850–83858.

[387] Frommeyer G, Schmidt M, Clauß C, et al. Further insights into the underlying electrophysiological mechanisms for reduction of atrial fibrillation by ranolazine in an experimental model of chronic heart failure. *Eur J Heart Fail* 2018; 14: 1322–1331.

[388] Chang C-J, Chen Y-C, Lin Y-K, et al. Rivaroxaban modulates electrical and mechanical characteristics of left atrium. *J Biomed Sci* 2013; 20: 17.

[389] Keldermann RH, ten Tusscher KHWJ, Nash MP, et al. Effect of heterogeneous APD restitution on VF organization in a model of the human ventricles. *Am J Physiol Heart Circ Physiol* 2008; 294: H764-774.

[390] Franz MR. The electrical restitution curve revisited: steep or flat slope--which is better? *J Cardiovasc Electrophysiol* 2003; 14: S140-147.

[391] Selvaraj RJ, Picton P, Nanthakumar K, et al. Steeper restitution slopes across right ventricular endocardium in patients with cardiomyopathy at high risk of ventricular arrhythmias. *Am J Physiol Heart Circ Physiol* 2007; 292: H1262-1268.

[392] Eisner DA, Diaz ME, Li Y, et al. Stability and instability of regulation of intracellular calcium. *Exp Physiol* 2005; 90: 3–12.

[393] Greiser M, Lederer WJ, Schotten U. Alterations of atrial Ca2+ handling as cause and consequence of atrial fibrillation. *Cardiovasc Res* 2011; 89: 722–733.

[394] Garcia-Dorado D, Ruiz-Meana M, Inserte J, et al. Calcium-mediated cell death during myocardial reperfusion. *Cardiovasc Res* 2012; 94: 168–180.

[395] Zhong M, Rees CM, Terentyev D, et al. NCX-Mediated Subcellular Ca2+ Dynamics Underlying Early Afterdepolarizations in LQT2 Cardiomyocytes. *Biophys J* 2018; 115: 1019–1032.

[396] Qu Z, Xie L-H, Olcese R, et al. Early afterdepolarizations in cardiac myocytes: beyond reduced repolarization reserve. *Cardiovasc Res* 2013; 99: 6–15.

[397] Li H, Scherlag BJ, Kem DC, et al. Atrial tachycardia provoked in the presence of activating autoantibodies to β2-adrenergic receptor in the rabbit. *Heart Rhythm Off J Heart Rhythm Soc* 2013; 10: 436–441.

[398] Carmeliet E. Repolarization reserve in cardiac cells. *J Med Biol Eng* 2006; 26: 97–105.

[399] Kulkarni K, Visweswaran R, Zhao X, et al. Characterizing Spatial Dynamics of Bifurcation to Alternans in Isolated Whole Rabbit Hearts Based on Alternate Pacing. *BioMed Res Int* 2015; 2015: e170768.

[400] Martišienė I, Jurevičius J, Vosyliūtė R, et al. Evolution of Action Potential Alternans in Rabbit Heart during Acute Regional Ischemia. *BioMed Res Int* 2015; 2015: e951704.

[401] Earm YE, Ho WK, So IS. Inward current generated by Na-Ca exchange during the action potential in single atrial cells of the rabbit. *Proc R Soc Lond B Biol Sci* 1990; 240: 61–81.

[402] Ho WK, Earm YE. Voltage dependence and kinetics of Na-Ca exchange tail current in rabbit atrial myocytes. *Ann N Y Acad Sci* 1991; 639: 465–467.

[403] Wang Z, Feng J, Shi H, et al. Potential Molecular Basis of Different Physiological Properties of the Transient Outward K+ Current in Rabbit and Human Atrial Myocytes. *Circ Res* 1999; 84: 551–561.

[404] Kohl P, Noble D, Hunter PJ, et al. Models of cardiac ventricular action potentials: iterative interaction between experiment and simulation. *Philos Trans R Soc Lond Ser Math Phys Eng Sci* 2001; 359: 1127–1142.

[405] Yuan D, Zheng P, Tan C, et al. Influence of Continuous Training on Atrial Myocytes IK1 and IKAch and on Induction of Atrial Fibrillation in a Rabbit Model. *Cardiol Res Pract* 2018; 2018: 3795608.

[406] Crossman DJ, Ruygrok PN, Ruygrok PR, et al. Changes in the organization of excitation-contraction coupling structures in failing human heart. *PloS One* 2011; 6: e17901.

[407] Steele EM, Steele DS. Automated Detection and Analysis of Ca2+ Sparks in x-y Image Stacks Using a Thresholding Algorithm Implemented within the Open-Source Image Analysis Platform ImageJ. *Biophys J* 2014; 106: 566–576.

[408] Tian Q, Schröder L, Schwarz Y, et al. Large scale, unbiased analysis of elementary calcium signaling events in cardiac myocytes. *J Mol Cell Cardiol* 2019; 135: 79–89.

[409] Hammer KP, Hohendanner F, Blatter LA, et al. Variations in local calcium signaling in adjacent cardiac myocytes of the intact mouse heart detected with two-dimensional confocal microscopy. *Front Physiol* 2015; 5: 517.

[410] Fernandez-Tenorio M, Niggli E. Stabilization of Ca2+ signaling in cardiac muscle by stimulation of SERCA. *J Mol Cell Cardiol* 2018; 119: 87–95.

[411] Sutanto H, Lyon A, Lumens J, et al. Cardiomyocyte calcium handling in health and disease: Insights from in vitro and in silico studies. *Prog Biophys Mol Biol* 2020; 157: 54–75.

[412] Noble D, Garny A, Noble PJ. How the Hodgkin–Huxley equations inspired the Cardiac Physiome Project. *J Physiol* 2012; 590: 2613–2628.

[413] Noble D. From the Hodgkin-Huxley axon to the virtual heart. *J Physiol* 2007; 580: 15–22.

[414] Lou Q, Li W, Efimov IR. Multiparametric Optical Mapping of the Langendorff-perfused Rabbit Heart. *J Vis Exp JoVE* 2011; 3160.

[415] Cooper J, Mirams GR, Niederer SA. High-throughput functional curation of cellular electrophysiology models. *Prog Biophys Mol Biol* 2011; 107: 11–20.